Thermodynamic analysis of falling-film absorbers for improving the efficiency of absorption machines

Arnat Mahamoudou

UNIVERSITÉ SAVOIE MONT BLANC

THÈSE

Pour obtenir le grade de

DOCTEURE DE L'UNIVERSITÉ SAVOIE MONT BLANC

Spécialité : **Energétique et Génie des Procédés**

Arrêté ministériel : 25 Mai 2016

Présentée par

Arnat MAHAMOUDOU

Thèse dirigée par **Nolwenn LE PIERRÈS** et **Julien RAMOUSSE**

préparée au sein du **Laboratoire LOCIE**

dans **l'École Doctorale SIE**

Analyse thermodynamique des absorbeurs à film tombant pour l'amélioration de l'efficacité des machines à absorption

Soutenue le **5 octobre 2022**,
devant le jury composé de :

Mme. Lingai LUO
Directrice de Recherche, CNRS, Université de Nantes, Présidente
M. Pierre NEVEU
Professeur, Université de Perpignan, Rapporteur
M. Romuald RULLIERE
Maitre de conférences HDR, INSA Lyon, Rapporteur
Mme. Nolwenn LE PIERRÈS
Professeure, Université Savoie Mont-Blanc, Directrice de thèse
M. Julien RAMOUSSE
Maitre de conférences HDR, Université Savoie Mont-Blanc, Directeur de thèse

Quand j'étais jeune, je disais tout le temps à ma famille et à mes amis que je voulais obtenir un doctorat. En quoi ? Je ne savais pas forcément. Aujourd'hui, j'ai réalisé un de mes plus grands rêves et dans un domaine qui me passionne. Je suis heureuse de pouvoir participer à cette transition énergétique que fait face le monde en obtenant le diplôme de docteur en génie des procédés et énergétique.

Oula, je dois ralentir un peu. Revenons au tout début de cette histoire.

Le 01 octobre 2019, je suis arrivée au laboratoire LOCIE pour travailler avec Nolwenn Le Pierrès et Julien Ramousse tout en étant loin d'imaginer la grande aventure que j'allais vivre. Cette aventure, je ne l'ai pas vécue seule et je n'aurai jamais atteint la ligne d'arrivée seule. Je tiens à remercier ici, toutes les personnes qui ont contribué à cette réussite allant des directeurs de thèses, aux collègues, aux amis et à la famille.

Mes premiers remerciements vont naturellement à mes directeurs de thèse Nolwenn et Julien. Merci à vous deux pour la confiance que vous m'avez démontrée dès le premier jour. J'ai énormément apprécié nos réunions qui étaient toujours très productives et dans la bonne humeur. Sachez que j'ai beaucoup appris de vous deux. Alors oui, merci pour toutes les connaissances que vous m'avez transmises au cours de ces trois années de thèse. Sans votre aide, votre soutien et votre bienveillance, le fruit de ce travail n'aurait pas été aussi savoureux. Vous êtes deux belles personnes que je chéris et estime de tout cœur. J'ai adoré faire ma thèse avec vous ! J'espère que j'aurai l'occasion de travailler avec vous dans le futur. Il me reste encore beaucoup à apprendre de vous.

Je remercie les différents membres du jury : Pierre Neveu, professeur à l'université de Perpignan et Romuald Rulliere, maître de conférences à l'INSA de Lyon qui ont accepté la lourde tâche de rapporteurs ainsi que Lingai Luo, directrice de recherche CNRS à l'université de Nantes pour avoir accepté de présider le jury. Vos remarques, discussions et commentaires, ont enrichi ce travail et l'ont rendu encore plus intéressant. Je tiens à vous remercier d'avoir pris de votre temps pour lire ce manuscrit et à vous dire que j'ai adoré les échanges que nous avons eues. Une petite attention spéciale à Pierre Neveu qui a pris le temps de corriger ma démonstration sur la création d'entropie locale. Elle n'était pas simple à faire mais le résultat est beau à voir. Merci pour cette implication.

A toute la famille LOCIE, je veux que vous sachiez que chacun d'entre vous a contribué à cette réussite. Je me suis toujours sentie bien à vos côtés, j'ai aimé apprendre à connaître chacun d'entre vous. Vous avez su m'accueillir et m'intégrer. Chacun d'entre vous m'a apporté quelque chose au cours de ces trois années : des conseils, une nouvelle façon de percevoir certaines choses, un gain d'expérience et de maturité, et beaucoup plus, je m'en souviendrai avant chacune de mes décisions. Aujourd'hui, je pars avec une larme au coin de l'œil en me remémorant ces nombreux souvenirs : Je vais les garder et les chérir. Je garderai une part de vous tous dans mon cœur et j'espère que j'ai pu moi aussi laisser une part de moi-même au LOCIE. Une mention spéciale à mon équipe de choc : Prince, Alessia L, Julie, Taini, Cédric, Romain, Alessia B. Merci pour tous ces moments passés ensemble en dehors du LOCIE pour apprendre à mieux se connaître, pour toutes ces soirées de « Time Bomb ». Merci Prince de me faire rire avec ta capacité de dormir à n'importe quel endroit et à n'importe quel moment. Merci Alessia L pour avoir améliorer ma culture de danse européenne et pour nous avoir fait profiter de ta magnifique voix. Merci à Taini pour toutes les parties de Basket et pour le matelas gonflable qu'on utilisait au lac en été. Merci Cédric d'avoir partagé un peu de chez toi, l'Alsace, avec nous. Tu as été un bon guide. Merci Romain pour ta simplicité et ta bonne humeur (tu remercieras aussi Justine pour moi). Merci à Alessia B pour les randonnées et pour les courbatures qui ont suivies.

Je remercie ma maman et mon papa qui sont loin physiquement mais que je garde dans une place spéciale dans mon cœur. Merci à vous deux pour tout votre amour, pour tous vos sacrifices et surtout pour toujours avoir cru en nous. Merci Papa et maman de vous être battus pour nous donner cette éducation. A Halid, Maher et Hannane (mes frères et sœur) merci de m'avoir toujours soutenu dans mes choix et mes décisions. Merci aussi pour tous vos : " Tu peux le faire Arnat, tu es la meilleure " vos encouragements m'ont permis de réaliser ce rêve de petite fille. Ce travail est le fruit de votre amour et je vous le dédie. J'espère qu'il vous a rendu autant fiers de moi que moi je le suis de vous tous. A Halid, Maher et Hannane, vous aussi vous pouvez réaliser vos rêves. Vous êtes capable de tout. Par expérience, je dirai qu'il faut juste avoir la volonté. Bon courage à vous trois.

Je ne peux remercier des personnes sans remercier la personne qui était au front avec moi, mon Mari, Hardi. Merci pour ton soutien quotidien, pour ta confiance en moi et pour ton écoute. Ta patience envers l'impatiente personne que je suis ne cessera de m'épater. Tu es le seul à vraiment savoir comment se sont déroulées ces trois années.

A toute ma famille et ma belle-famille, je vous dédie ce travail.

Enfin, à Allah, qui a mis des personnes comme vous *TOUS* sur mon chemin pour permettre la réalisation de ce travail. J'ai hâte de voir ce qu'il me réserve pour la suite.

Table of contents

Table of contents I

Abstract V

French abstract VI

Nomenclature VII

Extended Abstract in French 10

Contexte général 10

Objectifs de la recherche 11

Chapitre I. Etat de l'art sur les absorbeurs à film tombant 11

Chapitre II. Analyse thermodynamique d'un évaporateur à film tombant laminaire 14

Chapitre III. Analyse d'un absorbeur LiBr-H_2O à film tombant à l'échelle locale basée sur l'évaluation de la génération d'entropie 17

Chapitre IV. Optimisation multi-objectives d'un absorbeur à film tombant 20

Conclusions générales et perspectives 24

General introduction 26

Context of the present research 26

Research objectives 26

Thesis organization 29

Chapter I. Review of coupled heat and mass transfer studies in falling film absorbers: modeling, experimental and thermodynamic approaches 32

1.1. Introduction 33

1.2. Theoretical and modeling approaches 33

1.2.1 Problem description 33

1.2.2 Free falling film surfaces in the laminar regime 36

1.2.2.1 Flat plate absorbers 36

1.2.2.2 Vertical tube absorbers 39

1.2.2.3 Horizontal tube absorbers 40

1.2.2.4 Summary on laminar falling film absorption 42

1.2.3 Wavy-laminar flow regime 47

1.2.3.1 Flat plate absorbers 48
1.2.3.2 Vertical and horizontal tube absorbers 49
1.2.3.3 Summary on wavy falling film 49
1.3. Experimental studies 51
1.4. Thermodynamic approach 55
1.4.1 Flat plate absorbers 56
1.4.2 Tube absorbers 57
1.4.3 Summary of the thermodynamic approach 57
Conclusions and scope of this work 58

Chapter II. Thermodynamic analysis in laminar falling film evaporator 60
2.1. Introduction 61
2.2. Problem description 61
2.2.1 Evaporator description 61
2.2.2 Evaporator model description 62
2.2.2.1 Model Assumptions 62
2.2.2.2 Hydraulic model 63
2.2.2.3 Thermal model 64
2.2.2.4 Performance parameters 64
2.2.2.5 Entropy generation 65
2.3. Resolution method and operating conditions 68
2.3.1 Numerical solution 68
2.3.2 Grid size effects 68
2.3.3 Operating conditions 68
2.3.4 Model validation 69
2.4. Evaporator analysis 72
2.4.1 Overall analysis and reference case 72
2.4.2 Parametric study 76
2.4.2.1. HTF Reynolds number influence 76
2.4.2.2. Film Reynolds number influence 79
2.4.2.3. Influence of the temperature difference between the film inlet and the interface temperature 83
Conclusions and discussions on the evaporator 86

Chapter III. Analysis of a falling film LiBr-H_2O absorber at local scale based on entropy generation... 88
3.1. Introduction... 89
3.2. Absorber description... 89
3.2.1 Absorber model Assumptions... 91
3.2.2 Governing equations... 91
3.2.2.1 Falling film... 91
3.2.2.2 Heat transfer fluid... 92
3.2.2.3 Wall... 93
3.2.3 Boundary conditions... 93
3.2.4 Numerical resolution... 94
3.2.5 Entropy generation formulation... 95
3.2.5.1 Falling film... 100
3.2.5.2 Heat transfer fluid... 100
3.2.5.3 Wall... 101
3.3. Operating conditions and model validation... 101
3.3.1 Operating conditions... 101
3.3.2 Model validation... 102
3.4. Absorber analysis... 104
3.4.1 Absorbed mass flow rate for the limit cases – adiabatic and isothermal walls... 104
3.4.2 Entropy generation analysis for the limit cases... 105
3.4.3 Absorbed mass flow rates when considering HTF... 107
3.4.4 Local entropy generation analysis when considering the HTF... 108
3.4.5 Total entropy generation in the entire absorber when considering the HTF... 113
Conclusions... 115

Chapter IV. Second law analysis and multi-objective optimization of a falling film absorber... 116
4.1. Introduction... 117
4.2. Problem description and resolution... 117
4.3. MOO: Definition of the design variables and objective functions... 117
4.3.1 Design variables and operating conditions... 117
4.3.2 Definition of the objective functions... 118
4.4. Results and discussions... 119
4.4.1 Parametric analysis of the different sources of irreversibilities... 119

4.4.2 Impact of the HTF and film Reynolds numbers on the absorber performance at component scale 122
4.4.3 Multi-objective optimization (MOO) 126
4.4.3.1 Pareto front analysis for the absorbed mass flow rate (absorption chiller case) 128
4.4.3.2 Pareto front analysis for the recovered heat 129
Conclusions 131

General conclusions 133
Perspectives 136

Appendix 138
Bibliography 142

Abstract

The current increase of the energy demand is mainly due to the increase in energy consumption in the building-tertiary sector where 20% of the energy consumption is dedicated to air conditioning due to the increase of the average global temperature of 1°C. However, the use of conventional chiullers and heat pumps has a considerable impact on global warming. Acting in the building sector would therefore make it possible to considerably reduce its carbon impact and its consequences.

Sorption systems have raised the interest of the scientific community in recent years due to their energy efficiency, high energy density, and potential use for solar heat during summer periods. Absorption systems, in particular, appear to be a good alternative to the mechanical compression refrigeration systems for different reasons such as their low electrical consumption. The operation of these thermodynamic machines is based on the implementation of various heat and mass exchangers (absorber, desorber, evaporator and condenser). The objective of this present research is to characterize in detail the phenomena of coupled mass and heat transfer at the local and component scales in the most critical exchangers: *the evaporator and the absorber*. The approach adopted is based on the thermodynamic analysis of these exchangers, according to the recent developments of the Thermodynamics of Irreversible Processes (TIP), with the aim of identifying the various local sources of irreversibilities, responsible for a degradation of the overall performance of the system.

Chapter I provides a state of the art of the coupled heat and mass transfer models and applications of the thermodynamic of irreversible processes in the absorber, in order to understand the main assumptions and limits of the different models. For a deep understanding of entropy generation sources in simpler exchangers, **Chapter II** is devoted to the study of an evaporator before including the coupled heat and mass transfer encountered in absorbers in the next chapters. The heat transfer fluid and film energy balances are solved simultaneously through a 2D model using an implicit finite difference scheme. Local and overall analysis are performed in order to study the impact of parameters such as the heat transfer fluid and film Reynolds numbers and inlet film temperature on entropy generation (thermal and viscous irreversibilities) and on thermal and evaporation efficiencies for both co and counter-current configurations. The model is then, extended to the absorber. Thus, **Chapter III** investigates real absorber case by modelling coupled heat and mass transfers. The heat transfer fluid is assumed to flow in counter-current with the falling film and different heat transfer fluid flow regimes are studied and compared to the limit cases – adiabatic and isothermal walls. A local entropy generation formulation is set to identify the different sources of irreversibilities with the aim of locating and quantifying them. **Chapter IV** is divided in two parts. The first part allows an overall analysis of the different sources of entropy generation when considering different operating conditions. Further, an equilibrium factor is introduced to study the impact of the heat transfer fluid and film flow rates in the absorbed mass flow rate, transferred heat and entropy generation. The second part focuses on a multi-objective optimization. Two optimization approaches were used in order to determine the Pareto front and to validate the optimal solutions.

Keywords: falling film, entropy generation, local and overall analysis, absorber, absorption machines

French abstract

L'augmentation de la demande d'énergie est principalement due à l'augmentation de la consommation d'énergie dans les secteurs du bâtiment et du tertiaire où 20% de la consommation d'énergie est consacrée à la climatisation en raison de l'augmentation de la température moyenne mondiale de 1°C. Or, l'utilisation des appareils de chauffage et de climatisation conventionnels a un impact considérable sur l'environnement car ils contribuent au réchauffement climatique. Agir dans le secteur du bâtiment en produisant du froid et de la chaleur bas carbone permettrait de réduire considérablement son impact environnemental.

Ces dernières années, les systèmes à sorption ont suscité l'intérêt de la communauté scientifique en raison de leur bonne efficacité énergétique, haute densité énergétique, de leurs faibles pertes de chaleur et de leur utilisation potentielle pour le stockage de l'énergie solaire pendant les périodes saisonnières. Les systèmes à absorption, en particulier, semblent être une bonne alternative à la compression mécanique des systèmes de réfrigération standards pour différentes raisons. Le fonctionnement de ces machines thermodynamiques est basé sur la mise en œuvre de différents échangeurs de chaleur et de masse (absorbeur, désorbeur, évaporateur et condenseur). L'objectif de ce projet de recherche est de caractériser en détail les phénomènes de transferts couplés de masse et de chaleur, non seulement à l'échelle locale mais aussi à l'échelle du composant, l'échangeur le plus critique et le moins connu des machines à absorption à savoir *l'absorbeur*. L'approche adoptée est basée sur l'analyse thermodynamique de ces échangeurs, selon les développements récents de la Thermodynamique des Processus Irréversibles (TIP), dans le but d'identifier les différentes sources d'irréversibilités responsables d'une dégradation des performances globales du système.

Le **chapitre I** présente un état de l'art des modèles de transferts couplés de chaleur et de masse et des applications de la thermodynamique des processus irréversibles à l'absorbeur, afin de comprendre les principales hypothèses et les limites des différents modèles. Pour une meilleure compréhension des sources d'irréversibilités dans les échangeurs simples, le **chapitre II** est consacré à l'étude d'un évaporateur avant d'introduire les phénomènes plus complexes observés dans l'absorbeur. Les bilans thermiques du fluide caloporteur et du film sont résolus simultanément à travers un modèle 2D utilisant un schéma implicite de différences finies. Des analyses locale et globale ont été réalisées afin d'étudier l'impact de paramètres tels que les nombres de Reynolds du fluide caloporteur et du film mais aussi la température du film en entrée sur la création d'entropie (irréversibilités thermique et visqueuse) et sur les efficacités thermique et d'évaporation pour les configurations à co et contre-courant. Le **chapitre III** développe un modèle 2D d'absorbeur. Afin d'étudier le cas réel de l'absorbeur, le fluide caloporteur est supposé s'écouler à contre-courant et différents régimes d'écoulement du fluide caloporteur sont étudiés et comparés aux cas limites - parois adiabatique et isotherme. Une formulation locale de la création d'entropie est proposée pour identifier les différentes sources d'irréversibilités dans le but de les localiser et de les quantifier. Le **chapitre IV** permet une analyse globale du comportement des différentes sources de création d'entropie en considérant différentes conditions de fonctionnement. Le facteur d'équilibre est introduit pour étudier l'impact des débits du fluide caloporteur et du film sur le débit massique absorbé, le flux transféré et la création d'entropie. Une optimisation multi-objectifs est également réalisée. Deux approches d'optimisation ont été utilisées afin de déterminer le front de Pareto et de valider les solutions optimales.

Mots clés : film tombant, création d'entropie, analyses locale et globale, absorbeur, machines à absorption.

Nomenclature

A	Surface	(m^2)
a	Thermal diffusivity	$(m^2.s^{-1})$
C	Concentration in the solution	$(mol.m^{-3})$
$C_{LiBr,in}$	Mass concentration of LiBr in the solution	$\left(kg_{LiBr}.kg_{sol}^{-1}\right)$
C_p	Thermal capacity	$(J.K^{-1}.kg^{-1})$
D	Diffusion coefficient	$(m^2.s^{-1})$
$D_{H_2O-LiBr}$	Diffusion coefficient of LiBr in H_2O	$(m^2.s^{-1})$
e	Thickness	(m)
g	Gravitational acceleration	$(m.s^{-2})$
h	Global heat transfer coefficient	$(W.m^{-1}.K^{-1})$
h_a	Surfacic heat of absorption	$(J.kg^{-1}.m^{-2})$
h_{vap}	Molar enthalpy	$(J.mol^{-1})$
ΔH_{abs}	Latent heat of absorption	$(J.kg^{-1})$
$\Delta H_{liq-vap}$	Latent heat of evaporation of the film fluid	$(J.kg^{-1})$
j_k	Diffusive molar flux of species k	$(mol.m^{-2}.s^{-1})$
j_q	Heat flux within the fluid	$(W.m^{-2})$
k	Thermal conductivity	$(W.K^{-1}.m^{-1})$
k_1	Constant	$(-)$
L	Length of the evaporator/absorber	(m)
Le	Lewis number $\left(\frac{D_{B-A}}{a}\right)$	$(-)$
l	Width of the evaporator/absorber	(m)
$\dot{M}_{abs}$	Absorbed mass flow rate per unit of width	$(kg.s^{-1}.m^{-1})$
$\dot{m}_{abs}$	Mass flux density due to absorption	$(kg.s^{-1}.m^{-2})$
$\dot{m}$	Flow rate	$(kg.s^{-1})$
$\mathcal{M}_{LiBr}$	LiBr molar mass	$(kg.mol^{-1})$
Pr	Prandtl number $\left(\frac{\mu}{\rho a}\right)$	$(-)$
p	Pressure	(Pa)
$\dot{Q}$	Heat transfer rate per unit of width	$(W.m^{-1})$

q	Surface heat flux	$(\mathrm{W.m^{-2}})$
Ŕ	Equilibrium factor	$(-)$
Re	Reynolds number	$(-)$
$\dot{S}_{gen}$	Entropy generation rate	$(\mathrm{W.K^{-1}})$
$\dot{S}$	Entropy generation rate per unit of width	$(\mathrm{W.K^{-1}.m^{-1}})$
T	Temperature	(K)
u	Flow velocity	$(\mathrm{m.s^{-1}})$
$\bar{u}$	Mean velocity	$(\mathrm{m.s^{-1}})$
Y	Mass fraction	$(-)$

Greek symbols

Γ	Mass flow rate per unit of width	$(\mathrm{kg.s^{-1}.m^{-1}})$
γ	Chemical potential	$(\mathrm{J.mol^{-1}})$
δ	Boundary layer	(m)
ε	Efficiency	$(-)$
λ	Conductivity	$(\mathrm{W.K^{-1}.m^{-1}})$
μ	Dynamic viscosity	(Pa. s)
ρ	Volumetric mass	$(\mathrm{kg.m^{-3}})$
γ_k	Chemical potential	$(\mathrm{J.mol^{-1}})$
$\dot{\sigma}$	Volumic entropy generation rate	$(\mathrm{W.K^{-1}.m^{-3}})$
τ_{evap}	Evaporation rate	$(-)$
τ	Tensor of shear stresses	(Pa)

Subscripts

A	Absorbent
A + R	Absorbent + Refrigerant
abs	Absorbed
bulk	Bulk
d	Diffusive
exch	Exchanged
evap	Evaporated
f	Film

fluid	Heat transfer fluid or falling film
gen	Generated/generation
htf	Heat transfer fluid
hydro	Hydrodynamic
interface	Liquid – vapor interface
in	Inlet
m	Mass
max	Maximal
out	Outlet
R	Refrigerant
sat	Saturated
sol	Solution
th	Thermal
tot	Total
v	Viscous
vap	Vapor
w	Wall

Extended Abstract in French

Contexte général

Compte tenu de l'épuisement des ressources fossiles et des différents accords internationaux en faveur des objectifs environnementaux, les pays du monde cherchent à produire de l'énergie de manière plus efficace et durable. La forte croissance de la demande énergétique observée en Europe a incité la mise en place de stratégies et de politiques climatiques pour atteindre des objectifs clés à l'horizon 2030. Les objectifs de l'Union européenne, d'ici 2030, vise à réduire les émissions de gaz à effet de serre d'au moins 40% par rapport à 1990, à augmenter la part des énergies renouvelables d'au moins 32% et à améliorer l'efficacité énergétique d'au moins 32,5% (Commission européenne 2019).

L'augmentation de la demande énergétique est principalement due à une forte croissance démographique induisant ainsi, une augmentation de la consommation d'énergie dans les secteurs résidentiel et tertiaire où la consommation est passée de 43% à 49% entre 1990 et 2020, correspondant à une augmentation d'environ 650 à 800 TWh soit environ 23% (Ministre de la transition écologique 2021). Dans le secteur résidentiel, 20% de la consommation énergétique est dédiée à la climatisation en raison de l'augmentation de la température moyenne mondiale de 1°C (ADEME 2018). Or, l'utilisation des machines classiques de chauffage et de climatisation a un impact considérable sur l'environnement car elles contribuent à l'appauvrissement de la couche d'ozone et au réchauffement climatique conduisant à une augmentation du besoin de climatisation. Les scientifiques se retrouvent donc dans un cycle vicieux entre le besoin de chauffage et de climatisation et leur impact climatique. Il est, de ce fait, important d'agir dans le secteur du bâtiment afin de répondre aux besoins de climatisation et de chauffage de la population, tout en réduisant l'impact carbone des machines thermodynamiques utilisées. Cependant, ces systèmes thermodynamiques bas carbone doivent aussi être compétitifs face aux systèmes traditionnels autant en termes de performance qu'en termes de coût.

Ces dernières années, les systèmes à sorption ont suscité l'intérêt de la communauté scientifique en raison de leur faible consommation électrique, de leurs faibles pertes de chaleur et de leur utilisation potentielle pour le stockage de l'énergie solaire pendant les périodes saisonnières. Les systèmes à absorption, en particulier, semblent être une bonne alternative aux machines à compression traditionnelles pour différentes raisons. Ces machines sont des systèmes trithermes permettant de répondre à différents besoins dans le secteur du bâtiment (chauffage, rafraichissement, stockage de chaleur, voire production électrique) à partir de sources de chaleur à température modérée (inférieure à 120°C pour la majorité des applications), pouvant ainsi largement contribuer à réduire les consommations électriques et fossiles du secteur. En effet, les systèmes à absorption présentent certains avantages tels que :

- *Le moyen de comprimer le fluide :*
  - Mécanique dans le cas d'une machine traditionnelle,
  - Thermochimique dans le cas de la machine à absorption.
- *Le type d'énergie nécessaire à cette compression*
  - Électrique dans le cas d'une machine traditionnelle,
  - Thermique dans le cas de la machine à absorption.

Cependant, les machines à absorption sont connues pour leur faible rendement thermique, leur encombrement (taille des équipements) et la nécessité d'un énorme investissement initial par rapport aux machines traditionnelles (Amin Altamirano 2021). C'est dans ce contexte que de plus en plus d'études et d'expériences sont menées dans les unités de recherches autant françaises que mondiales dans l'objectif d'améliorer le coefficient de performance de ces machines afin de les rendre compétitives par rapport aux machines traditionnelles.

Le fonctionnement des machines thermodynamiques à absorption est basé sur la mise en place de différents types d'échangeurs de chaleur et de masse : absorbeur, désorbeur, évaporateur et condenseur (Fig. 1.1.). L'efficacité de ces machines est affectée par le couple absorbant-réfrigérant choisi (Kang et al. 2000 ; De Lucas et al. 2007 ; Wakim 2018 ; Li et al. 2018), la conception du système (Yoon et al. 2008 ; Gomri 2009 ; Erregueragui et al. 2015 ; Nikbakhti et al. 2020), les conditions de fonctionnement (Florides et al. 2003 ; Kaynakli et Kilic 2007 ; Wonchala et al. 2014 ; Keinath et al. 2017) mais aussi par la performance des différents composants. Les études ont conclu que l'absorbeur est le composant clé de toute machine d'absorption (Srikhirin, Aphornratana et al 2001 ; Izquierdo et al. 2008 ; Ibarra-Bahena et Romero 2014). Les performances de l'absorbeur ont un impact direct sur la taille et la charge thermique de tous les autres composants (Ibarra-Bahena et Romero 2014). En effet, l'amélioration des performances de l'absorbeur par l'obtention de meilleures conditions de fonctionnement permettrait d'augmenter le phénomène d'absorption, de maximiser la récupération de la chaleur libérée lors de l'absorption, de permettre une meilleure conception des composants et de réduire les coûts. De plus en plus d'études se focalisent sur l'étude de l'absorbeur afin d'améliorer ses performances dans le but d'impacter positivement les performances globales des machines à absorption.

Objectifs de la recherche

L'objectif de ce projet de recherche est de caractériser finement les phénomènes de transferts couplés de masse et de chaleur à l'échelle locale dans l'absorbeur. L'approche adoptée est basée sur l'analyse thermodynamique de ces échangeurs, selon les développements récents de la Thermodynamique des Processus Irréversibles (TPI), dans le but d'identifier les différentes sources locales d'irréversibilités, responsables d'une dégradation des performances globales du système. Ces études permettent de mieux comprendre les phénomènes physiques (thermiques et massiques) mis en jeu dans ces composants afin d'identifier les moyens d'optimiser les performances globales du système à partir des leviers identifiés à l'échelle locale.

Afin de répondre aux objectifs de recherche, la thèse a été structurée en quatre différents chapitres, qui sont basés sur des articles de journaux et de conférences nationales et internationales.

Chapitre I. Etat de l'art sur les absorbeurs à film tombant

L'objectif de ce premier chapitre est de regrouper les progrès scientifiques réalisés dans un type spécifique d'absorbeurs, en se basant sur les conclusions et recommandations de la revue réalisée par Killion et Garimella (2001). En effet, afin de développer un modèle adapté à l'absorbeur, une étude approfondie de l'état de l'art est nécessaire pour comprendre les phénomènes mis en jeu ainsi que les différentes hypothèses utilisées et les limites des modèles existants. Il existe différents types de configuration d'absorbeurs, à savoir : les absorbeurs à plaque, à membrane, à tubes verticaux et horizontaux pour différents modes d'absorption : film tombant, spray et bulles (Mehrez 2019). Le focus

est fait sur les absorbeurs à film tombant car ils sont plus flexibles et adaptés à différentes applications, sont relativement peu coûteux et offrent de grandes performances (Altamirano et al. 2020, Michel et al. 2017). Ce chapitre de l'état de l'art est divisé en deux parties. La description du fonctionnement d'un absorbeur à film tombant est donnée sur la Fig. 1.3. La première partie se concentre sur les approches théoriques, numériques et analytiques, utilisées et les hypothèses faites pour obtenir la distribution de température et de concentration sur un film tombant pour le cas d'un film à épaisseur constante et à épaisseur variable afin de comprendre les phénomènes physiques qui se produisent pendant le processus d'absorption. Les résultats des récentes études expérimentales à l'échelle locale sont également mentionnées dans cette partie. La deuxième partie est consacrée à l'application de la thermodynamique des processus irréversibles à ces absorbeurs. L'objectif étant d'identifier les différentes sources de création d'entropie et comment évoluent ces sources d'irréversibilités avec les conditions opératoires.

❖ Etudes théoriques et résultats expérimentaux

Etudes théoriques supposant une épaisseur de film constante

Dans leur revue, Killion et Garimella (2001) ont souligné l'importance de considérer des conditions aux limites plus réalistes, en considérant un fluide caloporteur, plutôt que de supposer une paroi adiabatique ou isotherme. En effet, dans le film, il y a le développement d'une couche limite thermique due à l'équilibre thermodynamique à l'interface liquide - vapeur, mais aussi une couche limite thermique due au fluide caloporteur. Dans les études récentes, des nombreux auteurs ont cherché à intégrer le fluide caloporteur dans l'analyse de l'absorbeur, cependant, aucun d'entre eux n'a analysé l'interaction à l'échelle locale. Le bilan énergétique à travers la paroi est fait au moyen d'un coefficient de transfert de chaleur global ou en supposant un profil linéaire de la température du fluide caloporteur (Rosa et al. 2020; Rogdakis, et al 2003; Bo et al. 2010; Wu 2016; Papaefthimiou et al 2006; Papaefthimiou et al. 2012; Babadi and Farhanieh 2005). Il est important de considérer le fluide caloporteur car son débit et sa température d'entrée influencent les performances de l'absorbeur. Bien que de nombreux travaux aient essayé de supprimer certaines des hypothèses courantes appliquées aux absorbeurs à film tombant afin de se rapprocher le plus possible des cas réels, de nombreuses hypothèses simplifiées restent jusqu'à présent, utilisées pour modéliser le transfert local de chaleur et de masse. Les plus utilisées sont la considération des propriétés physiques constantes du fluide de travail et l'équilibre thermodynamique à l'interface liquide-vapeur. D'une manière générale, les hypothèses rencontrées le plus souvent dans les modèles sont regroupées dans le Tableau 1.1. La plupart des études locales sont réalisées sur le couple LiBr-H_2O et peuvent se généraliser lors de l'utilisation de différents fluides de travail en raison des mêmes phénomènes physiques rencontrés.

Etudes théoriques supposant une épaisseur de film variable

Peu d'études ont examiné l'impact de l'hydrodynamique - écoulements ondulés et turbulents (Fig. 1.6) - sur le processus de transfert de chaleur et de masse rencontré dans les absorbeurs à film tombant (Sabir, Suen, and Vinnicombe 1996; García-Rivera et al. 2016; Killion and Garimella 2004b; Subramaniam and Garimella 2014; Subramaniam, Chandrasekaran, and Garimella 2021). Les améliorations du transfert de chaleur et de masse observées, lorsque l'impact de l'hydrodynamique est considéré, sont principalement dues à la convection et à la vitesse transversale associée, mais aussi à la présence de recirculation dans le film. Comme suggéré par Killion et Garimella (2001), l'hydrodynamique devrait être considérée simultanément de manière couplée avec les processus de

transfert de chaleur et de masse pour avoir une représentation plus réaliste de sa contribution sur le phénomène d'absorption. Cependant, la modélisation des ondes à la surface libre du film tombant reste très complexe.

La plupart des recherches considérant une épaisseur du film variable ont été réalisées sur des films tombant sur une plaque verticale. Plus récemment, les études se sont orientées vers les écoulements sur des absorbeurs à tubes horizontaux (Tableau 1.3). Plusieurs de ces études se limitent à l'étude d'un tube horizontal (Meyer 2014; Giannetti et al. 2017) et très peu d'entre elles étudient l'impact de l'écoulement du film d'un tube à un autre (Jeong and Garimella 2002; Killion and Garimella 2004a; Kyung, Herold, and Kang 2007b) (Fig. 1.5). En effet, l'impact des gouttelettes sur le tube suivant génère des ondes qui perturbent l'écoulement du film et le film est donc laminaire ondulé. De plus, la gravité et la tension de surface jouent un rôle majeur sur la formation des gouttelettes. Des études plus détaillées doivent être menées sur les absorbeurs à tubes horizontaux afin de mieux comprendre les différents phénomènes qui peuvent être rencontrés, car les études sur les gouttelettes et leur impact sur les phénomènes d'absorption sont très récentes.

Etudes expérimentales

Sur les modèles numériques et analytiques recensés, la plupart des auteurs ont supposé que l'écoulement du film est laminaire et uniforme et ont donc sous-estimé l'efficacité thermique et massique de l'absorbeur sachant que les films tombants sont naturellement ondulés (Tableau 1.2). La validation expérimentale reste alors indispensable afin de corriger les modèles théoriques et d'avoir une représentation plus réaliste des phénomènes locaux. Cette validation locale permettrait d'investiguer comment agir au niveau local pour améliorer le comportement à l'échelle de l'absorbeur comme le souligne (Killion et Garimella 2001). Cependant, très peu d'études expérimentales ont été trouvées et sont plus orientées vers l'études locales des phénomènes sur des absorbeurs à tubes horizontaux. De ce fait, plusieurs modèles numériques et analytiques restent jusqu'à lors non validés par des études expérimentales. Le tableau 1.4 résume les différents résultats clés des études expérimentales.

❖ Approche thermodynamique

Dans tout système, il existe des irréversibilités évitables/non évitables mais aussi endogènes/exogènes. Afin d'améliorer les performances de l'absorbeur, des actions doivent être mises en place pour réduire les irréversibilités évitables endogènes (Amidpour and Manesh 2021). Les irréversibilités inévitables sont celles qui ne peuvent être réduites en raison de contraintes physiques et économiques, tandis que les irréversibilités évitables sont celles obtenues par la différence entre les irréversibilités totales et les irréversibilités inévitables. Les irréversibilités endogènes d'un composant sont dues à l'inefficacité du composant lui-même lorsque tous les autres composants du système sont supposés être idéaux. Les irréversibilités exogènes sont obtenues par la différence entre les irréversibilités totales et endogènes. La thermodynamique des processus irréversibles permet d'identifier les différents phénomènes qui induisent des irréversibilités à l'échelle locale. Cette approche thermodynamique permet donc de mieux comprendre les différentes sources de création d'entropie. Les chercheurs s'accordent à dire que la création d'entropie est la somme des irréversibilités thermiques, visqueuses, convectives et diffusives (Equation 1.10). Jusqu'à présent, seul l'impact de la température d'entrée du film a été étudié dans le cas d'une plaque verticale, alors que pour un tube horizontal, l'impact du rayon du tube et du nombre de Reynolds du film sur la création

d'entropie a aussi été analysé. Le peu d'études retrouvées dans cette partie supposent une paroi adiabatique ou isotherme de l'absorbeur. Aucune de recherches menées n'a prise en compte l'effet du fluide caloporteur et de la paroi sur la création d'entropie.

❖ Conclusion

Ce chapitre présente l'état de l'art des études réalisées sur les machines à absorption en général et sur les absorbeurs à film tombant en particulier. Différentes approches numériques et analytiques sont décrites pour l'évaluation des profils locaux de température, de concentration et de vitesse pour des absorbeurs à plaque plane, à tubes verticaux et horizontaux. La littérature montre à quel point il est compliqué de valider les champs de température et de concentration locaux dans les films tombant obtenus à l'aide de modèles théoriques avec des résultats expérimentaux en raison de la précision de la technologie à utiliser : la plupart des études expérimentales ne fournissent que les températures et concentrations moyennes entre la paroi et l'interface du film. Par conséquent, les modèles de film tombant développés dans le cadre de cette thèse, ont été comparés avec d'autres résultats de simulation.

La condition limite non isotherme a un impact significatif sur le phénomène d'absorption. Il est donc important d'inclure l'étude du fluide caloporteur dans l'analyse du comportement de l'absorbeur. Dans le cadre de ce projet de thèse, un débit de fluide caloporteur non nul (non adiabatique) et non infini (non isotherme) est modélisé en utilisant les bilans locaux d'énergie et de quantité de mouvement. Le fluide caloporteur est considéré soit en régime laminaire (Rehtf < 2300) soit en régime turbulent (Rehtf > 4500) dans le but d'analyser son impact sur les films tombant - d'abord sur l'évaporateur (chapitre II) puis sur l'absorbeur à film tombant (chapitre III et IV).

Chapitre II. Analyse thermodynamique d'un évaporateur à film tombant laminaire

Avant d'étudier les phénomènes couplés de chaleur et masse observés dans un absorbeur à film tombant, un premier modèle simplifié a été développé pour étudier un évaporateur. Un film laminaire d'eau s'écoulant par gravité sur une plaque verticale chauffée par un fluide caloporteur – Fig. 2.1 –est étudié pour déterminer les champs de température et de création d'entropie locaux ainsi que le débit massique évaporé, en supposant une pression de saturation constante à l'interface libre, dans des configurations d'écoulement du fluide caloporteur à co-courant et à contre-courant. Les équations du fluide de transfert de chaleur et de l'énergie du film sont résolues simultanément par un modèle 2D utilisant un schéma implicite de différences finies.

Une analyse locale et globale de la création d'entropie est effectuée à travers l'ensemble de l'évaporateur - en considérant non seulement le film mais aussi le fluide caloporteur et la paroi afin de quantifier la part d'irréversibilités générées dans chaque milieu en fonction des conditions de fonctionnement. Connaître la distribution locale de la création d'entropie, permet de mieux comprendre les phénomènes physiques qui induisent des irréversibilités, et de les localiser à travers l'évaporateur dans l'objectif d'améliorer les performances des évaporateurs à film tombant. Par ailleurs, l'effet de la surchauffe et du sous-refroidissement du film ainsi que du nombre de Reynolds du fluide caloporteur et du film, sur l'efficacité d'évaporation ainsi que sur le taux d'évaporation et la création d'entropie est étudié. L'impact d'autres paramètres tels que la longueur de l'évaporateur est également analysé et les résultats sont donnés à la fois à l'échelle locale et à l'échelle des composants.

❖ Méthodes et équations

Les bilans thermiques sont écrits sur les différents médiums de l'évaporateur à savoir le fluide caloporteur, la paroi ainsi que le film tombant sur la base d'hypothèses simplificatrice telles que : fluides incompressibles, newtoniennes et de propriétés physiques constantes, écoulement laminaire, faible débit évaporé (épaisseur du film constant), température d'évaporation égale à la température de saturation et supposée constante tout au long de l'interface du film.

Dans un évaporateur, la création d'entropie est la somme d'irréversibilités thermiques et visqueuses. Les irréversibilités thermiques sont dues à la présence de gradient de température alors que les irréversibilités visqueuses sont causées par le mouvement du fluide (les frictions). De ce fait, des irréversibilités thermiques sont générées dans le film tombant, le fluide caloporteur et la paroi. Les irréversibilités thermiques totales de l'évaporateur sont alors égales à la somme des trois irréversibilités thermiques produites sur les trois médiums. Les irréversibilités visqueuses sont observées uniquement dans le film tombant et dans le fluide caloporteur : La somme de ces deux irréversibilités donne les irréversibilités visqueuses totales du composant.

❖ Analyse paramétrique

D'une manière générale, l'étude démontre que les créations d'entropie locale sont principalement observées proches de la paroi d'échange et à l'entrée des deux fluides (film et fluide caloporteur).

Influence du Reynolds du fluide caloporteur

Pour les deux configurations étudiées (à savoir co et contre-courant), plus le nombre de Reynolds du fluide caloporteur est élevé, plus la création d'entropie thermique globale est importante et plus l'efficacité thermique est faible. L'augmentation du nombre de Reynolds du fluide caloporteur de 500 à 2000 augmente la création d'entropie d'environ 44%, 51% et 66% pour L = 0.1, 0.3 et 0.5 m respectivement pour les deux configurations en raison du développement lent de la couche limite thermique et de l'augmentation de la chaleur transférée (pour un Re_f = 50, e_{htf} = 1 mm et $\Delta T = T_{f,in} - T_{f,sat}$ = 0 – Fig. 2.7). Le taux d'évaporation et le coefficient d'échange du fluide caloporteur sont aussi considérablement impactés par ce paramètre alors que le coefficient d'échange du film n'est pratiquement pas impacté.

Dans les conditions étudiées, l'irréversibilité thermique la plus élevée se situe dans le fluide caloporteur, suivi par celle dans le film – Fig. 2.8. L'irréversibilité thermique dans la paroi représente moins de 2% de la création d'entropie thermique totale. De plus, l'augmentation du nombre de Reynolds du fluide caloporteur conduit à une augmentation de l'ensemble des irréversibilités thermiques. Cependant, elle a plus d'impact sur l'irréversibilité thermique du film que sur les autres irréversibilités en raison de l'augmentation du phénomène d'évaporation : l'irréversibilité thermique dans le film passe de 32% à 43% de la création d'entropie thermique totale pour un Re_{htf} variant de 500 à 2000 dans les deux configurations. La Fig. 2.9 permet de visualiser l'évolution de la création d'entropie d'origine thermique avec le développement des couches limites thermiques. La création d'entropie visqueuse du fluide caloporteur augmente avec le nombre de Reynolds (augmentation des frictions). Elle est égale à zéro près de la plaque, ce qui s'explique par une vitesse égale à zéro et augmente paraboliquement, suivant l'équation (2.9), pour être maximale au centre du canal.

Influence du Reynolds du film

Le nombre de Reynolds du film tombant impacte aussi le comportement de l'absorbeur. En effet, l'efficacité d'évaporation diminue avec l'augmentation de la vitesse du film et avec la diminution de la longueur de l'évaporateur – Fig. 2.10 : l'augmentation du nombre de Reynolds du film conduit à une augmentation de l'épaisseur du film et donc à une augmentation de la résistance thermique, par conséquent une plus grande partie de l'énergie transférée du fluide caloporteur au film est utilisée pour augmenter la température du film - 6% de l'énergie transférée est utilisée pour augmenter la température du film en écoulement à contre-courant pour Re_f = 50 et L = 0.1 m contre 27% pour Re_f = 200. L'analyse de la création d'entropie visqueuse montre une augmentation de cette dernière avec l'augmentation du nombre de Reynolds du film et de la longueur de l'évaporateur. Cependant, la contribution des irréversibilités visqueuses totales sur la création d'entropie totale reste négligeable : pour Re_f = 50, cette contribution est d'environ 0.4% et 0.7% pour L = 0.1 m et L = 0.5 m respectivement contre 0.8% et 1.3% pour Re_f = 200.

Contrairement aux résultats obtenus lors de l'étude de l'impact du nombre de Reynolds du fluide caloporteur, l'augmentation du nombre de Reynolds du film entraîne une diminution de l'irréversibilité thermique dans le fluide caloporteur tandis que l'irréversibilité dans film est légèrement affectée – Fig. 2.12. La diminution de l'irréversibilité dans le fluide caloporteur est due à une diminution de la chaleur transférée à travers la paroi, causée par le développement lent de la couche limite thermique à l'intérieur du film due à augmentation de l'épaisseur du film et de la résistance thermique.

Influence de la température d'entrée du film

L'étude de la différence de température entre la température d'entrée du film et la température de saturation montre qu'un film sous-refroidi conduit à la création d'entropie thermique la plus élevée et au taux d'évaporation le plus faible (Fig. 1.13). Cela est dû au gradient de température élevé entre le fluide caloporteur et le film, qui entraîne une diminution de l'efficacité de l'évaporation. L'analyse montre également que l'évolution du taux d'évaporation avec la création d'entropie admet un minimal. Ce dernier est rencontré lorsque le ΔT = 1 K dans les conditions considérées.

Cependant, plus la température d'entrée du film est élevée, plus la création d'entropie thermique près de la paroi est faible et plus celle à l'interface est élevée – Fig. 2.14. A l'entrée du film, deux couches limites thermiques sont en cours de développement. La première est la couche limite thermique causée par le flux de chaleur transféré à travers la paroi, tandis que la seconde est la couche limite thermique causée par le phénomène d'évaporation à l'interface libre. Ainsi, même si la surchauffe conduit à une augmentation significative du taux d'évaporation en raison d'une efficacité d'évaporation élevée, la différence de température optimale doit être trouvée afin d'éviter une création d'entropie totale élevée. Pour les films surchauffés, l'efficacité d'évaporation est supérieure à l'unité car dans sa définition l'énergie transportée par le film à l'entrée n'est pas considérée. Il appartient à l'ingénieur de trouver un compromis entre la création d'entropie acceptable et le taux d'évaporation désiré, surtout si l'évaporateur est associé à d'autres composants.

❖ Conclusion

Dans cette étude, le nombre de Reynolds du film est limité à 200 au-delà de cette valeur, le film ne pourrait plus être considéré comme laminaire et le modèle développé n'est pas adapté aux films ondulés. L'analyse de l'impact du nombre de Reynolds du fluide caloporteur et du film sur la création

d'entropie, montre des tendances opposées de l'irréversibilité dans le fluide caloporteur. Ces paramètres peuvent donc être considérés comme des paramètres d'optimisation dans l'objectif de diminuer la création d'entropie tout en préservant les performances du composant. Par ailleurs, l'analyse paramétrique réalisé a permis de comprendre le développement des couches limites thermiques et leur impact sur la distribution de la création d'entropie dans l'ensemble de l'évaporateur (à savoir dans le fluide caloporteur, la paroi et le film tombant). Le modèle développé pour l'évaporateur à film tombant est étendu, dans le chapitre suivant, au cas d'un absorbeur à film tombant dans l'objectif de comprendre l'impact des transferts thermique et massique couplés dans la création des irréversibilités.

Chapitre III. Analyse d'un absorbeur LiBr-H_2O à film tombant à l'échelle locale basée sur l'évaluation de la génération d'entropie

Après avoir étudié et compris les phénomènes présents dans l'évaporateur, ce chapitre est consacré, d'une part, au développement d'un modèle pouvant simuler les phénomènes observés dans un absorbeur et d'autre part, à la formulation de la création d'entropie afin d'identifier les différentes sources d'irréversibilités. La particularité de cette étude consiste à l'introduction du fluide caloporteur en régime laminaire et en régime turbulent. Le but étant de comprendre l'impact de ce fluide, mal modélisé jusqu'à lors, sur les phénomènes rencontrés dans l'absorbeur. Les cas limites, à savoir les cas de parois adiabatiques et isothermes sont aussi étudiés afin de relever les différences entre les cas limites et les plus réalistes. L'étude se focalise principalement à ce qui se passe à l'échelle locale, cependant des résultats à l'échelle du composant sont aussi donnés.

❖ Description du problème

Une solution composée de l'absorbant (bromure de lithium, LiBr) et du réfrigérant (eau) qui s'écoule sous l'effet de la gravité sur une plaque verticale et en contact avec la vapeur d'eau à une pression de vapeur constante (P_{vap}) – Fig. 3.1. La solution entre dans l'absorbeur avec une concentration d'absorbant ($C_{LiBr,in}$) et une température ($T_{f,in}$) uniformes. La solution de LiBr reste en phase liquide, à l'entrée et dans tout l'absorbeur, tandis que la vapeur d'eau peut être absorbée ou désorbée par la solution (tout au long du processus) dépendamment de si le film est sous-refroidit ou surchauffé à l'entrée de l'absorbeur. La différence de potentiel chimique entre le film et la vapeur induit un transfert de masse de l'eau dans la solution par absorption. Cette absorption exothermique libère de la chaleur qui augmente la température du film. Les profils de température, de concentration et de vitesse sont représentés sur la Fig. 1.a. Les phénomènes de transfert de chaleur et de masse conduisent à la formation de couches limites thermiques ($\delta_{htf,th}$, $\delta_{f,th1}$, $\delta_{f,th2}$) et diffusives ($\delta_{f,m}$) dans le film comme le montrent les Fig. 1.b et 1.c. Dans cette étude, l'hydrodynamique dans le film et dans le fluide caloporteur est supposé totalement établie. $\delta_{htf,th}$ représente la couche limite thermique dans le fluide caloporteur due au changement de température causé par le transfert de chaleur avec la solution. $\delta_{f,th1}$ et $\delta_{f,th2}$ représentent les couches limites thermiques dans le film dues, respectivement, à la chaleur transférée du film au fluide caloporteur à travers la paroi, et à l'augmentation de la température du film causée par l'absorption à l'interface libre. L'absorption entraîne une augmentation de la concentration de réfrigérant dans le film et donc, $\delta_{f,m}$ représente la couche limite diffusive liée au transport du réfrigérant à travers le film. Comme le montre la Fig. 3.1, deux cas sont étudiés dans ce chapitre : un film sous-refroidi à l'entrée et un film à l'état d'équilibre à l'entrée.

❖ Résultats

Cas limites - parois adiabatiques et isothermes

Pour étudier le cas adiabatique, le film est supposé sous-refroidit, par rapport à l'interface, à l'entrée de l'absorbeur afin d'assurer une absorption. Pour le cas isotherme, deux cas sont étudiés : un cas où le film entre sous-refroidit et un autre cas où le film entre en équilibre thermodynamique.

Lorsque le film est supposé sous-refroidit, il n'y a pas de différence entre le cas adiabatique et le cas isotherme, proche de l'entrée – Fig. 3.3. En effet, les couches limites thermiques sont toujours en cours de développement et donc l'effet de la paroi n'est pas encore ressenti. La différence entre les deux cas limites se perçoit que lorsque $\delta_{f,th1} = \delta_{f,th2}$, le débit absorbé dans le cas adiabatique continue à décroitre du fait qu'il n'y a pas d'évacuation de la chaleur libérée à l'interface alors que dans le cas isotherme, il augmente du fait de la récupération de la chaleur.

L'analyse de la création d'entropie décrite sur la Fig. 3.4 montre que :

- A l'interface liquide-vapeur, les créations d'entropie d'origine massique dominent celles d'origine thermique. De plus, l'évolution de la création d'entropie en fonction de la distance à l'entrée est le même que celle du débit évaporé (Fig. 3.3. et 3.4).
- A la paroi, la création d'entropie d'origine thermique et celle d'origine massique tendent vers zéro pour le cas d'une paroi adiabatique non seulement à cause de la non récupération de la chaleur libérée à l'interface mais aussi à cause des faibles conductivité et diffusivité au sein du film tombant : de ce fait, ce sont les irréversibilités d'origine visqueuses qui dominent proche de la paroi. Dans le cas d'une paroi isotherme, l'analyse montre que les irréversibilités sont plus grandes au niveau de la paroi par rapport à celles à l'interface liquide-vapeur et sont d'origine thermique. Ceci s'explique par le gradient de température élevé entre le film et la paroi.

Cas considérant un fluide caloporteur de débit non nulle et fini

Après avoir étudié et analysé les deux cas limites, la suite du chapitre s'est focalisée sur l'introduction du fluide caloporteur permettant ainsi de modéliser des cas réels d'absorbeur. La Fig. 3.5 montre l'évolution du débit absorbé en fonction du Reynolds du fluide caloporteur tout au long de l'absorbeur lorsque le film est supposé être en équilibre thermodynamique avec la vapeur à l'entrée de l'absorbeur. Les résultats montrent une augmentation du débit absorbée en fonction de l'augmentation du Reynolds du fluide caloporteur. Cependant, deux comportements différents sont observés en fonction du régime d'écoulement du fluide caloporteur (laminaire ou turbulent). En effet, pour des faibles Reynolds du fluide caloporteur, le débit massique absorbé augmente à proximité de la sortie. Pour des nombres de Reynolds élevés - écoulements turbulents - et pour le cas isotherme, ce comportement n'est pas observé : l'augmentation du débit à la sortie est due, d'une part, au développement rapide des couches limites thermiques et d'autre part, au gradient de température élevé entre les deux fluides à des faibles Reynolds du fluide caloporteur. Pour une meilleure analyse et compréhension des phénomènes, l'analyse de la création d'entropie est faite à l'échelle locale et à l'échelle du composant.

- **Echelle locale**

En supposant un film à l'état d'équilibre, aucun phénomène ne se produit près de l'interface film-vapeur à l'entrée de l'absorbeur – Fig. 3.7. Le film transfère une partie de son énergie au fluide frigorifique à travers la paroi. Ce transfert diminue la température du film conduisant au développement de la couche limite thermique $\delta_{f,th1}$. À ce stade, aucun transfert de masse n'est observé. Par conséquent, à l'intérieur de la couche limite thermique $\delta_{f,th1}$, des irréversibilités dues au transfert thermique apparaissent et au-delà de cette couche limite, aucune génération d'entropie due au transfert thermique ou/et de masse n'est observée car le film est en condition d'équilibre. Le comportement est le même que celui observé dans l'évaporateur (Chapitre II). Cette irréversibilité thermique est élevée près de la paroi et diminue de la paroi vers l'interface du film pendant le développement de la couche limite thermique. La différence de potentiel chimique, générée une fois que $\delta_{f,th1}$ est complètement développé ($\delta_{f,th1} = e_f$) entre le film et la vapeur induit l'absorption de la vapeur d'eau dans la solution $LiBr/H_2O$, conduisant au développement de la couche limite diffusive $\delta_{f,m}$. Ainsi, à l'intérieur de la frontière diffusive, on observe à la fois des irréversibilités thermiques et massique. Pour le fluide caloporteur, une couche limite thermique $\delta_{htf,th}$ se développe en raison de l'augmentation de la température, dans le fluide caloporteur, induite par la chaleur reçue du film et conduit à la création d'entropie à l'intérieur de la couche limite. L'irréversibilité thermique observée dans le fluide caloporteur est élevée près de la paroi et diminue de la paroi vers le centre du canal du fluide caloporteur. Dans cette étude, le fluide caloporteur est en écoulement à contre-courant, ainsi la couche limite thermique $\delta_{htf,th}$ est observée vers la sortie l'absorbeur (entrée du fluide caloporteur). Des résultats quantitatifs sur la distribution de la création d'entropie sont donnés sur les Fig 3.7 et 3.8.

- **Echelle globale**

Dans les conditions étudiées, le taux de création d'entropie totale par unité de largeur de paroi est égal à 0.13 W. $K^{-1}.m^{-1}$ pour Re_{htf} = 2000 et à 0.2 W. $K^{-1}.m^{-1}$ pour Re_{htf} = 5000 (soit une augmentation de 54%). Cette augmentation de création d'entropie s'accompagne d'une augmentation du débit absorbé (4.7 10^{-4} $kg.m^{-1}.s^{-1}$ pour Re_{htf} = 2000 et 6.5 10^{-4} $kg.m^{-1}.s^{-1}$ pour Re_{htf} = 5000 soit une augmentation de 38%) et d'une augmentation du flux thermique dégagé (2000 $W.m^{-1}$ pour Re_{htf} = 2000 et 2600 $W.m^{-1}$ pour Re_{htf} = 5000 soit une augmentation de 30%). Les résultats montrent que dans les conditions étudiées, la création d'entropie est principalement produite à l'intérieur du film avec 49% de la création totale d'entropie pour Re_{htf} = 2000 contre 62% pour Re_{htf} = 5000 et est principalement due aux irréversibilités thermiques. Les irréversibilités massiques restent faibles puisque leur contribution est seulement d'environ 12% pour Re_{htf} = 2000 et 15% pour Re_{htf} = 5000 en raison de la faible zone affectée par la diffusion. Par conséquent, la contribution des irréversibilités produites au sein du fluide caloporteur et de la paroi doit être prise en considération car elle représente 51% de la création d'entropie totale pour Re_{htf} = 2000 et 37.5% pour Re_{htf} = 5000. Cependant, plus le nombre de Reynolds du fluide caloporteur est élevé, plus la contribution due aux irréversibilités thermiques est faible - 37% contre 5% pour Re_{htf} = 2000 et Re_{htf} = 5000 respectivement - et plus la contribution due aux irréversibilités visqueuses produite au sein du fluide caloporteur est élevée - 2% contre 16.5% pour Re_{htf} = 2000 et Re_{htf} = 5000 respectivement. La diminution de la contribution due aux irréversibilités thermiques dans le fluide caloporteur est due au faible gradient de température. De plus, l'augmentation du nombre de Reynolds du fluide caloporteur augmente significativement les irréversibilités thermiques dans le film en raison de la faible résistance thermique. Les irréversibilités thermiques à travers la paroi augmentent également avec l'augmentation de la vitesse du fluide caloporteur en raison de l'augmentation de la chaleur échangée.

❖ Conclusions

La formulation de la création d'entropie permet de conclure que dans un absorbeur, les irréversibilités sont uniquement dues aux irréversibilités thermiques, massiques et visqueuses : les phénomènes de couplage entre transferts thermique et massique se compensent et sont parfaitement réversibles. Le développement des couches limites thermiques et massiques impacte les phénomènes locaux et par conséquent la création d'entropie.

Par ailleurs, l'analyse des irréversibilités thermiques montre que ces dernières sont plus élevées à la paroi par rapport à l'interface, ce qui signifie que le phénomène thermique à la paroi, à savoir le transfert de chaleur à travers la paroi, domine le phénomène d'absorption à l'interface, à savoir la chaleur libérée pendant l'absorption exothermique de l'eau dans le film. De plus, les irréversibilités thermiques dominent largement celles d'origine massique.

L'analyse à l'échelle du composant montre que la création d'entropie est principalement produite dans le film tombant. Cependant, la somme des irréversibilités dans le fluide caloporteur et dans la paroi représente plus de 30% de la création d'entropie globale, ce qui démontre la nécessité d'intégrer les échanges avec le fluide caloporteur pour une analyse exhaustive.

Maintenant que les sources de création d'entropie sont identifiées, le chapitre suivant se concentre sur l'étude de l'impact des conditions opératoires afin de caractériser leur influence sur les irréversibilités produites.

Chapitre IV. Optimisation multi-objectives d'un absorbeur à film tombant

Après avoir analysé les phénomènes physiques qui se passent dans l'absorbeur et l'impact de ces phénomènes sur les performances du composant et sur les créations d'entropie, ce chapitre est dédié à l'optimisation de ce composant. Depuis plusieurs années, les auteurs s'accordent sur le fait que minimiser les créations d'entropie reviendrait à améliorer les performances des composants et par conséquent des systèmes.

Sur la base de l'étude bibliographique, il est clair que l'amélioration des performances de l'absorbeur améliorera considérablement les performances globales des machines à absorption. Cependant, il n'y a pas d'études dans la littérature qui ont abordé l'optimisation multi-objectifs (MOO) d'un absorbeur à film tombant, en intégrant des objectifs additionnels tel que les fonctions utiles à savoir le débit absorbé dans le cas des machines de réfrigération et la chaleur utile récupérée dans le cas des transformateurs de chaleur. L'objectif de ce travail est d'étudier toutes les variables de dimensionnement et de fonctionnement des absorbeurs à film tombant.

Ce chapitre se divise en trois grandes parties. Une première partie qui se focalise sur la compréhension de l'impact des variables sur les différentes sources d'irréversibilités, une deuxième partie qui introduit le facteur d'équilibre afin d'étudier l'impact des deux fluides de travail sur les performances de l'absorbeur et une dernière partie consacrée à l'optimisation multi-objectifs permettant de déterminer les solutions multi-optimales sous la forme d'un Front de Pareto.

❖ Description du problème

Le problème étudié dans ce chapitre est le même que celui étudié au chapitre III. Les variables de dimensionnement et paramètres opératoires considérées dans cette étude sont le nombre de

Reynolds du fluide caloporteur et du film, la température d'entrée du fluide caloporteur, la pression de vapeur, la longueur de l'absorber ainsi que l'épaisseur de la paroi d'échange. La plage de travail de ces différentes variables est regroupée dans le Tableau 4.1. L'étude se divise en trois parties. Les deux premières parties consistent à analyser les créations d'entropie et d'évaluer le facteur d'équilibre (ratio des deux débits de fluide) afin de comprendre l'impact des paramètres de travail sur les phénomènes mise en jeu dans l'absorbeur ainsi que sur la performance de l'absorbeur. La dernière partie a pour objectif de minimiser la création d'entropie ($\dot{S}$) de l'absorbeur tout en maximisant la fonction utile dépendamment du mode fonction de la machine à absorption. Pour les machines de réfrigération, le débit massique absorbé ($\dot{M}_{abs}$) à l'interface du film doit être maximisé tandis que pour les transformateurs de chaleur, l'objectif est de maximiser la chaleur récupérée ($\dot{Q}_w$) par le fluide caloporteur.

❖ Résultats et discussions

Analyse des irréversibilités

Dans cette partie, quatre cas d'études visant à absorber un débit du réfrigérant de 0.001 $kg.m^{-1}.s^{-1}$ sont étudiées (Tableau 4.2) afin d'analyser l'influence des conditions opératoires sur les créations d'entropie. Le cas 1 étant pris comme solution de référence, est utilisé pour comparer les autres solutions.

Les résultats ont démontré que pour un même débit de réfrigérant absorbé, la création d'entropie change en fonction des conditions opératoires considérées. La création d'entropie la plus faible obtenue entre ces quatre cas d'étude vaut 0.275 $W.K^{-1}.m^{-1}$ et est obtenu pour le cas 3, alors que la plus élevée vaut 0.491 $W.K^{-1}.m^{-1}$ et est obtenue pour le cas 4, soit une augmentation de 72%. Lors de l'analyse, il a été trouvé que les irréversibilités sont principalement concentrées dans le film tombant – Tableau 4.3, contrairement à l'étude faite dans l'évaporateur où les créations d'entropie étaient principalement produites dans le fluide caloporteur (Chapitre II). De plus, l'augmentation du nombre de Reynolds du film tombant induit une augmentation des irréversibilités produites au sein du film alors qu'une diminution de la température d'entrée du film tombant s'accompagne d'une diminution du nombre de Reynolds du film tombant (pour répondre à l'objectif d'un débit absorbé fixe) permettant ainsi de réduire les irréversibilités au sein du film. L'étude de ces différents cas d'études démontrent à quel point le débit du film tombant peut impacter les irréversibilités dans le film alors que les irréversibilités dans le fluide caloporteur et dans la paroi ne sont que faiblement impactées. Seule l'analyse du cas 4 montre une augmentation des irréversibilités dans le fluide caloporteur causée par l'augmentation du débit de ce dernier. Cependant, augmenter le nombre de Reynolds du fluide caloporteur revient à réduire le débit du film nécessaire pour absorber 0.001 $kg.m^{-1}.s^{-1}$. Par conséquent, une diminution des irréversibilités dans le film est aussi observée.

L'analyse du Tableau 4.3 ne permet pas de comprendre quel type d'irréversibilités est impacté. Cette information est donnée sur la Fig. 4.2. En effet, comme mentionné dans le chapitre III, les sources d'irréversibilités dans le film sont divisées en trois contributions : thermique, massique et visqueuse, alors que celles dans le fluide caloporteur ont été divisées en deux : thermique et visqueuse et seules les créations d'origines thermique sont observées dans la paroi de l'absorbeur. Les résultats montrent que les créations d'entropie d'origine visqueuses dans le film sont négligeables comparées aux autres types d'irréversibilités due au faible débit du film considéré. Les créations d'entropie d'origine visqueuses dans le fluide caloporteur, quant à elle, ne sont que faiblement impactées par le débit du film tombant et la température du fluide caloporteur. Seul le débit du fluide caloporteur a un impact

significatif sur cette dernière. Cependant, augmenter le débit du fluide caloporteur revient à réduire les irréversibilités d'origine thermique dans le fluide caloporteur dû au faible gradient de température observé. Les résultats montrent aussi qu'augmenter le débit du film revient à augmenter les irréversibilités rencontrées dans le film du fait de l'augmentation de la résistance thermique, entre le film et le fluide caloporteur, induisant ainsi une augmentation des irréversibilités d'origine thermique dans le film.

L'introduction du facteur d'équilibre, R, a permis de mieux comprendre l'impact des deux débits sur le débit de réfrigérant absorbé, le flux de chaleur récupéré ainsi que sur la création d'entropie. Ce coefficient permet de définir le mode opératoire de l'absorbeur comme l'explique Perier-Muzet and Stutz (2021) et Amin Altamirano (2021). Tout comme ces derniers, il a été trouvé que lorsque R tend vers 0, l'absorbeur a tendance à se comporter comme si la paroi d'échange était adiabatique alors que lorsque R tends vers l'infini, la paroi d'échange se comporte comme une paroi isotherme. De plus, l'impact du fluide caloporteur sur le débit absorbé ainsi que sur le flux échangé est plus visible en régime laminaire qu'en régime turbulent – Fig. 4.3.a, du fait d'une augmentation considérable du coefficient d'échange convectif. Le régime turbulent apparait à des ratios faibles lorsque le débit du film tombant augmente du fait de l'augmentation du maximum de flux transférable par la solution (le maximum de flux transférable par la solution est inversement proportionnel au facteur d'équilibre).

L'analyse de la Fig. 4.3.a, montre l'existence d'un nombre de Reynolds optimal pour le film tombant compris entre 20 et 120 en régime turbulent. L'analyse de la Fig. 4.4 montre que la création d'entropie augmente avec l'augmentation du nombre de Reynolds du film et du fluide caloporteur. Cependant, la création d'entropie est concave lorsque le fluide caloporteur est en régime d'écoulement laminaire alors qu'elle est convexe lorsque le fluide caloporteur est en régime d'écoulement turbulent. Ceci est principalement lié aux contributions différentes des irréversibilités du fluide caloporteur entre ces deux écoulements. En effet, dans le régime d'écoulement turbulent, la contribution de la création d'entropie d'origine visqueuse est plus élevée par rapport à la contribution de l'irréversibilité thermique. L'augmentation de la contribution visqueuse sur la création d'entropie rend la dérivée seconde de la création d'entropie totale négative dans le régime turbulent, alors que pour des faibles nombres de Reynolds du fluide caloporteur, la dérivée seconde de la création d'entropie totale est positive en raison de la faible contribution visqueuse. En conclusion, le phénomène visqueux joue un rôle majeur sur les performances de l'absorbeur. De plus, l'écart entre les régimes d'écoulement laminaire et turbulent augmente avec l'augmentation du débit d'entrée du film : l'augmentation du débit du film induit une augmentation significative de l'irréversibilité thermique du film qui augmente ainsi la création d'entropie pour un nombre de Reynolds du fluide caloporteur constant.

Optimisation multi-objectifs

La minimisation de la création d'entropie tout en maximisant l'effet utile de l'absorbeur (soit le débit absorbé ou le flux transféré) démontre un comportement antagoniste en thermodynamique en dimension finie. C'est dans ce contexte qu'une optimisation multi-objectif voit son intérêt afin de pouvoir soit maximiser l'effet utile en maintenant une certaine création d'entropie soit minimiser les irréversibilités pour un effet utile donné. Le front de Pareto obtenu à partir de cette optimisation mutli-objectif permet quant à lui de donner les paramètres opératoires permettant d'à la fois minimiser la création d'entropie tout en maximisant l'effet utile.

Les fronts de Pareto les deux cas d'études sont présentés sur les Fig. 4.5.a et 4.5.b en considérant un film entrant dans l'absorbeur à une concentration $C_{LiBr,in}$ = 60%, une température $T_{f,in}$ = 45.6°C et une pression P_{vap} = 1kPa. L'analyse de ces fronts montrent qu'une augmentation du débit absorbé et/ou du flux de chaleur récupéré s'accompagne d'une augmentation de la création d'entropie. L'étude montre qu'effectivement, la création d'entropie peut être minimisée tout en préservant les performances souhaitées de l'absorbeur en jouant sur les conditions opératoires. Cependant, le Front de Pareto montre aussi que l'augmentation du débit absorbé et/ou du flux transféré est associée à une augmentation de la création d'entropie. L'analyse de la Fig. 4.5.a permet de conclure à l'existence d'un optimum au-delà duquel le débit absorbé diminue alors que la création d'entropie augmente.

La suite de l'étude s'est focalisée sur l'analyse des solutions donnant le Front de Pareto afin de comprendre le comportement de l'absorbeur avec les variables opératoires mentionnées sur le Tableau 4.1. Plus l'absorbeur est long, plus le débit massique absorbé et la chaleur récupérée sont élevés du fait d'une surface d'échange plus élevée. Cependant, certaines contraintes telles que le coût, la taille et la stabilité du film tombant doivent être prises en compte avant de concevoir l'absorbeur. De plus, plus l'épaisseur de la paroi est faible, plus le débit massique absorbé et la chaleur récupérée sont élevés. En effet, une épaisseur de paroi plus fine permet de réduire la résistance thermique entre le film et le fluide caloporteur. Cependant, certaines contraintes telles que des problèmes mécaniques et de résistance doivent être prises en compte afin d'avoir des parois à la fois thermiquement efficaces et avec une bonne résistance mécanique. En conséquence, les paramètres de conception de l'absorbeur doivent être définis au début du projet en tenant compte de la capacité de l'absorbeur souhaité, du coût, de l'encombrement ainsi que des propriétés mécaniques. C'est seulement sur cette base que les paramètres de fonctionnement doivent être optimisés.

L'analyse des fronts de Pareto (Fig. 4.6 et 4.8) montre une augmentation du débit absorbé et du flux transféré avec l'augmentation du débit du film tombant et de la pression de vapeur et avec une diminution de la température d'entrée du fluide caloporteur. L'influence de la vitesse du fluide caloporteur sur les solutions de Pareto est faible : il est recommandé de travailler près du début du régime de turbulence du fluide caloporteur entre (5000 et 6000). En effet, pour des nombres de Reynolds du fluide caloporteur supérieur à 6000, le surplus de débit absorbé est faible comparé à l'augmentation de la création d'entropie engendrée. L'optimum observé sur la Fig. 4.5.a est expliqué par la variation du débit du film tombant : en effet, l'analyse du débit absorbé avec le débit du film montre que seuls les nombre de Reynolds du film inférieur à 50 sont représentés sur le front de Pareto. Il existe un débit du film au-delà duquel l'absorbeur n'est donc pas optimisé.

Les Fig. 4.6 et 4.8 donnent les paramètres optimaux à utiliser tout en indiquant le débit capable d'être absorbé ainsi que le flux capable d'être échangé. Le but étant de trouver un compromis entre la performance souhaitée et la création d'entropie qui sera générée.

❖ Conclusions

En utilisant le modèle développé dans le Chapitre III, cette partie du manuscrit s'est concentrée sur l'étude paramétrique des conditions opératoires afin d'étudie leur impact sur les performances de l'absorbeur. Un facteur d'équilibre est introduit afin d'analyser l'impact des débits des deux fluides sur les performances de l'absorbeur (le film est supposé être en régime laminaire alors que le fluide caloporteur peut être en écoulement laminaire ou turbulent).

Il a été montré que pour un même débit de réfrigérant absorbé, la création d'entropie produite peut-être plus ou moins élevée dépendamment des conditions considérées ce qui a permis de conclure

qu'une optimisation multi-objectifs devait être faite pour obtenir le front de Pareto (conditions opératoires permettant d'obtenir le maximum de débit absorbé ou chaleur transféré tout en minimisant la création d'entropie).

Conclusions générales et perspectives

❖ Conclusions générales

L'approche thermodynamique est un moyen intéressant permettant d'évaluer les performances des composants tout en identifiant les sources de création d'entropie. Une formulation de la création d'entropie dans les évaporateurs et dans les absorbeurs à film tombant a été proposée. La différence entre les deux est l'existence d'une irréversibilité due aux phénomènes de transfert massique uniquement présente dans le film dans l'absorbeur. Cette formulation thermodynamique de la création d'entropie dans l'absorbeur a permis de distinguer trois contributions d'irréversibilités dans le film à savoir : les irréversibilités thermique, massique et visqueuse, deux contributions d'irréversibilités dans le fluide caloporteur : irréversibilités thermique et visqueuse, et une contribution thermique au niveau de la paroi. La création d'entropie dépend fortement des conditions opératoires considérées. Ces conditions impactent différemment les phénomènes locaux (via le développement des couches limites) et par conséquent les irréversibilités. Les principales variables qui influencent les performances de l'absorbeur sont le débit du film tombant, la température d'entrée du fluide caloporteur ainsi que le débit du fluide caloporteur. L'analyse paramétrique a montré l'existence d'un nombre de Reynolds du film optimal au-delà duquel les performances de l'absorbeur diminuent en termes de débit absorbé. L'augmentation du débit absorbé et du flux transféré augmente plus rapidement avec la vitesse du fluide caloporteur en régime laminaire qu'en régime turbulent. Toutefois, les performances sont plus élevées en régime turbulent du fait des grands coefficients d'échange. Par ailleurs, il faut éviter de travailler avec des débits du fluide caloporteur trop élevés afin de minimiser la création d'entropie. Les fronts de Pareto présentés peuvent être utilisés comme abaque de dimensionnement pour l'absorbeur.

❖ Perspectives

Bien que le travail réalisé ait permis de mieux comprendre le comportement de l'absorbeur, des nombreuses perspectives sont ouvertes autant à l'échelle locale qu'à l'échelle du composant et du système :

▪ Echelle locale

Expérimentale

Les résultats locaux obtenus dans le cadre de ce travail mériteraient d'être validés au moyen d'une étude expérimentale. Une première piste serait l'utilisation des techniques d'imagerie utilisant la Fluorescence Induite par Laser (Planaire ou pas) à savoir la PLIF et la LIF ponctuelle développées au laboratoire LEMTA et récemment au LOCIE pour déterminer les champs de température et de concentration à l'échelle du film. Aujourd'hui, les méthodes précitées ne permettent que la détermination du champ de température. Une étude peut être menée pour voir la possibilité d'appliquer la méthode pour la détermination du champ de concentration.

Numérique

Le problème du mouillage (surface de plaque couverte par la solution) est un problème récurrent qui mérite d'être traité en profondeur. Le modèle développé, dans ce projet, considère un mouillage total et uniforme. Cependant, la réalité est tout autre : observation de ruisselets. Il serait intéressant d'inclure le taux de mouillage dans l'analyse afin de quantifier les différences entre un mouillage total et un mouillage partiel ainsi que leur impact sur les phénomènes locaux et par conséquent, sur les créations d'entropie.

Une des limites des modèles développés est la non adéquation des modèles à des nombres de Reynolds du film tombant supérieurs à 200. Les effets de vaguelettes à la surface du film et de recirculation potentielle dans le film sur les performances de l'absorbeur ne pourront pas être évalués avec le présent modèle. Un modèle un peu plus complet pourrait être développé mais nécessite des outils de simulations très complexe.

Les méthodes CFD utilisant des logiciels graphiques comme COMSOL semblent être des méthodes intéressantes pour la modélisation des phénomènes dans ce type de composant. Le fluide caloporteur en régime turbulent pourrait être mieux modéliser et les phénomènes dans les films tombant pour des nombres de Reynolds supérieur à 200 pourrait être mieux observés.

- **Echelle du composant**

Bien que ce projet de thèse ait permis d'identifier les différentes sources d'irréversibilités, de les localiser et de les quantifier autant dans l'évaporateur à film tombant que dans l'absorbeur, d'autres études restent à mener. Dans tout composant d'un système thermodynamique, il existe des irréversibilités endogènes et exogènes mais aussi des irréversibilités évitables et non évitables comme mentionnées dans la dernière partie du chapitre I. Il est donc important de pouvoir distinguer les différentes contributions afin d'être capable de quantifier la part de la création d'entropie qui peut être minimisé et celle où aucune action ne peut être faite.

- **Echelle du système**

L'optimisation multi-objectifs réalisée permets de déterminer les conditions opératoires les plus favorables pour minimiser la création d'entropie tout en préservant les performances de l'absorbeur. Toutefois, aucune analyse de l'impact de cette optimisation sur les autres composants des machines à absorption n'a été faite. Il est donc important d'étudier cet impact sur le coefficient de performance de ces machines.

General introduction

Context of the present research

Given the depletion of fossil resources and in view of various international agreements in support of environmental goals, countries aim to manage energy in an efficient and sustainable manner. In the European Union, climate strategies and policies are being implemented to achieve key targets for 2030 as the current global context shows a huge growth in energy demand. The European Union objectives, by 2030, are to cut greenhouse gas emissions by at least 40% compared with 1990, to increase the share of renewable energy by at least 32% and to improve energy efficiency by at least 32.5% (European Commission 2019).

The increase of the energy demand is mainly due to the increase in energy consumption in the building-tertiary sector where the energy consumption has increased from 43% to 49% between 1990 and 2020 (Ministre de la transition écologique 2021). In the building sector, 20% of the energy consumption is dedicated to air conditioning due to the increase of the average global temperature of 1°C (ADEME 2018). However, the use of conventional heating and cooling machines has a considerable impact on the environment as they contribute to global warming. Acting in the building sector would therefore make it possible to considerably reduce the carbon impact.

Sorption systems have raised the interest of the scientific community in recent years due to their high efficiency, high energy density, and potential use for solar energy during summer periods. Absorption systems, in particular, appear to be a good alternative to the mechanical compression of the standard refrigeration system for different reasons. Indeed, the absorption systems present some advantages such as:

- *The means of compressing the fluid:*
  - Mechanical in the case of a standard machine,
  - Thermochemical in the case of the sorption machine.

- *The type of energy needed for this compression*
  - Electrical in the case of a standard machine,
  - Thermal in the case of the sorption machine.

However, absorption machines are known for their big size and high initial cost compared to standard machines. In this context, more and more studies are conducted to reduce the initial investment and size of these machines by improving the performance of its components in order to make them competitive compared to standard machines.

Research objectives

Absorption machines work with four main components: a desorber (or generator), a condenser, an evaporator and an absorber. The principle is based on the affinity between the refrigerant and the absorbent. The operating principle is presented in Fig. 1 and in the Oldham diagram (Fig. 2).

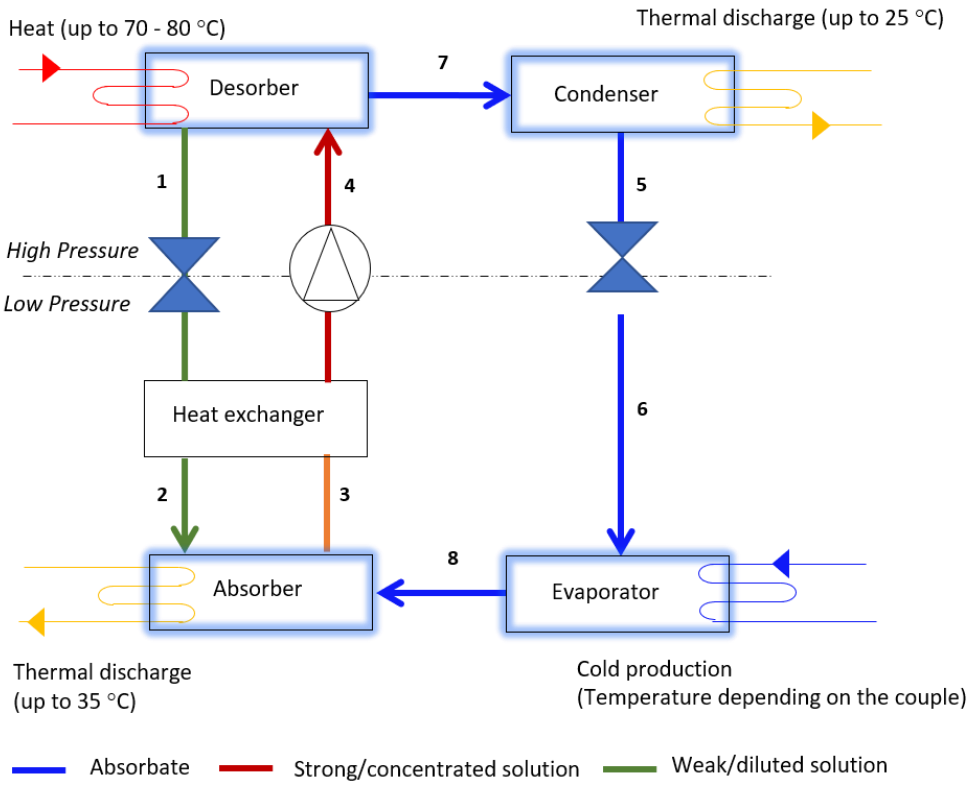

Figure 1: Operating principle of an absorption machine

In the case of refrigeration cycles, the desorber and the condenser operate at high pressure (P_{high}, Fig. 2), while the absorber and the evaporator operate at low pressure (P_{low}, Fig. 2). The refrigerant is separated from the absorbent–refrigerant solution by supplying heat at high temperature (endothermic operation) in the desorber; a concentrated salt solution (1, Fig. 1) and a refrigerant in vapor form (7, Fig. 1) are obtained. This vapor is condensed by heat exchange with a coolant fluid: this condensation allows heat recovery at medium temperature. From the condenser (5), it passes through a valve allowing it to move from high pressure to low pressure (6) and afterwards evaporate (8) using low temperature heat before reaching the absorber. In the absorber, the vapor is absorbed by the expanded concentrated salt solution (2) coming from the desorber, discharging heat at medium temperature (exothermic operation). Thus, the solution obtained is diluted (3) and is pumped back to the desorber (4) closing the cycle. A heat exchanger can be used between the solution flowing from the absorber and the desorber to increase the efficiency of the system.

The operating temperatures greatly depend on the absorbent–refrigerant couple. Many criteria must be taken into account for the couple choice (Srikhirin, Aphornratana, and Chungpaibulpatana 2001; ASHRAE 2001; Sun, Fu, and Zhang 2012). Lithium bromide/water ($LiBr/H_2O$) and water/ammonia (H_2O/NH_3) couples are the most common working fluids (Altamirano, Stutz, et al. 2019a). Equations have been developed for calculating the thermodynamic properties of the $LiBr/H_2O$ couple (Kaita 2001; Yuan and Herold 2005; Cheng and Liang 2012) and the H_2O/NH_3 couple (Kherris et al. 2013; Deepak et al. 2017). However, there are several other couples used in absorption machines (Cerezo et al. 2011; Ghyadh et al. 2018; Dardouch et al. 2020).Heat and mass transfer coefficients of falling film and correlations were studied by (Islam et al. 2003; Fujita and Hihara 2005; Narváez-Romo et al. 2017). In

this work, the focus is on the LiBr-H_2O couple for three reasons. The first one is that it is one of the most used couple, the second one is that it is simpler to model compared to the couple ammonia water (because of the non-volatility of lithium) and finally because the observed phenomena can be exported to other non-volatile couples.

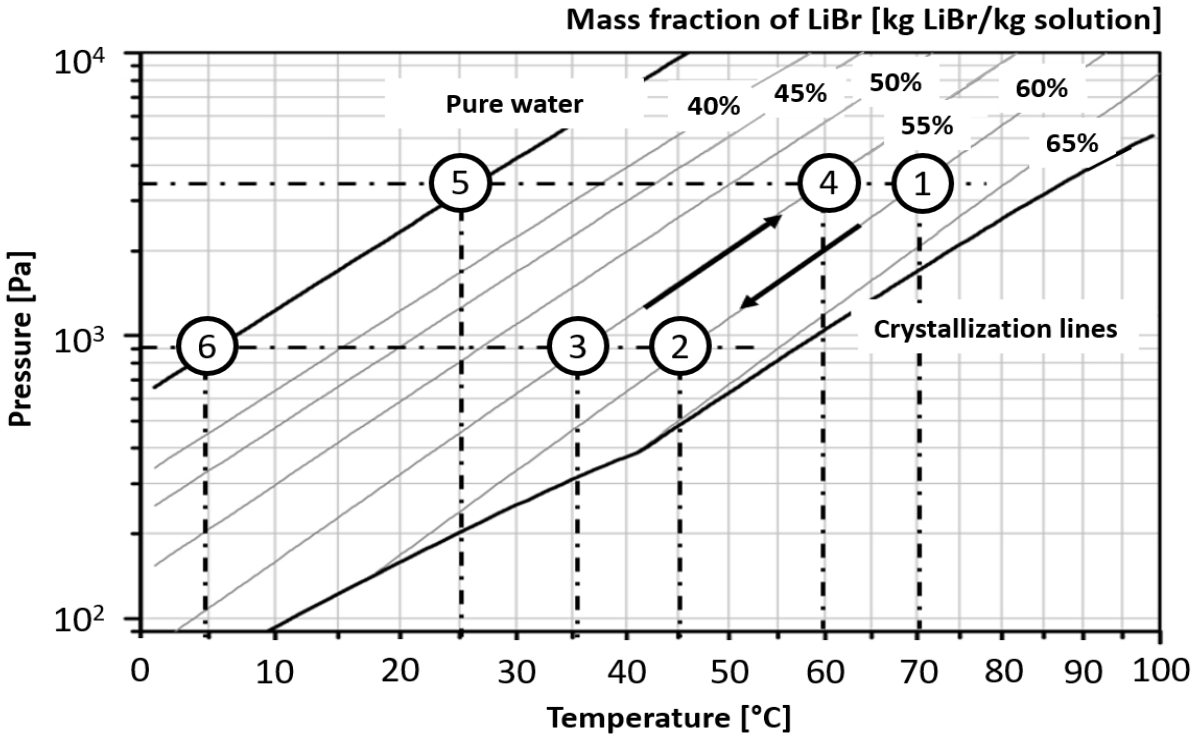

Figure 2: Oldham diagram for the LiBr - water solution

The efficiency of these machines is affected by the chosen absorbent–refrigerant couple (Kang, Kunugi, and Kashiwagi 2000; De Lucas, Donate, and Rodríguez 2007; Wakim 2018; Li et al. 2018), system design (Yoon et al. 2008; Gomri 2009; Erregueragui et al. 2015; Nikbakhti et al. 2020) and operating conditions (Florides et al. 2003; Kaynakli and Kilic 2007; Wonchala, Hazledine, and Goni Boulama 2014; Keinath, Garimella, and Garrabrant 2017) but also by the performance of the different components. Studies concluded that the absorber is the key component of any absorption machine (Srikhirin, Aphornratana, and Chungpaibulpatana 2001; Izquierdo et al. 2008; Ibarra-Bahena and Romero 2014). Its performance has a direct impact on the size and heat load of all the other components (Ibarra-Bahena and Romero 2014). Indeed, improving absorber performance by achieving improved operating conditions would increase the absorption phenomenon, maximize recovery of the heat released during absorption, enable better component design and reduce costs.

There are different types of heat and mass exchangers configurations, namely: plate, membrane, vertical and horizontal tube exchangers for different modes: falling film, spray and bubbles (Mehrez 2019). This work will focus on falling film exchangers as they are more flexible and suitable for different applications, are relatively low cost and offer great performance (Altamirano et al. 2020). In addition, falling film exchangers provide a good exchange surface between the liquid and vapour phases, and facilitate heat transfer from the liquid–vapor interface to the heat transfer fluid (HTF) (Michel, Le Pierrès, and Stutz 2017). Furthermore, a review comparing falling film absorbers with bubble absorbers (Triche 2018), shows that despite the greater wetted area of bubble absorbers, falling film plate heat

exchangers are more attractive due to their compactness and the high heat transfer coefficient they can achieve. These absorbers are more flexible and suitable for different applications, are relatively low cost and offer great performance (Altamirano et al. 2020).

Consequently, the objective of this present research is to characterize in detail the phenomena of coupled mass and heat transfer at the local scale in the most critical components: the evaporator and the absorber. The approach adopted is based on the thermodynamic analysis of these exchangers, according to the recent developments of the Thermodynamics of Irreversible Processes (TIP), with the aim of identifying the various local sources of irreversibilities, responsible for a degradation of the overall performances of the system. These studies allow to better understand the physical, thermal and mass phenomena involved in these components in order to identify ways to optimize the overall performance of the system from the levers identified at the local scale.

Thesis organization

In order to address the research objectives, the thesis was structured in the following chapters, which are based on results that were presented in peer-reviewed journal and conference papers.

Chapter I is an up-to-date review of coupled heat and mass transfers models and applications of the thermodynamic of irreversible processes in the key components of absorption machines, since the 2000s. The objective is to report the scientific advances made in a specific type of absorber, namely, the falling film ones, since the review made by Killion and Garimella's (2001), in order to understand the most suitable approach that has to be used in this project to analyze the absorber performance. This chapter is divided in two parts. The first part focuses on the theoretical approaches used and assumptions made to find the temperature and concentration distribution over a falling film for both smooth and wavy-laminar falling liquid film in order to deeply understand the physical phenomena that occur during the absorption process. Experimental studies at the local scale are also mentioned in this part. The second part is dedicated to the application of the thermodynamic of irreversible processes to these absorbers to understand how this approach can be used to further understand the phenomena encountered during the absorption phenomenon.

Chapter II is devoted to the study of an evaporator. Indeed, before studying the coupled heat and mass phenomena observed in an absorber, a first simplified model has been developed to study an evaporator, where no mass transfer occurs. In this second chapter an evaporative water laminar falling film flowing by gravity on a vertical plate heated by a HTF is studied to determine the local temperature, entropy generation and evaporated mass flow, assuming constant saturation pressure at the free interface, in co-current and counter-current configurations. The HTF and film energy equations are solved simultaneously through a 2D model using an implicit finite difference scheme. Local and overall analysis were performed in order to study the impact of parameters such as the heat transfer fluid and film Reynolds numbers and inlet film temperature on entropy generation (thermal and viscous irreversibilities) and on thermal and evaporation efficiencies. Comparison with literature results was performed for the model validation.

Chapter III deals with the development of an absorber 2D model. Here, an absorbing solution of laminar LiBr-H_2O falling film flowing by gravity on a vertical plate heated by a heat transfer fluid is studied to determine the local temperature, concentration and velocity fields from a numerical resolution considering both mass and energy transport equations through a model using an implicit finite difference scheme. In order to investigate realistic absorber cases, the heat transfer fluid is assumed to flow in counter-current with the falling film and different heat transfer fluid flow regimes are studied and compared with the limit cases– adiabatic and isothermal walls. Details about the

physical phenomena observed are given. A local entropy generation formulation is performed to identify the different sources of irreversibilities with the aim of locating and quantifying them. The impact of the heat transfer fluid flow regime (laminar and turbulent flow) on the entropy generation and absorber performance has been discussed. Comparison with numerical models from the literature results was performed for the model validation.

Chapter IV allows, in one hand, a parametric analysis of the falling film absorber, and in the other hand, its multi-objectives optimization. Two optimization approaches were used in order to determine the Pareto front and to validate the multi-optimal solutions. Two case studies were considered: the case where the absorber is used in an absorption chiller and the case where it is used in a heat transformer. The objective, in the first case study, is to maximise the absorbed mass flow rate when minimizing the entropy generation while, in the second case study, the objective is to maximize the recovered heat by the heat transfer fluid while minimizing the entropy generation. An analysis is also made to study the behavior of the different sources of entropy generation when considering different operating conditions.

CHAPTER I

Chapter I. Review of coupled heat and mass transfer studies in falling film absorbers: modeling, experimental and thermodynamic approaches

Based on:

Article: Mahamoudou, Le Pierrès and Ramousse (2022). Review of Coupled Heat and Mass Transfer Studies in Falling Film Absorbers: Modeling, Experimental and Thermodynamic Approaches. *International Journal of Refrigeration,* vol 136, p.229-244, January 2022. DOI: 10.1016/j.ijrefrig.2022.01.024

Conference: Mahamoudou, Le Pierrès and Ramousse. Uptodate review of coupled heat and mass transfer models and applications of the thermodynamic of irreversible processes in falling film absorbers, *15th International Conference on Heat Transfer, Fluid Mechanics and Thermodynamics (HEFAT2021),* presented online in July 26-28, 2021.

1.1. Introduction

As explained in the introduction, there are different types of absorber configuration, namely: plate, membrane, vertical and horizontal tube absorbers for different absorption modes: falling film, spray and bubbles (Mehrez 2019). This review focuses on falling film absorbers. The main objective of this study is thus to provide an overview of the different ways of solving coupled heat and mass problems, and use of the thermodynamics of irreversible processes to understand heat and mass transfer phenomena over a falling film absorber at limited flow regimes. This work focuses on studies undertaken since 2000 and updates the conclusions of Killion and Garimella's (2001) critical review of coupled heat and mass transfer models. Thus, this paper is divided into two parts. First, the theoretical approaches used to find the temperature and concentration distribution over a falling film are reviewed for both smooth and wavy-laminar falling liquid film. Experimental studies at the local scale are also mentioned. Application of the thermodynamic of irreversible processes to these absorbers is presented subsequently.

1.2. Theoretical and modeling approaches

1.2.1 Problem description

Improvement of falling film absorber performance requires an understanding of the phenomena encountered. The performance of an absorber can be improved by improving its efficiency and/or effectiveness depending on the situation. In absorbers, thermal and mass effectiveness and efficiency can be defined as follows:

- Mass effectiveness can be defined as the ratio of the actual vapor flow rate absorbed in the component to the vapor flow rate in an ideal absorber where the absorbent leaves the absorber with an equilibrium concentration at the same temperature as the entering cooling medium (Islam, Wijeysundera, and Ho 2006; Perier-Muzet and Stutz 2021).
- Thermal effectiveness can be defined as the ratio of the heat transfer rate collected by the heat transfer fluid to the maximum heat transfer rate that could be collected by this fluid (Islam, Wijeysundera, and Ho 2006; Perier-Muzet and Stutz 2021). The maximum transferable flux in an absorber is achieved in an infinitely long counter-flow absorber.
- Absorber efficiency can be defined as the ratio of the heat transfer rate collected by the heat transfer fluid to the heat transfer rate released during the absorption phenomenon at the solution free interface.

These ratios are often used at the component level to quantify the performance of absorbers (Rogdakis and Papaefthimiou 2002; Islam, Wijeysundera, and Ho 2006; Perier-Muzet and Stutz 2021). The highest efficiency is usually reached when effectiveness is low. Indeed, in a heat exchanger, the energy losses to the surroundings are low for small lengths, allowing to obtain a high efficiency but also a low effectiveness. However, the effectiveness increases with the length of the exchanger to be maximal for an infinite exchanger that leads to a decrease of its efficiency due to the increase of heat losses to the environment. However, there are very few studies at local scale that define these ratios. The local

studies performed so far are more focused on studying the behavior of absorbers when subjected to different operating conditions or design conditions. Fig 1.1 shows the detailed flow of a solution on a vertical plate and in contact with vapor refrigerant. At the solution–vapor interface, the chemical potential difference induces a mass transfer process from the vapor to the solution by absorption. This exothermic absorption releases heat that increases the falling film temperature. Depending on machine design, two extreme cases arise: Adiabatic wall and Isothermal wall.

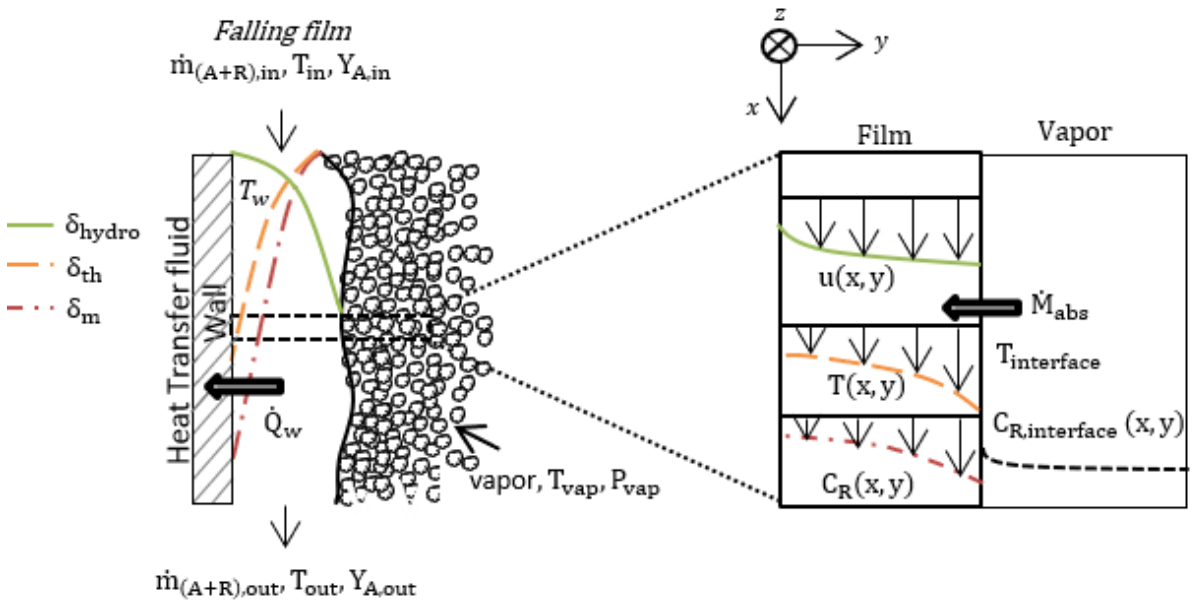

Figure 1.1: Schematic description of heat and mass transfer in flat plate falling film absorbers

The falling film flows from the top to the bottom; however, the vapor and the heat transfer fluid flows depend on the absorber configuration. The heat transfer fluid can be in counter–or co–current with the solution for plate and vertical tube absorbers, or in cross–flow for horizontal tubes. The vapor may be either in counter–or co–current with the falling film (Kwon and Jeong 2004; Govindaraju 2005; Fan and Luo 2017; Tahir et al. 2019). Although some researchers assert that the interaction between the mass and the heat transfer is negligible and they could be studied independently (Deng and Ma 1999), other studies show that falling films are the core of thermal and mass phenomena strongly coupled to falling film hydrodynamics (Raisul Islam, Wijeysundera, and Ho 2004; Goel and Goswami 2005b; 2005a; Fernández-Seara, Uhía, and Sieres 2007). The coupling between these phenomena can be realized through two boundary conditions: the vapor pressure equilibrium and energy balance at the interface (Killion and Garimella 2001; Gonzalez 2005). The first boundary says not only that the vapor and solution interface temperature must be the same but also that at any contact point between solution and vapor, the vapor pressure of each species in the film must be equal to the partial pressure of each species in the vapor side – Equation (1.1):

$$\begin{cases} T_{f,interface} = T_{vap,interface} \\ P_{vap} = f\left(T_{f,interface}, C_{interface}\right) \end{cases} \quad (1.1)$$

The second condition states that as a mass is transferred from the vapor to the liquid phase, there is a change in enthalpy known as the heat of absorption (H_a) resulting in a heat source at the interface – Equation (1.2):

$$h_a \dot{m}_{\text{abs}} = \lambda_f \left(\frac{\partial T}{\partial y}\right)_{interface} \tag{1.2}$$

Thus, in order to understand the absorber and predict its performance, it is essential to solve the heat and mass transfer simultaneously and not as independent functions. Moreover, these phenomena lead to the formation of the diffusive δ_m, thermal δ_{th} and hydrodynamic δ_{hydo} boundary layers in the solution.

For more than 50 years, these phenomena have been studied through three main equations: momentum, energy and mass conservation. Falling film absorption models are generally based on the assumption listed below (Yoon et al. 2005):

- The falling film solution is Newtonian and incompressible;
- Steady-state regime is fully developed;
- All thermo-physical properties of the liquid and vapor are assumed constant and independent of temperature and concentration;
- Vapor pressure equilibrium exists between the vapor and the liquid at the interface, and is uniform in the vapor phase;
- No heat transfer in the vapor phase;
- The Dufour and Soret effects are neglected: The Dufour effect implies an energy flux due to the chemical potential gradient. The Soret effect is its reciprocal and it implies a gradient of concentration due to the temperature gradient;
- Negligible dissipation effects and pressure gradients.

Moreover, one of the following hypotheses is made at the vapor–solution interface: finite dilution or infinite dilution. The dilution is said to be infinite when the vapor absorption does not affect the concentration of the absorbent in the falling film. This infinite dilution assumption remains valid only if the absorbed flow is very low compared with the solution flow. In this case, Equation (1.3) gives the absorbed flow rate at the interface (Yoon et al., 2005)

$$\dot{m}_{\text{abs}} = \left[-\rho D_{R-A} \frac{\partial C_R}{\partial y}\right] \tag{1.3}$$

However, in real cases, vapor absorption dilutes the concentrated solution. In this case, Equation (1.4) can be used at the interface (Nakoryakov and Grigor'eva, 2010):

$$\dot{m}_{\text{abs}} = \left[-\rho \left(\frac{D_{R-A}}{C_A}\right) \frac{\partial C_R}{\partial y}\right] \tag{1.4}$$

Despite the significant progress made between 1977 and 2000, work remains to be done at local scale to deeply understand the absorption phenomenon (Killion and Garimella 2001):

- Some hypotheses have yet to be validated;
- Resolution of hydrodynamic phenomena should be studied with heat and mass balances;
- More experimental studies must be carried out to validate the models.

The next paragraphs summarize the mathematical models in the literature. The analytical and then numerical solutions developed to solve the problem of coupled heat and mass transfer over a smooth and wavy-laminar falling film are analyzed starting with flat plates, then horizontal and ending with vertical absorbers.

1.2.2 Free falling film surfaces in the laminar regime

In a smooth laminar regime, the fluid layers are linear and slide in parallel with no disruption between them. A summary of the main assumptions and methods used to study the phenomena in falling film absorbers operating in the smooth laminar regime are given in Table 1.1.

1.2.2.1 Flat plate absorbers

Flat plate heat exchanger technologies are increasingly used in industry due to their compactness, excellent heat transfer characteristics and low cost (Ayub 2003; Abu-Khader 2012), which is also of interest in the specific case of absorbers.

- **Analytical studies**

The first studies of coupled heat and mass phenomena were carried out 45 years ago by (Nakoryakov and Grigor'eva 1977) for a smooth laminar LiBr/H_2O falling film flowing over an isothermal vertical plate. In addition to the assumptions mentioned above, they assumed:

- The velocity in the laminar film is uniform;
- The shear forces exerted by the vapor on the solution are neglected;
- The diffusion and thermal phenomena are neglected in the streamwise direction;
- The absorbed flow rate is negligible compared to the solution flow rate: constant falling film thickness and infinite dilution;
- The concentration at the interface varies linearly with the interface temperature;
- There is no heat transfer to the vapor;
- There are no-condensable gases in the solution.

Under these assumptions, (Nakoryakov and Grigor'eva 1977) solved the following equations system (1.5):

$$\begin{cases} u_x = u_{x,in} \\ u_x \dfrac{\partial T}{\partial x} = a_f \dfrac{\partial^2 T}{\partial y^2} \\ u_x \dfrac{\partial C}{\partial x} = D_{R-A} \dfrac{\partial^2 C}{\partial y^2} \end{cases} \quad (1.5)$$

By developing an exact solution in another study, the same author concluded that the phenomena

within the falling film depend on the Lewis number ($D_{R\text{-}A}/a$), the Prandtl number ($\mu_f/a_f\rho_f$), the Reynolds number ($4u_x e_f\rho/\mu_f$), another dimensionless number Ka ($h_a k_1/C_p$) and the initial film state parameters. Near the inlet, the thermal boundary layer is not yet developed, the interface temperature remains almost constant while far from the inlet, the temperature profile becomes linear and decreases (Nakoryakov et al., 2003). Another dimensionless number conditions the change in the layer thickness: the Froude number ($e_{in}\, g/u_{x,in}$) (Nakoryakov et al., 2011).

More recently Nakoryakov and Grigor'eva (2010) showed that a uniform velocity profile underestimates the temperature and concentration profiles for an adiabatic exchanger whatever the Lewis number for the LiBr/H_2O couple. In an isothermal exchanger, the opposite tendency is observed for small Lewis numbers.

Heat and mass transfer analysis in the entrance region of the falling film were carried out by (Nakoryakov, Grigoryeva, and Bartashevich 2011; Vladimir E. Nakoryakov and Bartashevich 2017) using analytical method: self-similar solution and corrections were derived when taking into account the film thickness change due to mass inflow in absorption. They concluded that the Froud number is the main one that defines the film thickness change.

- **Numerical studies**

Karami and Farhanieh, (2009) studied the LiBr/H_2O absorption process by considering variable film thickness with vapor absorption and variable film properties under the same conditions as Grigor'eva and Nakoryakov (1977). The Nusselt solution, equation (1.6), which assumes a symmetrical parabolic velocity profile was considered:

$$u_x(y) = \frac{3}{2}\bar{u}\left[2\left(\frac{y}{e_f}\right) - \left(\frac{y}{e_f}\right)^2\right] \qquad (1.6)$$

They explained the slow decrease of the interface temperature and absorbent concentration far from the inlet by the rapid decrease of the vapor pressure driving force.

Flores (2014) studied the LiBr/H_2O couple in an adiabatic and an isothermal exchanger according to two different scenarios: imposed and unknown variable surface temperature. A 'partially-established' zone and an 'established' zone appeared after introducing the thermal and mass boundary layers. Flores (2014) underscored the importance of coupling thermal and mass phenomena in falling film absorber studies.

Mittermaier and Ziegler (2014) assumed variable thermophysical solution properties and an additional differential heat of solution released in the bulk due to growth of the concentration boundary layer in the flow direction. According to them, the effect of the additional heat is slightly larger than that of the variable properties, but both remain low especially for sorption couples with high transport properties, such as LiBr/H_2O.An investigation of a NH_3 /H_2O solution was carried out by Triché et al. (2017) assuming a saturated solution at the vapor–solution interface and constant film thickness. The vapor is in co–current flow with the falling film solution. They explained (Fig. 1.2) that at the inlet of the absorber, the desorbed vapor phase contains water at low concentration and ammonia at high concentration, so the water is desorbed from the liquid phase to the vapor phase ($Y_{A,vap} > 1$). At the top of the plate, the average ammonia mass fraction on the vapor side ($Y_{R,vap}$) is higher than that at the vapor interface ($Y_{R,i,vap}$). Along the plate, the ammonia mass fraction on the vapor side ($Y_{R,vap}$)

decreases and $(Y_{R,i,vap})$ increases as the ammonia is absorbed. Then, the vapor phase becomes more concentrated in water and so the water is absorbed from vapor to the liquid phase ($Y_{A,vap} < 1$). The liquid interface $(Y_{R,i,s})$ and the average liquid phase $(Y_{R,s})$ ammonia mass fraction increases along the absorber. Thus, for a NH_3/H_2O solution, it is important to know the impact of water desorption on ammonia absorption near the inlet.

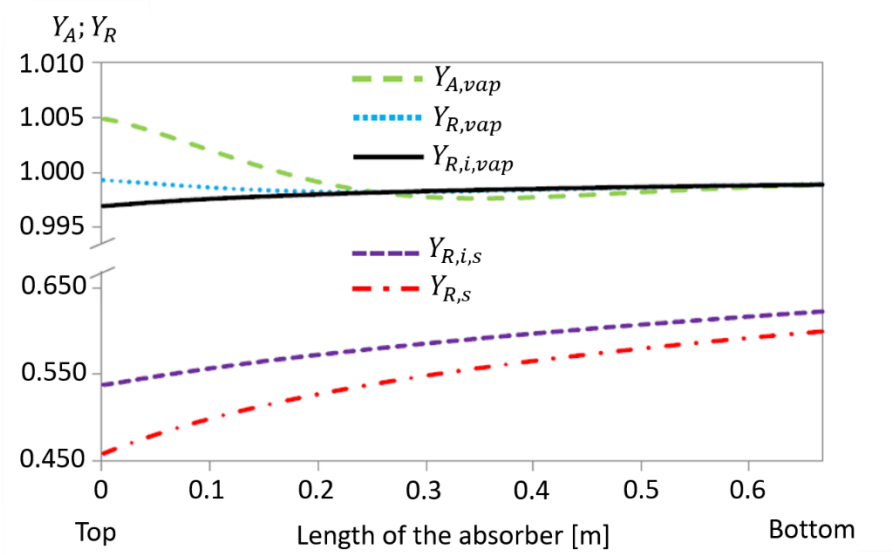

Figure 1.2: Ammonia concentrations in the vapor and liquid phase along the absorber length adapted from (Triché et al., 2017)

The study of a lithium bromide – water film flowing on a cooled horizontal wall under the action of co and counter-current surround flow of saturated water vapor was investigated by Bartashevich (2018) under the same assumptions as in (Nakoryakov and Grigor'eva 2010; Nakoryakov, Grigoryeva, and Bartashevich 2011) . A linear velocity profile was considered as shown in (1.7):

$$u(y) = \left(\frac{y\tau}{\mu}\right) \tag{1.7}$$

Where τ is the film surface shear stress. This study is one of the few studies that considers that the liquid film flows under the action of the external tangential stress on the film surface.

Recently Habib et al. (2019) studied $LiBr/H_2O$ absorption adopting a Reynolds number of 30 for the film and introducing the shear stress at the interface. They confirmed that a part of the heat energy released at the interface is transferred to the vapor phase. At the entrance, the vapor temperature is lower than at the interface and increases with the streamwise direction toward the equilibrium temperature. The absorption rate in the entrance region is limited by the inlet flow temperature.

Rosa et al. (2020) developed a model with the same assumptions as Triché et al. (2017). At the interface, the ammonia and water mass fractions were calculated using a thermodynamic model. Both liquid and vapor mass transfer resistances were studied: the liquid phase controls the mass transfer resistance while the heat fluid transfer controls heat transfer resistance under their conditions.

1.2.2.2 Vertical tube absorbers

Vertical tube absorbers are widely used in industry. The modeling of this kind of absorber is quite similar to that of plate absorbers. In addition, many authors have used Cartesian coordinates to solve the vertical tube problem.

- **Analytical resolution**

Mortazavi and Moghaddam, (2016) studied the absorption of H_2O in a LiBr/H_2O falling film and solved the same problem as Meyer (2014) for horizontal tubes using the same resolution method. Mortazavi and Moghaddam (2016) compared the results obtained when a linear film velocity profile is assumed with those obtained for a uniform velocity profile assumption. They noted an overestimation of the absorption rate of about 30% when uniform velocity is used compared to a more realistic linear profile.

Wu (2016) used cylindrical coordinates to solve their problem whereas previous works considered Cartesian coordinates. The same resolution method as Meyer and Ziegler (2014) has been used to study a LiBr/H_2O falling film. Wu (2016) confirms, as for the flat plate configuration, that the thermal boundary layer develops faster than the diffusive boundary layer. For short tubes, the concentration profile results agree with those of Meyer and Ziegler (2014).

- **Numerical resolution**

Gommed et al. (2001) studied the impact of the coolant inlet temperature, and inlet temperature and concentration of the solution on ammonia-water falling film absorption inside a vertical tube. The coolant temperature is an important parameter in the absorber design and the same result was highlighted by Rogdakis et al. (2003). The latter explained the importance of applying an energy balance on the coolant side instead of just carrying out the two limit cases of adiabatic and isothermal absorbers, as the coolant flow rate significantly affects the absorption process.

Bo et al. (2010) investigated numerically absorption in aqueous LiBr solution falling film. The convective boundary condition at the cooling water side was considered by assuming linear heat transfer fluid temperature. The McNeely (1979) equation at the interface was considered. They added a term corresponding to the inter-diffusion equation (1.8), as in (Yoon et al 2005).

$$u_x \frac{\partial T}{\partial x} + u_y \frac{\partial T}{\partial y} = a_f \left(\frac{\partial^2 T}{\partial x^2} + \frac{\partial^2 T}{\partial y^2} \right) + \frac{1}{\rho_f c_{p,f}} \frac{\partial}{\partial y} \left(\sum_{i=1}^{2} \rho_f D_i \frac{\partial C_i}{\partial y} h_i \right) \tag{1.8}$$

The subscripts 1 and 2 here correspond to LiBr and H_2O respectively. The absorbed flow over 1 m is 6.5% greater when the falling film properties are assumed constant. The difference found is higher than that of Kawae et al. (1989): 5% for 10 m.

Hosseinnia et al. (2017) included the inter-diffusion and the Soret and Dufour effects in their mass and energy equations (Equation 1.9).

$$\begin{cases} u_x \dfrac{\partial T}{\partial x} = a_f \left(\dfrac{\partial^2 T}{\partial x^2} + \dfrac{\partial^2 T}{\partial y^2} \right) + \dfrac{1}{\rho_f c_{p,f}} \dfrac{\partial}{\partial y} \left(\displaystyle\sum_{i=1}^{2} \rho D_i \frac{\partial C_i}{\partial y} h_i \right) + \frac{\mathcal{N} D_{sol}}{c_{p,f}} \left(\dfrac{\partial^2 C}{\partial x^2} + \dfrac{\partial^2 C}{\partial y^2} \right) \\ u_x \dfrac{\partial C}{\partial x} = D_{R-A} \left(\dfrac{\partial^2 C}{\partial x^2} + \dfrac{\partial^2 C}{\partial y^2} \right) + D_{sol} \left(\dfrac{\partial^2 T}{\partial x^2} + \dfrac{\partial^2 T}{\partial y^2} \right) \end{cases} \tag{1.9}$$

Where $\mathcal{N} = T_0 \left(\frac{\partial \mu^*}{\partial C}\right)_{T,P}$ is the Dufour parameter, μ^* the chemical potential of the solution, T_0 a reference temperature at which $\mathcal{N}$ is calculated, $D_S = \frac{S_T}{D_{R-A}}$ the thermo-diffusion coefficient ($m^2.s^{-1}.K^{-1}$) and S_T the Soret coefficient (K^{-1}).

Hosseinnia et al. (2017) found that for water vapor absorption in LiBr solution, there is an increase in the average heat flow and in the average absorbed mass of 9.5% and 4% respectively due to the introduction of inter-diffusion and Soret-Dufour effects. The effect of the variation of physical properties of the solution on the heat of absorption and the absorbed mass flow is less than 5%.

Aminyavari et al. (2017) studied the absorption of ammonia in water and considered the convective heat and mass transfer coefficients between the liquid and the interface, but also between the convective heat and mass transfer coefficients between the liquid and the wall. The energy released is five times greater at the inlet of the absorber than at the outlet.

1.2.2.3 Horizontal tube absorbers

Although horizontal tube absorbers have high heat and mass transfer coefficients (Ding et al. 2018), they are complex to model because the solution has three regimes. It flows as a falling film over the tube, as half drops (drop formation) at the bottom of the tube and as drops (drop fall) from one tube to another (Fig. 1.3). Despite these complexities, there is literature on the modeling of horizontal absorbers.

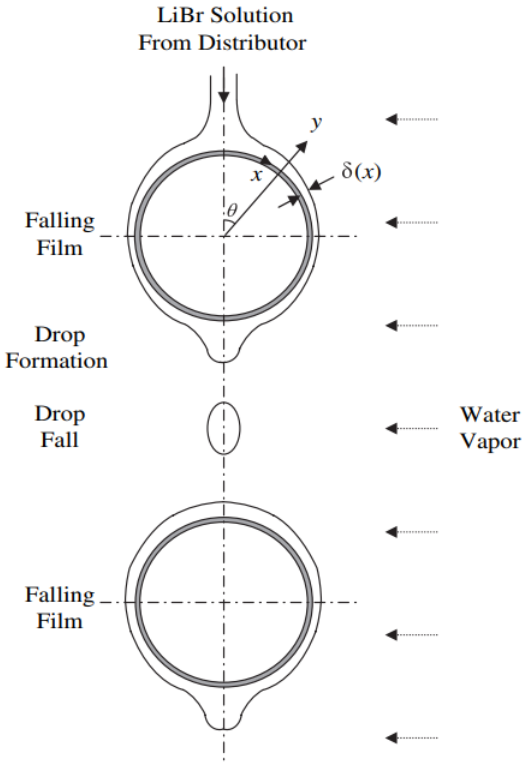

Figure 1.3: Description of the three different flow regimes for a horizontal tube absorber (Kyung, Herold, et Kang 2007)

- **Analytical resolution**

Falling film over horizontal tubes has not been studied much analytically (Killion 2003). However, progress has been made. Meyer and Ziegler (2014) and Meyer (2014) used the Laplace transform. The partial differential equations for an isothermal wall were solved by considering a uniform film velocity. Their results show good agreement with Nakoryakov and Grigor'eva (2010) when the wall temperature is equal to the inlet flow temperature.

Following Jeong and Garimella (2002) who used a numerical resolution, Giannetti et al. (2017) found that partial wetting reduces the local mass transfer over the whole surface at reduced mass flow rates. The wetting ability was defined as the ratio of the rivulet to the total width. The average wetting behavior of the LiBr/H_2O falling film was estimated by minimizing the kinetic and surface tension energy. The solution not only considered the partial wetting effect but also the shape of the cylinder, the temperature of the coolant and the inlet conditions of the solution.

Instead of using the Nusselt's equation which assumes a symmetrical parabolic velocity profile, Zhang and Gao (2016) developed the film thickness and velocity equations based on the linear superposition principle and on the method of separation of variables with the aim of analyzing the effect of the inertial force on the velocity in the entrance region to study an ammonia-water falling film. Giannetti et al. (2018) investigated the same problem as Giannetti et al (2017). If the wettability decreases, the Nusselt number decreases when decreasing the Reynolds number. However, if the effect of wettability is not included the Nusselt number increases when decreasing the Reynolds number. As conclusion, a horizontal-tube falling film absorbers can realize high heat and mass transfer rates with compact size and negligible pressure losses. They compared their results with some experimental studies namely (Soto Francés and Pinazo Ojer 2003; Kyung, Herold, and Kang 2007a; Lubis et al. 2017) and found no agreement. Indeed, in those experimental studies, authors did not consider the wettability effect although total wetting could not be achieved.

- **Numerical resolution**

Facing the challenge of analytical resolution of such complex flows, numerical resolutions have also been used to model horizontal tube absorbers. Although there is no analytical resolution that includes the three different regimes, almost all numerical resolutions consider it. Jeong and Garimella (2002) studied the LiBr/H_2O couple and explained that the absorption is adiabatic during the drop formation and the drop fall. The authors concluded that vapor absorption occurs primarily in the film and droplet-formation region of the flow and that the absorption is negligible in the droplets between the tubes. The film thickness and the velocity are both affected by the wetting ratio. Depending on the flow rate and the wetting ratio, 50% of the total absorption occurs in the droplets. Jeong and Garimella (2004) also analyzed the performance of lithium bromide absorbers for different tube diameters, spacing, and pass arrangements. It was observed that smaller tube diameters provide a significantly better absorber performance than larger tube diameters. Babadi and Farhanieh (2005) studied the absorption of LiBr/H_2O on a completely wetted horizontal tube assuming constant film thickness and both normal and transverse velocity in the range of Reynolds number from 5 to 100. The heat transfer coefficient is high at the inlet due to the large difference temperature between the incoming solution and the heat transfer fluid. At the bottom of the falling film, this coefficient decreases significantly due to the increase in the thickness of the film.

By incorporating an appropriate thermodynamic and transport phenomena formulation, Papaefthimiou et al. (2006 ; 2012) studied a LiBr-H_2O solution. The thermophysical properties of the superheated water vapor was estimated using a real gas equation of state avoiding saturation approximations at the liquid – vapor interface and using Helmholtz's relationship. The considered heat transfer fluid Reynolds number was 4500 and the energy balance was set through an overall heat transfer coefficient. They concluded that the increase of the solution mass flow rate results in the reduction of the solution outlet temperature and concentration: above a certain value of the solution mass flow rate, adding tubes does not contribute to the solution's cooling.

Using a parametric analysis with simplified mathematical model, the actual film thickness was estimated by Lee et al. (2005) by assuming that the half circumference of the tube as a vertical wall. Kyung et al. (2007b) made the same assumptions, as Babadi and Farhanieh (2005), to analyze the effect of inlet subcooling. In drop formation and fall regimes, they examined the dynamic regime and derived the corresponding energy and mass equations. 60% of the bulk LiBr mass fraction change occurs during the drop formation if the heat transfer fluid is not subcooled. However, there is almost no change in temperature and mass fraction in the drop fall regime.

Considering the spherical coordinates problem, Harikrishnan et al. (2011) found that the interface temperature and heat flux at the tube increase with the solution flow rate for the R-134a-DMAC couple. Moreover, the surface temperature gradient between the inlet and the outlet decreases with the flow rate. This is because the rate of thermal diffusion to the wall decreases for high flow rates with an increase in film thickness. An increase in the bulk solution temperature and interface temperature is also observed.

Ben Hafsia et al. (2015) carried out the analysis in Reynolds number range from 10 to 100. Two contradictory phenomena occur in the drop regimes. The first is the increase of the bulk temperature due to adiabatic absorption leading to a decrease in the absorption process. The second is the increase in the contact area between the liquid and the generated vapor water leading to an increase in the absorption phenomenon. Like Kyung et al. (2007b), they found that absorption is higher in the droplet regime than in falling film. However, they also mentioned that 74% to 77% of the absorption process occurs in the droplets when the inlet temperatures of cooling water and poor solution are 28°C and 41.25°C respectively.

Nguyen et al. (2018) studied the heat and mass transfer of NH_3-H_2O falling film using the Nusselt's theory to model the film hydrodynamics. Their study shows that the same equation could be used to analyze the LiBr-H_2O and NH_3-H_2O behavior at local scale. The solution flow rate, cooling water temperature and solution concentration (28%-31%) have significant impact on the heat and mass transfer coefficient.

Zhang et al. (2019) stated that the falling film absorption process can be divided into four regimes: falling film regime on the tube surface, pendant droplet on the underside of the tube, liquid column regime between tubes and falling droplet regime between tubes, in order to have a more accurate description of the droplets between tubes.

1.2.2.4 Summary on laminar falling film absorption

Killion and Garimella (2001) pointed out the importance of considering more realistic boundary conditions, than assuming adiabatic or/and isothermal wall. In the film, there is the development of a thermal boundary layer due to the thermodynamic equilibrium at the liquid – vapor interface, but also

a thermal boundary layer due to the heat transfer fluid. In recent studies, many authors aimed to add the coolant fluid study in their scope. None of them analyzed the interaction at local scale, the energy balance through the wall was done by means of an overall heat transfer coefficient or by assuming a linear profile of the coolant temperature. Studies showed that the heat transfer fluid flow and inlet temperature influence not only the total mass absorption but also the outlet solution temperature and concentration. The review also shows that the impact of variable thermophysical properties on the absorbed mass flow is still not enough studied. Further investigations have to be carried out to have a more realistic idea of their impact. Although many works tried to remove some of the common assumptions applied on falling film absorbers, many simplified ones are until now used to model the local heat and mass transfer. Some of them are mentioned in table 1.1. From the suggestion of Killion and Garimella (2001), many studies investigated the different types of droplets by studying not only their impact on heat and mass transfer but also by determining the part of the absorption that occurs in those regions. Most of the local analyses are performed on the LiBr-H_2O couple because of the same physical phenomena encountered when using different working fluids.

Table 1.1: Syntheses of main hypotheses and methods of resolution used for the study of phenomena in falling film absorbers – laminar regime

Geometry	Author	Wall type (boundary condition)	Film thickness	Fluid properties	Solution type	Velocity profile	Type of dilution	Reynolds number range	Comments
Plates	(Nakoryakov and Grigor'eva 1977)	Isothermal	Constant	Constant	Analytic	Uniform	Infinite	-	
	(Yoon et al.2005)	Isothermal	Constant	Constant	Numerical	Parabolic	Infinite	8–20	Study of inter–diffusion
	(Nakoryakov and Grigor'eva, 2010)	Adiabatic Isothermal	Constant	Constant	Series expansion method	Constant	Finite	12, 44, 94	Lewis number <<1 Kapitza number = 5-20
	(Nakoryakov et al. 2011)	Large thickness (Concentration boundary layer not fully developed)	Variable	Constant	Self-similar solution	Uniform	Semi-finite	-	Lewis number = 0.01 Peclet number = 400 Froude number = 0.5
	(Flores 2014)	Adiabatic Isothermal	Constant	Constant	Numerical	Parabolic	Finite	20–220	Established and partially – established zone
	(Mittermaier and Ziegler 2014)	Isothermal	Constant	Variable	Numerical	Uniform	Infinite	-	Study of inter-diffusion. Lewis number = 100
	(Vladimir E. Nakoryakov and Bartashevich 2017)	Isothermal	Constant	Constant	Analytical	Uniform	Finite		Applied at the entry region. Results use as initial conditions Lewis number < 1
	(Habib et al. 2019)	Isothermal	Constant	Variable	Numerical	Two components	Infinite	5–150	Study of the vapor phase and added shear stresses to their equations
	(Rosa et al.2020)	Non-isothermal	Constant	Constant	Differential algebraic model	Uniform	-	49–300	The flow is one dimensional as in Aminyavari et al. (2017); Triché et al. (2017) The vapor and liquid are in co-current flow while the coolant is in counter-current flow

Vertical tubes	(Rogdakis et al, 2003)	Heat Transfer fluid model	Constant	Constant	Implicit finite difference scheme	Parabolic	Infinite	50–100	Application of the energy balance on the coolant side
	(Bo et al. 2010)	Coolant heat transfer coefficient is used to model the heat transfer fluid	Constant	Constant	Numerical resolution (CFD software and Fluent)	Parabolic	Infinite	-	Absorbed mass fluxes of 0.0002–0.0022 $kg.s^{-1}.m^{-2}$ Lewis number is in order of magnitude of 100
	(Mortazavi and Moghaddam, 2016)	Adiabatic	Constant	Constant	Laplace	Linear	Infinite	-	Lewis number = 100, 257 Stefan number = 0.1
	(Wu 2016)	Coolant heat transfer coefficient is used to model the heat transfer fluid	Constant	Constant	Laplace	Uniform	Infinite	-	Lewis number = 100, 200 Biot number = 0.1, 1 Stefan number = 0.1
	(Hosseinnia et al. 2017)	Isothermal	Constant	Variable	Numerical	Parabolic	Infinite	75	Study of the inter-diffusion phenomenon and the Soret and Dufour effects
Horizontal tubes	(Jeong and Garimella 2002)	Coolant heat transfer coefficient is used to model the heat transfer fluid	Impacted by the wet ratio	Constant	Numerical	Parabolic and Impacted by the wet ratio	-	>100	Three different regimes were studied: Falling film, drop formation and drop fall. Linear temperature was assumed across the film. Wetting ratio is included.
	(Papaefthimiou, Karampinos, and Rogdakis 2006; Papaefthimiou et al. 2012)	an overall heat transfer coefficient is used to model the heat transfer coefficient	Variable	Constant	Method-of-lines approach	Two components	Infinite	< 50	Effect of the heat transfer fluid; Non-ideal gas is assumed for the stream; Incorporation of a more appropriated thermodynamic properties.
	(Babadi and Farhanieh, 2005)	Isothermal	Variable	Constant	Numerical	Two components	Finite	5–100	
	(Lee et al. 2005)	Coolant heat transfer coefficient is used to model the heat transfer fluid	Constant	Constant	Numerical	Parabolic	infinite	8-88 for the film flow 2200-3320 for ammonia gas	Estimation of the falling film thickness using a parametric analysis

(Meyer, 2014; Meyer and Ziegler 2014)	Adiabatic Isothermal	Constant	Constant	Laplace	Uniform	Semi-infinite	-	Study carried out with Cartesian coordinates Lewis number = 100, 200 Modified Stefan number = 0.1
(Q. Zhang and Gao 2016)	Non-isothermal	Constant	Constant	Analytical	Two components	-	237, 2373, 4746	New velocity and film thickness for horizontal tube: the inertial force is considered
(Giannetti et al. (2017), (2018))	Isothermal	Variable	Constant	Separation of variables	Two components	Finite	1–175	Partial wetting
(Nguyen, Hiep-Chi Le, and Quoc-An Hoang 2018)	Isothermal	Constant	Constant	-	Two components	Finite	10-300	NH_3-H_2O Impact of the operating condition on heat and mass transfer coefficients between the interface and the tube wall
(H. Zhang et al. 2019)	Non-isothermal	Constant	Constant	Numerical	Parabolic	-	32	Four different regimes considered Partial wetting = 0.8 vapor absorption rate of droplet regime can reach about 50% at high solution flow rate

1.2.3 Wavy-laminar flow regime

Rotem and Neilson (1969) affirm that there are three distinct flow regimes depending on the Reynolds number (Table 1.2). The Nusselt theory is valid only for low Reynolds Number due to hydrodynamic instabilities encountered at high Reynolds number (Miller 1998). More recently, the study conducted by Seol and Lee (2005) confirmed that the formation of waves at the free interface of the solution increases the absorption performance.

Table 1.2: Type of flow corresponding to the Reynolds number (Rotem and Neilson 1969)

Type of flow	**Reynolds number**
Laminar flow without rippling of the free surface	Re < 13
Laminar flow without rippling (wavy) of the free surface	13 < Re < 500
Turbulent flow	500 < Re

According to Brauner (1989), waves may be classified into two different categories: capillary or inertial laminar waves. The capillary waves have low amplitude, are sinusoidal with regular frequency (Fig. 1.4.a). When increasing the Reynolds number, inertial waves appear. They are also called roll waves and have high amplitude (Fig. 1.4.b).

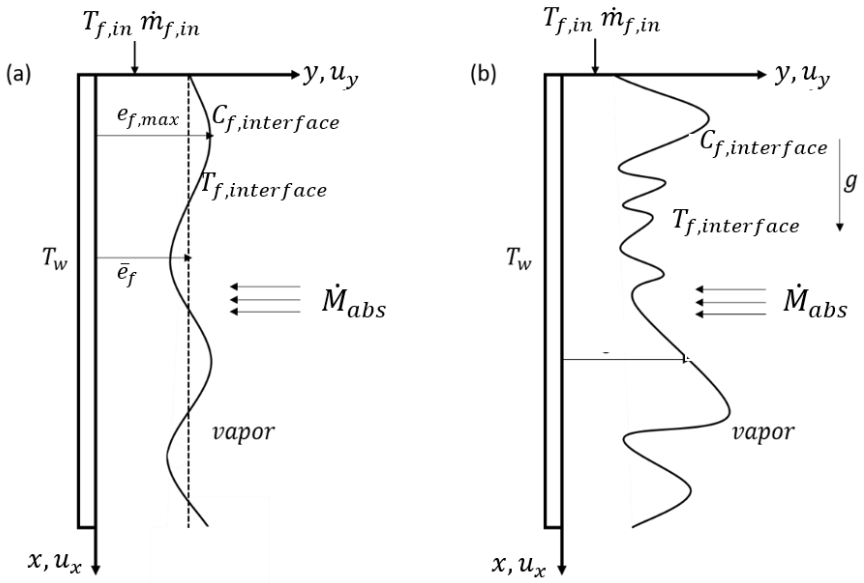

Figure 1.4: Schematic description of (a) sinusoidal wavy – laminar and free-wavy laminar flow regimes; (b) wavy – laminar flow regime without the sinusoidal shape assumption

The presence of recirculation regions may be observed in the roll waves. The roll-wave equation taking into account heat and mass transfer through the liquid–vapor interface has been derived by Nakoryakov et al. (2012). Although hydrodynamics of falling liquid film plays a major role in heat and mass transfers, the general aspects of the free-surface wave generation are still poorly understood (Nakoryakov, Ostapenko, and Bartashevich 2012). Although many authors studied the falling film hydrodynamic (Demekhin, Kalaidin, and Rastaturin 2005; Boudlal and Liapidevskii 2012; Chhay et al. 2017; Qiu 2018; Q. Wang et al. 2020; Cellier and Ruyer-Quil 2020) only few works have been carried out the effect of waves on the heat and mass transfer phenomena in an absorber and only few were

found after 2000. Indeed, many authors still assume uniform laminar falling film flow even at Reynolds number up to 100 as shown in the previous section. Falling film absorbers in the wavy-laminar flow regime are discussed in the following sections and the Table 1.3 summarizes the different results.

1.2.3.1 Flat plate absorbers

Sabir et al., (1996) assumed constant LiBr/ H_2O thermo physical properties and no recirculation of the liquid at $\mathrm{Re} = 100$. They explained that wave characteristics depend on the Reynolds number, falling film length and physical properties of the liquid. Wavy flow improves thermal and mass transfer and the improvement was not due to recirculation but to the transverse component velocity $(y\ axis)$ – which is absent in smooth flows and the convection associated with it.

Islam et al. (2009) focused on inertial waves with recirculation rather than regular periodic wavy film for LiBr/H_2O couple and found that temperature and concentration profiles fluctuate with the waves. Fig. 1.5 shows the evolution of the streamlines, temperature and concentration for wavy film versus downstream distance. At the entrance of the absorber, the absorption rate is slightly higher in a smooth film than in a wavy one as the waves are in the developing stage. Afterwards, the solution recirculation induced by wave, brings the cold and salt concentrated solution to the interface. This phenomenon favors the absorption of water due the high potential gradient at the interface. Moreover, the recirculation also allows the increase of the absorption phenomenon by removing heat from the interface. Given the low diffusivity of the absorbent for the LiBr/H_2O couple, the transfer of vapor into the film is limited and consequently the absorption rate decreases.

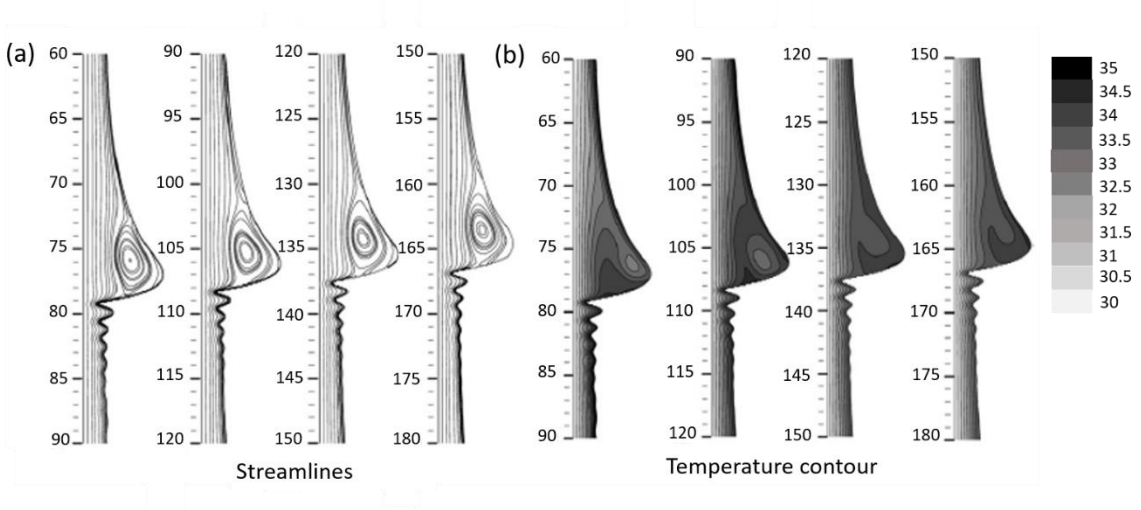

Figure 1.5: (a) Streamlines (b) temperature contour and (c) concentration contour of wavy film (Islam et al 2009)

A two-dimensional numerical simulation was performed by Bo et al. (2011) in order to investigate the effect of solitary waves on heat and mass transfer by considering a thin film flow of LiBr/H_2O solution for a film Reynolds number of 100. The recirculation flow induced by the solitary waves moves the high temperature and concentration from the wave front to the wave rear and the enhancement of the absorption rate is observed on the capillary waves formed in front of solitary wave. The capillary wave region is the one with the most absorption rate contribution with 52.8% followed by the wave rear region, 38% and then the wave front region, 9.2%. The enhancement ratio is 34.2% for the heat transfer coefficient and 23.6% for the mass transfer coefficient.

1.2.3.2 Vertical and horizontal tube absorbers

García-Rivera et al. (2016) studied the absorption of H_2O in a LiBr/H_2O solution over a vertical tube and focused their work on Reynolds numbers between 20 and 320, considering variable fluid properties in the streamwise direction with temperature and concentration. The number of waves formed and their velocity were determined. Heat and mass transfers are at a maximum at an optimal Reynolds number of 196, and beyond this optimal value, a decrease in absorption is observed

Horizontal tube absorbers were also studied. Indeed, Killion and Garimella (2004) calculated the surface area and volume of the droplet. Although many authors considered uniform film flow on the tube surface, Subramaniam and Garimella (2014) considered that the flow actually occurs as wavy film on the tube surface and as droplets in the inter-tube space. They successfully modeled the effect of mixing and waves caused by droplet impact on heat and mass transfer with a 3D model and temporal resolution for low Reynolds number < 500. They found that gravity and surface tension are the two main forces acting on the fluid.

Subramaniam et al. (2021) developed a 2D numerical model and considered the impact of the surface tension. Plots of temperature, concentration, velocity and local heat and mass transfer coefficients are presented and discussed for different inlet concentrations, temperatures, flow rates and coolant temperatures. The results were compared with those found by Subramaniam and Garimella (2014) when using a 3D model. They explained that the 2D model does not account the enhancement due to the axial propagation but still accounts for the most of the key elements of the flow.

1.2.3.3 Summary on wavy falling film

Not enough studies investigated the impact of the hydrodynamics – wavy and turbulent flows – on the heat and mass transfer process encountered in falling film absorbers. The heat and mass transfer enhancements are mainly due to the convection and the transversal velocity associated, but also to the presence of recirculation. As suggested by Killion and Garimella (2001) and in recent work, the hydrodynamics should be considered simultaneously in a coupled manner with the heat and mass transfer processes to have a more realistic representation of its contribution on the absorption phenomenon. One of the main simplifications to the governing equations is the use of uniform laminar falling film on horizontal tubes surface which is not true when considering more than a single tube. The impact of droplets on the next tube generates waves that mix the film flow and so the film is wavy laminar. Moreover, gravity and surface tension play a major role on droplet formation. More detailed studies must be carried out on horizontal tube absorbers in order to better understand the different phenomena that can be encountered, as the studies on droplets and their impact on the absorption phenomena are very recent.

Table 1.3: Syntheses of wavy-flow regime studies with key assumptions, specific details and key findings.

Geometry	Study	Fluid pair/conditions	Key assumptions	Specific details	Key findings
Flat plate absorbers	(Sabir et al., 1996)	LiBr/H_2O Re = 100	Isothermal wall. Linear dependency of concentration and temperature at the liquid–vapor interface.	At lower Reynolds numbers, the mixing (recirculation) effect is low. Inertial waves without recirculation.	At low Reynolds numbers, enhancement of the absorption rate is not due to recirculation as there is no mixing at these Reynolds numbers. The convection associated with the vertical component of the velocity is responsible for enhancement of the transfer phenomena. Mass transfer is improved when operating at higher Lewis numbers and lower heat of absorption.
	(Islam et al., 2009)	LiBr/H_2O (%LiBr: 55)	Isothermal wall. Inertial waves with recirculation.	Surface tension is a function of interface temperature and concentration.	Solitary waves produce recirculation, and the latter enhances the absorption rate
Vertical tube absorbers	(García-Rivera et al., 2016)	LiBr/ H_2O Re = 20–320	Variable fluid properties in the streamwise direction with temperature and concentration.	The number of waves and their velocity are determined using the Orr-Sommerfeld Equation (Goussis and Kelly 1991).	Heat and mass transfers have their maximum at an optimal Reynolds number of 196. Absorption performance decreases beyond this Reynolds number value in the conditions studied.
Horizontal tube absorbers	(Killion and Garimella 2004a)	LiBr/ H_2O (%LiBr: 53.44%)		CFD representation	Determination of surface area and volume of droplets.
	(Subramaniam and Garimella 2014)	LiBr/ H_2O (%LiBr: 65%) Re < 500	At the interface, the equilibrium parameters are determined using the (Yuan and Herold 2005) method Wavy film on the tube surface	CFD representation 3D model Surface tension considered	The droplet does not only impact the mixture of the film concentration but also generated axial propagation that play an important role on heat and mass enhancement.
	(Subramaniam, Chandrasekaran, and Garimella 2021)	LiBr/ H_2O Re < 500	At the interface, the equilibrium parameters are determined using the (Yuan and Herold 2005) method Wavy film on the tube surface	CFD representation 2D model Surface tension considered	The droplet impact leads to the mixture of the film concentration and allow to form a new surface for the absorption. Determination of local heat and mass transfer coefficients.

1.3. Experimental studies

Numerical and theoretical approaches are an interesting first step in understanding phenomena but validation through experimental work is important. This section summarizes the experimental work carried out on falling films. Despite the recommendation in (Killion and Garimella 2001), there is not much experimental work on coupled heat and mass transfer at the local scale due to the complexity involved and the measuring devices required.

Miller and Keyhani, (2001) set up a loop to measure film thickness, and wave amplitude and frequency for a LiBr/H_2O falling film at Re = 290. They used high speed video recordings to detect even the smallest changes in falling film thickness over a vertical tube. The film thickness was time-averaged. Wave amplitude is affected by the flow rate of the falling film and the outer diameter of the tube. Unfortunately, they did not give results on how hydrodynamics affect heat and mass transfer. The same authors used thermographic phosphors to measure the temperature profile along the length of the absorber tube (Miller and Keyhani 2001a). They found that the concentration gradient in the flow direction is almost constant.

The study of heat and mass transfer during water absorption in LiBr/H_2O solution by Takamatsu et al. (2003) for film Reynolds number in the range of 50 to 550 on vertical tubes showed that the surface is completely wetted for a film Reynolds number of 130 and higher. They explained that decreasing the film Reynolds number below 130 or increasing the tube length leads to a decrease of heat and mass transfer due to the breakdown of the liquid film to rivulet. The analysis was made by observing the tube inside using an industrial endoscope.

The assumption of a smooth laminar film is not valid over horizontal tubes (Killion and Garimella 2002; Killion and Garimella 2003; Killion and Garimella 2004a; Killion and Garimella 2004b; Subramaniam and Garimella 2009). Indeed, they studied the flow in horizontal tube absorbers using high-speed visualization in combination with quantification algorithm. Depending on the solution flow rate and the diameter of the tube, the droplet can either be detached or not before it hits the next tube. The impact of the droplet on the next tube causes waves and oscillations that play an important role in heat and mass transfer. The surface tension role in the mechanics of drop formation was also underlined. Killion and Garimella (2004) also showed that the flow affected absorption and in turn the absorption affects the flow characteristics due to variation in fluid properties.

High speed and high resolution videos using phothron digital camera were used by Bohra et al. (2019) to study falling film for Reynolds numbers between 34 and 102. This study is the first one to detail film and droplets in a water-ammonia falling film. As in the case of LiBr-H_2O, they found that the droplets offer additional surface area for absorption. Absorber pressure and solution concentration impact the absorber performance by impacting the thermophysical properties, film thickness, residence time and droplet-site spacing.

The experimental study conducted by Zhang et al. (2019) was divided into two parts: the image acquisition experiments using high-speed camera shooting and the falling film absorption experiment. The variation of the surface area and volume with time were determined. They showed that vapor is mainly absorbed in the falling-film and droplet regime, while it is negligible in the liquid column regime and falling droplet regime. Under low solution Reynolds number, the absorption phenomenon decreases with solution flowing down the tube bundle. As the solution flow rate increases, the amount

of vapor absorption in falling film regime gradually decreases, and the effect of the droplets between tubes becomes more and more significant.

On numerical and analytical models, most authors assumed to be under a uniform laminar film flow and so underestimated the thermal and mass effectiveness of the absorber knowing that falling film are naturally wavy. Experimental validation will allow to correct the theoretical models and to have a more realistic representation of the local phenomena. This local validation is important as it may be possible to broaden the scope of absorber improvement by studying how to act at the local level to improve behavior at absorber scale as highlighted in (Killion and Garimella 2001). Table 1.4 summarizes the different key findings of the experimental studies.

Table 1.4: Syntheses of experimental studies with key assumptions, specific details and key findings.

Authors	Geometry	Fluid pair/conditions	Specific details	Key findings
(Miller and Keyhani 2001a)	Single stainless-steel absorber Tube diameter: 0.01905 m Tube length: 1.524	Mass fraction: 60%, 62%, 64% LiBr-H_2O Absorber pressure: 1.0, 1.3, 1.5 kPa Inlet coolant temperature: 35°C Reynolds = 290	Thermographic Phosphor Data One tube: droplets not considered	Linear heat and mass transfer coefficients along the film length; Bulk concentration gradient approximately constant in the flow direction: Constant flux approximation can be used to solve the heat and mass transfer problem.
(Miller and Keyhani 2001b)	Tube length: 0.7 m	Mass fraction: 55% LiBr- H_2O Tube diameter: 9.53, 12.7, 19.05 mm	Video recordings	Film thickness measurements at different position; Impact of the tube diameter on the wavy flow; The average film thickness for a wavy-laminar flow is small compared to that of smooth laminar.
(Killion and Garimella 2003)	Single column of 6 horizontal tubes Tube diameter: 12.7 mm	-	High-speed digital video camera by photron Resolution 1024 x 1024 at 500 frames. s^{-1} 512 x 240 pixels	The nature of the waves and oscillations generated from the detachment of droplet and their frequency depend on design parameters, film flow rate, thermophysical properties such as fluid viscosity, surface tension and density.
(Killion and Garimella 2004b)	9 copper tubes Tube diameter: 15.9 mm Tube length: 0.5 m Tube center -to – center spacing: 31.8 mm	Mass fraction: 53.44% LiBr- H_2O Pressure: 1 kPa Reynolds < 100	Surface tension considered 7.3 10^{-2} $N.m^{-1}$ for water 9.1 10^{-2} for LiBr High-speed digital video camera by photron Resolution 1024 x 1024 at 500 frames. s^{-1}	Evolution of droplet surface area and volume Horizontal tubes elongate the droplets in the direction of the tube axis; The behaviour of droplets can be impacted by the interaction of neighbouring ones; The assumption that films are well distributed along the top surface does not hold if the droplet that arrives at the top is in discrete drops.
(Subramaniam and Garimella 2009)	-	Mass fraction: 65% LiBr- H_2O Reynolds < 110	Time step used 0.2 ms	Droplet impact and detachment causes circumferential and axial waves and oscillations of the liquid film; The droplet account for 4.4% of the total absorption; Non-uniform wavy films around the tubes.
(Bohra, Lee, and Garimella 2019)	Tube assembly Tube outer diameter. 9.5 mm Tube wall thickness 0.7 mm Tube length 0.292 m Number of rows 6 Number of columns 4 Horizontal pitch 30.5 mm Vertical pitch 20.1 mm Width 0.120 m Height 38.1 mm	H_2O/NH_3 Re = 34 - 102	Realistic absorber pressure: 150, 345 and 500 kPa High speed and high-resolution videos using photron digital	The dominant flow mode is observed in the droplet mode for the range the experiments. They are droplets that grown by themselves due to the absorption and those that are driven by the momentum carried by the impacting droplets. For a pressure of 345 kPa, mass fraction 25%, film flow rate 0.0019 kg. s^{-1}: Droplet diameter ~ 5 mm; Droplet site spacing ~ 18 mm; Droplet formation time 0.21 s; Film residence time ~ 0.134 s

	Capillary tube outer diameter 1.5 mm Number of rows 4			
(H. Zhang et al. 2019)	14 copper plain tubes Tube diameter: 16 mm Tube length: 0.5 m	Mass fraction: 56% LiBr-H_2O Pressure: 1 kPa Reynolds < 100	Image acquisition experiments using high-speed camera shooting and falling film absorption experiment; High – speed camera shooting frequency: 1000 frame. s^{-1} 256 x 240-pixel image	vapor is mainly absorbed in the falling-film and pendant droplet regime.

1.4. Thermodynamic approach

The concept of applying the thermodynamic of irreversible processes on a system with the aim of reducing exergy destruction was introduced by McClintock (1951) to design heat exchangers. Over the years, different approaches that use the thermodynamic of irreversible processes have been developed to evaluate and optimize thermodynamic systems. Two such approaches are the most popular: entropy generation analysis (EGA) and entropy generation minimization (EGM) (Sciacovelli, Verda, and Sciubba 2015). The latter explained that EGA is the method of identification and reduction of thermodynamic irreversibilities while EGM is the method of minimizing the losses of a system by respecting constraints. Entropy generation minimization was introduced by Bejan (1996) and has been widely used to optimize different types of heat exchangers (Hong, Du, and Wang 2017; Kiyasatfar 2018; Pussoli 2012; Zarea et al. 2014). The idea is to find the improved operating conditions or dimensions that give a lower entropy generation rate with respect to certain constraints. The first principle can be used to calculate the energy balance of any absorption machine component, but the second principle also provides information on entropy production (or exergy destruction) in each component (Fartaj 2004).

Before discussing optimization, it is important to identify, locate and quantify the entropy generation sources. A second law analysis of an LiBr/H_2O absorption chiller was investigated by Myat et al. (2011) and found that it can be reduced by optimizing input parameters such as the inlet solution temperature and the flow rates of the different components but also by optimizing the heat transfer area of the component.

For each component of absorption machines, there are avoidable and unavoidable irreversibilities, but also endogenous and exogenous irreversibilities (Kelly 2008). The idea of splitting the irreversibilities/exergy destruction was proposed by Morosuk and Tsatsaronis (2009) and Tsatsaronis and Park (2002). The theoretical basis for splitting the exergy destruction using thermodynamic cycle analysis was often discussed (Tsatsaronis and Park 2002; Morosuk and Tsatsaronis 2006a; Morosuk and Tsatsaronis 2006b; Morosuk and Tsatsaronis 2008; Morosuk and Tsatsaronis 2009). The unavoidable irreversibilities are those that cannot be reduced due to physical and economic constraints while the avoidable irreversibilities are those obtained by the difference between the total and the unavoidable irreversibilities. The endogenous irreversibilities of a component are due to inefficiency within the component itself when all the other components of the system are assumed to be ideal. The exogenous irreversibilities are obtained by the difference between the total and endogenous irreversibilities. Only the part of avoidable irreversibilities should be considered for the improvement of any system and components (Amidpour and Manesh 2021) by improving the component efficiency for the endogenous avoidable irreversibilities and by optimizing/improving the overall system/other components for the exogenous avoidable irreversibilities. The exergy destruction of the different components of a single-effect LiBr/H_2O absorption refrigeration cycle is mainly endogenous and the endogenous irreversibilities are mostly unavoidable for the desorber and absorber, unlike endogenous irreversibilities in the evaporator and condenser (Gong and Goni Boulama 2014).

Thu et al. (2013) found that an increase in the solution circulation ratio, defined as the ratio between the flow rate of the diluted solution coming from the absorber and the vapor coming from the evaporator of a LiBr/H_2O absorption refrigeration cycle, results in an increase of the endogenous irreversibilities of the absorber and the desorber.

Altamirano, Le Pierrès, et al. (2019b) developed an innovative bi-adiabatic system configuration of a LiBr/H_2O solar absorption system, determined the optimum conditions for a nominal cooling capacity of 5 kW and studied the exergy destruction of the system. This new configuration uses conventional heat exchangers for heat transfers and adiabatic mass exchangers for mass transfers for both absorption and desorption processes. The highest entropy generation is concentrated in the adiabatic desorber and absorber. They explained this result by the low mass efficiencies considered for both adiabatic exchangers (0.4 and 0.6) and the impact of the enthalpy of mixing.

As the absorber is one of the most critical components, some researchers have focused on it and on understanding how local entropy is generated depending on the scale, controls on patterns and processes change. Entropy generation in an absorber is due to different phenomena: heat transfer, mass transfer, hydrodynamics of the falling film.. Most thermodynamic studies in the literature examines local entropy generation $\left(S'''_{gen}\right)$ rate using the Hirschfelder et al. (1954) equation (1.10):

$$\dot{\sigma} = \overrightarrow{q_f} \cdot \vec{\nabla}\left(\frac{1}{T}\right) + \frac{\overline{\overline{\tau}}:\overline{\overline{\nabla}}(\overrightarrow{u})}{T} - \frac{1}{T}\overrightarrow{j_{vap}} \cdot \vec{\nabla}\left(\gamma_{vap}\right) \qquad \text{with } \overrightarrow{q_f} = -\lambda_f\vec{\nabla}(T) - h_{vap}\vec{j}_{vap} \qquad (1.10)$$

The first term on the right is the entropy generation due to heat transfer; the second term is due to viscous flow and the third term to the mass transfer.

At local scale, few studies have applied the thermodynamic approach to falling film absorbers due to their complexity. In the following paragraphs, those that have applied this approach to plate and tube absorbers are analyzed.

1.4.1 Flat plate absorbers

Chermiti et al. (2011) studied the absorption of CO_2 by H_2O at constant temperature and pressure in co-current flow. They studied a laminar falling film flowing down an adiabatic vertical plate. The mass flux transferred by convection is much greater than that transferred by diffusion. Moreover, the entropy generation is due to the mass transfer phenomenon near the interface and to the viscosity near the wall. This entropy generation is overall greater near the interface and decreases with the film thickness until reaching a minimum corresponding to the minimum of mass irreversibilities before increasing due to the viscous irreversibilities

Chermiti et al. (2013) also considered that absorption occurs at a constant temperature and so there is no heat irreversibilities. The evolution of the viscous and mass entropy generation with the film temperature is studied. Viscous entropy generation increases with the film temperature while in the diffusive boundary layer, mass transfer irreversibilities increases with an increase in film thickness and temperature. As the convective mass transfer irreversibilities increases with the temperature it induces an increase of the film fluid velocity. Beyond the diffusive boundary layer, mass transfer irreversibilities decreases with a decrease in the film fluid temperature.

Thermodynamic studies concerning the coupled effects in absorption chiller absorbers are recent. Hidouri et al. (2013) considered an adiabatic absorber with the NH_3/H_2O couple and included the irreversibilities due to heat transfer in their study. Entropy generation due to the heat and mass coupling caused by the thermodynamic equilibrium is almost 200 times the heat transfer irreversibilities at the interface. The heat transfer irreversibilities here is defined as the irreversibilities due to the thermal conduction phenomenon only, which is different from the heat and mass coupled entropy generation related to the simultaneous heat and mass gradients. In addition, the higher the difference in temperature between the interface and the wall, the higher the total entropy generation but that the viscous irreversibilities are not affected by that temperature gradient.

1.4.2 Tube absorbers

Giannetti et al. (2015a; 2015b) carried out a study of absorption in a LiBr/H_2O solution over a horizontal cooled tube. In the streamwise direction, the viscous irreversibilities have a parabolic profile and that the diffusion mass transfer and viscous irreversibilities are negligible. Moreover, total entropy generation is dominated by the heat irreversibilities. Total entropy generation increases with decreasing tube thickness, inlet film temperature and solution mass flow rate for Reynolds numbers between 4 to 28 (Giannetti et al. 2015a). The irreversibilities due to the coupled effects of mass convection and heat transfer has a critical impact on the total entropy generation. Fig. 1.6 shows the evolution of the entropy generation per unit of tube length (Eg) versus the Reynolds number and shows a minimal value (Giannetti et al. 2016). Thus, for each tube radius, the operating conditions that leads to the minimum entropy generation could be determined.

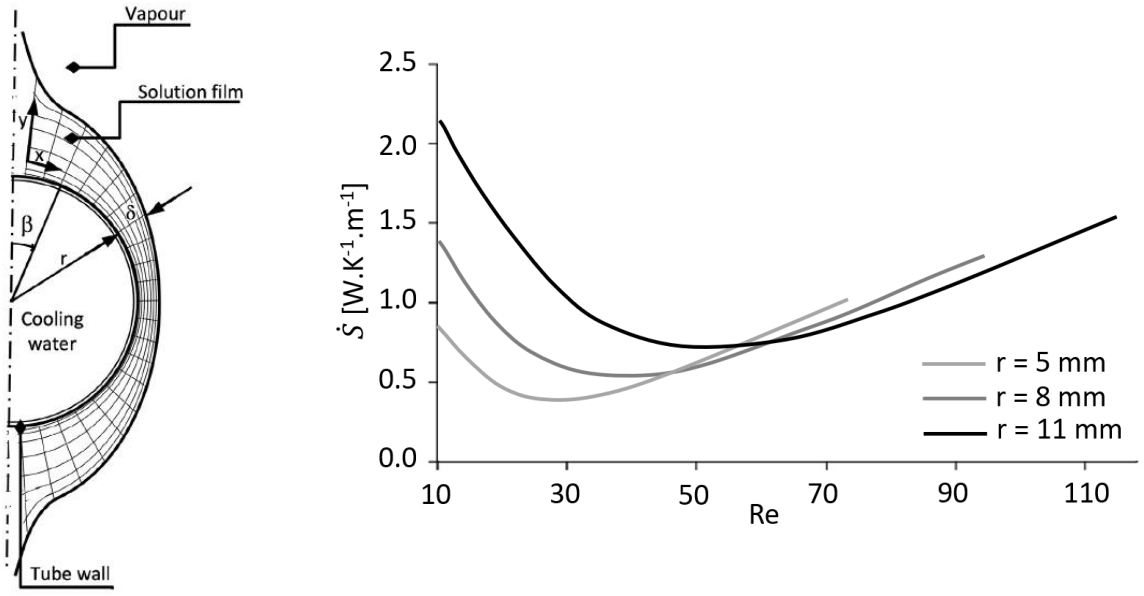

Figure 1.6: Entropy generation per unit of tube length (E_g) as a function of Reynolds number of the flow for different tubes radius values (Giannetti et al. 2016)

1.4.3 Summary of the thermodynamic approach

In all systems there are avoidable/unavoidable but also endogenous/exogenous irreversibilities. In order to improve the absorber performance, actions must be set to reduce the endogenous avoidable irreversibilities. Thermodynamic of irreversible processes is applied at local scale to better understand the different sources of these entropy generations. Researchers agree that the local entropy generation rate is the sum of thermal, viscous, convective and diffusive irreversibilities. Until now, only the impact of the film inlet temperature, tube radius and of the Reynolds number on the entropy generation is analyzed. The focus should be to identify, locate and quantify the sources of entropy generation but also to deeply understand the different contributions on the entropy generation with the aim of identifying the parameters and regions of the falling film (or absorber) on which to act at the local level for better performance at the component level.

Conclusions and scope of this work

This chapter presented the state of the art of studies carried out on absorption machines in general and on absorbers at low solution regime flows in particular. Different numerical and analytical approaches are described for the evaluation of local temperature, concentration and velocity profiles for flat plate, vertical and horizontal tube absorbers.

The analysis of the literature shows how much it is complicated to validate the local falling film temperature and concentration obtained using theoretical models with experimental results due to the sensor precision needed: most experimental studies only provide bulk temperatures and concentrations between the wall and the film interface. Consequently, the falling film models developed in this thesis, were compared with other numerical results.

The non-isothermal boundary condition has a significant impact on the absorption phenomenon. For many years, searchers focus on studied the falling film absorber assuming either adiabatic or isothermal condition. More recently, some of them started to include a HTF by assuming linear coolant temperature profile or overall heat transfer coefficient. In the present work, this assumption is eliminated and a non-null non-infinite HTF is modelled properly using local energy and momentum balances. The HTF is considered to flow either in laminar ($Re_{htf} < 2300$) or turbulent ($Re_{htf} > 4500$) regime with the aim of analyzing its impact on falling film phenomena – firstly on falling film evaporator (chapter II) then on falling film absorber (chapter III). The transitional flow regime ($2300 < Re_{htf} < 4500$) is not studied as it is complex to model due to lack of correlations.

More recently, studies demonstrated the importance of the second law of thermodynamics: the entropy generation analysis has been accepted as a method for heat exchanger's design and optimization. However, before talking about optimization, the sources of entropy generation need to be identified, located and quantified. The application of the TIP on entropy generation is recent, thus, the identified studies from the literature are not sufficient to give definitive conclusions on the entropy generation of the absorbers both at local and component scales. In the following chapters, a formulation of the local entropy generation is carried out – by applying the thermodynamic of irreversible process (TIP) – in order to identify the different sources of entropy generation associated to the operation of the evaporator and absorber (chapter II and III). Although the two limit cases – adiabatic or isothermal – were investigated, this thesis is the first one which includes the wall and the heat transfer fluid in the analysis of the entropy generation of a falling film absorber. To go further in the study, a parametric analysis is performed in chapter IV and Pareto fronts for chillers and heat transformers via a multi-objective optimization are given and discussed.

CHAPTER II

Chapter II. Thermodynamic analysis in laminar falling film evaporator

Based on:

Article: Mahamoudou, Ramousse, Cellier and Le Pierrès. Thermodynamic Analysis in Laminar Falling Film Evaporator. *Applied Thermal Engineering*, accepted on 7 June 2022. DOI: 10.1016/j.applthermaleng.2022.118814.

Conference: Mahamoudou, Ramousse and Le Pierrès. Thermodynamic analysis of a falling film evaporator, *34th International Conference on Efficiency, Cost, Optimization, Simulation and Environmental Impact of Energy Systems (ECOS2021),* Hybrid format, Sicily (Italy), in June 28-July 2, 2021.

Conference: Mahamoudou, Le Pierrès and Ramousse. Analyse du profil de température et de création d'entropie dans un évaporateur à film tombant. *Acte du congrès annuel de la Société Française de Thermique (SFT 2021),* Belfort, June 01-03 2021, https://doi.org/10.25855/SFT2021-040.

2.1. Introduction

Before studying the coupled heat and mass phenomena observed in a falling film absorber, a first model was developed to study a falling film evaporator. There are different ways to model the evaporator, either by analytical or numerical methods. However, the application of the thermodynamic of irreversible processes (TIP) to this component is still very limited according to the literature.

In this chapter, three novelties compared to what can be found in the literature can be highlighted. The first particularity is the study of the film by describing the thermal coupling between the HTF and the film through the wall. The HTF is modeled by considering the 2D heat transfer equation instead of calculating an overall heat transfer coefficient or assuming limit cases, which allows to model more realistic cases. The second particularity is the local analysis of the entropy creation through the whole evaporator - considering not only the film but also the HTF and the wall in order to quantify the share of irreversibilities generated in each medium depending on the operating conditions: most authors have applied the TIP, at the local scale, only on the film. Knowing the local distribution of the entropy generation, allows to better understand the physical phenomena which induce irreversibilities, and to localize them through the evaporator. It is therefore a way to improve the performance of falling film evaporators while minimizing the impact of their irreversibilities on the other components of the absorption machines. The third point to emphasize is the link made between the local and global phenomena of the evaporator.

The effect of film superheating and subcooling, as well as the Reynolds number of the HTF and the film, on the thermal and evaporation efficiencies, as well as on the evaporation rate and entropy creation, is studied. The impact of other parameters such as the length of the evaporator is also analyzed and results are given both at the local and component scales.

2.2. Problem description

2.2.1 Evaporator description

The study and analysis of the entropy generation produced during the evaporation process requires an understanding of the heat and viscous phenomena encountered. Fig. 2.1 shows a laminar film of incompressible liquid that enters the evaporator component at $x = 0$. The film flows down under the gravity effect (from the top to the bottom) over a vertical plate heated by means of a HTF. The latter can be in co–current (from the top to the bottom) or counter–current (from the bottom to the top) with the falling film. The HTF enables to increase the film temperature and then to evaporate a part of it at the free interface, assumed at constant saturation temperature along the film (constant pressure).

The heat and viscous transfer phenomena lead to the formation of the thermal δ_{th} boundary layer in the HTF ($\delta_{htf,th}$) and in the film ($\delta_{f,th}$). From Fig. 2.1, $x = 0$ and $x = L$ at the input and output of the absorber respectively while the axis y is equal to zero at the center of the HTF channel and to $e_{htf} + e_w + e_f$ at the falling film interface. The axis $y_1 \in [0, e_f]$, it varies from the heated plate – film side – until the film interface while the axis $y_2 \in [0, e_{htf}]$, it varies from the heated plate – HTF side to the center of the HTF channel thickness to.

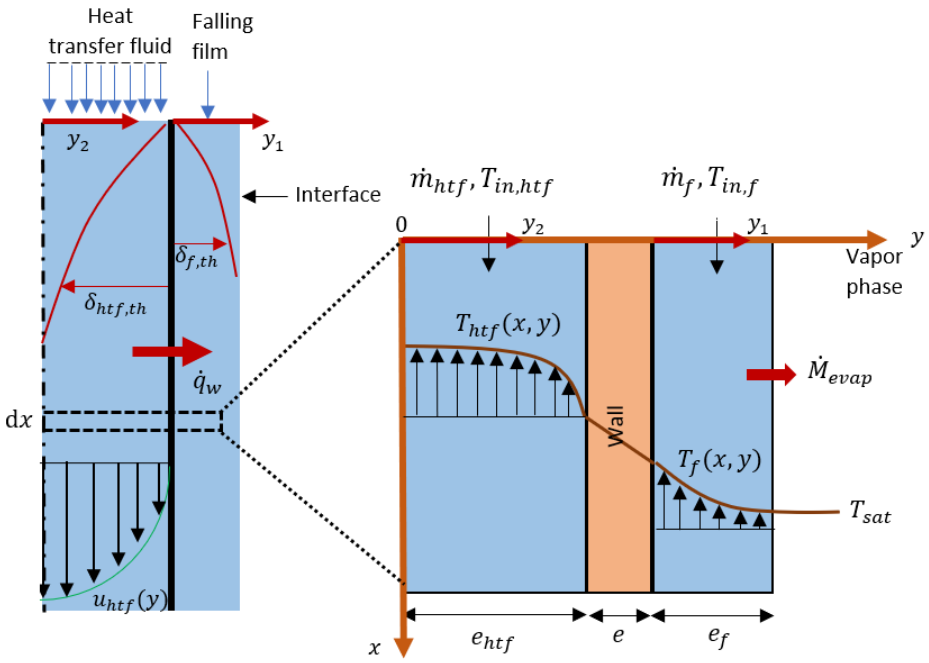

Figure 2.1: Description of a vertical falling film evaporator at local scale

2.2.2 Evaporator model description

2.2.2.1 Model Assumptions

Heat transfer is greatly intensified in the presence of capillary and solitary waves in the film (Kalliadasis et al. 2012). However, this paper will be limited to the modeling of falling film in the established laminar regime where these wave phenomena are attenuated (Flores 2014) as the falling film Reynolds number is considered to be lower or equal to 200. Moreover, as the impact of edge effect in this falling film is almost non-existent and as the vertical plate is assumed to be smooth and without corrugation, a 2D model seems to be appropriate to model the problem. However, for heat transfer fluids flowing over ribbed or corrugated plates, it is strongly advised to take into account the impact of edge effects by using 3D models. In formulating this model, the following assumptions were made:

- The falling film flow is assumed to be laminar, one-dimensional and fully developed hydrodynamically throughout.
- The liquid solution is incompressible, Newtonian and its physical properties (the viscosity, thermal conductivity and specific heat) are assumed constant since the flow is in steady-state and the temperature difference between the evaporator inlet and outlet is small – about 5°C.
- The evaporated mass is negligible compared to the inlet mass flow rate of the film ($\dot{m}_{evap} \ll \dot{m}_f$). Indeed, the film thickness is assumed to be small compared to the length of the evaporator and the interfacial shears are negligible. Consequently, the mass flow rate of the film $\dot{m}_f$ is assumed constant so as its thickness e_f along x.
- The evaporation process occurs at constant pressure, so that the saturation temperature T_{sat} at the interface is constant along x.
- Thermodynamic equilibrium is assumed at the interface
- There are no shear forces exerted on the film by the vapor at the interface.

2.2.2.2 Hydraulic model

2.2.2.2.1 Falling film

As the falling film flow is assumed to be laminar, one-dimensional and fully developed hydrodynamically throughout and no shear forces is assumed at the free interface, a Nusselt profile, equation (2.1), can be used for the film velocity (Brauner 1991).

$$u_f(y_1) = \frac{\rho_f g}{\mu} {e_f}^2 \left(\frac{y_1}{e_f} - \frac{1}{2} \left(\frac{y_1}{e_f} \right)^2 \right) \tag{2.1}$$

with $u_f(0) = 0$ and $\dfrac{\partial u_f(e_f)}{\partial y_1} = 0$

The following parameters can be determined knowing the mass flow rate per unit of width of the film.

The mass flow rate per unit of width of the film is given in equation (2.2):

$$\Gamma_f = \frac{\dot{m}_f}{l} = \rho_f \, e_f \bar{u}_f \tag{2.2}$$

The mean velocity is defined as in equation (2.3), (Incropera et al. 2006):

$$\bar{u}_f = \frac{1}{\rho_f A_f} \int \rho_f u_f(y_1) dA_f \tag{2.3}$$

For a Nusselt profile with constant density, it reduces to equation (2.4):

$$\bar{u}_f = \frac{1}{e_f} \int u_f(y_1) dy = \frac{\rho_f g}{3\mu_f} {e_f}^2 = \frac{2}{3} u_{f,max} \tag{2.4}$$

From the two above equations, the film thickness can easily be determined through the equation (2.5):

$$e_f = \left(\frac{3\mu_f \Gamma_f}{\rho_f^2 g} \right)^{\frac{1}{3}} \tag{2.5}$$

The film Reynolds number is defined as in equation (2.6):

$$Re_f = \frac{4\Gamma_f}{\mu_f} \tag{2.6}$$

2.2.2.2.2 Heat transfer fluid

For the HTF, both mass flow rate per unit of width and the channel thickness are known, thus the mean velocity and the HTF Reynolds number are defined in equation (2.7) and (2.8) respectively:

$$\bar{u}_{htf} = \frac{\Gamma_{htf}}{2e_{htf} * \rho_{htf}} \tag{2.7}$$

$$Re_{htf} = \frac{2\rho_{htf} \bar{u}_{htf} e_{htf}}{\mu_{htf}} \tag{2.8}$$

For the HTF, the Poiseuille equation is used to determine the velocity profile through the equation (2.9) with respect to the following: incompressible and Newtonian fluid; high channel length compared to the channel thickness; laminar flow through a constant cross-section and no fluid acceleration:

$$u_{htf}(y_2) = 3\bar{u}_{htf}\left(\left(\frac{y_2}{e_{htf}}\right) - \frac{1}{2}\left(\frac{y_2}{e_{htf}}\right)^2\right) \tag{2.9}$$

with $u_{htf}(0) = 0$ and $\dfrac{\partial u_{htf}(e_{htf})}{\partial y_2} = 0$

2.2.2.3 Thermal model

According to the above hypothesis, the heat balance in the different medium can be expressed as following:

In the falling film, the energy balance is given by the equation (2.10):

$$\rho_f C_{p,f} u_f(y_1)\frac{\partial T_f(x,y_1)}{\partial x} = \lambda_f\left(\frac{\partial^2 T_f(x,y_1)}{\partial y_1^2} + \frac{\partial^2 T_f(x,y_1)}{\partial x^2}\right) \tag{2.10}$$

Through the wall, equation (2.11):

$$\frac{\partial T_w(x,y)}{\partial y} = \frac{T_{htf}(x,e_{htf}) - T_f(x,e_{htf}+e_w)}{e_w} \tag{2.11}$$

In the HTF, equation (2.12):

$$\rho_{htf} C_{p,htf} u_{htf}(y_2)\frac{\partial T_{htf}(x,y_2)}{\partial x} = \lambda_{htf}\left(\frac{\partial^2 T_{htf}(x,y_2)}{\partial {y_2}^2} + \frac{\partial^2 T_{htf}(x,y_2)}{\partial x^2}\right) \tag{2.12}$$

The energy equation on the heat transfer fluid side is solved by assuming a symmetry at the center of the channel. To solve the problem, the followings boundary conditions are considered:

At $y_1 = 0$ and $y_2 = e_{htf}$	$\lambda_{htf}\left(\dfrac{\partial T_{htf}}{\partial y_2}\right)_{y_2=e_{htf}} = \lambda_f\left(\dfrac{\partial T_f}{\partial y_1}\right)_{y_1=0}$
At $y_1 = e_f$	$T_f(x,e_f) = T_{sat}$
At $y_2 = 0$	$\left(\dfrac{\partial T_{htf}}{\partial y_2}\right)_{y_2=0} = 0$

2.2.2.4 Performance parameters

To measure the performance of the falling film evaporator, the following parameters are defined:

- The overall heat transfer coefficient per unit of width is defined as in equations (2.13) and (2.14):

$$h_{htf} = \int_0^L \frac{\lambda_{htf}\left(\dfrac{\partial T_{htf}}{\partial y_2}\right)_{y_2=e_{htf}}}{\left(T_{bulk,htf}(x) - T_{htf}(x,\ e_{htf})\right)}\,dx \tag{2.13}$$

$$h_f = \int_0^L \frac{\lambda_f \left(\frac{\partial T_f}{\partial y_1}\right)_{y_1=0}}{\left(T_f(x,\ 0) - T_{bulk,f}(x)\right)}\ dx \tag{2.14}$$

With

$$T_{bulk,fluid}(x) = \frac{\iint \rho_{fluid} C_{p,fluid} u_{fluid} T_{fluid}(x,y) dy}{\rho_{fluid} C_{p,fluid} \bar{u}_{fluid} A}$$

Where the subscript fluid here can either be the HTF or the falling film.

- The thermal efficiency of the falling film evaporator is classically defined as in equation (2.15):

$$\varepsilon_{th} = \frac{\dot{Q}_{htf}}{\dot{Q}_{max}} \tag{2.15}$$

with $\dot{Q}_{max} = \dot{m}_{htf} C_{p,htf} (T_{htf,in} - T_{f,in})$

- The evaporated mass flow rate is calculated at the interface as in equation (2.16):

$$\dot{m}_{evap} = \frac{\dot{Q}_{f,interface}}{\Delta H_{liq-vap}} \tag{2.16}$$

With

$$\dot{Q}_{f,interface} = \int_0^l \left(\int_0^L \lambda_f \left(\frac{\partial T_f}{\partial y_1}\right)_{y_1=e_f} dx \right) dz = l \int_0^L \lambda_f \left(\frac{\partial T_f}{\partial y_1}\right)_{y_1=e_f} dx$$

- The evaporation efficiency of the falling film evaporator is defined as in equation (2.17):

$$\varepsilon_{evap} = \frac{\dot{m}_{evap} \Delta H_{liq-vap}}{\dot{Q}_{htf}} \tag{2.17}$$

with $\dot{Q}_{htf} = l \int_0^L \lambda_{htf} \left(\frac{\partial T_{htf}}{\partial y_2}\right)_{y_2 = e_{htf}} dx$

- The total evaporation rate is defined as in equation (2.18):

$$\tau_{evap} = \frac{\dot{m}_{evap}}{\dot{m}_f} \tag{2.18}$$

2.2.2.5 Entropy generation

2.2.2.5.1 Local entropy generation

Analysis of irreversibilities in the evaporator is essential to identify, locate and quantify the different sources of entropy generation. Indeed, the second law of thermodynamics provides a measure of entropy generation rate and irreversibilities within a system or process aiming to characterize the efficiency of the transfer process. In this section, the entropy generation at local scale is described. All

along x, negligible pressure drop is assumed. Some extra assumptions are needed in order to formulate the entropy generation namely:

- No chemical reactions.
- Steady state regime of the two-dimensional flow.
- Gravity-driven laminar flow of Newtonian incompressible liquid film.
- The irreversible processes take place near equilibrium

Under the problem formulation and the mentioned assumptions, the entropy generation rate is given by Hirschfelder et al. (Hirschfelder, Curtiss, and Bird 1954) and Haase (Haase 1990) as the sum of the product of thermodynamic forces and fluxes – equation (2.19):

$$\dot{\sigma} = \sum_{k} \vec{X}_k \vec{J}_k \tag{2.19}$$

With $\vec{X}$ and $\vec{J}$ are the driving force and the flux of the k phenomenon respectively.

In the study case, the only phenomena present are those due to heat transfer and hydrodynamics, as there is no chemical reaction and no mass transfer (the water and vapor are pure), thus the local entropy generation can be written as equation (2.20):

$$\dot{\sigma}_{fluid} = \underbrace{-\vec{J}_{q,fluid}\overrightarrow{grad}\left(\frac{1}{T}\right)}_{\text{Thermal entropy generation}} + \underbrace{\frac{\bar{\bar{\tau}}:\bar{\bar{\nabla}}(\vec{V})}{T}}_{\text{Viscous entropy}} \tag{2.20}$$

With $\overrightarrow{J_{q,fluid}} \cdot = -\lambda_{fluid}\overrightarrow{grad}(T)$ for conductive heat transfer

By developing the above equation with respect to equations (2.3) and (2.5), the local entropy generation can be expressed as in equation (2.21):

$$\dot{\sigma}_{fluid}(x,y) = \frac{\lambda_{fluid}}{T_{fluid}(x,y)^2}\left[\left(\frac{\partial T_{fluid}(x,y)}{\partial y}\right)^2 + \left(\frac{\partial T_{fluid}(x,y)}{\partial x}\right)^2\right] + \frac{\mu_{fluid}}{T_{fluid}(x,y)}\left(\frac{\partial u_{fluid}(y)}{\partial y}\right)^2 \tag{21}$$

Where the subscript fluid here can either be the HTF or the falling film.

2.2.2.5.2 Overall entropy generation

Here, the overall entropy generation will be defined in two different manners. Firstly, from the local definition by integration and secondly by applying the second law of thermodynamics directly to the whole falling film exchanger.

- **Overall entropy generation calculated from local modeling**

The global entropy generation is obtained by integration of the equation (2.21) as following, equation (2.22):

$$\dot{S}_{gen} = \iiint \dot{\sigma}_{tot} dxdydz$$
$$= l\int_0^L \int_0^{e_{htf}} \left(\dot{\sigma}_{htf,th} + \dot{\sigma}_{htf,v}\right) dxdy + l\int_0^L \int_{e_{htf}}^{e_{htf}+e_w} \dot{\sigma}_{w,th}\, dxdy$$
$$+ l\int_0^L \int_{e_{htf}+e_w}^{e_{htf}+e_w+e_f} \left(\dot{\sigma}_{f,th} + \dot{\sigma}_{f,v}\right) dxdy \quad (2.22)$$

The first integral gives the thermal and viscous irreversibilities in the HTF, the second integral represents the thermal irreversibilities through the wall – no viscous irreversibilities is observed in the wall as the latter is impermeable. The thermal and viscous irreversibilities in the film is given by the third integral.

The two contributions of the entropy generation, namely the thermal and viscous entropy generations, could be distinguished as following:

$$\dot{S}_{gen} = \dot{S}_{gen,th} + \dot{S}_{gen,v}$$

The thermal entropy generation is defined in equation (2.23), while the viscous entropy generation is defined in equation (2.24)

$$\dot{S}_{gen,th} = \dot{S}_{gen,htf,th} + \dot{S}_{gen,f,th} + \dot{S}_{gen,w,th} \quad (2.23)$$

$$\dot{S}_{gen,v} = \dot{S}_{gen,htf,v} + \dot{S}_{gen,f,v} \quad (2.24)$$

- **From the second law of the thermodynamics applied to the whole exchanger**

By application of the second law of the thermodynamic to the whole falling film exchanger with phase change, the entropy generation is given by the equation (2.25):

$$\dot{S}_{gen,th} = \dot{m}_{htf} c_{phtf} \ln\left(\frac{T_{htf,out}}{T_{htf,in}}\right) + \frac{\dot{m}_{evap}\Delta H_{liq-vap}}{T_{sat}} + \dot{m}_f c_{pf} \ln\left(\frac{T_{f,out}}{T_{f,in}}\right) \quad (2.25)$$

The first contribution of the thermal entropy generation in the above equation, represents the entropy variation due to the temperature gradient in the HTF, while the second and third ones represent the entropy variation in the falling film due to the phase change at the film free interface and to the temperature gradient. By using equations (2.15) and (2.17), equation (2.25) can be rewritten as in equation (2.26):

$$\frac{\dot{S}_{gen,th}}{\dot{m}_{htf} c_{htf}} = ln\left(1 - \varepsilon_{th}\left(1 - \frac{T_{f,in}}{T_{htf,in}}\right)\right) + \varepsilon_{evap}\varepsilon_{th}\left(\frac{T_{htf,in} - T_{f,in}}{T_{sat}}\right)$$
$$+ \frac{1}{R_p} ln\left(\varepsilon_{th} R_p \left(1 - \varepsilon_{evap}\right)\left(\frac{T_{htf,in}}{T_{f,in}} - 1\right) + 1\right) \quad (2.26)$$

Where the dimensionless parameter R_p is defined as,

$$R_p = \frac{\dot{m}_{htf} c_{p,htf}}{\dot{m}_f c_{p,f}} \quad (2.27)$$

2.3. Resolution method and operating conditions

2.3.1 Numerical solution

The resolution of the thermal and hydrodynamic models is done by applying a finite difference discretization on the spatial derivative terms using the Julia programming language, then numerically solving the system of non-linear equations obtained using the Trust-Region Method (Conn, Gould, and Toint 2000) to obtain the solution for a steady state condition. A first-order backward difference is used in the x-direction while a second-order central difference is adopted in the y-direction for both fluids. The numerical domain was discretized into N nodes in the x-direction, M nodes in the y_2-direction and P nodes in the y_1-direction. Initially, a matrix $N \times (M + P)$ that contains the initial HTF temperature in the $N \times M$ and the inlet film temperature in the $N \times P$ is defined. The function developed in the code contains boundary conditions and loop controls. Iteration is required for each step to fill the matrix with the new temperature values until the boundary conditions (paragraph 2.2.3) are satisfied in the steady-state conditions. The absolute and relative tolerance errors are set to have a value of 10^{-6} and 10^{-8} respectively. Knowing the temperature field in both fluids, the evaporated mass flow rate is calculated at the free interface and the local entropy generation is determined in the whole domain.

2.3.2 Grid size effects

In order to investigate the grid size effect, runs were performed with 160 × (40 + 40), 500 × (40+40), 600 × (40+40), 750 × (40+40), 160×(30+30), 600×(30+30), 750×(30+30) and 750×(50+50). The total evaporated mass is calculated for the different runs, leading to a maximum difference of 2% in terms of evaporated mass flow rate for a reference case Re_{htf} = 1000, Re_f = 49.8, δ_{htf} = 2 mm. The 500 × (40 +40), meshes were chosen in the final calculation as the running time increases from 245 seconds for 160 × (40+40) to 2500 seconds for 600 × (40+40). The chosen meshes have a running time of around 1200 seconds. However, the study of the grid size effect shows that an increase in the flow rate of the HTF requires an increase in the number of meshes in order to remain on results where the maximum difference is 2% in terms of evaporated mass flow rate. Increasing the mesh size means increasing the computation time - about 1h10 per simulation for the case of Re_{htf} = 2000. Because of the long compu tation time, the 500×(40+40) has been retained even for simulations different to the reference case, and this even if the maximum deviation of the evaporated mass flow rate is no longer 2% but around 6% for Re_{htf} = 2000. To conclude, the mesh size was chosen by making a compromise between the ma ximal acceptable variation of evaporated mass flow rate and running time. In the following the same mesh grid –500×(40+40) – is used for all simulations.

2.3.3 Operating conditions

The evaporator considered in this study is an evaporator that can be used in absorption systems for building heating and cooling. The parameters used here are in accordance with the studies carried out in the LOCIE laboratory in the framework of the improvement of absorption machines (Perier-Muzet and Stutz 2021). The main design characteristics of the evaporator are summarized in Table 2.1. The behavior of the evaporator is studied by analyzing the impact of the evaporator length on the evaporated mass flow rate, entropy generation and on the thermal and evaporation efficiencies.

Table 2.1: Main design characteristics of the evaporator

Configuration	Co and counter HTF flow
Evaporator length (L)	0.1 – 0.5 m
Thickness of the wall (e)	3×10^{-3} m
Conductivity of the wall (λ_w)	500 $W.K^{-1}.m^{-1}$
Width of the evaporator (l)	0.1 m
Thickness of the HTF channel	1.75×10^{-3} - 4×10^{-3} m

The chosen film fluid and HTF for the simulation are both water. Thus, the evaporation temperature T_{sat} is maintained at 300.0 K for a saturation pressure of 3.4 kPa (Saul and Wagner 1987) and the evaporation heat (ΔH_{liq_vap}) is 2549 kJ/kg (Florides et al. 2003)– see Appendix 1 and 2 for the used equations. Table 2.2 summarizes the main operating parameters used for the simulation. To study the impact of the falling film and HTF Reynolds numbers on the evaporated mass flow rate, a parametric study was conducted by considering Reynolds number between 49.8 and 200 (Perier-Muzet and Stutz 2021) and between 500 to 2000 for the falling film and the HTF respectively.

Table 2.2: Fluids characteristics (Salvagnini and Taqueda 2004; Qiu 2018)

	Γ, kg. m^{-1}. s^{-1}	λ, $W.K^{-1}.m^{-1}$	ρ, $kg.m^{-3}$	Cp, $J.K^{-1}.kg^{-1}$	T_{in}, K	Re,-
Heat transfer fluid	0.4 – 1.6	0.61	997.5	4178.0	305	500 – 2000
Film	0.01 – 0.04	0.61	997.5	4178.0	300 – 302.5	49.8 – 200

The study was made for both co and counter-current configurations with the aim of analyzing their performance and studying the impact of both configurations on the local and overall entropy generation for different film inlet temperature, falling film and heat transfer fluid Reynolds but also for different evaporator length.

2.3.4 Model validation

For the validation of the model, two different comparison points were considered. The first point is to validate the model by comparing only the thermal entropy generation obtained using equations (2.22) and (2.26) for counter-current configuration. Fig. 2.2 shows the evolution of the thermal entropy generation obtained by integration using the equation (2.22) with the thermal entropy generation of the equation (2.26) for different HTF Reynolds number using the design characteristics mentioned in Table 2.1 and the parameters in Table 2.2. The film Reynolds number is assumed equal to 49.8, the evaporator length equal to 0.5 m and the HTF channel thickness equal to 2 mm.

The black line represents the ideal case where the entropy generation obtained from equation (2.22) is equal to the one obtained from equation (2.26). From this figure, it can be concluded a great agreement between the two entropy generations as the maximum deviation is about 7% and the mean deviation is less than 5%. The deviation when increasing the Reynolds number is linked to the mesh chosen as the test grid has been performed for HTF Reynolds number equal to 1000. In order to reduce the incertitude and error, in the following section, the parametric analysis is done mainly by assuming a Re_{htf} = 1000.

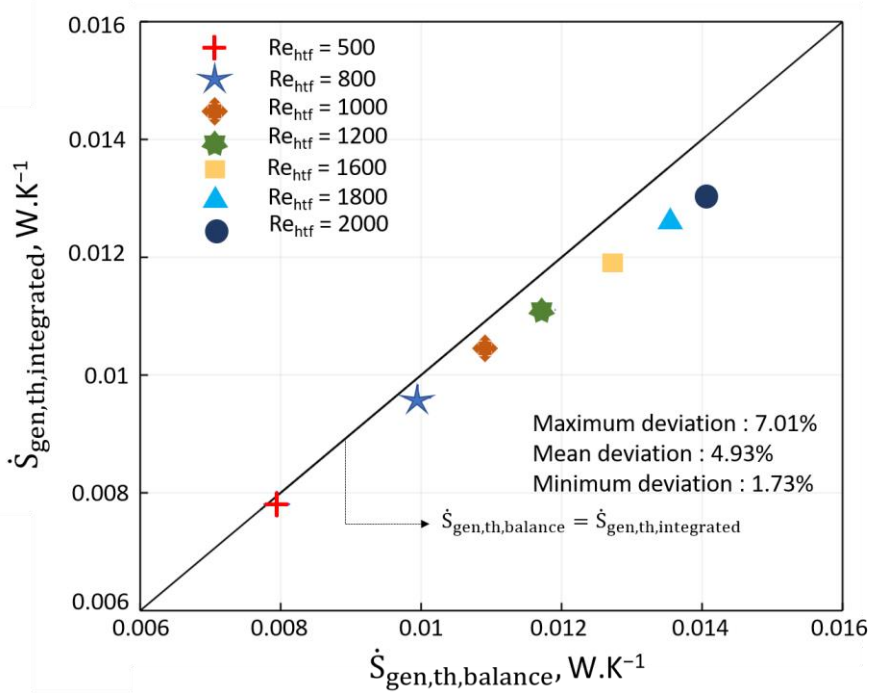

Figure 2.2: Comparison of the entropy generations for different Reynolds number and for counter-current configuration

The second point is a comparison of the present work with the analytical results of Flores (Flores 2014) in order to validate the falling film model by assuming an adiabatic wall and a constant temperature at the film interface. The difference of temperature between the interface and the inlet temperature of the film is equal to 2°C. The comparison is carried out using non-dimensional variables, namely, $\varsigma = \frac{y_1}{e_f}$ coordinate in y_1 direction and temperature θ. In Flores (Flores 2014), the plate length is divided into two parts. Near the entrance of the exchanger corresponds to the part where the thermal boundary layer is not yet fully developed while the second part corresponds to the fully thermally developed region.

In the entrance region, the non-dimensional temperature is defined as in equation (2.28):

$$\theta = \frac{T_f(x,\ y_1) - T_f(x,\ 0)}{T_f(x,\ e_f) - T_f(x,\ 0)} = \left(\frac{e_f - \delta_{f,th}}{\delta_{f,th}}\right)^2 - 2\,\frac{(e_f - \delta_{f,th})e_f}{\delta_{f,th}^2}\varsigma + \left(\frac{e_f}{\delta_{f,th}}\right)^2 \varsigma^2 \qquad (2.28)$$

The evolution of the temperature through the film thickness at different x positions for the entrance region is shown in Fig. 2.3. As it can be seen, great agreement is observed between the two models as the mean deviations is about 0.7% even if the maximal absolute deviation is 100%. Indeed, at x = 4.5×10^{-5} m and ς = 0.77, the non-dimensional temperature obtained by Flores is 0 while the one obtained with the present model is 0.06. The same figure shows that the thermal boundary layer grows more rapidly in the present model than in the one developed by Flores. This result can be explained by the impact of the temperature parabolic profile assumed by Flores.

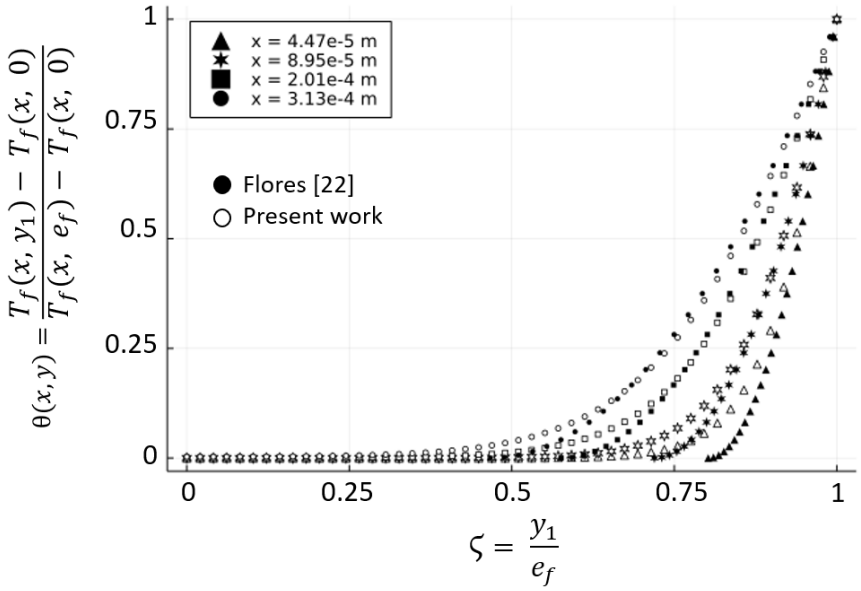

Figure 2.3: Validation of the model by comparing the present work with those of Flores [22]

In the fully developed region, the non-dimensional temperature is defined as in equation (2.29):

$$\theta = \frac{T_f(x,\ y_1) - T_{bulk,f}(x)}{T_f(x,\ e_f) - T_{bulk,f}(x)} = \frac{T_f(x,\ 0) - T_{bulk,f}(x) + \left(T_f(x,\ e_f) - T_f(x,\ 0)\right)}{T_f(x,\ e_f) - T_{bulk,f}(x)}\varsigma^2 \qquad (2.29)$$

Fig. 2.4 shows the temperature evolution through the film thickness at different x positions. It shows a great agreement between this model and the one developed by (Flores 2014) mainly far from the inlet of the evaporator.

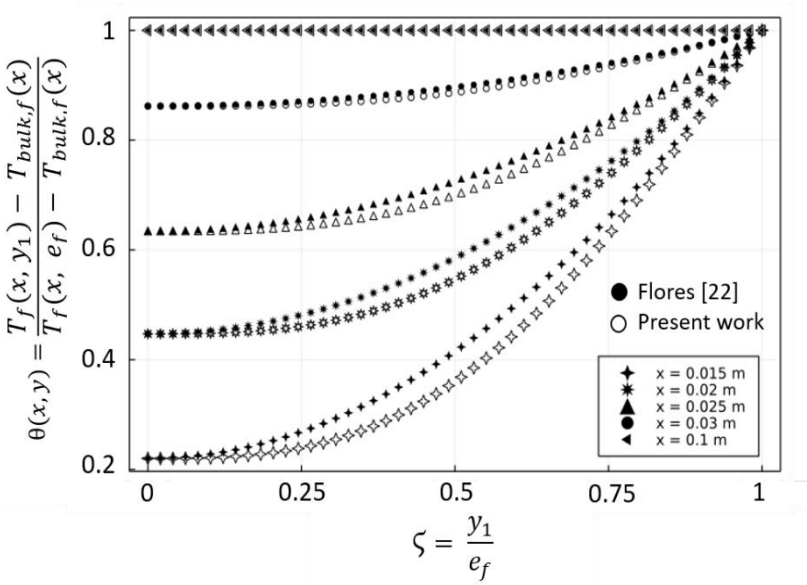

Figure 2.4: Validation of the model by comparing the present work with those of Flores (2014)

Indeed, the maximum deviation is about 14% and is found near the entrance of the fully developed region. The deviation decreases with the increase of the film length to be almost equal to 0.7% at x = 0.1 m.

2.4. Evaporator analysis

In this section, results of the present study are presented. First, the analyze of equation (2.26) is done in order to have an overview of the evolution of the thermal entropy generation with the evaporation and thermal efficiencies at the component scale. Afterwards, a local analysis is performed to deeply understand the local behavior of a falling film evaporator. To do that, the impact of the heat transfer fluid Reynolds number, Re_{htf} = [500 – 2000], falling film inlet temperature, $T_{in,f}$ (K) = {298.00, 299.00, 300.0, 301.0, 302.0, 303.0} and of the film Reynolds number, Re_f = [49.8 – 150], on the evaporation process and entropy generation rate are determined, presented and analyzed for a saturation temperature of 300.0 K and for both heat transfer fluid flow configurations. In the following, only the mass flows and inlet temperatures are assumed the same for both configurations as inputs of the model.

2.4.1 Overall analysis and reference case

Fig. 2.5 shows the temperature profile in the HTF, film and wall. As excepted, the temperature decreases from the channel centre to the film interface as the heat flux is transferred from the HTF fluid to the film.

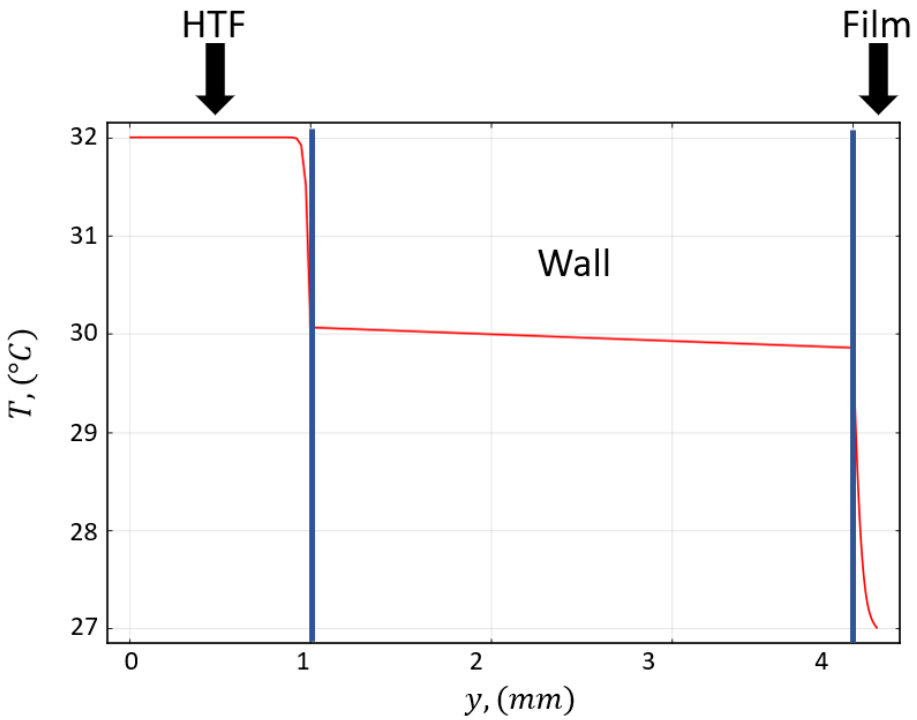

Figure 2.5: Temperature profile through the HTF, wall and film side at x = 0.0005 m

From equation (2.26), the thermal entropy generation varies with the thermal efficiency, the R-value and the evaporation efficiency. Here, the impact of these parameters on the thermal entropy generation is discussed for a reference case where Re_f = 49.8 and $\dot{m}_{htf}$ = 0.04 m. s^{-1}. The HTF inlet temperature is equal to 305 K whereas the film inlet temperature is assumed equal to the interface film temperature (300 K). Fig. 2.6 shows the evolution of the thermal entropy generation with the evaporation and thermal efficiencies using equation (2.26). The thermal entropy generation increases

with the increase of the evaporation efficiencies. The thermal entropy generation also presents a maximum value depending on the thermal efficiency.

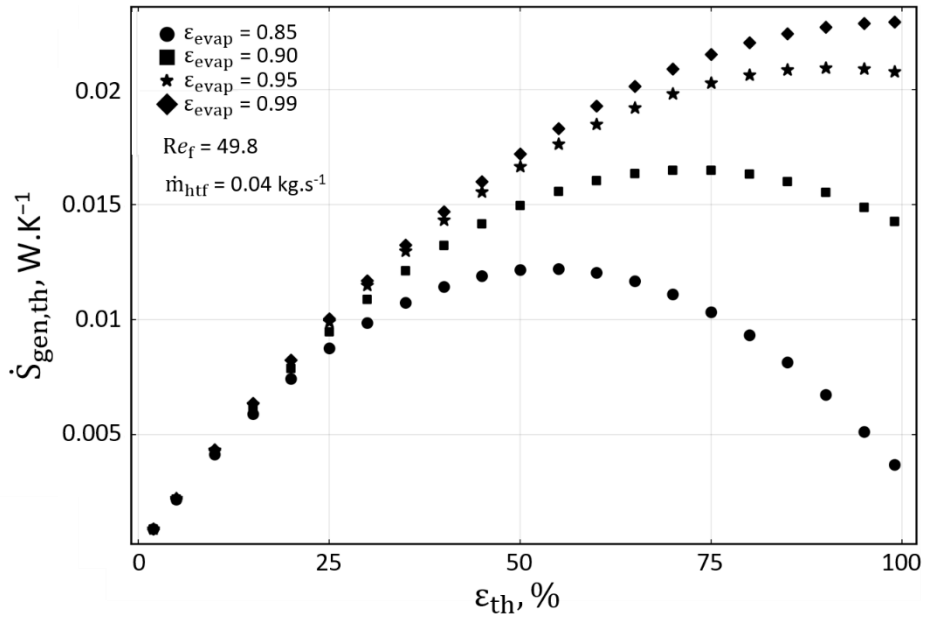

Figure 2.5: Evolution the thermal entropy generation with the thermal and evaporation efficiencies

For the considered mass flows, the analysis shows that the evaporation efficiency cannot be below 83%. The analysis at component scale of the thermal entropy generation does not give any information about the reason why the evaporator cannot work with an evaporation efficiency lower than 0.83 for high thermal efficiency. Local study is then important in order to have more information on thermal entropy generation sources and evolution.

Fig. 2.7 shows the evolution of the total entropy generation through the film thickness and along the plate length for the same previous reference case – e_{htf} = 2mm, $\dot{m}_{htf}$ = 0.04 m. s^{-1}, HTF Reynolds number of 1000, film Reynolds number of 49.8 and a temperature difference between the inlet and the interface of the film (ΔT) equal to 0. However, the focus is on the thermal entropy generation as the total viscous irreversibilities are 100 times lower compared to the total thermal ones.

In the film, when assuming a temperature difference between the inlet and the interface of the film (ΔT) null, at the entrance, only the thermal boundary layer due to the heat transferred from the HTF to the film is in developing stage, leading to the increase of the film temperature. Inside this thermal boundary layer, thermal irreversibilities is observed due to the heat transfer and these irreversibilities are higher near the wall and decrease with the development of the boundary layer. Beyond this thermal boundary layer, no phenomenon occurs, as the film temperature is equal to the interface temperature and thus, no thermal irreversibilities is observed. Consequently, for both configurations, the main entropy generation is located near the wally_1 = 0 (for the film) where the temperature gradient is higher and so the transfer is larger and this, even after the complete development of the thermal boundary layer in the falling film.

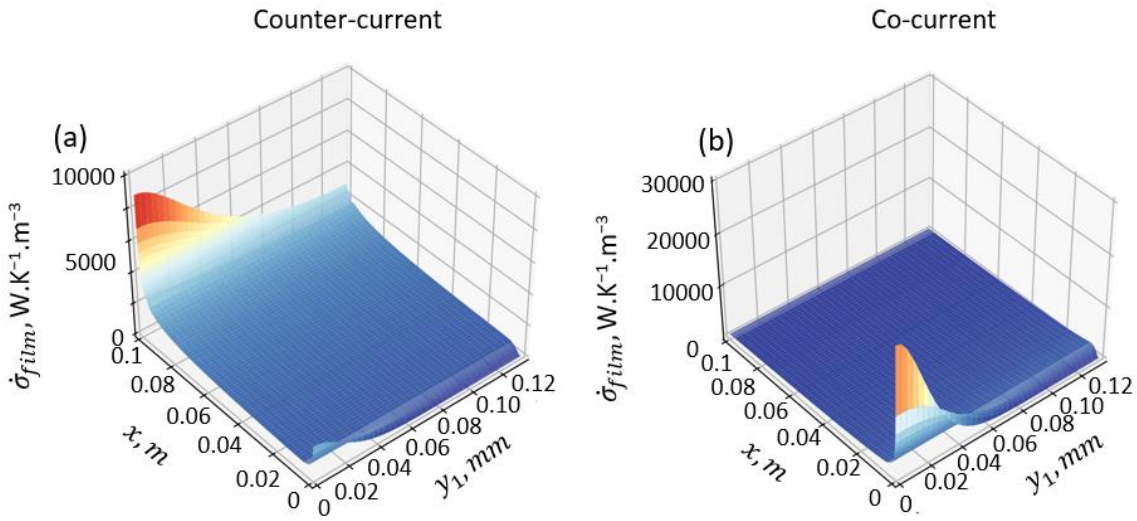

Figure 2.7: Thermal entropy generation through the film for both co and counter-current configurations, Re_{htf} = 1000, Re_f = 49.8, e_{htf} = 2mm and ΔT = 0 K

Indeed, the irreversibilities are higher near the wall compared to the film interface: the heat transferred from the HTF to the film is high compared to the evaporation phenomenon under the studied conditions. For counter-current, Fig. 2.7.a, the maximal local entropy generation is around 10 000 W. K^{-1}. m^{-3} while for co-current, Fig. 2.7.b, the maximal local entropy generation is around 30 000 W. K^{-1}. m^{-3} (three times higher than in counter-current flow). However, the local entropy generation in the co-current configuration rapidly decreases along the x axis due to the decrease of the heat flux through the wall. The decrease of the heat flux transferred from the HTF to the film also leads to the decrease of the evaporated mass flow rate. For the counter-current flow (Fig. 2.7.a), the entropy generation variation along the x axis is small compared to the entropy generation variation in co-current flow, due to the almost constant small temperature gradient observed in the evaporator with this configuration leading to a slight variation of the heat transfer flux through the wall. Fig. 2.7.a shows that the local entropy generation in the falling has a minimum value in the flow direction corresponding to the position where the thermal boundary layers of both fluids are fully developed.

Moreover, for a considered configuration (counter or co-current), the thermal entropy generation in the HTF and in the film are of the same order of magnitude near the plate – slightly higher in the heat transfer fluid side as shown in Fig. 2.8. This is due to the heat flux conservation through the wall and to the fact that both fluids considered are water (same conductivity). In the HTF, a thermal boundary layer is also observed due to the decrease of the temperature linked to the heat flux transferred to the film.

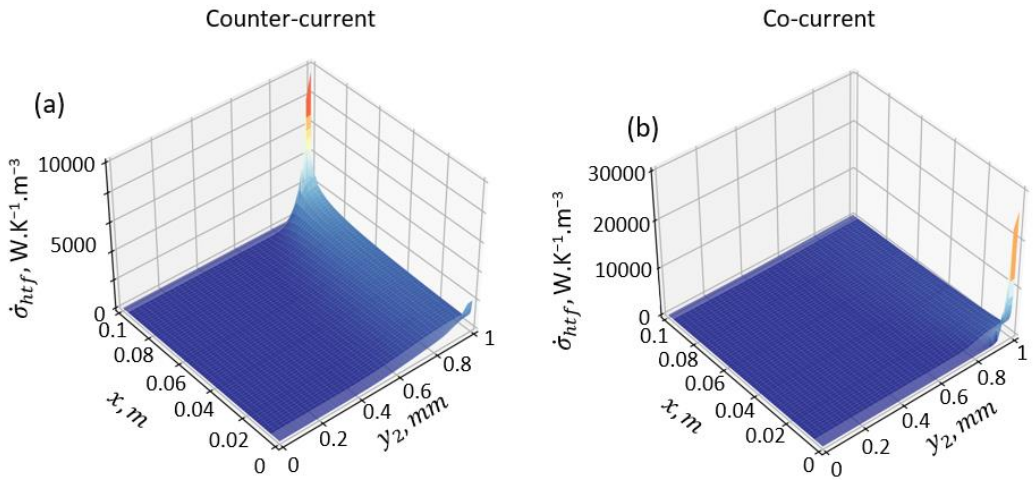

Figure 2.8: Thermal entropy generation through the film for both co and counter-current configurations, Re_{htf} = 1000, Re_f = 49.8, e_{htf} = 1mm and ΔT = 0 K

Depending on the flow configuration, the thermal boundary layer develops from the top to the bottom or from the bottom to the top. Moreover, due to the fix channel thickness, the laminar HTF flow assumption (leading to a slow development of the thermal boundary layer), the small HTF conductivity, and to the small Prandtl number – around 5 -, the thermal irreversibilities within the HTF quickly decreases from the wall to the channel center. The thermal entropy generation through the wall is small. For co-current flow, it varies from around 29 W. K^{-1}. m^{-3} at the entrance to 0.6 W. K^{-1}. m^{-3} at the bottom of the evaporator. However, for counter-current flow, the thermal entropy generation through the wall varies from 11 W. K^{-1}. m^{-3} at the bottom of the evaporator then decreases until reaching a minimal value of around 0.7 W. K^{-1}. m^{-3} before increasing to 3 W. K^{-1}. m^{-3} at the top of the evaporator. In counter flow configuration, the increase of irreversibilities observed at the bottom of the falling film evaporator near the wall is due to the thermal boundary layer development and to the large temperature difference between the two sides of the wall caused by the HTF uniform temperature imposed at the bottom of the evaporator. Indeed, this phenomenon implies the existence of a minimum value of the heat flux transferred from the HTF to the film, along the x axis: consequently, a minimum value of thermal entropy generation is also observed. In conclusion, in counter-current flow, the irreversibilities are mainly concentrated near the wall at the bottom of the evaporator (x = 1 m, y_2 = 1 mm) for the HTF and (x = 1 m, y_1 = 0) for film and a little near the entrance (x = 0, y_2 = 1 mm) and (x = 0, y_1 = 0). However, in co-current flow, the irreversibilities are concentrated near the wall at the entrance of the evaporator (x = 0, y_2 = 1 mm) for the HTF and (x = 0, y_1 = 0) for the film.

Knowing the local distribution of the entropy generation, allows to better understand the physical phenomena which induce irreversibilities, and to locate them through the evaporator. It is therefore a way to understand the interest of minimizing entropy generation and to improve the performance of falling film evaporators while minimizing the impact of their irreversibilities on the other components of absorption machines. In the type of falling film evaporators studied here, the main parameters that impact their performance are the HTF Reynolds number and temperature, the vapor pressure, the film inlet temperature and mass flow rate but also the evaporator length and wall thickness. In the following, the focus is to understand how some of the above-mentioned parameters influence the total entropy generation – in the HTF, wall and film – and then to analyze how this impact is done by studying the local distribution mainly at the region where the entropy generation is the highest.

2.4.2 Parametric study

2.4.2.1. HTF Reynolds number influence

In this section, the impact of the heat transfer fluid mass flow rate on the entropy generation and efficiencies is discussed by varying the HTF Reynolds number. Fig. 2.9 shows the evolution of the overall thermal entropy generation and of the thermal efficiency with the increase of the heat transfer fluid Reynolds number. For both configurations, the higher the Reynolds number, the higher the overall thermal entropy generation and the lower the thermal efficiency. The increase of the overall entropy generation is due to the increase of the HTF heat capacity rate. Therefore, the heat flux transferred from the HTF to the film also increases leading to an increase of the evaporated mass flow rate while the decrease of the thermal efficiency is due to the increase of the maximum transferrable flux from the HTF to the film. For a given HTF Reynolds number, the increase of the evaporator length leads to an increase of the total thermal entropy generation and of the thermal efficiency. Moreover, the increase of the HTF Reynolds number from 500 to 2000 increases the entropy generation of about 44%, 51% and 66% for L = 0.1, 0.3 and 0.5 m respectively for both configurations due to the slow development of the HTF thermal boundary layer encountered at high HTF Reynolds number and to the increase of the heat transferred when increasing the evaporator length. Another conclusion is the larger counter-current configuration performance (thermal efficiency) compared to the co-current one with the increase of the evaporator length as expected. Indeed, when considering small evaporator length, there is almost no difference in terms of performance between both configurations – the thermal efficiency difference is less than 5% for Re_{htf} = 2000 and L = 0.1 m. It can be concluded that to benefit from the performances offered by the counter-current configuration compared to those offered by the co-current configuration, it is preferable to consider longer falling film evaporators. However, longer evaporators are associated to higher entropy generation that can have significant impact on the other components of the absorption machine. Moreover, other drawbacks such as cost and size must also be considered.

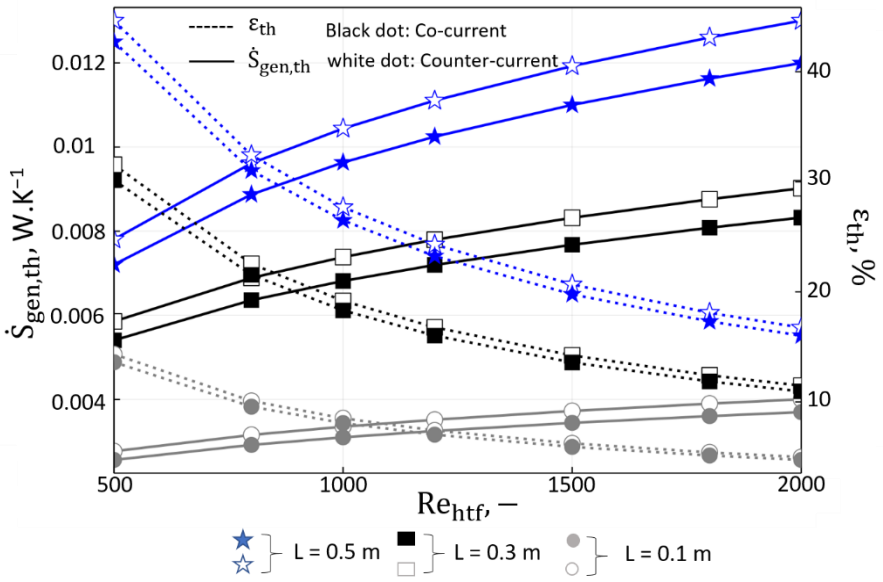

Figure 2.9: Overall entropy generation and thermal efficiency versus the heat transfer fluid Reynolds number and the evaporator length for e_{htf} = 2mm and ΔT = 0 K

This conclusion is also made by analyzing the evaporation rate for both configurations in Table 2.3. Indeed, Table 2.3 shows the evolution of the evaporation mass flow rate and of the evaporation

efficiency with the evaporator length and HTF Reynolds number. The Reynolds number of the HTF does not have a large impact on the evaporation efficiency but its increase leads to the increase of the evaporation rate. Indeed, the evaporation efficiency is defined as the ratio of the evaporation flux at the film interface to the transferred flux from the HTF to the film. The increase of the HTF Reynolds number leads to an increase of both terms. However, the amount of energy needed to increase the film temperature is quite the same as the evaporation efficiency mainly depends on the film properties.

Table 2.3: Evolution of the evaporation mass flow rate, evaporation efficiency and heat transfer coefficients with the HTF Reynolds number and with the evaporator length

		Evaporation rate %		Evaporation efficiency %		h_f $W.m^{-1}.K^{-1}$		h_{htf} $W.m^{-1}.K^{-1}$	
L m	Re_{htf} -	Co-current	Counter-current	Co-current	Counter-current	Co-current	Counter-current	Co-current	Counter-current
0.1	500	2.18	2.2	97.78	93.33	712	730	244	247
	1000	2.59	2.62	97.68	93.78	713	729	286	290
	1500	2.84	2.89	97.66	94.04	713	729	316	322
	2000	3.03	3.08	97.59	94.22	714	728	341	348
0.3	500	4.93	5.03	99.57	97.09	2132	2156	610	613
	1000	5.99	6.13	99.51	97.35	2134	2156	681	685
	1500	6.66	6.83	99.48	97.42	2135	2156	738	743
	2000	7.16	7.36	99.46	97.6	2136	2156	786	792
0.5	500	7.01	7.2	99.93	98.01	3553	3581	963	966
	1000	8.69	8.93	99.86	98.17	3556	3581	1044	1048
	1500	9.73	10.02	99.83	98.28	3558	3581	1116	1120
	2000	10.51	10.83	99.81	98.40	3559	3581	1178	1183

The HTF and film heat transfer coefficients per unit of width are both calculated from the equations (2.13) and (2.14) and are also gathered in Table 2.3. it shows that the overall heat transfer fluid coefficient of the HTF increases with the increase of its Reynolds number for both configurations. This can be explained by the slow development of the thermal boundary layer when increasing the heat transfer fluid Reynolds number and by the increase of the energy capacity of the HTF. In addition, the analysis shows a higher heat transfer coefficient in the case of counter-current flow due to the small temperature pinch encountered. The higher the heat transfer fluid velocity and the higher the HTF heat transfer coefficient difference between both configurations. The falling film heat transfer coefficient variation is very small, less than 1%, with the increase of the heat transfer fluid velocity for both configurations as the heat transfer coefficient of a fluid depends only on the fluid thermophysical properties (assumed constant), fluid flow (assumed laminar) and exchange configuration. The HTF Reynolds number does not affect the heat transfer coefficient of the film in this case nor the evaporation efficiency; however, it increases the evaporation mass flow rate as the heat transferred through the wall also increases. The evaporator length also impacts significantly the heat transfer coefficient of both fluids – an increase of around 80% when assuming an evaporator length of 0.5 m compared to an evaporator length of 0.1 m. Fig. 2.10 shows the impact of the HTF Reynolds number on the HTF, wall and film irreversibilities for L = 0.1 m. Under the studied conditions, the highest thermal irreversibilities is situated in the HTF, followed by the film. The wall thermal irreversibilities represents less than 2% of the total thermal entropy generation. Moreover, the increase of the HTF Reynolds number leads to an increase of the whole thermal irreversibilities. However, it impacts more

the film thermal irreversibilities than the other irreversibilities due to the increase of the evaporation phenomenon: the contribution of the film thermal irreversibilities increases from 32% to 43% of the total thermal entropy generation from Re_{htf} = 500 to 2000 and for both configurations.

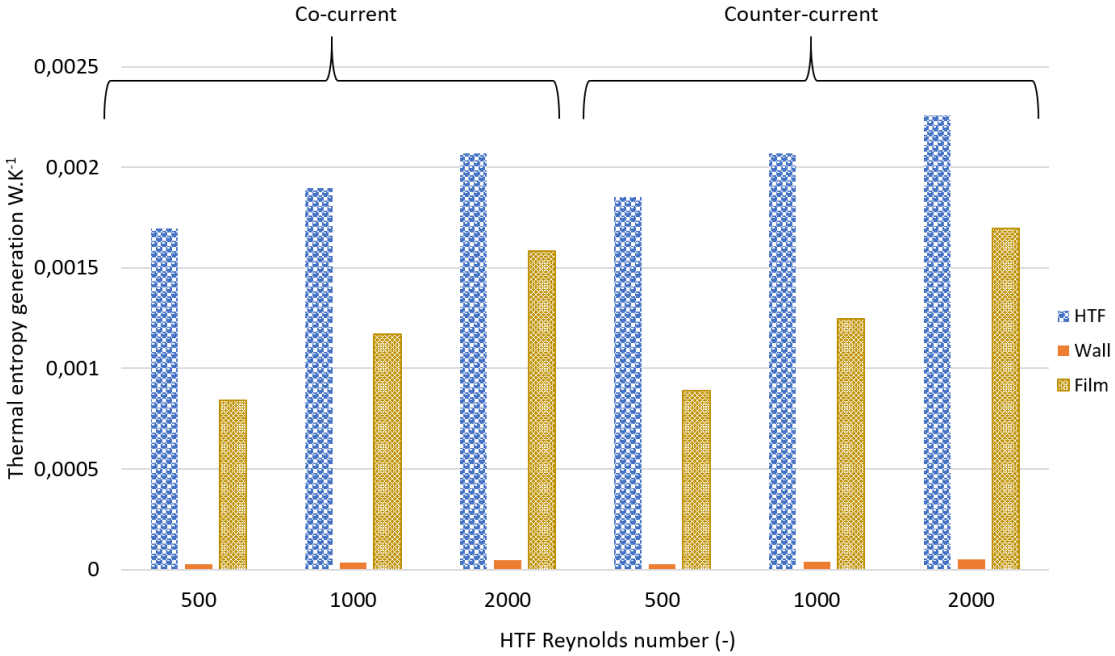

Figure 2.10: Evolution of the entropy generation in the HTF, wall and film with the HTF Reynolds number for co-current and counter-current configurations

It is interesting to understand how the HTF Reynolds number impacts the local thermal entropy generation to understand the result obtained at the component scale. Fig. 2.11 shows the evolution of the film thermal entropy generation along the film thickness and for different heat transfer fluid Reynolds numbers at the entrance of the evaporator (x = 0 m) and at the bottom (x = 0.1 m) for ΔT = 0 K, Re_f = 49.8, e_{htf} = 2 mm and for both co and counter-current flows.

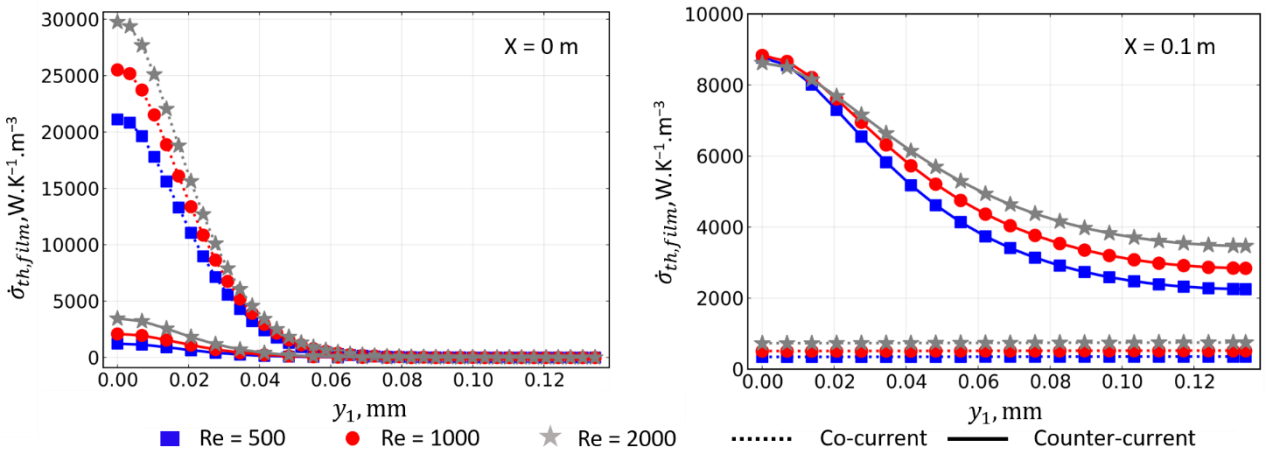

Figure 2.11: Evolution of the film thermal entropy generation versus the film thickness for different heat transfer fluid Reynolds number at x = 0 m and x = 0.1 m for ΔT = 0 K for both counter and co – current flows.

The increase of the overall thermal entropy generation with the HTF Reynolds number (Fig. 2.9 and 2.10) is explained by an increase of the local thermal entropy generation for both configurations as

shown in Fig. 2.11. Indeed, the higher the HTF Reynolds number, the higher the local irreversibilities due to the increase of the heat transferred through the wall and consequently the higher is the evaporated mass flow rate: the quick development of the film thermal boundary layer caused by the increase of the HTF velocity – small thermal resistance – allows to evaporate earlier a part of the film. At the entrance near the wall, it is more than six times higher in co-current than in counter-current flow due to the large temperature gradient, while it is equal to zero at the free interface – region not yet impacted by the heat transfer as the thermal boundary layer of the film is still in its developing stage: no phenomenon occurs as the film temperature is equal to the interface temperature. At the bottom (x = 0.1 m), the thermal entropy generation is more than 2 times higher in the counter-current configuration than in co-current one: The heat transferred from the heat transfer fluid to the film is lower in the co-current configuration and the temperature difference is larger in counter current flow. The variation of the thermal entropy generation with the film thickness, at x = 0.1 m, is very small, less than 0.6% whatever the heat transfer fluid Reynolds number in the case of a co-current flow configuration. This result can be explained by the complete development of the thermal boundary layer at x = 0.1 m and by the fact that almost all the energy transferred from the plate to the film is used for the evaporation. Near the wall ($y_1 = 0$), The variation of the thermal entropy generation with x is higher in the co-current flow due to the monotonically decrease of the heat transferred from the HTF to the film.

The study of the local viscous entropy generation of the two fluids shows – not presented here – that it is no affected by the flow configuration. For the film, the local entropy generation due to the fluid friction is equal to zero at the free interface and increases along the film thickness to be maximal, around 8 $W.K^{-1}.m^{-3}$, at the wall, $y_1 = 0$. This result is in accordance with the second term of equation (2.21) as the velocity profile is parabolic. From the previous results, it can be concluded that the film viscous irreversibilities are negligible compared to the thermal irreversibilities. For the heat transfer fluid, the analysis shows that the local viscous entropy generation depends on the HTF Reynolds number. The increase of the HTF Reynolds number and of the evaporator length lead to a significant impact of the viscous entropy generation contribution on the overall one. Indeed, the contribution of the fluid friction irreversibilities on the total entropy generation for L = 0.5 m, under the studied conditions, varies from 4% to 18% and from 3% to 17% for co and counter flows respectively when varying the HTF Reynolds from 500 to 2000. Locally, the HTF viscous entropy generation is equal to zero near the plate which is explained by a velocity equal to zero. This viscous entropy generation increases parabolically, following equation (2.10), to be maximal at the center of the channel. The local viscous entropy generation along x is almost constant – variation of about 0.4%. It can be concluded that the effect of the local temperature on this viscous irreversibilities is small. The higher the Reynolds number, the higher the local friction irreversibilities near the center. To conclude here, the thermal boundary layer plays a significant role on the local entropy generation distribution and consequently on the overall one. The variation of the HTF Reynolds number leads to the variation of the HTF mass flow rate when assuming constant HTF channel thickness, but one could also change the HTF mass flow rate by changing the HTF channel thickness and assuming constant HTF Reynolds number. Thus, both parameters namely the HTF Reynolds number and the channel thickness could be used as parameters of optimization to find the optimal geometry and heat transfer fluid velocity that will lead to a minimal overall entropy generation and an acceptable evaporation rate.

2.4.2.2. Film Reynolds number influence

In this section, the impact of the film Reynolds number on the falling film evaporator is studied. The analysis is limited at the overall scale as the distribution at local scale of the irreversibilities are similar as those studied previously in section 2.4.2.1. The HTF Reynolds number is maintained at 1000, the

channel thickness is equal to 2 mm and the film inlet temperature is assumed to be equal to the interface temperature (saturation temperature). As in the previous analysis, the difference of temperature between the film and HTF inlet temperatures is about 5°C. Fig. 2.12 shows the impact of the film Reynolds number on the evaporation efficiency. The latter decreases with the increase of the film velocity and with the decrease of the evaporator length. Indeed, increasing the film Reynolds number leads to an increase of the film thickness and thus to an increase of the thermal resistance, consequently more of the energy transferred from the HTF to the film is used to increase the film temperature – 6% of the transferred energy is used to increase the film temperature in counter-current flow for Re_f = 50 and L = 0.1 m against 27% for Re_f = 200. The difference of the evaporation efficiency is smaller when considering a co-current flow as only 3% of the transferred energy is used to increase the film temperature for Re_f = 50 and L = 0.1 m against 16% for Re_f = 200. Moreover, the higher the evaporator length, the higher the evaporation efficiency. Consequently, for an infinite evaporator length, the evaporation efficiency would be equal to 1. The smaller the evaporator length, the higher the difference of the evaporation efficiency between both configurations and between Re_f = 50 and Re_f = 200. The evaporation efficiency is higher for co-current flow than for counter-current flow.

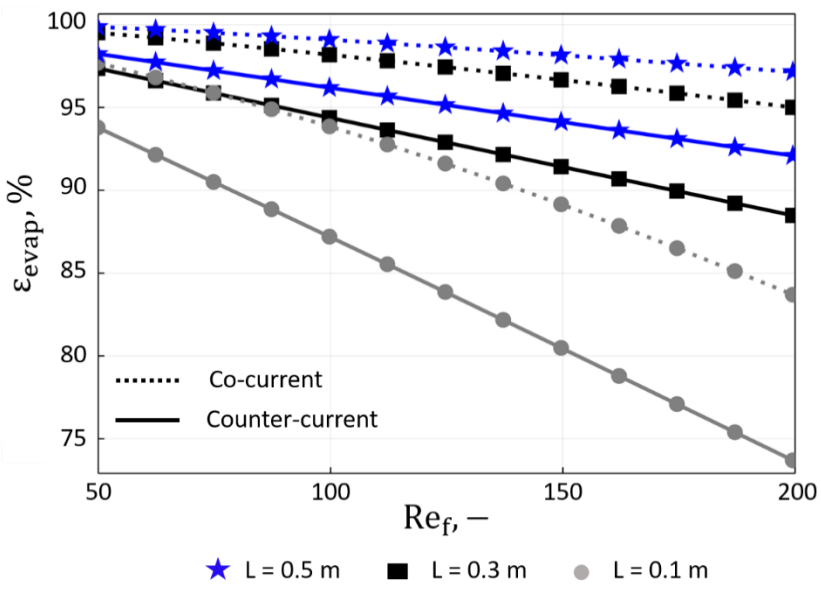

Figure 2.12: Evaporation efficiency evolution with the film Reynolds number for different evaporator length

As shown in Fig. 2.6, the evaporation efficiency cannot be lower than 0.83 for Re_f = 50, $\dot{m}_{htf}$ = 0.04 m. s^{-1}. Indeed, the evaporation efficiency decreases either by considering small evaporator length or by increasing the film thickness (film Reynolds number). However, for an evaporator length of 0.1 m and Re_f = 50, the evaporation efficiency is already up to 0.9 for both configurations which means that there is no evaporator length that leads to a lower evaporation efficiency with a high thermal efficiency.

The decrease of the evaporation efficiency due to the increase of the film Reynolds number leads to a decrease of the entropy generation and evaporation mass flow rate as shown in Fig. 2.13. Moreover, increasing the evaporator length leads to an increase of the difference between Re_f = 50 and 200. Indeed, the increase of the film Reynolds number, from 50 to 200, leads to a decrease of the entropy generation of about 8 % for L = 0.1 m against 14% for L = 0.5 m for a co – current flow. For high film Reynolds numbers, almost no difference is noticed for both configurations in term of evaporated mass

flow due to the high thermal resistance between the plate and the film that leads to the slow thermal boundary layer development. In order to take advantage of the flow configuration impact at high film Reynolds number, engineers should also work at high HTF Reynolds number however that also means increasing the thermal entropy generation as explained in the section 2.4.2.1.

The analysis of the viscous entropy generation shows an increase of the latter with the increase of the film Reynolds number and evaporator length. However, the contribution of the total viscous irreversibilities on the total entropy generation remains negligible. Indeed, for Re_f = 50, this contribution is about 0.4% and 0.7% for L = 0.1 m and L = 0.5 m respectively against 0.8% and 1.3% for Re_f = 200.

The study of the thermal efficiency shows a decrease of the latter with the increase of the film Reynolds number as the film velocity has an impact on the energy transferred by the HTF to the film. However, this decrease is small – for counter flow, the thermal efficiency is 27.7% and 25.16% for (Re_f = 50, L = 0.5 m) and (Re_f = 200, L = 0.5m) respectively against 26.5% and 23.8% for co-current flow.

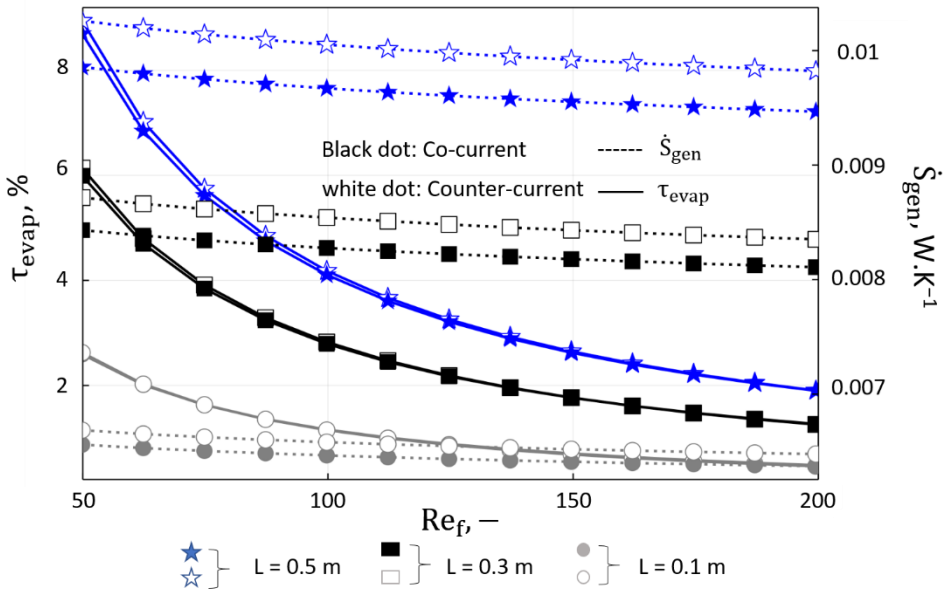

Figure 2.13: Evaporation mass flow rate and entropy generation versus the film Reynolds number and for different evaporator length and for Re_{htf} = 1000, e_{htf} = 2 mm and ΔT = 0 K

The distribution of the thermal irreversibilities within the HTF, wall and the film are given in Fig. 2.14. Unlike to the results obtained when studying the impact of the HTF Reynolds number, the increase of the film Reynolds number leads to the decrease of HTF thermal irreversibilities while the film irreversibilities is slightly affected.

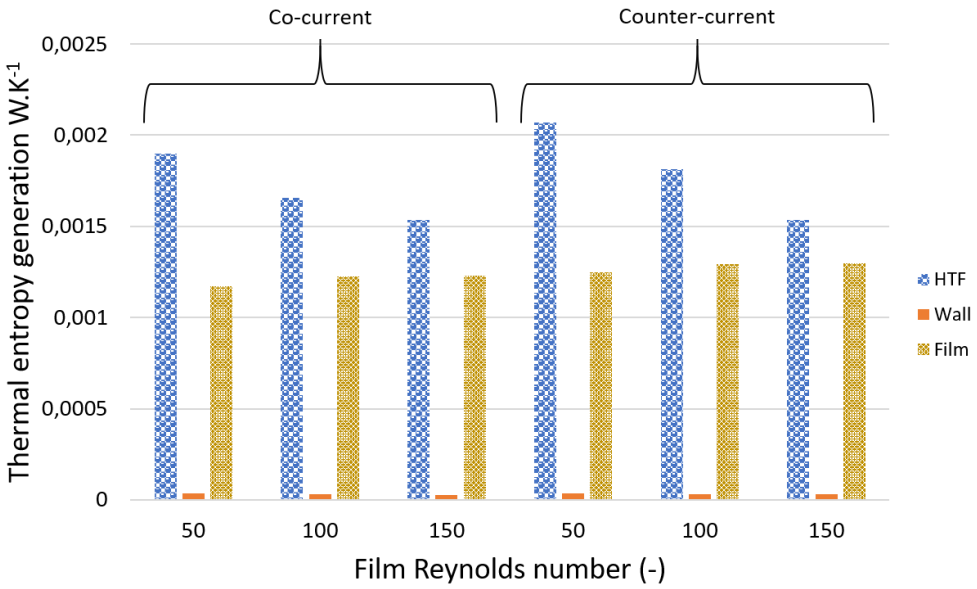

Figure 2.14: Evolution of the HTF, wall and film thermal entropy generation for different film Reynolds number and for both configurations

The decrease of the HTF irreversibilities is due to a decrease of the heat transferred from the HTF to the film caused by the slow development of the thermal boundary layer within the film due to the increase of the film thickness and consequently by the increase of the thermal resistance. This also explains the slight increase of the film thermal irreversibilities. Indeed, the film thermal irreversibilities goes from around 37% of the total thermal entropy generation for Re_f = 50 to 43% for Re_f = 150 while the HTF irreversibilities decreases from 61% to 53% for Re_f = 50 to Re_f = 150 respectively. The wall irreversibilities contribution remains negligible less than 1.5%. In conclusion, the wall is the medium with the less entropy generated.

Table 2.4 gives the heat transfer coefficient of the film and of the HTF for different film Reynolds number. The film heat transfer coefficient increases of about 35% with the decrease of the film Reynolds number – from 200 to 50 – due to the decrease of the thermal resistance. The heat transfer coefficient of the HTF also increase with the decrease of the film Reynolds number; However, its impact is low – less than 3%.

Table 2.4: Evolution of the evaporation mass flow rate and evaporation efficiency with the HTF Reynolds number and with the evaporator length

		h_f $W.m^{-1}.K^{-1}$		h_{htf} $W.m^{-1}.K^{-1}$	
L m	Re_f -	Co-current	Counter-current	Co-current	Counter-current
0.1	50	713	730	286	290
	100	570	597	284	293
	150	504	538	282	295
	200	466	506	280	297
0.3	50	2134	2156	681	685
	100	1695	1732	682	690
	150	1484	1533	681	693
	200	1353	1412	679	696
0.5	50	3557	3581	1044	1048

100	2823	2865	1046	1054
150	2468	2524	1047	1059
200	2245	2315	1046	1062

In conclusion, the film Reynolds number plays a significant role on the transfer phenomenon as increasing it leads to a low evaporator performance – the entropy generation variation is small and linear while the evaporation rate decrease is significative. It can also be concluded from paragraph 4.2.1 and 4.2.2 that for laminar HTF flow regime, the main thermal irreversibilities of a falling film evaporator is concentrated in the HTF, followed by the film thermal irreversibilities, while the wall irreversibilities is almost negligible.

In this study, the film Reynolds number is limited to 200 as higher to that value, the film could not be considered laminar anymore and the developed model is not adapted for wavy films. When designing the falling film evaporator, engineers should determine the adequate film Reynolds number by considering HTF characteristic and operating conditions.

2.4.2.3. Influence of the temperature difference between the film inlet and the interface temperature

In this section the impact of the film inlet temperature is studied. Indeed, the film inlet temperature can be controlled by adjusting the operating conditions of the other components of absorption machines while the interface temperature of the evaporator can be controlled by assuming a constant vapor pressure. The evolution of the overall thermal entropy generation with the evaporation rate and with the evaporation efficiency by considering different film inlet temperatures (298 to 303 K) and constant interface temperature (300 K) is shown in Fig. 2.15. The subcooled film leads to the highest thermal entropy generation and the lowest evaporation rate. This is due to the high temperature gradient between the HTF and the film leading to a decrease of the evaporation efficiency. That means that a large part of the energy transferred from the HTF to the film serves only to increase the film temperature. The thermal entropy generation created by the temperature difference between the film inlet temperature and the saturation temperature plays also an important role on the film thermal entropy generation. To have efficient evaporator, engineers should avoid subcooled film at the entrance in most applications. The analysis also shows that the minimum thermal entropy generation is encountered when the ΔT = 1 K under the considered conditions. Indeed, with this small difference, the thermal entropy generation through the wall is reduced compared to the case where ΔT = 0 K and the local irreversibilities created near the interface due to the overheating of the film has a small contribution on the overall thermal entropy generation.

However, the higher the film inlet temperature, the lower the thermal entropy generation near the wall and the higher the one at the interface. Thus, even if the overheating leads to a significant increase of the evaporation rate due to a high evaporation efficiency, the optimal temperature difference should be found in order to avoid high total entropy generation. Indeed, for overheated films, the evaporation efficiency is more than unity as in its definition the energy transported by the film at the inlet is not considered. It is up to the engineer to find comprise between the acceptable entropy generation and evaporation rate mainly if the evaporator is in conjunction with other components and can lead to a higher overall entropy generation and consequently to a lower system performance.

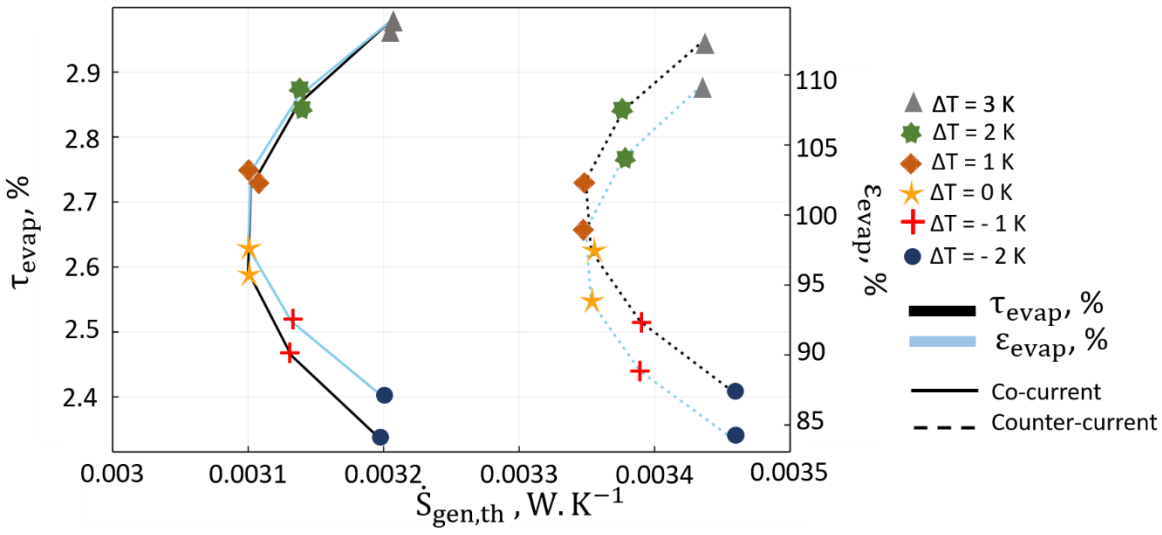

Figure 2.15: Thermal entropy generation versus the evaporation efficiency and the total evaporation for different film inlet temperature, Re_{htf} = 1000 and e_{htf} = 2 mm

The larger the evaporator length and the lower the impact of the inlet film temperature on the evaporated mass flow rate (Table 2.5). Moreover, the thermal efficiency is significantly impacted by the inlet film temperature – not shown. Indeed, the decrease of the film inlet temperature from 303 to 298 K leads to a decrease of 70% of the thermal efficiency for both configurations whatever the evaporator length.

The film inlet temperature has also an impact on the heat transfer coefficients as shown in Table 2.5. The heat transfer coefficient of the HTF decreases almost linearly with the increase of the film inlet temperature for a counter-current flow while the opposite trend is found for the co-current configuration. The heat transfer coefficient of the film decreases with the increase of the film inlet temperature for both configurations. However, the impact of the film inlet temperature remains low for both fluids – less than 5%.

Table 2.5: Evolution of the evaporation mass flow rate and evaporation efficiency with ΔT and with the evaporator length

		τ_{evap} %		h_f W.m^{-1}. K^{-1}		h_{htf} W.m^{-1}. K^{-1}	
L m	ΔT K	Co-current	Counter-current	Co-current	Counter-current	Co-current	Counter-current
0.1	-2	2.3	2.4	723	752	280	294
	0	2.59	2.62	713	729	285	290
	2	2.85	2.84	703	705	292	284
	3	2.97	2.95	698	692	296	280
0.3	-2	5.74	5.93	2145	2188	675	689
	0	5.99	6.13	2134	2156	678	685
	2	6.24	6.3	2124	2125	688	678
	3	6.36	6.43	2119	2109	691	672
0.5	-2	8.45	8.75	3567	3617	1038	1052
	0	8.7	8.93	3556	3581	1044	1048
	2	8.93	9.13	3547	3547	1051	1041
	3	9.05	9.22	3542	3531	1055	1034

The analyze of the behavior of the film when the latter is subcooled or overheated at the entrance of the evaporator gives more details about the distribution of the irreversibilities. The impact of the overheated and subcooled film is mainly observed near the entrance when the thermal boundary layer due to the transfer of energy from the HTF to the falling film is still in the developing stage, as shown in Fig. 2.16 for a HTF Reynolds number of 1000, a channel thickness of 2 mm and a film Reynolds number of 49.8. It can be seen that at x = 0 m and near the wall (y_1 = 0), the local thermal entropy generation is high when the film inlet temperature is subcooled and decreases with the increase of ΔT, for both configurations. Indeed, the higher the temperature difference between the inlet film and the HTF temperature, the higher the local entropy generation near the wall due to the large temperature gradient and the thermodynamic disequilibrium. At the top, two thermal boundary layers are in developing stage. The first one is the thermal boundary layer caused by the heat flux transferred from the HTF to the film while the second one is the thermal boundary layer caused by the evaporation phenomenon at the free interface. This can be observed in Figure 2.16 at the top (x = 0 m): the thermal entropy generation is null between y_1 = 0.05 mm and y_1 = 0.09 mm.

Moreover, when overheating or subcooling the film at the entrance, there is a significant disequilibrium near the free surface due to the temperature difference between the film inlet temperature and the saturation temperature: the local entropy generation is up to 100 000 $W.K^{-1}.m^{-3}$ for $|\Delta T|$ = 2 K against zero for ΔT = 0 K. Indeed, at ΔT = 0 K, there is no heat transfer and consequently no evaporation occurs at the free interface. However, the overheating allows evaporating a part of the falling film whereas the subcooling leads to the condensation of the saturated vapor. At x = 0.0015 m, the inflexion point at the middle of the film thickness is explained by the thermal boundary layer development due to the heat transferred from the HTF to the film and by the evaporation/condensation phenomenon that already occurs at the free interface due to the overheated/subcooled film.

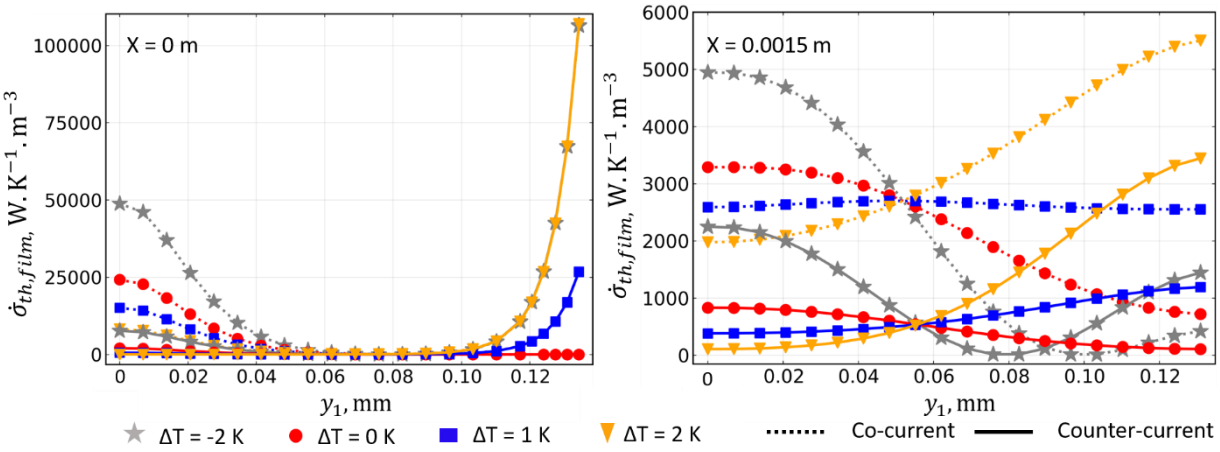

Figure 2.16: Evolution of the film thermal entropy generation versus the film thickness for different inlet film temperature at x = 0 m and x = 0.0015 m for counter-current and co-current flow configurations ($T_{htf,\,in}$ = 305 K, $T_{f,interface}$ = 300K)

In terms of configuration, no differences are observed at x = 0 m, near the interface (y_1 = 0.13 m), this is due to the fact that the thermal boundary layer is not fully developed and so, the impact of the flow configuration is not felt: the irreversibilities observed, at the entrance near the interface, are only due

to the evaporation/condensation that occurs when the film is overheated or subcooled. However, differences are observed near the wall where the local thermal entropy generation in co-current flow is higher than that of the counter-current flow. At x = 0.0015 m, the film is still in its developing stage but the difference between the local entropy generations decreases. For $\Delta T = -2K$, the thermal entropy generation is drastically reduced near the interface as the temperature already tends to the interface temperature. Once the film temperature near the interface is equal to the interface temperature, the condensation process stops. The evaporation phenomenon starts once the film temperature near the interface is higher than the interface temperature.

At the bottom of the evaporator (x = 0.1 m), the impact of overheating/subcooling the film at the inlet is not at all observed – thermal boundary layer completely developed – and the local thermal entropy generation is higher in counter-current than in co-current flow. The analysis of the thermal entropy generation along the x axis shows that less than 20% of the x axis is impacted by the overheating/subcooling of the film. Moreover, under the studied conditions, the analysis shows that the film inlet temperature impacts the thermal entropy generation of the heat transfer fluid only near the wall and is very small elsewhere.

The impact of the film inlet temperature on the viscous entropy generation of the film is very small. Indeed, the viscous entropy generation decreases with the increase of the film inlet temperature. However, the difference of the viscous entropy generation in the film for $T_{in,f}$ = 300.0 K and $T_{in,f}$ = 302.5 K is less than 0.01%.

To summarize, although the increase of the film inlet temperature leads to an increase of the evaporated mass flow, the thermal entropy generation should be studied in order to find the film inlet temperature that should be considered to minimize the thermal entropy generation mainly when the falling film evaporator is used in cofunction with other system – as it has an impact on the whole system performance. Moreover, the local analysis shows that at the entrance of the evaporator, the behavior of the latter due to the film inlet temperature – at the free interface (x = 0, y_1 = 0.13 m) – is the same whatever the flow configuration.

Conclusions and discussions on the evaporator

This chapter deals with the study of a laminar falling film evaporator in the case where the plate is heated by a HTF and for co and counter-current HTF flow configurations. The aim was to evaluate the effect of the operating conditions, namely, the inlet film temperature and film/HTF Reynolds number but also the film length on the evaporation rate and on the overall and local entropy generations. The impact of the above-mentioned parameters on the entropy generation was investigated at the overall scale and an analysis was performed at the local scale for a deep understanding of the thermal entropy generation distribution. Different parameters were defined to evaluated the performance of the considered evaporator, namely the evaporator efficiency, total evaporation mass flow rate and the thermal efficiency.

The impact of the thermal boundary layers on the local phenomena and consequently on the local and thus overall entropy generation has been investigated. When assuming $\Delta T = 0$ K only the thermal boundary layer due to the heat flux transferred from the HTF to the film is observed within the film while when assuming $\Delta T \neq 0$K, two thermal boundary layers are observed: the one described above and the one due to the evaporation/condensation at the film free interface.

The sources of entropy generation in falling film evaporator are the fluid friction and the temperature gradient. The local viscous entropy generation of the film and of the HTF are almost not impacted by the film inlet temperature and by the film Reynolds number. However, the HTF Reynolds number impacts the HTF local viscous entropy generation and consequently its contribution to the overall entropy generation. Furthermore, the increase of the film inlet temperature leads to an increase of the local thermal entropy generation near the free surface while it leads to a decrease of this entropy generation near the wall. The results show that the entropy generation is mainly due to heat transfer fluid irreversibilities followed by the film irreversibilities while the contribution of the wall irreversibilities to the entropy generation remains low. The increase of the HTF Reynolds number leads to an increase of all medium contributions due to the increase of thermal resistance while the increase of film Reynolds number leads to a decrease of the contribution of the HTF irreversibilities explained by a decrease of the heat transferred from the HTF to the film.

This model is extended, in chapter III, to the analysis of the entropy generation with the absorption phenomenon in a falling film absorber. Indeed, unlike to the falling film evaporator model, the absorber model takes into account the mass transfer within the film and the coupling effect between the thermal and mass phenomena at the free interface of the film.

CHAPTER III

Chapter III. Analysis of a falling film LiBr-H_2O absorber at local scale based on entropy generation

Based on:

Article: Mahamoudou, Ramousse and Le Pierrès. Analysis of a falling film LiBr-H_2O absorber at local scale based on entropy generation. *International Journal of Heat and Mass Transfer*, (198) 123425 September 2022. DOI: doi.org/10.1016/j.ijheatmasstransfer.2022.123425

3.1. Introduction

After having studied and understood the phenomena present in a falling film evaporator in chapter II, the following chapter is devoted, on the one hand, to the development of a model which can simulate the phenomena observed in an absorber and, on the other hand, to the formulation of the entropy generation in order to identify the various sources of irreversibilities.

As explained in previous chapters, the consideration of the HTF on the model of the absorber allows to simulate more realistic cases. The HTF is assumed to flow either in laminar or turbulent flow regime. In chapter II, only the laminar flow regime was considered for the HTF as it already gives good insights about the phenomena that occur. One of the objectives of this chapter is also to understand the impact of the HTF, poorly modeled until now, on the phenomena encountered in the absorber. The limit cases, namely the adiabatic and isothermal wall cases are also studied in order to note the differences between the limit cases and the realistic ones. Due to the high efficiency generally observed in counter current flow regime, only this configuration is discussed in the following. The study focuses mainly on what happens at the local scale, however results at the component scale are also given.

3.2. Absorber description

Improvement of falling film absorber performance requires an understanding of the phenomena encountered. Figure 3.1 shows a solution composed of the absorbent (lithium bromide, LiBr) and refrigerant (water) which flows down under the effect of gravity over a vertical plate and in contact with water vapour at a fixed pressure (P_{vap}). The solution enters the domain at x = 0 with a uniform absorbent concentration ($C_{LiBr,in}$) and temperature ($T_{f,in}$). The LiBr remains in the liquid phase while the water vapour may be absorbed or desorbed by the solution. The chemical potential difference between the film and the vapour induces a mass transfer process from the vapour to the solution by absorption. This exothermic absorption releases heat that increases the falling film temperature. The temperature, concentration and velocity profiles are presented in Fig. 1a. The heat and mass transfer phenomena lead to the formation of the thermal ($\delta_{htf,th}, \delta_{f,th1}, \delta_{f,th2}$) and diffusive ($\delta_{f,m}$) boundary layers in the film as shown in Fig. 1b and 1c. The hydrodynamics in the film and heat transfer fluid are assumed to be fully developed, thus, hydrodynamic boundary layers are not represented. The thermal boundary layers $\delta_{f,th1}$ and $\delta_{f,th2}$ represent the distance from the wall and the interface respectively to a point where the local temperatures reach 99% of the falling film bulk temperature. The thermal boundary layer $\delta_{htf,th}$ represents the distance from the wall to a point where the locale temperatures reach 99% of the HTF bulk temperature, while the diffusive boundary layer $\delta_{f,m}$ represents the distance from the interface to a point where the local concentration reaches 99% of the falling film bulk concentration.

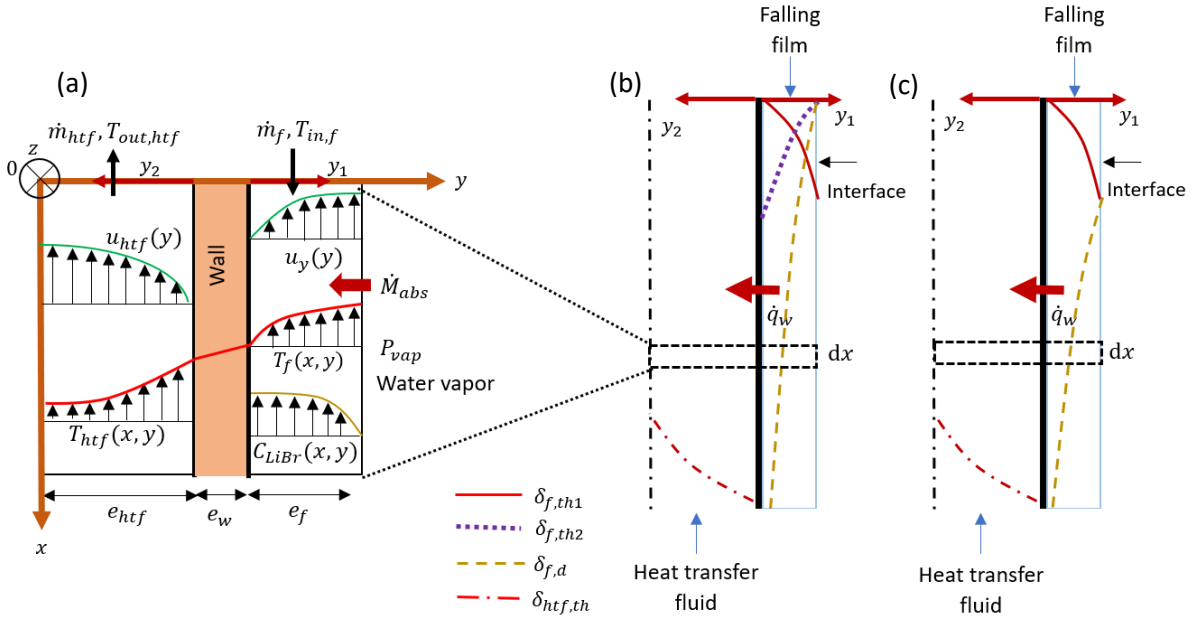

Figure 3.1: Description of falling film absorber at local scale, (a) Temperature, concentration and velocity profiles, (b) boundary layers when assuming subcooled film at the inlet, (c) boundary layers when assuming film at equilibrium condition at the inlet

The HTF flows between two vertical flat plates. A symmetrical distribution of the HTF temperature and velocity is assumed making it possible to study only half of the channel. Here, the falling film flows from the top to the bottom while the HTF is in counter-current with the solution. $x = 0$ and $x = L$ are the inlet and outlet of the absorber respectively, while the y axis is equal to zero at the centre of the HTF channel and to $e_{htf} + e_w + e_f$ at the falling film interface. The y_1 axis $\in [0, e_f]$ ranges from the heated plate – film side – to the film interface while the y_2 axis $\in [0, e_{htf}]$ ranges from the heated plate – HTF side to the centre of the HTF channel thickness. $\delta_{htf,th}$ represents the thermal boundary layer in the HTF due to the temperature change caused by the heat transfer with the solution. $\delta_{f,th1}$ and $\delta_{f,th2}$ represent the thermal boundary layers in the film due to the heat transferred from the film to the HTF through the wall, and to the increase in the film temperature caused by the absorption at the free interface, respectively. The absorption results in increasing the refrigerant concentration in the film and thus $\delta_{f,m}$ represents the diffusive boundary layer related to the transport of the refrigerant though the film. As shown in Fig. 1, two cases are studied in this paper: a subcooled film at the inlet that leads to the development of a thermal boundary layer due to the exothermic absorption phenomenon $\delta_{f,th2}$ (the absorption phenomenon starts at x = 0, Fig. 1b) and a film at equilibrium at the inlet (the absorption phenomenon only starts after the development of $\delta_{f,th1}$, consequently, $\delta_{f,th2}$ is not observed). Two thermal limit cases arise in the absorber: the adiabatic and isothermal wall. Any HTF cooled absorber with non-infinite nor null coolant flowrates range between these two limit cases. The heat generated at the solution–vapour interface is transferred into the HTF through the wall.

This study focuses on understanding the local phenomena which occur in the two fluids by examining the impact of the development of the boundary layers on their behaviour.

3.2.1 Absorber model Assumptions

As in (Mahamoudou et al. 2022), this work is limited to the modelling of falling film exchangers in established laminar regimes where wave phenomena are attenuated (Flores 2014): typically, the solution Reynolds number ranges between 5 and 200. In formulating this model, the following assumptions were made:

- Steady state regime of the two-dimensional flows.
- The liquid solution is Newtonian and its physical properties are constant and independent of temperature and concentration.
- There is no chemical reaction.
- The plate is completely wetted.
- The solution at the liquid – vapour interface is considered to be in equilibrium with vapour $T_f(x, e_f) = T_{eq}\left(P_{vap}; C_{LiBr}(x, e_f)\right)$ and the absorption process occurs at constant pressure (P_{vap}).
- The water vapour is pure and homogeneous.
- The absorbed mass is negligible compared to the mass flow rate of the film ($\dot{m}_{abs} \ll \dot{m}_f$). Indeed, the film is in steady state and laminar regime.
- Film thickness is assumed constant in both y_1 and (the not modelled) z axis.
- The LiBr is considered to be non-volatile; hence the mass transfer resistance in the gas phase is neglected (Nakoryakov, Grigoryeva, and Bartashevich 2011).
- There are no shear forces exerted on the film by the vapour.
- The irreversible processes take place near equilibrium.

3.2.2 Governing equations

The governing differential equations are the energy and species balance equations in Cartesian coordinates. In the following, the equations are written for the HTF, the wall and the falling film.

3.2.2.1 Falling film

By solving the momentum equation assuming no shear forces at the free interface, a parabolic profile, commonly called the Nusselt profile, is obtained as in equation (3.1) (Babadi and Farhanieh 2005; Bo et al. 2010) .

$$u_f(y_1) = \frac{\rho_f g}{\mu_f} {e_f}^2 \left(\frac{y_1}{e_f} - \frac{1}{2}\left(\frac{y_1}{e_f}\right)^2\right) \tag{3.1}$$

The refrigerant absorbed at the interface diffuses into the film and its absorption generates heat at the free interface which is conducted through the film thickness. Under the assumptions mentioned above, the heat and mass transfer in the film are described by the mass and energy balances through the system (3.2):

$$\begin{cases} \rho_f C_{p,f} u_f(y_1) \dfrac{\partial T_f(x,y_1)}{\partial x} = \lambda_f \left(\dfrac{\partial^2 T_f(x,y_1)}{\partial y_1^2} + \dfrac{\partial^2 T_f(x,y_1)}{\partial x^2} \right) \\ u_f(y_1) \dfrac{\partial C_{LiBr}(x,y_1)}{\partial x} = D_{H_2O-LiBr} \left(\dfrac{\partial^2 C_{LiBr}(x,y_1)}{\partial y_1^2} + \dfrac{\partial^2 C_{LiBr}(x,y_1)}{\partial x^2} \right) \\ C_{H_2O} = 1 - C_{LiBr} \end{cases} \quad (3.2)$$

3.2.2.2 Heat transfer fluid

The HTF is assumed to recover the heat released by the film. Assuming that both the HTF mass flow rate per unit of width (in the z axis) and the channel thickness ($2e_{htf}$) are known, the HTF mean velocity is determined as equation (3.3):

$$\bar{u}_{htf} = \frac{\Gamma_{htf}}{2e_{htf}\rho_{htf}} \quad (3.3)$$

❖ *Laminar flow*

In the laminar flow case, the Poiseuille equation is used to determine the velocity profile through equation (3.4) with respect to the following assumptions: incompressible and Newtonian fluid; high channel length compared to the channel thickness; laminar flow through a constant cross-section and no fluid acceleration:

$$u_{htf}(y_2) = 3\bar{u}_{htf} \left(\left(\frac{y_2}{e_{htf}} \right) - \frac{1}{2} \left(\frac{y_2}{e_{htf}} \right)^2 \right) \quad (3.4)$$

with $u_{htf}(0) = 0$ and $\dfrac{\partial u_{htf}(e_{htf})}{\partial y_2} = 0$

In this case, the energy balance equation is written as equation (3.5), and no mass transfer is involved in the HTF:

$$\rho_{htf} C_{p,htf} u_{htf}(y_2) \frac{\partial T_{htf}(x,y_2)}{\partial x} = \lambda_{htf} \left(\frac{\partial^2 T_{htf}(x,y_2)}{\partial y_2^2} + \frac{\partial^2 T_{htf}(x,y_2)}{\partial x^2} \right) \quad (3.5)$$

❖ *Turbulent flow*

In the turbulent flow regime case, the energy balance equation can be written as in equation (3.6):

$$\rho_{htf} C_{p,htf} u_{htf}(y_2) \frac{\partial T_{htf}(x,y_2)}{\partial x} = \frac{\partial}{\partial y_2} \left(\left(\lambda_{htf} + \varepsilon_h(y_2) \right) \frac{\partial T_{htf}(x,y_2)}{\partial y_2} \right) \quad (3.6)$$

Where ε_h is the eddy thermal diffusivity that introduces the turbulence in the energy equation. The Poiseuille equation cannot be used anymore to determine the velocity profile. Thus, the turbulent velocity and eddy thermal diffusivity must be determined. The fluid layer in the channel thickness can be divided in three regions. The following expressions are explained and derived in (Bird, Stewart, and Lightfoot 1960; Han 2012; Mascarenhas and Mudawar 2013; Shukri 2016):

- Wall layer

$$\frac{\varepsilon_m}{\nu} = 0 \qquad \text{and} \qquad u_{htf}^{+} = y^{+} = \frac{u_{htf}}{u^*} \qquad 0 \leq y^{+} \leq 5$$

- Overlap Layer

$$\frac{\varepsilon_m}{\nu} = 0.2y^{+} - 1 \qquad \text{and} \qquad u_{htf}^{+} = 5\ln(y^{+}) - 3.05 \qquad 5 \leq y^{+} \leq 30$$

- Outer layer

$$\frac{\varepsilon_m}{\nu} = 0.4y^{+} - 1 \quad \text{and} \quad u_{htf}^{+} = 2.5\ln(y^{+}) + 5 \qquad y^{+} \geq 30$$

With $y^{+} = \frac{u^* y_2 \rho_{htf}}{\mu_{htf}}$ and ε_m is the eddy momentum diffusivity assumed to be equal to ε_h (the eddy thermal diffusivity) as the turbulent Prandtl number is close to one in turbulent flow.

$$Pr_{turbulent} = \frac{\varepsilon_m}{\varepsilon_h} \approx 1$$

The friction velocity u^*, is determined using the Blasius equation (Shukri 2016).

$$u^* = \bar{u}_{htf}\left(\frac{f}{8}\right)^{0.5}$$

Where f is the friction factor and is given by (Shukri 2016) as:

$$\frac{1}{\sqrt{f}} = 2\log\left(Re\sqrt{f}\right) - 0.8$$

3.2.2.3 Wall

The material used for the wall is stainless steel and as only the conduction phenomenon is observed, the wall temperature varies linearly within the wall thickness and the energy balance equation through the wall is written as in equation (3.7):

$$\frac{\partial^2 T_w(x,y)}{\partial y^2} = 0 \tag{3.7}$$

3.2.3 Boundary conditions

At the inlet, the solution enters the absorber at a uniform concentration and temperature:

$$\text{At } x = 0 \text{ and } \forall\ y_1 \qquad T_f(0,y_1) = T_{f,in} \quad \text{and} \quad C_f(0,y_1) = C_{LiBr,in}$$

The wall is impermeable meaning that there is no mass transfer from the film to the HTF, thus:

$$\text{At } y_1 = 0 \text{ and } \forall\ x \qquad \left.\frac{\partial C_{LiBr}(x,y_1)}{\partial y_1}\right)_{y_1=0} = 0$$

For the wall thermal boundary conditions, heat flux conservation implies:

$$\text{At } y_1 = 0 \text{ and } \forall\, x \qquad \lambda_f \frac{\partial T_f(x,y_1)}{\partial y_1}\Big)_{y_1=0} = \lambda_w \frac{\partial T_w(x,y)}{\partial y}\Big)_{y = e_{htf} + e_w}$$

And

$$\text{At } y_2 = 0 \text{ and } \forall\, x \qquad \lambda_{htf} \frac{\partial T_{htf}(x,y_2)}{\partial y_2}\Big)_{y_2 = e_{htf}} = \lambda_w \frac{\partial T_w(x,y)}{\partial y}\Big)_{y = e_{htf}}$$

At the solution – vapor interface (y_1 = e_f and $\forall\ x$), thermodynamic equilibrium is assumed (see Appendix 3).

$$\text{At } y_1 = e_f \text{ and } \forall\, x \qquad T_f(x, e_f) = T_{eq}\left(C_{LiBr}(x, e_f), P_{vap}\right)$$

Where $T_f(x, e_f)$ and $C_{LiBr}(x, e_f)$ are the interfacial temperature and concentration respectively, both unknown function of x.

At a given vapour pressure, either a linear relationship is assumed between the interface temperature and refrigerant concentration (Islam, Wijeysundera, and Ho 2006) or the equation developed by McNeely (1979) is assumed. Indeed, both equations are studied here for comparison (see Appendix 3).

At the free interface, the absorbed flux is equal to the released heat by the exothermic absorption process. Hence, the energy conservation at the free interface is written as follows (Arroiabe, Martinez-Agirre, and Mounir Bou-Ali 2022):

$$\text{At } y_1 = e_f \text{ and } \forall\, x \qquad \lambda_f \frac{\partial T_f(x,y_1)}{\partial y_1}\Big)_{y_1 = e_f} = \dot{m}_{\text{abs}}(x)\Delta H_{abs}$$

Where

$$\dot{m}_{\text{abs}}(x) = \rho_f D_{H_2O-LiBr} \frac{\partial C_{LiBr}(x,y_1)}{\partial y_1}$$

At the bottom of the absorber, the HTF enters the absorber at a uniform temperature.

$$\text{At } \forall\, y_1 \text{ and } x = L \qquad T_{htf}(L, y_2) = T_{htf,in}$$

3.2.4 Numerical resolution

In the present model, it is assumed that the saturated pressure $P_{vap,sat}$ and temperature $T_{vap,sat}$ in the vapour phase are known conditions in the system. Moreover, the temperature $T_{f,in}$, LiBr concentration $C_{LiBr,in}$ and mass flow rate $\dot{m}_{f,in}$ of the inlet solution are also known, as well as the inlet temperature $T_{htf,in}$ and mass flow rate $\dot{m}_{htf}$ of the HTF.

The thermal, mass and hydrodynamic balances are resolved by applying a finite difference discretisation on the spatial derivative terms using the Julia programming language (*Julia*), then numerically solving the system of non-linear equations obtained using the Trust-Region Method (Conn et al. 2000) to solve for a steady state condition. A first-order backward difference is used in the x-direction while a second-order central difference is adopted in the y-direction for both fluids. The

numerical domain is discretised into N nodes in the x-direction, M nodes in the y_2-direction and P nodes in the y_1-direction for temperature and concentration. Initially, a matrix $N \times (M + P)$ that contains the initial HTF temperature, film temperature and concentration is defined. The function developed in the code contains boundary conditions and loop controls. Iteration is required for each step to fill the matrix with the new temperature and concentration values until the boundary conditions (Section 3.2.3) are satisfied in the steady-state condition. The absolute and relative tolerance errors are set to 10^{-6} and 10^{-8} respectively. A mesh grid of 300×(70+40) is adopted in the simulations as study of the grid size effect shows a maximum difference of less than 1% in terms of absorbed mass flow rate. Once the temperature and concentration at the free interface are known, the absorbed mass flow rate and the heat transfer flux at the free interface and through the wall can be determined. The temperature, concentration and velocity fields make it possible to carry out local irreversibilities analysis using the entropy generation formulation.

3.2.5 Entropy generation formulation

The thermodynamic of irreversible processes has been applied to analyse local irreversibilities. The aim of introducing the second law analysis is to identify the different sources of entropy generation during the absorption process. The temperature, concentration and velocity fields obtained by solving the numerical 2D equation detailed in Section 3.2.2 to Section 3.2.4 are used to determine local entropy generation. This study enables location of the different sources of entropy generation by identifying the sites where they are generated through the absorber and quantifying them. Moreover, it is of great importance to quantify the contribution of each irreversibilities to total entropy generation as they affect the operation of the absorber and therefore its performance. For greater comprehension, the thermodynamic of irreversible processes is also applied when considering the two limit cases, namely for adiabatic and isothermal walls. However, the introduction of an HTF in counter-current configuration enables a more realistic evaluation of entropy generation within the entire system. Unlike previous studies focusing on entropy generation in the film, this paper also evaluates entropy generation in the wall and the HTF.

The total entropy generation is given in here as the sum of the product of thermodynamic forces and fluxes:

$$\dot{\sigma} = \sum_k \vec{X}_k \cdot \vec{J}_k$$

where $\vec{X}$ and $\vec{J}$ are the driving force and the flux of the k phenomenon respectively. The formulation of the entropy generation has been developed based on the work done by Neveu (2002) Indeed, for an open system, the mass conservation can be written as:

$$\frac{d}{d}\iiint \rho \, dV = \sum_k \dot{m}_k \tag{3.8}$$

Whereas the mass flow rate is given as in equation (3.9):

$$\dot{m}_k = \iint -\rho_k (v_k - v) \cdot n \, dS = \iint -j_k \cdot n \, dS \tag{3.9}$$

The barycentric velocity $\boldsymbol{v}$ is defined by $\rho \boldsymbol{v} = \sum_k \rho_k v_k$, with $\sum_k \rho_k = \rho$. Consequently,

$$\sum_k j_k = 0$$

By using the transport theorem expressed in Appendix equation (A4-8), the equation (3.8) and (3.9) give:

$$\iiint \left(\frac{\partial \rho}{\partial t} + \nabla.(\rho v)\right) dV = \iint - \sum_k j_k \cdot n \, dS \tag{3.10}$$

Thus,

$$\frac{\partial \rho}{\partial t} = \dot{\rho} = -\nabla.(\rho v) \tag{3.11}$$

The balance of the k specie when assuming no chemical reaction can be written as:

$$\frac{dM_k}{dt} = \frac{d}{dt} \iiint \rho x_k dV = \iint -j_k \cdot n \, dS \tag{3.12}$$

Thus, from the transport theorem (A4-10):

$$\rho \dot{x}_k = \nabla j_k \tag{3.13}$$

Moreover, the first thermodynamic principle of an open system is:

$$\frac{dE}{dt} = \dot{q} + \dot{w} + \sum_k \dot{m}_k h_k \tag{3.14}$$

For an arbitrary volume V(t), whose center of gravity moves at speed $\boldsymbol{v}$, the fluxes q̇, ẇ, $\dot{m}_k$, h_k are expressed as:

$$\dot{q} = \iint -j_q \cdot n \, dS \tag{3.15}$$

$$\dot{w} = \iint \left(-p\bar{\bar{I}} + \bar{\bar{\tau}}\right) \cdot v \cdot n \, dS + \iiint \rho F \cdot v \, dV \tag{3.16}$$

$$\dot{m}_k h_k = \iint - \varrho_k h_k (v_k - v) \cdot n \, dS = \iint -j_k h_k \cdot n \, dS \tag{3.17}$$

With

($-p\bar{\bar{I}}+\bar{\bar{\tau}}$): stress tensor (pressure and viscous) ($Pa.m^{-2}$),

F: force acting on the volume per unit mass (N/kg), e.g., gravity g

h_k: specific constituent enthalpy k (J.kg^{-1})

By using equation (3.15), (3.16) and (3.17), equation (3.14) become:

$$\frac{dE}{dt} = \frac{d}{d}\iiint \rho e dV = \iint -\left[j_q + \left(-p\bar{\bar{I}} + \bar{\bar{\tau}}\right)\cdot v + \sum_k j_k h_k\right]\cdot n\, dS + \iiint \rho F \cdot v\, dV$$

Thus, by using the equation (A4-10) and Gauss theorem:

$$\iiint \rho \dot{e} dV = \iiint \left(-\nabla\cdot\left[j_q + \left(-p\bar{\bar{I}} + \bar{\bar{\tau}}\right)\cdot v + \sum_k j_k h_k\right] + \rho F \cdot v\right) dV \quad (3.18)$$

Where,

$$-\nabla\cdot\left[\left(-p\bar{\bar{I}} + \bar{\bar{\tau}}\right)\cdot v\right] = p\,\nabla\cdot v - \bar{\bar{\tau}}:\nabla v + v\cdot\nabla\cdot\left(p\bar{\bar{I}} + \bar{\bar{\tau}}\right)$$

Thus, equation (3.18) become:

$$\rho\dot{e} = -\nabla\cdot\left(j_q + j_k h_k\right) - p\nabla\cdot v + \bar{\bar{\tau}}:\nabla v - v\cdot\nabla\cdot\left(p\bar{\bar{I}} - \bar{\bar{\tau}}\right) + \rho F\cdot v$$

And by replacing e by $u + v\cdot v/2$,

$$\rho(\dot{u} + v\cdot\dot{v}) = -\nabla\cdot\left(j_q + j_k h_k\right) - p\nabla\cdot v + \bar{\bar{\tau}}:\nabla v - v\cdot\nabla\cdot\left(p\bar{\bar{I}} - \bar{\bar{\tau}}\right) + \rho F\cdot v \quad (3.19)$$

By arranging the equation (3.19), it can be written as:

$$\left[\rho\dot{u} + \nabla\cdot\left(j_q + j_k h_k\right) + p\nabla\cdot v - \bar{\bar{\tau}}:\nabla v\right] + v\cdot\left[\rho\dot{v} + \nabla\cdot\left(p\bar{\bar{I}} - \bar{\bar{\tau}}\right) - \rho F\right] = 0 \quad (3.20)$$

Galilean invariance requires that this expression, deduced from the 1stprinciple, be independent of the reference frame. In a reference frame in uniform translation at speed $\boldsymbol{v_0}$ with respect to the initially chosen reference frame, equation (3.20) becomes:

$$\rho\dot{u} + \nabla\cdot\left(j_q + j_k h_k\right) + p\nabla\cdot v - \bar{\bar{\tau}}:\nabla v + (v + v_0)\cdot\left[\rho\dot{v} + \nabla\cdot\left(p\bar{\bar{I}} - \bar{\bar{\tau}}\right) - \rho F\right] = 0 \quad (3.21)$$

Thus

$$\rho\dot{v} + \nabla\cdot\left(p\bar{\bar{I}} - \bar{\bar{\tau}}\right) - \rho F = 0 \quad (3.22)$$

$$\rho\dot{u} + \nabla\cdot\left(j_q + j_k h_k\right) + p\nabla\cdot v - \bar{\bar{\tau}}:\nabla v = 0 \quad (3.23)$$

The expressions (3.22) and (3.23) respectively give the conservation of momentum and internal energy for an open system:

$$\rho\dot{v} = -\nabla\cdot\left(p\bar{\bar{I}} - \bar{\bar{\tau}}\right) + \rho F \quad (3.24)$$

$$\rho\dot{u} = -\nabla\cdot\left(j_q + j_k h_k\right) - p\nabla\cdot v + \bar{\bar{\tau}}:\nabla v \quad (3.25)$$

If the volume V(t) is small enough to consider the pressure p and the temperature T uniform in the domain, the Gibbs equation expresses the relation existing between the intensive properties characterizing the volume V(t):

$$du - Tds + pd\left(\frac{1}{\rho}\right) - \sum_k \gamma_k dx_k = 0 \tag{3.26}$$

with

x_k: mass titer of component k (-)

γ_k: chemical potential of component k (J.kg^{-1})

The Gibbs equation (3.26) reflects the assumption of local equilibrium, namely mechanical and thermal equilibrium. Dividing by dt, we obtain

$$\dot{u} - T\dot{s} + \dot{\rho}\left(\frac{p}{\rho^2}\right) - \sum_k \gamma_k \dot{x}_k = 0 \tag{3.27}$$

Multiplying the Gibbs equation (3.27) by ρ and expressing the Lagrangian derivatives according to the expressions (3.25), (3.12) and (3.14), we obtain

$$\rho\dot{s} = \frac{1}{T}\left[-\nabla\cdot\left(j_q + j_k h_k\right) - p\nabla\cdot v + \bar{\bar{\tau}}:\nabla v - \frac{p}{\rho}\left(-\rho\cdot\nabla(v)\right) - \sum_k \gamma_k(\nabla j_k)\right]$$

Thus,

$$\rho\dot{s} = \frac{1}{T}\left[-\nabla\cdot\left(j_q + j_k h_k\right) + \bar{\bar{\tau}}:\nabla v + \sum_k \gamma_k \nabla j_k\right] \tag{3.28}$$

In order to obtain the expressions for entropy flow and entropy production, the expression (3.18) must be put in the form $\rho\dot{s} = \nabla.\mathbf{j} + \dot{\sigma}$

$$\rho\dot{s} = \frac{1}{T}\left[-\nabla\cdot\left(\frac{j_q + j_k h_k}{T}\right) + \left(j_q + j_k h_k\right)\cdot\nabla\left(\frac{1}{T}\right) + \frac{\bar{\bar{\tau}}:\nabla v}{T} + \sum_k \nabla\left(j_k\frac{\gamma_k}{T}\right)\right]$$

By replacing h_k by $\mu_k + Ts_k$ as $h_k - \mu_k = Ts_k$, this equation become:

$$\rho\dot{s} = -\nabla\cdot\left(\frac{j_q + j_k s_k}{T}\right) + \left(j_q + j_k h_k\right)\cdot\nabla\left(\frac{1}{T}\right) + \frac{\bar{\bar{\tau}}:\nabla v}{T} - j_k\nabla\left(\frac{\gamma_k}{T}\right) \tag{3.29}$$

Thus, by applying equation (A11), equation (3.29) becomes:

$$\frac{\partial(\rho s)}{\partial t} = -\nabla\cdot\left(\frac{j_q + j_k s_k}{T} + \rho v s\right) + \left(j_q + j_k h_k\right)\cdot\nabla\left(\frac{1}{T}\right) + \frac{\bar{\bar{\tau}}:\nabla v}{T} - j_k\nabla\left(\frac{\gamma_k}{T}\right) \tag{3.30}$$

Moreover,

$$\nabla\left(\frac{\gamma_k}{T}\right) = \frac{\partial\left(\frac{\gamma_k}{T}\right)}{\partial T}\nabla T + \frac{\partial\left(\frac{\gamma_k}{T}\right)}{\partial\gamma_k}\nabla\gamma_k \tag{3.31}$$

That gives

$$\nabla\left(\frac{\gamma_k}{T}\right) = \frac{\partial\left(\frac{\gamma_k}{T}\right)}{\partial T}\nabla T + \frac{1}{T}\nabla\gamma_k$$

From the Gibbs-Helmholtz relation:

$$-\frac{H}{T^2} = \left(\frac{\partial\left(\frac{G}{T}\right)}{\partial T}\right)_P$$

That allows writing

$$-\frac{\sum_k H_k N_k}{T^2} = \frac{\partial\left(\frac{\sum_k \gamma_k N_k}{T}\right)}{\partial T}$$

And therefore,

$$-\frac{H_k}{T^2} = \frac{\partial\left(\frac{\gamma_k}{T}\right)}{\partial T}$$

Thus, equation (3.31) become:

$$\nabla\left(\frac{\gamma_k}{T}\right) = -\frac{h_k}{T^2}\nabla T + \frac{1}{T}\nabla\gamma_k = -h_k\nabla\left(\frac{1}{T}\right) + \frac{(\nabla\gamma_k)_T}{T}$$

By introducing this equation in the equation (3.30),

$$\frac{\partial(\rho s)}{\partial t} = -\nabla\cdot\left(\frac{j_q + j_k s_k}{T} + \rho v s\right) + j_q\cdot\nabla\left(\frac{1}{T}\right) + \frac{\bar{\bar{\tau}}:\nabla v}{T} - j_k\frac{(\nabla\gamma_k)_T}{T}$$

That allows to write the entropy flow $j_s$and the volume entropy generation $\dot{\sigma}_s$

$$j_s = \frac{j_q + j_k s_k}{T} + \rho v s \tag{3.32}$$

$$\dot{\sigma} = j_q\cdot\nabla\left(\frac{1}{T}\right) + \frac{\bar{\bar{\tau}}:\nabla v}{T} - j_k\frac{(\nabla\gamma_k)_T}{T} \tag{3.33}$$

Thus, for k species, equation (3.33) is written as in (3.34):

$$\dot{\sigma} = \overrightarrow{j_q}\cdot\vec{\nabla}\left(\frac{1}{T}\right) - \sum_k c_k\overrightarrow{v_k}\cdot\left(\frac{1}{T}\vec{\nabla}\gamma_k\right) + \frac{\bar{\bar{\tau}}:\overline{\overline{grad}}(u)}{T} \tag{3.34}$$

Hence, when assuming a continuous, open and isotropic system that contains a fluid composed of k species, total entropy generation only results from the addition of heat, mass and hydrodynamic irreversibilities, each of them being positive. No coupling can be found between the thermal or mass phenomenon with the friction one due to the difference in tensor degree. Indeed, the coupling effects are related to the Soret and Dufour effects. The Dufour effect implies an energy flux due to the chemical potential gradient while the Soret effect is its reciprocal and implies a mass flux due to the

temperature gradient. Thus, the entropy variation due to the Dufour and Soret effects compensate each other. In the following section, the entropy generation equation is written for each part of the absorber, namely, the film, the heat transfer fluid and the wall.

3.2.5.1 Falling film

Due to the thermal, concentration and velocity gradients along the falling film, a nonequilibrium state is encountered causing entropy generation. The volumetric rate of entropy generation in the falling film is given by equation (3.35) according to equation (3.34):

$$\dot{\sigma}_f = \overrightarrow{J_{q,f}} \cdot \vec{\nabla}\left(\frac{1}{T_f}\right) - \frac{1}{T_f}\sum_k \overrightarrow{J_k} \cdot \vec{\nabla}(\gamma_k) + \frac{\bar{\bar{\tau}} : \overline{\overline{grad}}(\vec{u}_f)}{T_f} \tag{3.35}$$

The first term of the right-hand side of equation (3.35) represents entropy generation due to heat transfer $\dot{\sigma}_{th,f}$, the second term is due to mass transfer $\dot{\sigma}_{m,f}$ while the third is due to fluid friction $\dot{\sigma}_{vis,f}$.

By developing the above equation, with respect to system of equations (3.2), the volumetric rate of entropy generation in the film can be written as in equation (3.36):

$$\begin{aligned}\dot{\sigma}_f(x,y_1) = {} & \frac{\lambda_f}{T_f(x,y_1)^2}\left[\left(\frac{\partial T_f(x,y_1)}{\partial y_1}\right)^2 + \left(\frac{\partial T_f(x,y_1)}{\partial x}\right)^2\right] \\ & - \frac{1}{T_f(x,y_1)}\left(j_{LiBr,x}\frac{\partial \gamma_{LiBr}(x,y_1)}{\partial x} + j_{LiBr,y_1}\frac{\partial \gamma_{LiBr}(x,y_1)}{\partial y_1}\right) \\ & + \frac{\mu_f}{T_f(x,y_1)}\left(\frac{\partial u_f(y_1)}{\partial y_1}\right)^2\end{aligned} \tag{3.36}$$

Where $j_{LiBr,x}$ and j_{LiBr,y_1} are the diffusive fluxes in the x and y_1 direction respectively and can be written as:

$$\vec{j}_{LiBr,x} = \frac{\rho_{LiBr-sol}}{\mathcal{M}_{LiBr}} D_{H_2O-LiBr}\frac{\partial \vec{C}_{LiBr}(x,y_1)}{\partial x}$$

and

$$\vec{j}_{LiBr,y_1} = \frac{\rho_{LiBr-sol}}{\mathcal{M}_{LiBr}} D_{H_2O-LiBr}\frac{\partial \vec{C}_{LiBr}(x,y_1)}{\partial y_1}$$

$\rho_{LiBr-sol}$ is the density of the LiBr in the aqueous LiBr solution. The partial chemical potential at each (x, y_1), is calculated using the Yuan and Herold (2005) correlations and the concentration and temperature fields obtained after solving the numerical model described in Section 3.2.

3.2.5.2 Heat transfer fluid

In the HTF, entropy generation is only due to heat transfer and fluid friction as there is no mass transfer. Consequently, the volumetric rate of entropy generation is given by equation (3.37):

$$\dot{\sigma}_{htf} = \overrightarrow{J_{q,htf}} \cdot \vec{\nabla}\left(\frac{1}{T_{htf}}\right) + \frac{\bar{\bar{\tau}} : \bar{\bar{\nabla}}(\vec{u}_{htf})}{T_{htf}} \tag{3.37}$$

The first term of the right-hand side of equation (3.37) represents entropy generation due to heat transfer $\dot{\sigma}_{th,htf}$ while the second is due to fluid friction $\dot{\sigma}_{vis,htf}$.

By developing equation (3.20), the HTF volumetric rate of entropy generation is written as (3.38):

$$\dot{\sigma}_{htf}(x,y_2) = \frac{\lambda_{htf}}{T_{htf}(x,y_2)^2}\left[\left(\frac{\partial T_{htf}(x,y_2)}{\partial y_2}\right)^2 + \left(\frac{\partial T_{htf}(x,y_2)}{\partial x}\right)^2\right] + \frac{\mu_{htf}}{T_{htf}(x,y_2)}\left(\frac{\partial u_{htf}(y_2)}{\partial y_2}\right)^2 \tag{3.38}$$

3.2.5.3 Wall

Through the wall, there is no mass transfer and obviously no fluid friction. Consequently, the wall volumetric entropy generation is only due to the heat transfer as (3.22):

$$\dot{\sigma}_w(x,y) = \dot{\sigma}_{w,th} = \overrightarrow{J_{q,w}} \cdot \overrightarrow{grad}\left(\frac{1}{T_w}\right) = \frac{\lambda_w}{T_w(x,y)^2}\left[\left(\frac{\partial T_w(x,y)}{\partial y}\right)^2 + \left(\frac{\partial T_w(x,y)}{\partial x}\right)^2\right] \tag{3.39}$$

The total entropy generation rate per unit of wall width is as equation (3.23):

$$\dot{S}_{tot} = \iint \dot{\sigma}_{tot}\, dxdy = \iint \dot{\sigma}_{htf}\, dxdy + \iint \dot{\sigma}_w\, dxdy + \iint \dot{\sigma}_f\, dxdy$$
$$= \iint \left(\dot{\sigma}_{htf,th} + \dot{\sigma}_{htf,v}\right) dxdy + \iint \dot{\sigma}_{w,th}\, dxdy + \iint \left(\dot{\sigma}_{f,th} + \dot{\sigma}_{f,v} + \dot{\sigma}_{f,m}\right) dxdy \tag{3.40}$$

3.3. Operating conditions and model validation

3.3.1 Operating conditions

The absorber considered in this study is a falling film absorber which can be used in absorption systems, for example for building heating and cooling systems using a LiBr/H_2O couple. The main design characteristics of the absorber are the same as those used by Perier-Muzet and Stutz, (2021) and are summarized in Table 3.1. In the whole study, the inlet HTF temperature is set equal to 35°C.

Table 3.1: Main design characteristics of the absorber

Configuration	Counter HTF flow
Plate height (L)	0.3 – 0.5 m
Thickness of the wall (e_w)	3.10^{-3} m
Conductivity of the wall (λ_w)	16 $W.K^{-1}.m^{-1}$
Thickness of the half HTF channel (e_{htf})	1.10^{-3} m

The absorber pressure is assumed to be equal to 1kPa – the saturated vapour temperature of 7°C is given knowing the vapour pressure (Appendix 1) – and the properties of LiBr solution and of the HTF

are derived from the correlation presented in Yuan and Herold (2005). Table 3.2 lists the operating conditions of the HTF and of the falling film.

Table 3.2: Physical properties of LiBr solution and HTF

Properties	values
Film density (ρ_f)	1700.3 $kg.m^{-3}$
HTF density (ρ_{htf})	997.5 $kg.m^{-3}$
Film dynamic viscosity (μ_f)	5.350 10^{-3} Pa.s
HTF dynamic viscosity (μ_{htf})	8.02 10^{-4} Pa.s
Film thermal conductivity (λ_f)	0.43095 $W.m^{-1}. K^{-1}$
HTF thermal conductivity (λ_{htf})	0.61 $W.m^{-1}. K^{-1}$
Diffusion coefficient ($D_{H2O-LiBr}$)	1.6175 10^{-9} $m^2. s^{-1}$
Heat of absorption (ΔH_{abs})	2772.7 $kJ.kg^{-1}$
Film specific heat ($C_{p,f}$)	1567.5 J. $K^{-1}.kg^{-1}$
HTF specific heat ($C_{p,htf}$)	4178.0 J. $K^{-1}.kg^{-1}$

The film Reynolds number is assumed to be constant and equal to 50 corresponding to a film thickness of 0.33 mm while the HTF Reynolds number ranges from 500 to 2000 in laminar flow and up to 5000 for turbulent flow. Indeed, although the film Reynolds number has a high impact on the temperature and concentration distributions, the impact of this parameter has already been extensively studied in the literature, in contrast to the Reynolds number of the HTF (Giannetti et al. 2015b; 2016).

3.3.2 Model validation

The interfacial temperature and concentration of the present work were compared with the numerical results obtained by Huaylla (2017) and Karami and Farhanieh (2009) to validate the model. Huaylla (2017) developed a numerical 1D model while Karami and Farhanieh (2009) developed a numerical 2D model to study the LiBr/H_2O absorption along a vertical plate. In the present work, the thermodynamic equilibrium at the interface was modelled using the two most used equations to determine their agreement and to assess the accuracy of the model: i.e., that of Islam et al (2006) – equation (A3 - 1) Appendix 3 – and that of McNeely (1979) – equation (A3 - 2) Appendix 3. Both Eckert-Schneider relation and Fick mass absorbed expressions are also analysed (Arroiabe et al. 2022). For the purpose of validating the model, the simulation was performed under the same operating conditions as those of Karami and Farhanieh (2009), following Huaylla (2017). The cooling water is in counter-current flow to the flow of the falling film and its temperature change is assumed to be linear. The conditions are listed in Table 3.3.

Table 3.3: Parameters used for validation

Parameters	Values
Plate height, L (m)	1.0
System pressure, P (kPa)	1.0
Film inlet temperature, $T_{f,in}$ (°C)	45.6
Film inlet concentration, $C_{LiBr,in}$ (%)	60.0
HTF inlet temperature, $T_{htf,in}$ (°C)	32
HTF outlet temperature, $T_{htf,in}$ (°C)	36
Film Reynolds number, Re_f (-)	20.5

Figure 3.2 shows good agreement between the model developed in the present study and those developed by Karami and Farhanieh (2009) and Huaylla (2017) as they share the same order of magnitude, although the present models are close to Karami's results. This can be explained by the fact that Huaylla (2017) used the Hellman and Grossman (1996) equation to model the equilibrium correlation between the temperature, the LiBr mass fraction and the vapour pressure at the interface while Karami and Farhanieh (2009) used the McNeely (1979) correlation.

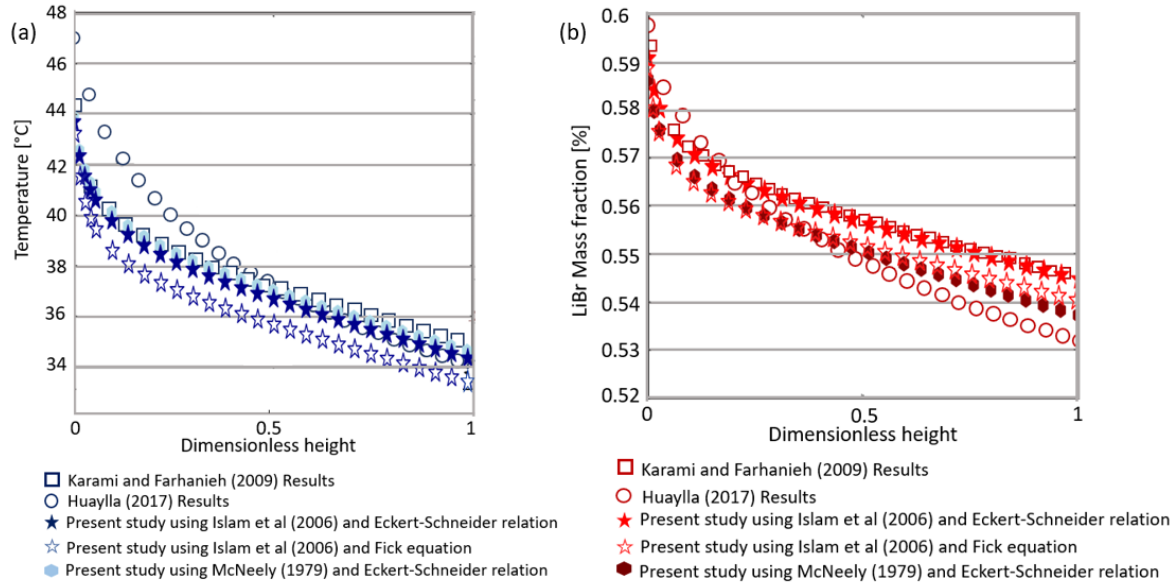

Figure 3.2: Validation of the model

However, for temperature a mean deviation of about 0.32°C is observed between our models and the Huaylla model while a mean deviation of 0.25°C is observed between our models and Karami's model (Fig. 3.2a). For the concentration, a mean deviation less than 3% of LiBr is observed (Fig. 3.2b). The difference between the present study using McNeely (1979) correlation and the Karami's model may be explained by the fact that Karami and Farhanieh (2009) considered the x and y-components of the velocity while in this study, only the x-component of the velocity is considered. Good agreement is also observed between the Islam et al (2006) equilibrium equation and that of McNeely (1979). Indeed, for temperature a maximum deviation of 1°C is observed between the two equilibrium equations while for the LiBr concentration, a maximum deviation of 1.03% of LiBr is observed. Using the McNeely (1979) equation induces a higher absorption of refrigerant compared to the Islam et al (2006) equation. The deviation between the two correlations increases with an increase in the film length.

Moreover, the absorbed mass flow rate calculated using the Eckert-Schneider relation shows an overestimation of the water absorbed into the film when comparing the result with the variation of the mass fraction of LiBr within the film. However, the estimated absorbed mass flux is in line with the inlet/outlet change in mass fraction of LiBr within the film when the Fick equation is considered. Thus, in the following, the film length is assumed to be equal to or less than 0.5 m in order to minimise the deviation, and the Islam et al (2006) correlation using the Fick equation is used.

3.4. Absorber analysis

The main results presented here are those considering laminar HTF flows, but turbulent HTF flows are also discussed based on the problem formulation. Thus, studying low HTF flows enables greater understanding of the local phenomenon and some qualitative results can be extended to turbulent HTF flows.

3.4.1 Absorbed mass flow rate for the limit cases – adiabatic and isothermal walls

A general analysis was carried out for typical conditions of a flat plate absorber, working with inlet HTF temperature of 35°C. For the adiabatic case, the film is assumed to be subcooled at the inlet compared to equilibrium conditions ($C_{LiBr,in}$ = 60%, $T_{f,in}$ = 45.6°C) with the inlet film temperature set at 43°C. Indeed, this condition is required as no phenomenon occurs when assuming that the film is at equilibrium at the inlet. For the isothermal cases, two simulations were performed: one assuming equilibrium conditions for a vapour pressure of 1 kPa at the interface ($C_{LiBr,in}$ = 60%, $T_{f,in}$ = 45.6°C) and another assuming subcooled film at the inlet ($C_{LiBr,in}$ = 60%, $T_{f,in}$ = 43°C) to study the behaviour of the absorber. Figure 3.3 shows the evolution of the absorbed mass flow rate for adiabatic and isothermal cases along the length of the 0.3 m long plate.

Near the inlet of the film – for small x values, the behaviour is the same for adiabatic and isothermal cases when assuming subcooled film at the inlet (solid red and dotted blue curves, Fig. 3.3). Indeed, although the film reaches thermodynamic equilibrium at the interface once it is in contact with the vapour, the thermal and mass boundary layers take some distance from the inlet absorber to be fully developed and so the isothermal or adiabatic wall assumption is yet to be achieved. Figure 3.3 also shows that the absorbed mass flow rate is greatest – around 2.6 10^{-3} kg.m^{-2}. s^{-1} – at the inlet due to the effect of the subcooled film which leads to a high driving force at x = 0. In case of overheated film at the inlet, the desorption phenomenon would be observed near the inlet (for small x values). For the adiabatic case, the absorbed mass flow rate decreases monotonically from the inlet to the outlet of the absorber, as the heat released at the free interface is not removed from the absorber. Hence, the film temperature quickly increases leading to thermodynamic equilibrium in the entire component: only the thermal and diffusive boundary layers ($\delta_{f,th2}$, $\delta_{f,m}$) develop. For the isothermal case when assuming subcooled film at the inlet, the absorbed mass flow rate decreases as the thermal boundary layer $\delta_{f,th2}$ and the diffusive boundary layer $\delta_{f,m}$ are in the developing stage, until the constant temperature at the wall starts to be achieved at the interface – the position where $\delta_{f,th1} = \delta_{f,th2}$ (x ≈ 0.012 m) – see Fig. 3.1b.

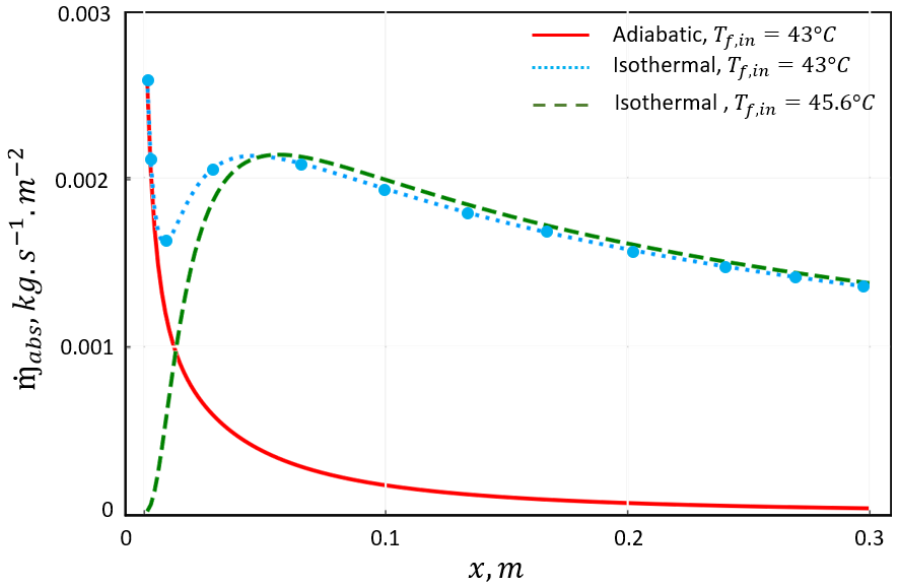

Figure 3.3: Absorbed mass when assuming adiabatic and isothermal cases and a subcooled film inlet ($C_{LiBr,in}$ = 60%, $T_{f,in}$ = 43°C)

Afterward, the absorbed mass increases slightly due to removal of the heat released at the interface before decreasing again as the temperature at the interface tends toward the wall temperature. However, when assuming equilibrium conditions at the inlet of the film (green dashed curve, Fig. 3.3) the absorbed mass is close to zero at the inlet (x = 0) as the driving force of mass transfer is null. Under the effect of the isothermal wall, heat is removed at the wall with the development of the thermal boundary layer $\delta_{f,th1}$ within the film. Once $\delta_{f,th1}$ is completely developed (x ≈ 0), the absorbed mass increases with the development of the diffusive boundary layer ($\delta_{f,m}$) as seen in Fig. 1c, due to the increase in the driving force induced by heat transfer, until reaching a maximum value (x ≈ 0.048 m). Then, the absorbed mass decreases as in the case of subcooled film at the inlet (dashed blue curve, Fig. 3.3) due to the decrease in the temperature difference between the wall and the film. In the case where inlet equilibrium conditions is assumed at the inlet of the film, development of the thermal boundary layer $\delta_{f,th2}$ is not observed as there is no temperature gradient between the film interface and the film inlet. After the development of $\delta_{f,th1}$, the absorption phenomenon takes place, and therefore, heat of absorption is released. However, the thermal boundary layer $\delta_{f,th2}$ is not observed as temperature gradient is already observed in the whole film thickness due to the complete development of $\delta_{f,th1}$ according to the thermal boundary layer definitions given in paragraph 3.2. Consequently, the film temperature gradient changes in the film thickness due to the HTF and the absorption phenomenon.

3.4.2 Entropy generation analysis for the limit cases

The falling film is the source of several phenomena leading to the generation of different types of irreversibilities within the film. The falling film volumetric entropy generation is determined for any (x, y_1) points using equation (3.8). The evolution of the volumetric entropy generation at the film-vapour interface is shown in Fig. 3.4 under subcooled conditions, with $T_{f,in}$ = 43°C. At the film interface and

whatever boundary conditions applied at the wall side, both thermal and mass irreversibilities have the same shape as the absorbed mass flow rate shown in Fig. 3.3.

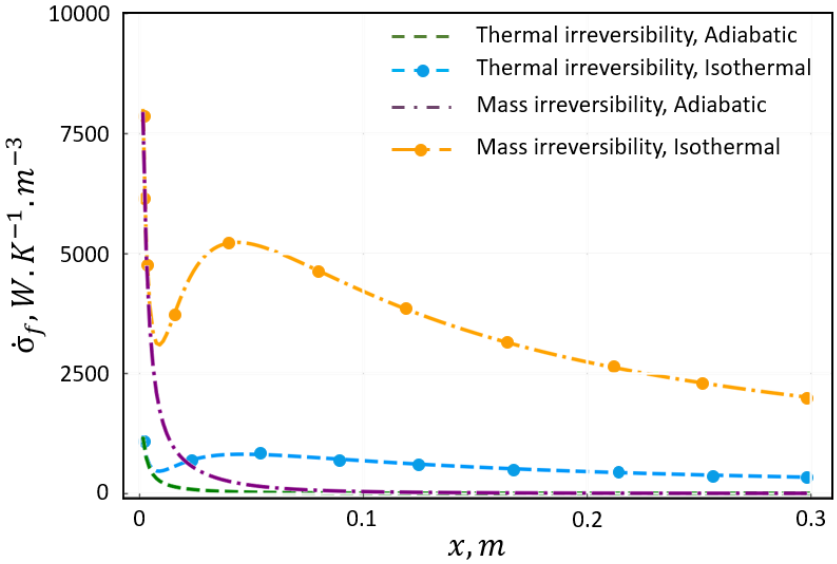

Figure 3.4: Entropy generation at the film interface for isothermal and adiabatic cases when assuming subcooled conditions ($C_{LiBr,in}$ = 60%, $T_{f,in}$ = 43°C) at the film inlet for a Re_f = 50

However, for both limit cases, the mass irreversibilities is higher – more than two times at the inlet – than the thermal irreversibilities. Once the boundary layers are developed, the difference between the thermal and mass irreversibilities decreases with the film length because the temperature and concentration tend to equilibrium. It can be concluded that at the free interface, the contribution of mass irreversibilities on entropy generation is high compared to that of thermal irreversibilities.

Although only the irreversibilities at the free interface are represented in Fig. 3.4, a discussion about the behaviour of the entire film for both limit cases are given in the following section. Indeed, analysis of entropy generation through the entire film shows that for the case of an adiabatic absorber, the irreversibilities are concentrated at the interface ($y_1 = e_f$) and decrease with x. Moreover, as the heat released at the interface is not removed and the wall is impermeable, the thermal and mass irreversibilities are equal to zero near and at the wall during the development of the thermal $\delta_{f,th2}$ and diffusive $\delta_{f,m}$ boundary layers. Thus, only viscous irreversibilities applies near the wall and it is of an order of magnitude of 20 $W.K^{-1}.m^{-3}$. The analysis also shows that the thermal boundary layers develop faster than the diffusive boundary layer, which means that the thermal resistance is lower than the diffusive resistance. However, analysis of the entropy generation through the entire film for an isothermal case shows a different trend. Entropy generation is higher at the inlet of the film and at the wall (x = 0 and y_1 = 0) and is mainly caused by the thermal irreversibilities. Furthermore, it is around 38 000 $W.K^{-1}.m^{-3}$ and 70 000 $W.K^{-1}.m^{-3}$ when assuming subcooled film and equilibrium conditions respectively at the inlet, which corresponds to four times and eight times the irreversibilities observed at the film interface (Fig. 3.4). This is not only due to the low diffusion of the absorbed vapour – the irreversibilities due to the mass transfer is null near the wall – but also to the high temperature difference between the wall and the inlet film (a difference of 8°C and 10.6°C when assuming subcooled film and equilibrium conditions at the inlet, respectively) leading to a high heat transfer flux at the wall. Here, the viscous irreversibilities is negligible as the thermal irreversibilities dominates near the wall.

3.4.3 Absorbed mass flow rates when considering HTF

After analysing the behaviour of the absorber for the two limit cases, the focus is on a more realistic absorber with finite non-null HTF flow. To study the impact of the HTF, the inlet conditions of the LiBr/H_2O film have been set to equilibrium (pressure = 1 kPa, $C_{LiBr,in}$= 60% and $T_{f,in}$= 45.6°C) and the inlet HTF temperature is equal to 35°C. Before analysing the absorbed mass flow rate and entropy generation, the local temperature and concentration profiles are given in Fig. 3.5. As excepted, the HTF temperature increases from the bottom to the top while the film temperature increases from the top to bottom.

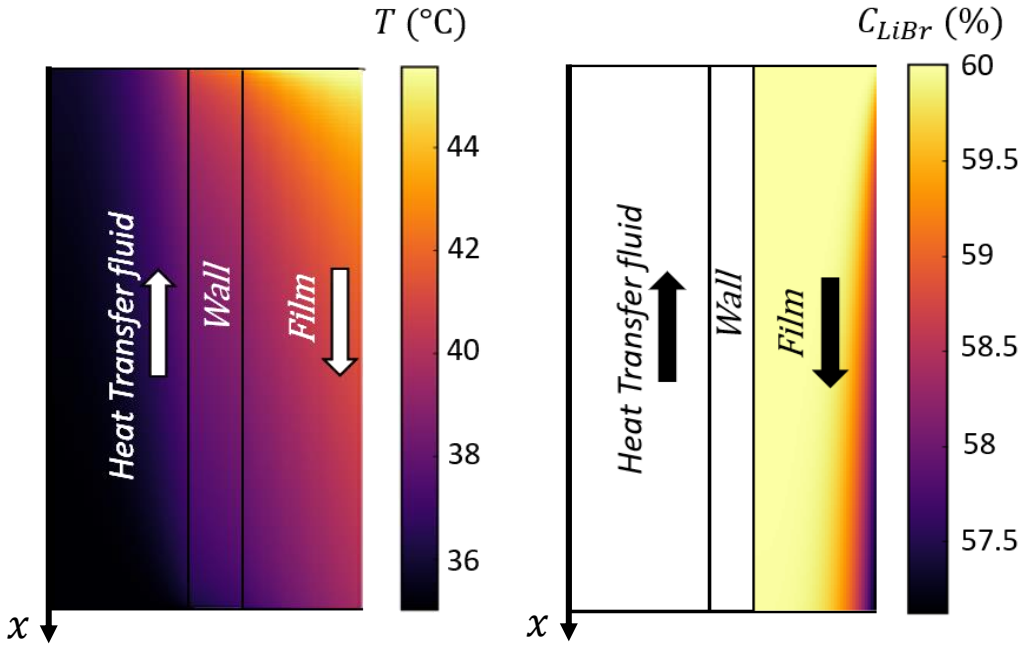

Figure 3.5: Locale temperature and concentration profiles for Re_{htf} = 2000

The absorbed mass flow rates obtained when varying the HTF Reynolds number are plotted in Fig. 3.6. Heat transfer fluid flow numbers larger than 4500 are typically turbulent, while those below 2300 are laminar.

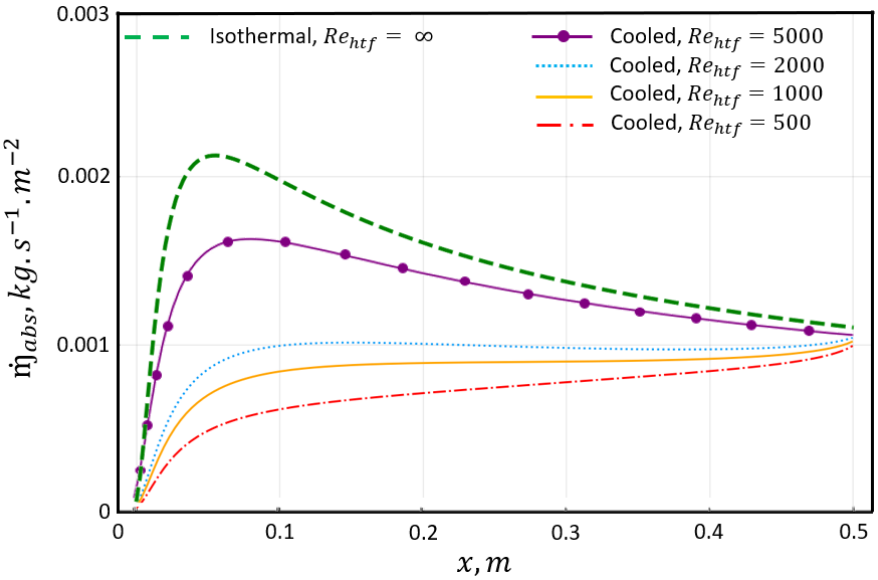

Figure 3.6: Evolution of the absorbed mass flow rate assuming laminar and turbulent heat transfer fluid (HTF) flow along the absorber length in the case of equilibrium condition of the film at the inlet

The behaviour of the absorbed mass flow rate is similar to the one explained in Section 3.4.1 for the case of an isothermal wall for $Re_{htf} = 5000$ to $Re_{htf} = \infty$, corresponding to the turbulent flow regime. As expected, the absorbed mass flow rate increases with an increase in the HTF velocity due to an increase in the heat transferred from the film to the HTF. However, what is of great interest is why the absorbed mass flow increases close to the outlet for HTF in a laminar flow regime (low Reynolds numbers), as shown in Fig. 3.6. Indeed, this behaviour is not observed for high Reynolds numbers – turbulent HTF flows – and $Re_{htf} = \infty$ – as in an isothermal case. Near the top of the absorber, the absorption phenomenon is induced by the heat transfer from the film to the HTF which creates thermodynamic disequilibrium between the film and the vapour. However, the phenomena occurring at the outlet differ from those at the inlet. The imposed uniform temperature of the HTF at x = 0.5 m leads to a high temperature difference between the two sides of the wall and consequently to a high heat flux. The increase of the absorbed mass flow rate at the bottom of the absorber is due to thermal and mass phenomena. In terms of thermal phenomenon, it is first due to the development of the HTF thermal boundary layer and second to the large temperature gradient between the two sides of the wall encountered for a low Reynolds number: the lower the Reynolds number, the hotter the film at the bottom and thus the higher the temperature gradient between both fluids. However, the large temperature gradient between the HTF and the film interface allows to have a high driving concentration at the bottom of the absorber and thus an increase of the absorbed mass flow rate. Consequently, the higher the HTF Reynolds number, the lower the increase phenomenon at the absorber outlet.

3.4.4 Local entropy generation analysis when considering the HTF

The local analysis enables representation of the distribution of irreversibilities by locating and quantifying the different sources of entropy generation. In this section, absorber entropy generation considering finite non-null HTF flow rates is discussed. Figure 3.7 summarises the different

irreversibilities distributions through the entire absorber when assuming equilibrium conditions ($T_{f,in} = T_{eq}(C_{LiBr,in}, P_{vap})$) with respect to the different boundary layers as represented in Fig 3.1b, by focusing in on the top and bottom of the absorber. In Fig. 3.7, viscous entropy generation is not presented. However, it should be mentioned that there is friction irreversibilities in the entire HTF and film, the hydrodynamic boundary layer is assumed to be fully developed for both fluids. When assuming a film is at equilibrium, no phenomena occur near the film-vapour interface at the inlet of the absorber. As explained in Section 3.4.3, the film transfers a part of its energy to the HTF through the wall. This transfer decreases the film temperature leading to the development of the thermal boundary layer $\delta_{f,th1}$. At this stage, no mass transfer is observed. Consequently, inside the thermal boundary layer $\delta_{f,th1}$, irreversibilities due to the thermal transfer appear and beyond this boundary layer, no entropy generation due to thermal and/or mass transfer is observed as the film is at equilibrium. This thermal irreversibilities is high near the wall where transfers exist and decreases from the wall to the film interface during the development of the thermal boundary layer. The chemical potential difference between the film and the vapour generates once $\delta_{f,th1}$is completely developed ($\delta_{f,th1} = e_f$) and induces the absorption of the water vapour into the LiBr/H_2O solution, leading to the development of the diffusive boundary layer $\delta_{f,m}$. Thus, inside the diffusive boundary both thermal and mass irreversibilities are observed. No mass transfer occurs in the HTF so there is no mass irreversibilities. However, a thermal boundary layer $\delta_{htf,th}$ develops due to the increase in temperature of the HTF induced by the heat received from the film, leading to thermal entropy generation inside the boundary layer. The thermal irreversibilities observed in the HTF is high near the wall and decreases from the wall to the centre of the HTF channel. In this study, the HTF is in counter-current flow, so the thermal boundary layer $\delta_{htf,th}$ is observed at the bottom of the absorber.

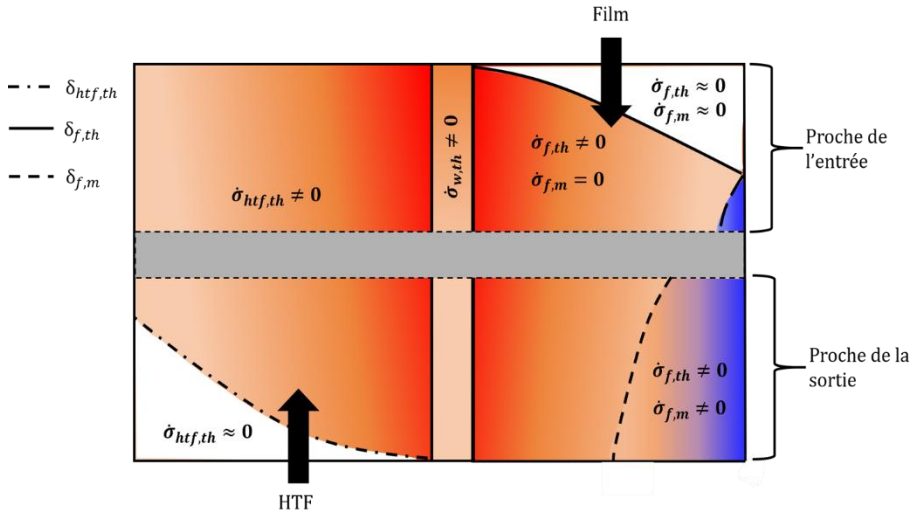

Figure 3.7: Local entropy generation through the whole absorber

Through the wall, only thermal transfer appears. Thus, only thermal irreversibilities is observed and varies only with x. Therefore, development of the boundary layers has a significant impact on the local phenomena and consequently on entropy generation. However, it is important to mention that under the study conditions of the present work, the thermal boundary layer $\delta_{f,th1}$develops quickly due to the low film Reynolds number and thus to the low thermal resistance.

In the following section, the entropy generation distribution is represented by simulating an absorber under the study conditions to quantify them. Figure 3.8 shows the evolution of irreversibilities through

the film and the HTF for Re_{htf} = 2000. Note that the irreversibilities due to the fluid friction are not plotted for both fluids as they are negligible (between 40 and 400 times lower) compared with the other sources of entropy generation. Both viscous irreversibilities of the film and of the HTF are equal to zero at the free interface and at the HTF channel centre respectively and are greatest at the wall – 20 $W.K^{-1}.m^{-3}$ for the film and 15 $W.K^{-1}.m^{-3}$ for the HTF, for Re_{htf} = 2000 (following a parabolic profile). Figures 3.8a and 3.8b allow better visualisation of the thermal and mass irreversibilities distribution. Figure 3.8a shows that the mass irreversibilities in the film increases with the increase in x from 0 to 1250 $W.K^{-1}.m^{-3}$. The maximum value of the mass irreversibilities is located at the bottom of the absorber, at the interface (x = L = 0.5 m, $y_1 = e_f$ = 0.33 mm) where the absorbed mass flow rate is greatest. However, only a quarter of the film thickness is influenced by the mass irreversibilities due to the low diffusion of the absorbed vapour into the film. Indeed, from the wall to the penetration distance of the diffusing water, the mass irreversibilities is equal to zero due to the null gradient of concentration. Afterward, it increases following the diffusive flux which is responsible for the mass transfer through the film thickness.

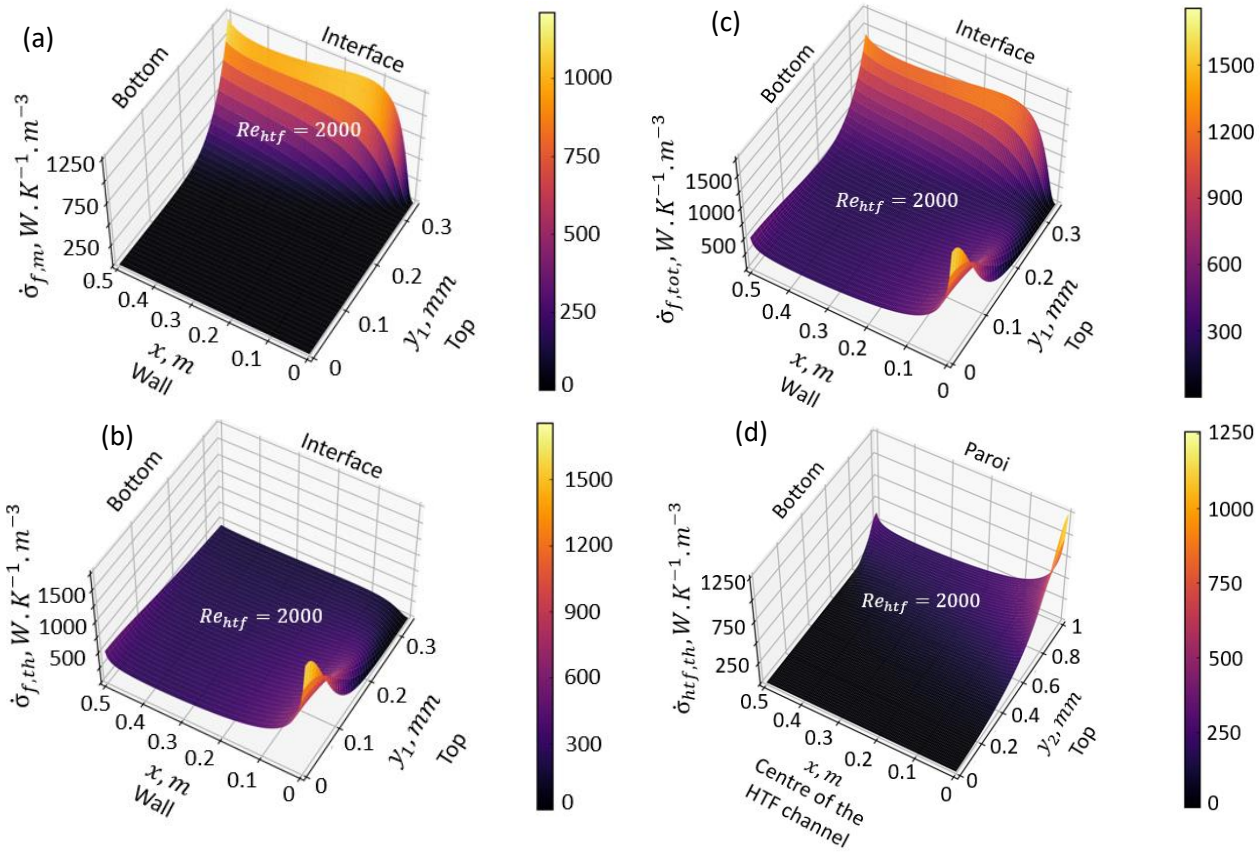

Figure 3.8: Evolution of the volumetric entropy generation (a) mass irreversibilities and (b) thermal irreversibilities through the film, (c) total entropy generation through the film and (d) thermal irreversibilities in the heat transfer fluid (HTF) for Re_f = 50, $T_{f,in}$ = 45.6°C, $C_{LiBr,in}$ = 60%

When the film is overheated or subcooled at the inlet, the maximum of the mass irreversibilities is observed at this position (x = 0 m) due to the high mass transfer driving force which is induced. Indeed, due to the thermodynamic equilibrium assumption at the free interface, the mass and heat transfer

strongly depend on the initial and boundary conditions such as the inlet film temperature and concentration, the solution flow rate and the working fluid properties.

The film thermal irreversibilities at the wall has the same profile as the heat flux transferred from the film to the HTF, while at the interface it has the same profile as the heat flux released due to absorption. Hence, the increase in the HTF velocity leads to an increase in the thermal irreversibilities at the wall ($y_1 = 0$) caused by an increase in the heat transfer flux exchanged as mentioned in Section 3.4.3. However, the thermal irreversibilities in the solution at the wall remains higher than at the interface under the study conditions: the heat transfer at the wall is higher (around 2400 $W.m^{-1}$) than the heat released during the absorption process (around 1800 $W.m^{-1}$) due to the large temperature gradient between the film and the HTF. Near the interface ($y_1 = e_f = 0.33$ mm), the thermal irreversibilities increases with x due to the increased absorption phenomenon. Near the wall ($y_1 = 0$), it decreases with x due to a decrease in the heat flux transferred from the film to the HTF before increasing at the outlet due to the imposed uniform temperature at the outlet of the absorber. Thus, unlike the mass irreversibilities which is observed in only a quarter of the film, thermal irreversibilities is observed throughout the entire film except at x = 0 m and $y_1 = e_f = 0.33$ mm where no phenomenon occurs due to the equilibrium assumption. Figure 3.8c shows the total volumetric entropy generation of the film which is the sum of the thermal, viscous and mass irreversibilities. It shows that the total entropy generation is of the same order of magnitude throughout the film except at the inlet as the HTF is in laminar flow (see the following paragraph for the case of a turbulent HTF flow). At the interface, 85% of the volumetric entropy generation is due to mass irreversibilities while the rest is due to thermal irreversibilities. At the wall ($y_1 = 0$), the thermal irreversibilities in the film dominates with a contribution greater than 95% and low friction irreversibilities. The total entropy generation through the film shows a local minimum in the film thickness except at the inlet as shown in Fig. 3.8c, where the irreversibilities are greatest near the wall due to the heat transfer flux and decrease with the film thickness to be equal to zero at x = 0, $y_1 = e_f = 0.33$ mm due to the equilibrium conditions assumed. The thermal irreversibilities in the HTF is presented in Fig. 3.8d, and shows that thermal irreversibilities is mainly situated near the wall ($y_2 = e_{htf} = 1$ mm) and decreases to a minimum near the centre ($y_2 = 0$) where it is assumed to be symmetrical.

For turbulent HTF flows, the film entropy generation is mainly ruled by thermal entropy generation near the wall due to the high heat exchange as shown in Fig. 3.9.

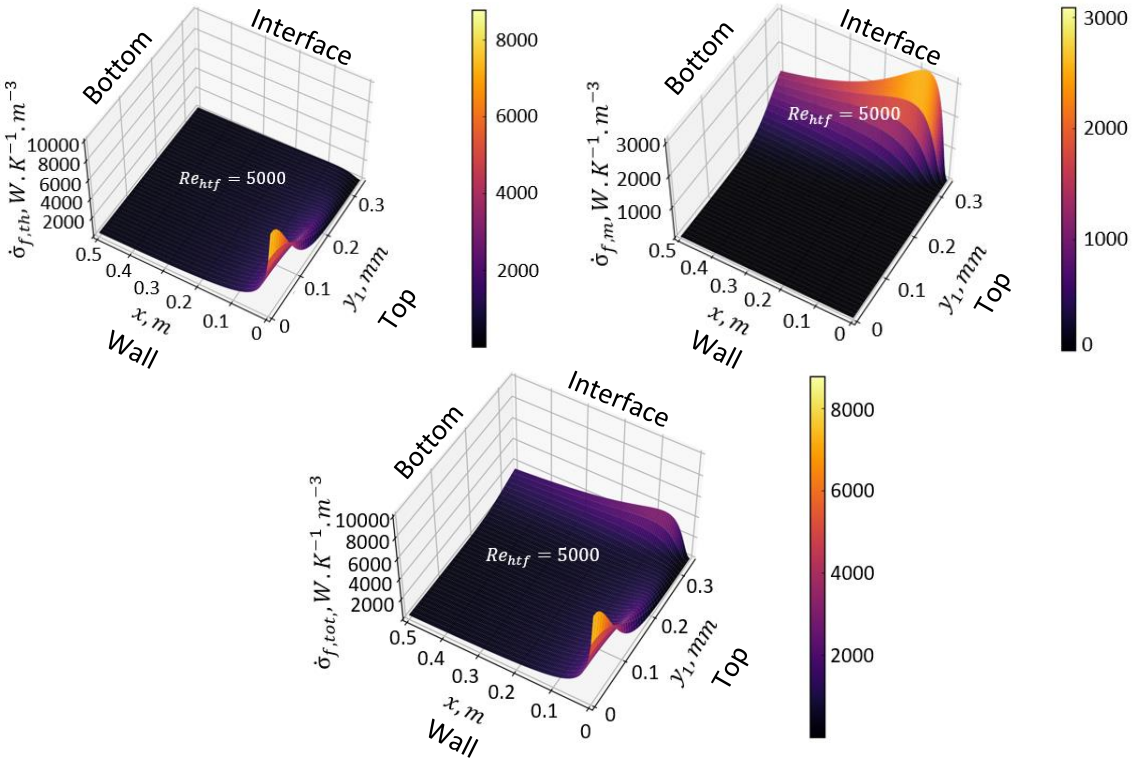

Figure 3.9: Evolution of the volumetric entropy generation (a) thermal irreversibility and (b) mass irreversibility through the film, (c) total entropy generation through the film for Re_f = 50, $T_{f,in}$ = 45.6°C, $C_{LiBr,in}$ = 60%

This thermal entropy generation decreases along the x-axis as the heat transfer flux decreases. One of the main conclusions for Re_{htf} = 5000 is that increasing the HTF velocity leads to an increase in the transferred heat flux and consequently of the absorbed mass flow rate as the heat transfer resistance decreases. However, it also leads to a significant increase in the irreversibilities of the entire falling film. It varies from 0 at x = 0 and y_1 = 0.33 mm to almost 9000 $W.K^{-1}.m^{-3}$ at x = 0 and y_1 = 0 for turbulent flow in Fig. 3.9.a against 1800 $W.K^{-1}.m^{-3}$ for a laminar HTF flow. There is an increase of almost five times of what is observed when assuming Re_{htf} = 2000. The mass entropy generation at the film-vapour interface increases with an increase in the mass transfer driving force before decreasing when the interface temperature tends to the wall temperature in Fig. 3.9.b: a maximum value of about 2000 $W.K^{-1}.m^{-3}$ is observed for Re_{htf} = 3000. The total entropy generation in the film is presented in in Fig. 3.9.c gives an idea of the impact of HTF velocity on entropy generation compared to Fig. 3.8.c.

Figure 3.10 shows the local evolution of entropy generation within the film at position x = 0.07 m (to ensure that $\delta_{f,th1}$ is completely developed) for Re_{htf} = 2000. As explained above, thermal irreversibilities is higher near the wall (y_1 = 0) and decreases to a minimal value at the free interface (y_1 = e_f = 0.33 mm).

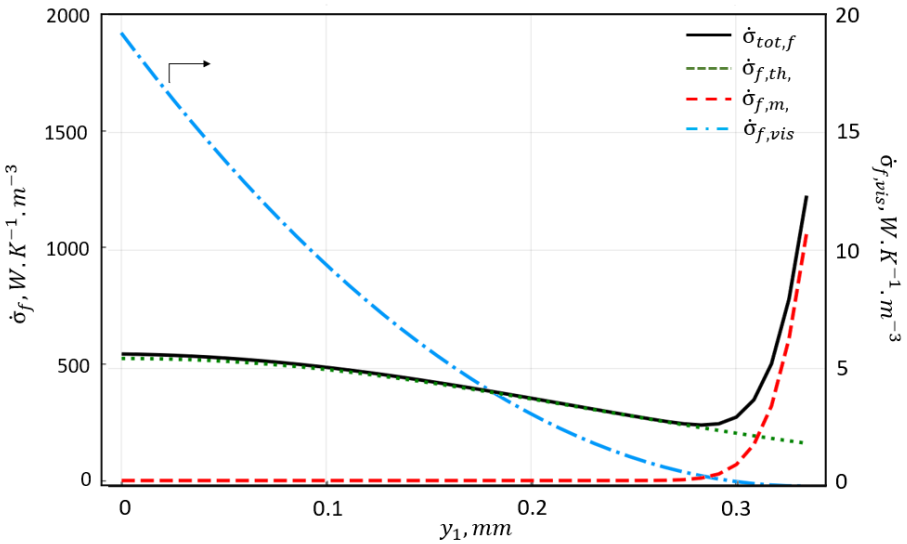

Figure 3.10: Evolution of entropy generation through the film thickness at x = 0.07 m for Re_f = 50, $T_{f,in}$ = 45.6°C, $C_{LiBr,in}$ = 60%

The mass irreversibilities is null from the wall to the mass boundary layer and then increases within the mass boundary layer with an increase of y_1 to a maximum at the free interface ($y_1 = e_f = 0.33$ mm). As the entropy generation for a given x position is the sum of the different contributions, it is dominated by thermal irreversibilities near the wall and by the mass irreversibilities after reaching the mass boundary layer near the interface. The viscous irreversibilities remains negligible. The sum of these different contributions shows a minimum entropy generation value with the film thickness (y_1 = 0.28 mm). The minimum is observed at the penetration distance of the diffusing vapour inside the film mass boundary layer. It is produced by the wall heat transfer, friction and coupled heat and mass transfer at the interface. The same behaviour is observed for the turbulent HTF flow.

3.4.5 Total entropy generation in the entire absorber when considering the HTF

Figures 3.11 and 3.12 present the contribution of each entropy generation source on the total entropy generation rate of the absorber for Re_{htf} = 2000 and Re_{htf} = 5000 respectively. Under the study conditions, the total entropy generation rate per unit of wall width is equal to 0.13 W. $K^{-1}.m^{-1}$ for Re_{htf} = 2000 and 0.2 W. $K^{-1}.m^{-1}$ for Re_{htf} = 5000 (an increase of 54%). The increase in the HTF Reynolds number leads to an increase in entropy generation but also to an increase in the absorbed mass at the interface and in the recovered heat of the HTF as shown in Table 3.4.

Table 3.4: Evolution of the entropy generation, absorbed mass flow and heat exchanged with the HTF Reynolds number

Re_{htf}, -	$\dot{S}$, $W.K^{-1}.m^{-1}$	$\dot{M}_{abs}$, $kg.m^{-1}.s^{-1}$	$\dot{Q}_w$, $W.m^{-1}$
500	0.09	0.35×10^{-3}	1573
1000	0.11	0.42×10^{-3}	1820
2000	0.13	0.47×10^{-3}	2000
5000	0.2	0.65×10^{-3}	2600

The results show that under the study conditions, entropy generation is mainly produced within the film with 36% of the total entropy generation for Re_{htf} = 2000 against 47% for Re_{htf} = 5000, largely due

to thermal irreversibilities. The mass irreversibilities remains low as its contribution is only about 12% for Re_{htf} = 2000 and 15% for Re_{htf} = 5000 due to the low penetration zone.

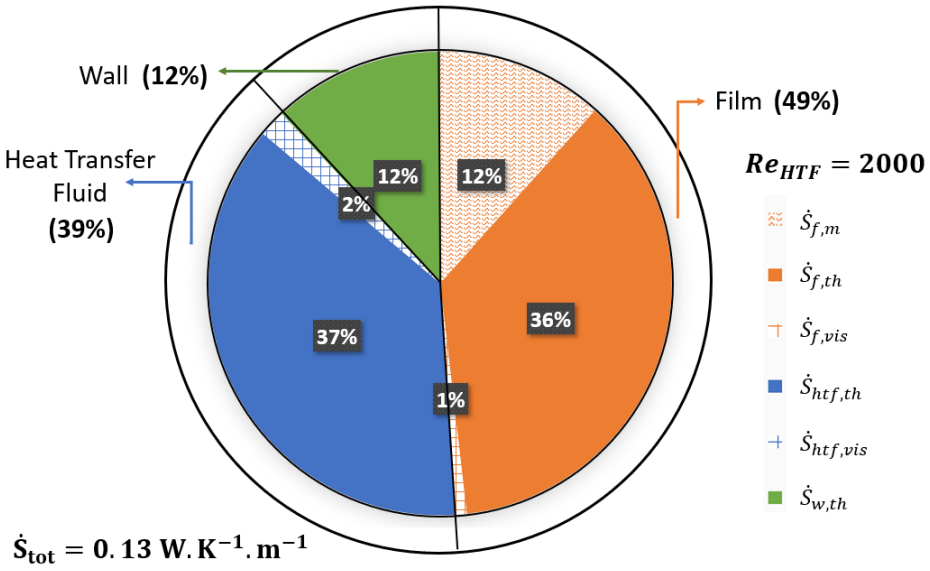

Figure 3.11: Contribution of each entropy generation source to the total entropy generation for Re_{htf} = 2000

Consequently, the contribution of irreversibilities produced within the HTF and the wall must be taken into consideration as they represent 51% of the total entropy generation for Re_{htf} = 2000 and 37.5% for Re_{htf} = 5000. However, the higher the HTF Reynolds number, the lower the contribution of thermal irreversibilities – 37% against 5% for Re_{htf} = 2000 and Re_{htf} = 5000 respectively – and the higher the contribution of the viscous irreversibilities produced within the HTF – 2% against 16.5% for Re_{htf} = 2000 and Re_{htf} = 5000 respectively. The decrease of the thermal irreversibilities contribution within the HTF is due to the low temperature gradient.

Moreover, increasing the HTF Reynolds number, significantly increases the thermal irreversibilities within the film due to the low thermal resistance. The thermal irreversibilities through the wall also increases with the increase in the HTF velocity due to the increase in heat exchanged. For the two limit cases, it is customary to study only irreversibilities within the film to gain an overall understanding of local phenomena induced during the absorption process and their impact on entropy generation. However, this does not properly address real cases due to the high contribution of irreversibilities within the HTF and wall to the component entropy generation. For real absorber cases, the HTF and its contribution to entropy generation has to be considered.

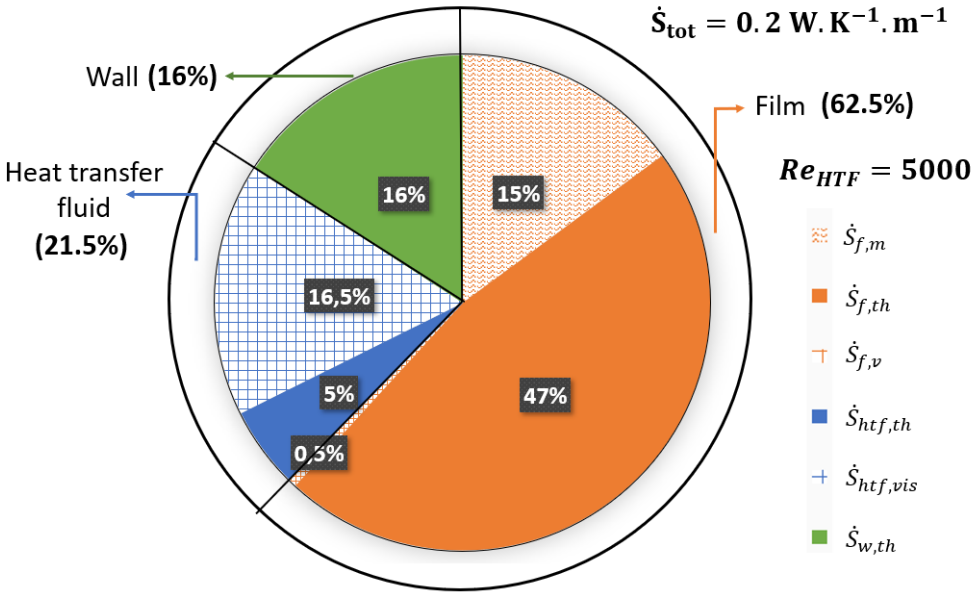

Figure 3.12: Contribution of each entropy generation source to the total entropy generation for Re_{htf} = 5000

Conclusions

In the present chapter, the thermodynamic of irreversible processes has been applied to determine local volumetric entropy generation based on the contribution of different irreversibilities sources. The entropy generation sources have been analysed to better understand their origin and behaviour. Unlike to the chapter II where the entropy generation was found to be higher in the HTF for a falling film evaporator, the analysis shows that in a falling film absorber, the main entropy generation is produced in the film. Some differences have been observed when assuming a laminar and turbulent HTF flow, mostly at the bottom of the absorber. Indeed, an increase of the local phenomenon is observed at the bottom of the absorber due to the thermal boundary development in the HTF and to the small temperature gradient observed at the end of the absorber at low HTF Reynolds numbers.

The thermal phenomenon seems to play a major role on the entropy generation compared to the mass phenomenon due to the low diffusion of the water into the solution. The thermal phenomenon represents more than 90% and 80% of the overall entropy generation for Re_{htf} = 2000 and Re_{htf} = 5000 respectively under the studied conditions. However, no parametric analysis has been performed to study the impact of the operating conditions on the local irreversibilities. This is the focus of the first part of the chapter IV.

CHAPTER IV

Chapter IV. Second law analysis and multi-objective optimization of a falling film absorber

Based on:

Article: Mahamoudou, Le Pierrès and Ramousse. Second law analysis and multi-objective optimization of a falling film absorber. Submitted to International Journal of refrigeration on September 19th 2022.

4.1. Introduction

After having understood the physical phenomena that take place in the absorber and their impact on the performance of the component and on the entropy generation (as detailed in chapter III), this chapter is dedicated to the parametric analysis and optimization of the absorber.

Based on the literature review performed in chapter I, it is clear in the context of this research, that improving the performance of the absorber will significantly improve the overall absorption machines. Indeed, in the perspective of optimizing the absorption machines, Giannetti et al (2016) explained that the system performance can be improved by acting on a single device irreversibilities, in this case, the device in question is the absorber.

As for now, there are no studies in the literature that have addressed multi-objective optimization (MOO) of a falling film absorber. The objective here is to study all the design and operating variables of falling film absorbers with the aim of maximizing the useful effect (either the absorbed mass flow rate or the recovered heat through the wall) while minimizing the entropy generation in a perspective of improving the absorber performance.

This chapter is divided into three main parts. The first part focuses on understanding the impact of the variables on the different type of irreversibilities encountered on the absorber, the second part introduced the equilibrium factor to analyze the impact of different fluid flow rate ratios on the absorber performance while the last part is dedicated to the multi-objective optimization to determine the Pareto Front.

4.2. Problem description and resolution

In the film, both energy and mass balances are simultaneously solved considering a laminar falling film (Re_f = [5, 120]). The heat transfer fluid can either be in laminar (Re_{htf} < 2300) or turbulent (Re_{htf} > 4500) flow regimes. The transition flow regime (2300 < Re_{htf} < 4500) is not studied in this paper due to the lack of relevant correlations. In the Section 4.4.1 and 4.4.3, only the turbulent flow regime – 5000 < Re_{htf} < 10000 – is considered for the HTF, to represent realistic cases (Medrano and al 2002; Perier-Muzet and Stutz 2021). However, the laminar flow regime is investigated in Section 4.4.2.

The equations and resolution of the numerical problem are the same as those presented in chapter III section 3.2. The resolution of the problem presented in chapter III allows obtaining the temperature, concentration and velocity fields in the film, the temperature and velocity fields in the HTF and the temperature field in the wall. From these values, local entropy generation, absorbed mass flux and heat flux can be calculated. Therefore, the overall falling film absorber entropy generation $(\dot{S})$, absorbed mass flow rate ($\dot{M}_{abs}$) and recovered heat ($\dot{Q}_w$) are obtained by integrating the local values.

4.3. MOO: Definition of the design variables and objective functions

4.3.1 Design variables and operating conditions

In the present study, there are six independent variables that impact absorber performance. The influence parameters of these kind of absorbers are, namely:

- the operating conditions: HTF and film Reynolds numbers, inlet HTF temperature, vapor pressure.
- the design parameters: absorber length and wall thickness.

The chosen ranges for each variable are shown in Table 4.1 based on typical operating conditions of absorbers in absorption machines (Michel, Le Pierrès, and Stutz 2017; Perier-Muzet and Stutz 2021). The inlet conditions of the solution are kept constant (the film enters the absorber at $C_{LiBr,in}$ = 60% and $T_{f,in}$ = 45.6°C) and equilibrium condition along the whole film interface $\left(P_{vap} = P_{eq,f}\left(T_f, C_{LiBr}\right)\right)$.

Table 4.1: Chosen design variables of the absorber

variables	From	To
HTF Reynolds number, (-)	50	10000
Film Reynolds number, (-)	5	120
Inlet HTF temperature, (°C)	30	38
Vapor pressure, (kPa)	0.8	1.2
Absorber length, (m)	0.3	0.8
Wall thickness, (m)	0.0002	0.003

For the study of the absorber phenomena – Section 4.4.1, and for the implementation of the MOO model – Section 4.4.3, only the turbulent flow regime – from 5000 to 10000 – is considered for the HTF to represent realistic cases (Medrano and al 2002; Perier-Muzet and Stutz 2021). In order to extent the analysis of the equilibrium factor on the absorber behavior, laminar flow regime is also investigated in Section 4.4.2. The objective functions considered on the MOO model are introduced in the following section.

4.3.2 Definition of the objective functions

As explained, the minimization of the entropy generation while maximizing the useful power is most of the time antagonistic in thermodynamic of a finite size (Kaushik, Tyagi, and Kumar 2017). To optimize the absorber, the objective functions are defined with the aim of maximining the thermodynamic absorber performance while maximizing the useful power ($\dot{Q}_W$ or $\dot{Q}_{int}$). Indeed, Maximizing the released heat at the interface means maximizing the absorbed mass flow rate. Thus, the objective functions are defined with the aim of minimizing the entropy generation $\left(\dot{S}\right)$ of the absorber while maximizing the useful effect – either the absorbed mass flow rate or the recovered heat.

The advantage of the MOO method is that it allows obtaining not only one but various best solutions. The obtained solutions could each be the ideal solution, depending on other priority. These best solutions are known as Pareto front. Indeed, the Pareto Front represents the front of all the solutions that cannot be dominated, which means where no objective can be improved without deteriorating another one (Ranajeet et al. 2017). The MOO problem is solved using two different methods in the following. First, a discrete MOO resolution of the objective functions was obtained by considering discrete values of the design variables and looping to get as many cases as possible. All $\dot{M}_{abs}$, $\dot{Q}_w$, $\dot{S}$ obtained values were plotted and a non-dominated definition of pareto front was used to determine the ideal solutions (L. Wang, Ng, and Deb 2011; Zio and Bazzo 2011). Thus, with this first method, both non-dominated and dominated solutions are represented. The second method is to solve the MOO problem by applying one of the most popular MOO algorithms which is the non-dominated sorting genetic algorithm II (NSGA II) (Yusoff, Ngadiman, and Zain 2011). NSGA II is a numerical optimization

technique based on population. With this second method, the Pareto front is directly obtained. In all simulations, the population size was chosen to be equal to 60, with a crossover probability of 0.6 and mutation probability of 0.08. This method gives a rather larger distribution of the design variables on their interval whereas with the discrete method, there are only localized solutions – to have a distribution similar to the one given by the NSGA II method, it is necessary to increase the discretization step of the intervals. However, the computational time is much longer. The discrete method is a very tedious method because the probability of finding optimal solutions is very low and requires a small discretization of the intervals, i.e. a large number of iterations. The NSGA II method allows to directly obtain the Pareto front. This method minimizes the data processing; however, it can require a lot of iteration due to the number of population and generation that has to be considered.

4.4. Results and discussions

As mentioned before, the results section is divided in three parts. The first part aims to study and analyze the different phenomena and irreversibilities encountered in absorber, the second part is based on the analysis of the absorber behavior at component scale by introducing an equilibrium factor between the film and HTF Reynolds numbers, while the last part addresses the MOO model for optimization.

4.4.1 Parametric analysis of the different sources of irreversibilities

In this first part of the results section, the entropy generation is analyzed with the aim of understanding how operating parameters impact the irreversibilities. The design parameters have been set equal to 0.8 m and 0.003 m for the absorber length and wall thickness respectively and the vapor pressure to 1 kPa.

In order to analyze the impact of the operating conditions on the entropy generation, the behavior of the absorber is studied for a targeted absorption rate of 0.001 $kg \cdot m^{-1} \cdot s^{-1}$ ($\pm$ 1%) of the refrigerant. Here, only the HTF and film Reynolds numbers and HTF inlet temperature were modified to achieve the targeted absorbed mass flow rate.

The absorbed mass flow rate is a result of the model, thus, in order to have the parameters that allow to obtain the target absorbed mass flow rate, a parametric analysis was performed. Four case studies are selected and gathered in Table 4.2. From Case 1 to Case 2, the HTF inlet temperature and Reynolds number were fixed and a parametric analysis was performed on the film Reynolds number.

From Case 1 to Case 3 and from Case 1 to Case 4, decreasing the HTF inlet temperature to 32°C or increasing the HTF Reynolds number to 10 000 increases the heat transfer from the film to the HTF and consequently, the temperature gradient between the HTF and the film interface increases allowing the absorbed mass flow rate to increase. Thus, in order to obtain the target absorbed mass flow rate, the Reynolds number of the film must be decreased: a parametric analysis was performed to obtain the corresponding value of the film Reynolds number.

Table 4.2: Design variables to achieve an absorbed mass flow rate of 0.001 kg.m^{-1}. s^{-1}, In bold the modified variables and in italics those impacted to reach the target of the absorbed mass flow.

	Case 1	Case 2	Case 3	Case 4
$T_{htf,in}$, (°C)	35	35	32	35
Re_{htf}, (-)	5000	5000	5000	10000
Re_f, (-)	60	80	20	50

The objective here, is to understand the impact of these different case studies on the different phenomena by analyzing Table 4.3 and Figure 4.2. In the film, the irreversibilities are divided in three contributions: thermal, mass and viscous irreversibilities while in the HTF, only thermal and viscous irreversibilities are observed. As the wall is impermeable, only thermal irreversibilities can be observed as explained in chapter III. Figure 4.2 allows evaluating the contribution of the above-mentioned irreversibilities while Table 4.3 shows the distribution of irreversibilities between the different medium of the absorber, namely, the HTF, wall and film for the four case studies. As in chapter III, the main irreversibilities of the absorber are in the film and are dominated by thermal irreversibilities followed by mass irreversibilities. The contribution of the viscous irreversibilities of the film on the overall entropy generation is negligible: less than 0.5% for the four cases.

Table 4.3: Repartition of the entropy generation through the HTF, wall and film to achieve an absorbed mass flow rate of 0.001 kg. s^{-1}.m^{-1}

	Case 1	Case 2	Case 3	Case 4
Film irreversibilities, (W.K^{-1}.m^{-1})	0.176	0.198	0.170	0.172
Wall irreversibilities, (W.K^{-1}.m^{-1})	0.040	0.044	0.037	0.039
HTF irreversibilities, (W.K^{-1}.m^{-1})	0.068	0.070	0.068	0.28
Total, (W.K^{-1}.m^{-1})	0.284	0.312	0.275	0.491
		+9.8%	-3.2%	+72%

A difference of entropy generation of 78% between cases 3 and 4 is observed – the highest and lowest entropy generation among the four case studies. In the following, the different case studies are compared to case 1. The entropy generation in case 1 is 0.284 W.K^{-1}.m^{-1} of which more than 62% is due to irreversibilities in the film where both heat and mass transfer occur, while the HTF and the wall contribute for 24% and 14% respectively.

From case 1 to case 2, only the film Reynolds number is changed – it is 33% higher. Results show an increase, mainly, of the film irreversibilities leading to an increase of the overall entropy generation of about 9.8%. The increase of the film irreversibilities is due to an increase of the film thermal

irreversibilities: the thermal resistance in the falling film (e_f/λ_f) increases as the film thickness increases - caused by the increase the film Reynolds number from 60 to 80 (for free surface flow, increasing the film Reynolds number leads to an increase in film thickness and vice versa. However, this is not true for a flow in a channel for example). This increase of thermal resistance leads to a decrease of the driving concentration gradient between the interface and the film and consequently to the decrease of the mass irreversibilities (Fig.4.2).

As shown for case 3, a decrease of the HTF temperature increases the temperature gradient between the HTF and the film. Consequently, the heat transferred from the film to the HTF and the absorbed mass flow rate at the interface increase. Thus, to maintain the target of 0.001 kg· s^{-1}·m^{-1} of absorbed mass flow rate, the solution Reynolds number has to be reduced and consequently the entropy generation also decreases (3.2%). Indeed, decreasing the inlet HTF temperature allows reducing the film thermal irreversibilities and increasing the mass irreversibilities and HTF thermal irreversibilities. The HTF viscous irreversibilities is not affected as Re_{htf} is not changed. The decrease of the film thermal irreversibilities is mainly due to the decrease of the film Reynolds number allowing to decrease the thermal resistance within the film as the film thickness decreases. However, the wall and HTF thermal irreversibilities increase as the temperature gradients between the HTF and the film increase.

Case 4 show that an increase of the HTF Reynolds number allows reducing the film Reynolds number compared to case 1 as the increase of the HTF Reynolds number increases the heat transferred through the wall and thus increases the driving concentration at the interface: the absorbed mass flow rate increases. The increase of the HTF Reynolds number leads to a significant increase of the HTF irreversibilities – almost five times as much as for case 1. However, it allows reducing both film and wall irreversibilities but not enough to reduce the overall entropy generation. The increase of the HTF Reynolds number leads to a decrease of the film thermal resistance as the film Reynolds number is reduced and thus, the film is thinner. However, a significant increase of the HTF viscous irreversibilities is observed due to the increase of fluid friction. Increasing the HTF Reynolds number also leads to a smaller temperature gradient within the HTF due to the high convective phenomenon encountered in turbulent flow, and consequently, to a decrease of the HTF thermal irreversibilities.

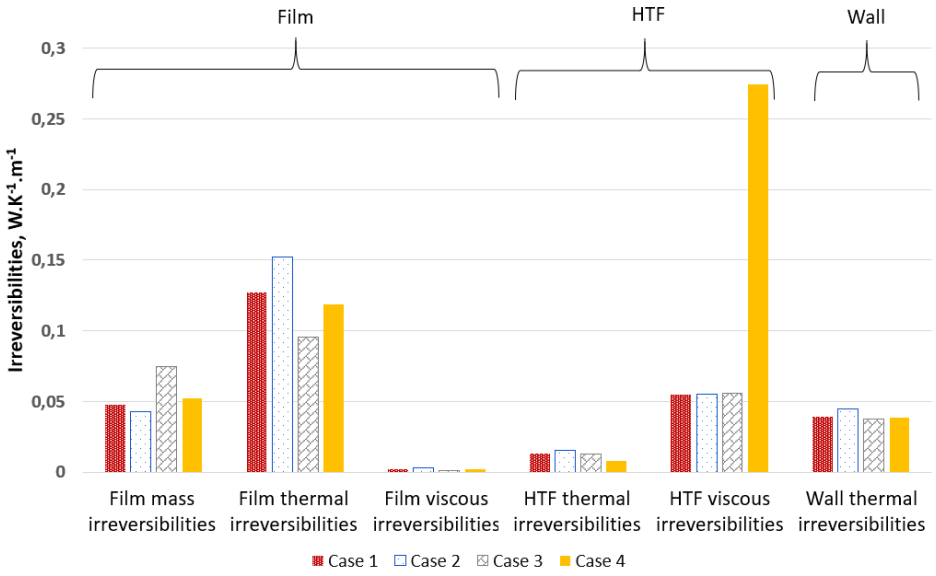

Figure 4.2: Evolution of the different types of irreversibility within the absorber

As a conclusion of this study, to decrease the entropy generation of an absorber, the focus should be on decreasing the film irreversibilities – mainly the film thermal irreversibilities – without increasing the HTF ones – mainly the HTF viscous irreversibilities. To do so, a compromise between the HTF and

film Reynolds number must be found. However, this compromise may be complicated to find as the different irreversibilities sources are coupled.

4.4.2 Impact of the HTF and film Reynolds numbers on the absorber performance at component scale

As in Section 4.4.1, the design parameters have been set equal to 0.5 m and 0.003 m for the absorber length and wall thickness respectively and the vapor pressure to 1 kPa. To study the impact of the HTF and film Reynolds numbers on the absorber performance, the equilibrium factor defined by Altamirano (2021) and Perier-Muzet and Stutz (2021) can be used. It provides engineers with working flow ratios between the two fluids to achieve a certain absorber performance. Thus, according to Perier-Muzet and Stutz (2021), the equilibrium factor is defined as "the ratio between the maximum transferable heat flux of the heat transfer fluid and the maximum transferable heat flux of the solution" as in equation (4.4):

$$\mathrm{R} = \frac{\dot{Q}_{htf,max}}{\dot{Q}_{f,max}} = \frac{\dot{m}_{htf}[h_{htf,out}(T_{max}) - h_{htf,in}]}{\dot{m}_{f,in}h_{f,in} - \dot{m}_{f,out,iso}h_{f,out,iso}(T_{htf,in}, C_{LiBr,out,iso}) + \dot{M}_{abs,iso}\Delta H_{abs}} \quad (4.4)$$

Where $T_{max} = T_{f,in}$ as the film is assumed to enter the absorber at equilibrium condition.

In the following, the absorbed mass flow rate, transferred heat and entropy generation are studied to evaluate their evolution for different values of HTF and film Reynolds number using the equilibrium factor defined in equation (4.4). The HTF inlet temperature is assumed equal to 30°C while the film Reynolds numbers ranges from 10 to 120 and the HTF Reynolds number ranges from 50 to 10000. Figure 4.3 shows the absorbed mass flow rate and the transferred heat versus the equilibrium factor for different values of film Reynolds number.

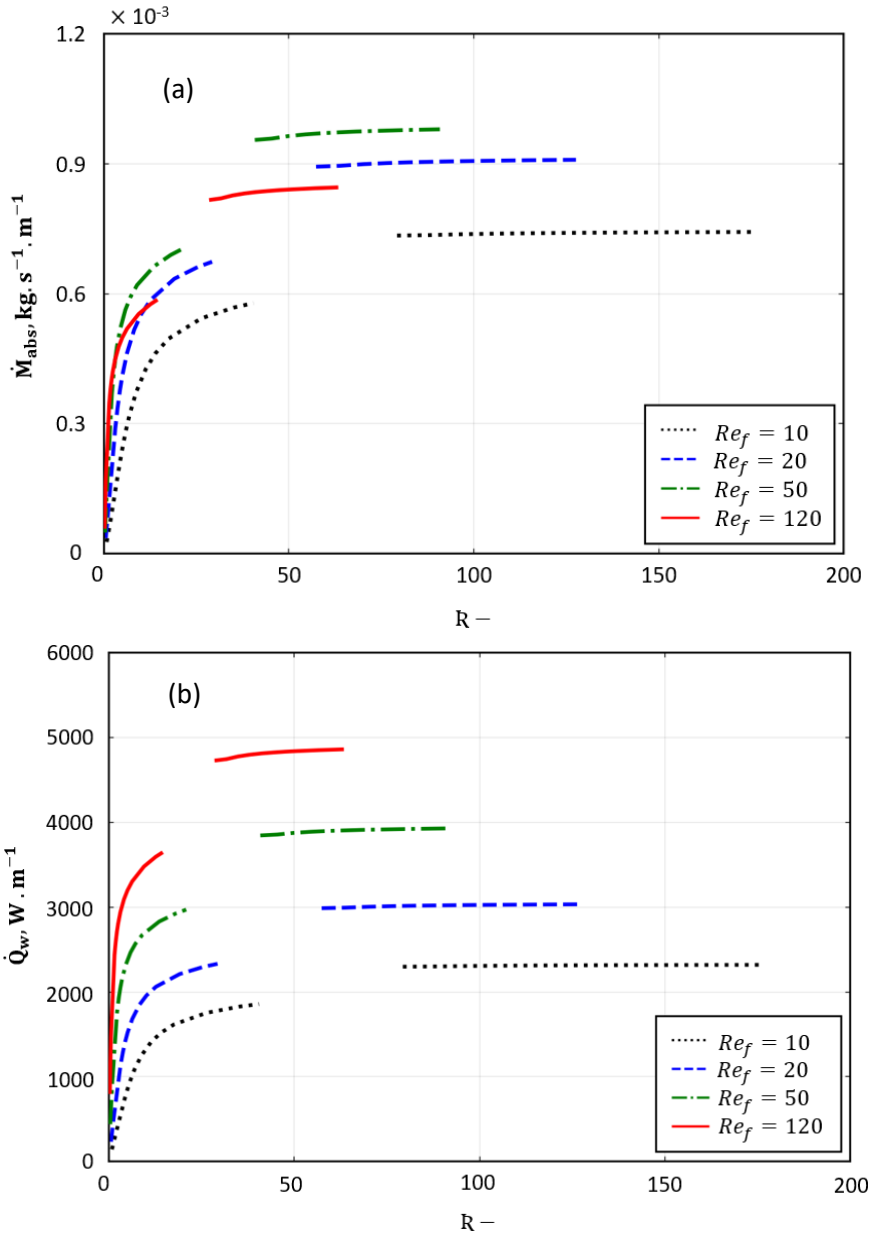

Figure 4.3: Absorbed mass flow rate (a) and transferred heat (b) for different solution inlet and HTF Reynolds numbers in counter-flow configuration.

As in Perier-Muzet and Stutz (2021), both figures – figures 4.3.a et 4.3.b – show the two limit cases of an absorber, namely the adiabatic and isothermal absorbers. For an adiabatic absorber, the heat released at the film interface by the exothermic absorption is not removed (the absorbed mass flow rate is thus the lowest) while for an isothermal case, the heat released at the film interface is removed by a heat transfer fluid with an infinite flow rate to keep the HTF temperature constant (the absorbed mass flow rate is thus the highest). Thus, when the ratio Ʀ tends to zero, the absorber is adiabatic (Re_{htf} = 0) while it works like an isothermal absorber (Re_{htf} = ∞) when the ratio tends to infinity. Therefore, the increase of Ʀ is due to an increase of the Re_{htf} and thus to an increase of the $\dot{Q}_{htf,max}$ as for a given film Reynolds number $\dot{Q}_{f,max}$ remains constant.

Figure 4.3.a shows the increase of the absorbed mass flow rate with the increase of the equilibrium factor because of the increase of the transferred heat as shown in figure 4.3.b. The increase of the transferred heat (due to the increase of the HTF Reynolds number and thus, to the HTF heat capacity) allows, in one hand, reducing the outlet temperature of the solution and in other hand, increasing the driving concentration gradient between the interface and the film. Consequently, the increase of the equilibrium factor caused by the increase of the HTF Reynolds number leads to the increase of the absorbed mass flow rate for a given film Reynolds number.

As expected, a gap is observed between the laminar and turbulent flow regimes for the absorbed mass flow rate and the transferred heat for a given film Reynolds number. Indeed, the convective heat transfer coefficient significantly increases from laminar to turbulent flow. The increase of this convective coefficient reduces the thermal resistance between the film and the HTF and consequently, allows increasing the transferred heat through the wall. The increase of the transferred heat reduces the film temperature and thus, increases the driving concentration gradient between the film and the interface leading to a significant increase of the absorbed mass flow rate.

The observed gap appears earlier when increasing the film Reynolds number due to the increase of the maximum transferable heat in the solution leading to a decrease of the equilibrium factor, $\mathcal{R}$ (see the definition of the $\mathcal{R}$ factor, equation (4.4)). Moreover, the impact of the HTF Reynolds number, in turbulent flow regime, on the absorbed mass flow rate and on the recovered heat is not as significant as it is in laminar flow regime. Indeed, in turbulent flow regime – under the studied conditions – the limiting flow is the solution as $\mathcal{R} > 1$ and thus the thermal resistance within the HTF is low compared to the other transfer resistances as shown when analyzing the irreversibilities sources – Figure 4.2: the lower the HTF Reynolds number, the higher the thermal irreversibilities associated and the higher its impact on the absorbed mass flow rate and recovered heat.

As in Perier-Muzet and Stutz (2021), an optimal film Reynolds number for the absorbed mass flow rate (figure 4.3.a) is observed due to the two antagonist phenomena produced when increasing the film Reynolds number. Indeed, the increase of the latter tends to increase, on the one hand, the absorption phenomenon at the film interface due to the thickening of the mass boundary layers. On the other hand, it increases the thermal resistance between the interface and the heat transfer fluid (due to the increase of the film thickness) and consequently, leads to a decrease of the chemical potential difference between the interface and the film. That last observation confirms the difficulties particularly encountered for absorption chillers optimization without using a MOO.

For turbulent flow regime, the optimal Reynolds number observed is between 20 and 120 for the conditions considered in this study, while for laminar flow regime, two different scenarios are observed. When $\mathcal{R} < 2.7$, the optimum film Reynolds number is 120: the absorbed mass flow rate increases with the increase of the film Reynolds number (figure 4.4). When $\mathcal{R}$ ranges from 2.7 to 2300, the optimum film Reynolds number is 20 and 120 (for the studied cases). However, the study of the transferred heat with the equilibrium factor does not show an optimum value: the heat transferred from the film to the HTF increases with the increase of the HTF Reynolds number (as the HTF heat capacity increases) and with the film Reynolds number. The entropy generation is also impacted by both film and HTF Reynolds number as shown in Figure 4.5.

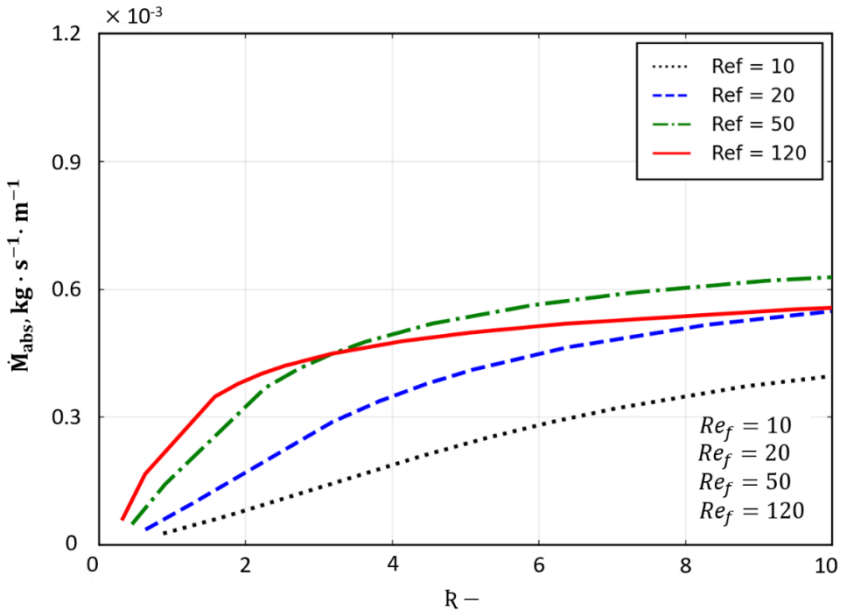

Figure 4.4: Zoom of figure A-1 (a) Entropy generation versus the equilibrium factor R and the inlet solution Reynolds number

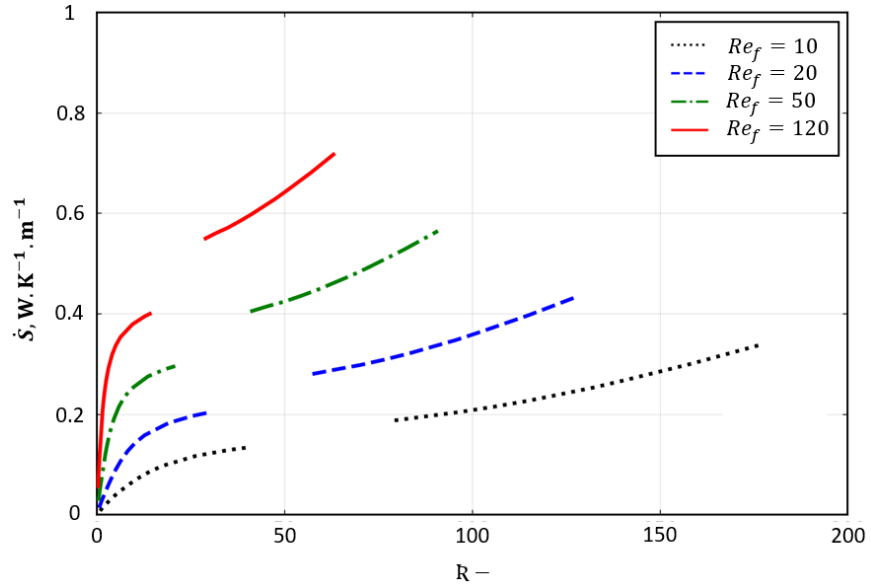

Figure 4.5: Entropy generation versus the equilibrium factor R and the inlet solution Reynolds number

The analysis shows that the overall entropy generation increases with the increase of the film and HTF Reynolds number as explained in Section 4.4.1. However, the entropy generation is concave when the HTF is in laminar flow regime while it is convex when the HTF is in turbulent flow regime. This is mainly linked to the behavior of the HTF irreversibilities between these two flows. Indeed, in turbulent flow regime, the contribution of the viscous entropy generation is high compared to the thermal irreversibilities contribution (Table 4.3).

Moreover, this increase of the viscous irreversibilities contribution on the entropy generation makes the second derivative of the overall entropy generation negative in the turbulent regime, whereas for small Reynolds numbers of the heat transfer fluid, the second derivative of the overall entropy

generation is positive due to the small viscous contribution. In conclusion, the viscous phenomenon plays a major role on the performance of the absorber. As in Figure 4.3.b, the analyzes of the figure 4.5 shows that the entropy generation cannot be minimized when increasing either the film or the HTF Reynolds numbers. Moreover, the gap between the laminar and turbulent flow regimes increases with the increase of the film inlet flow rate. As shown in the previous paragraph, the increase of the film inlet flow rate is associated to a significant increase of the film thermal irreversibilities that rises the overall entropy generation produced.

4.4.3 Multi-objective optimization (MOO)

In this section, results of the MOO are presented. The optimization results are showed in Figure 4.6. The Pareto front of the $\dot{M}_{abs}$ versus the entropy generation $\dot{S}$ is reported in figure 4.6.a while the one obtained for $\dot{Q}_{abs}$ versus $\dot{S}$ is given in Figure 4.6.b. The Pareto front is shown along with all solutions explored by both methods, namely the dominated solutions (blue dots) and the optimal solutions (red squares or black stars). The analysis of these figures shows that the NSGA-II model (red squares) does not cover all the Pareto solutions obtained with the discrete method (black stars), this can be explained by the limited number of generations set up to only 30. The number of generations in this study is set to 30, as the population is set to 60, due to the large computational time need to calculate the local temperature and concentration in the HTF, film and wall (one simulation takes more than 50 minutes to be done). However, both MOO methods give similar trend of the Pareto front. Figure 4.6 shows the possibility of minimizing the entropy generation while increasing the absorbed mass flow rate or transferred heat.

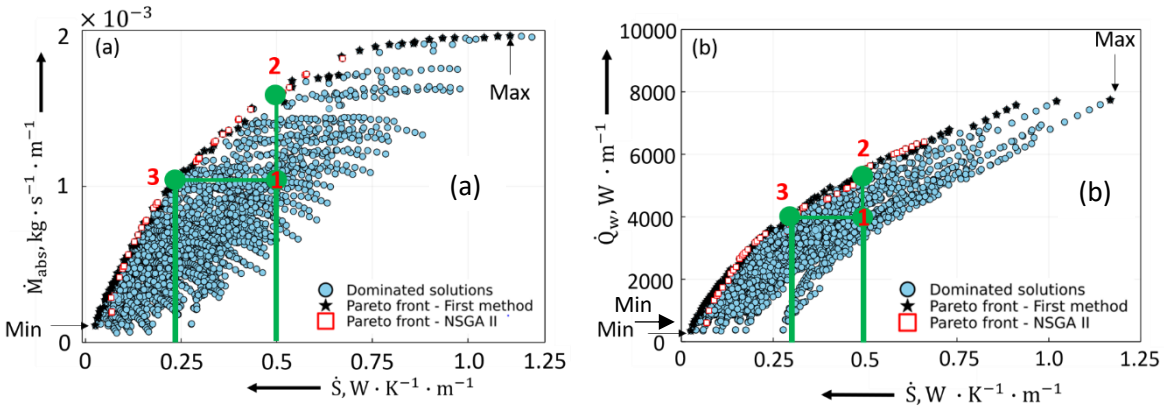

Figure 4.6: Multi-objective Pareto results for $\dot{M}_{abs}$ and $\dot{S}$ of optimal design points (a), for $\dot{Q}_W$ and $\dot{S}$ of optimal design points (b)

For the Pareto front solutions, the useful effect (the absorbed mass flow rate/ recovered heat) and the entropy generation are conflicting; an increase of the useful effect is accompanied by an increase of entropy generation (red squares or black stars) meaning that the minimal entropy generation is achieved for the lowest useful effect ($\dot{Q}_W$ or $\dot{M}_{abs}$). Moreover, analysis of Figure 4.6.a blue dots shows that the evolution of the absorbed mass flow rate with the entropy generation follows parabolic profiles. That highlights the existence of optimal design variables which allow to achieve maximal absorbed mass flow rate. Explanation about this optimal value is given in Section 4.4.3.1. However, this trend is not observed when analyzing the evolution of the recovered heat as a function of the entropy generation (Figure 4.6.b).

The design variables that give the minimal and maximal values of the Pareto fronts (see Min and Max points in figures 4.6.a and 4.6.b) for both type of absorbers are gathered in Table 4.4. The latter shows that the maximum absorbed mass flow rate and recovered heat are obtained when considering the maximum HTF Reynolds number, vapor pressure, absorber length and the minimal wall thickness and

HTF inlet temperature. The min, max and opt mentioned in Table 4.4 represented the minimal, maximal and optimal values of the variable range with respect to those given in Table 4.1. Moreover, the maximum recovered heat is obtained with the maximal film Reynolds number considered while to reach the maximum absorbed mass flow rate, an optimal film Reynolds number is obtained and is equal to 100 under the studied conditions. This result confirms those obtained during the analysis of the absorber performance with the equilibrium factor – see Section 4.4.2.

The longer the absorber, the higher the absorbed mass flow rate and recovered heat. This was expected as longer absorber offers higher exchange surface. However, some constraint such as cost, size and stability of the falling film stability (wettability) will have to be also considered before designing the absorber.

Moreover, the lower the wall thickness, the higher the useful effects. Indeed, thinner wall allow reducing the thermal resistance between the film and the HTF. However, constraints such as mechanical and strength problems (due to the pressure difference between both fluids) must be considered in order to have thermally efficient wall with good mechanical resistance. As a result, the design parameters of the absorber should be defined at the beginning of the project, taking into account the capacity of the desired absorber, the cost, the space requirement as well as the mechanical properties.

Table 4.4: Design variables for extremal points of the two case studies. The italic min/max/opt values in the table identify if the value is the minimum/maximum/optimal value for the study range defined in Table 4.1

		Heat transformer		Absorption chiller	
	objectives	Min $\dot{S}$	Max $\dot{Q}_w$	Min $\dot{S}$	Max $\dot{M}_{abs}$
Values of the objective's functions	$\dot{Q}_w, (W.m^{-1})$	350	7741	*350*	*7422*
	$\dot{M}_{abs}, (kg.s^{-1}.m^{-1})$	*0.0001*	*0.00195*	0.0001	0.00196
	$\dot{S}, (W.K^{-1}.m^{-1})$	0.026	1.17	0.026	1.11
Design variables	HTF Reynolds number, (-)	5000 *(min turbulent)*	10000 *(max)*	5000 *(min turbulent)*	10000 *(max)*
	Film Reynolds number, (-)	5 *(min)*	120 *(max)*	5 *(min)*	100 *(opt)*
	Inlet HTF temperature, (°C)	38 *(max)*	30 *(min)*	38 *(max)*	30 *(min)*
	Vapor pressure, (kPa)	0.8 *(min)*	1.2 *(max)*	0.8 *(min)*	1.2 *(max)*
	Absorber length, (m)	0.3 *(min)*	0.8 *(max)*	0.3 *(min)*	0.8 *(max)*
	Wall thickness, (m)	0.0002 *(min)*	0.0002 *(min)*	0.0002 *(min)*	0.0002 *(min)*

In the following, the focus is made on the optimization of the absorber considering the absorber mode mentioned in Section 4.3.2 – either chiller or heat transformer, under the design variables defined in Table 4.1 for the HTF and film Reynolds numbers, the vapor pressure and the HTF inlet temperature. In the following sections, only the Pareto front solutions given by the NSGA II method are discussed.

4.4.3.1 Pareto front analysis for the absorbed mass flow rate (absorption chiller case)

Figures 4.7 and 4.8 illustrate the change of $\dot{M}_{abs}$ and $\dot{S}$, respectively, versus the design variables (only the pareto front solutions are discussed). They show an increase trend of both objective functions with the increase of vapor pressure and film Reynolds number. However, the trend is opposite for the HTF inlet temperature. The analyze of figure 4.6.a shows that the existence of a maximum absorbed mass flow rate (observed in figure 4.6.a) is given by an optimal film Reynolds number. The same observation is found in the absorber analysis performed in Section 4.4.2. Indeed, for the considered conditions gathered in Table 4.1, the absorbed mass flow rate obtained in the Pareto front (Figure 4.7.a), increases with the increase of the film Reynolds number. However, the maximum Re_f observed, under the study conditions, is almost equal to 100 as shown in Table 4.4: beyond Re_f = 100, the absorbed mass flow rate is not on the Pareto front. This is explained by a decrease of the absorbed mass flow rate and an increase of the entropy generation when further increasing the film Reynolds number due to the two antagonist phenomena explained in section 4.4.2. Consequently, beyond the optimal film Reynolds number, all the solutions obtained are dominated by those located before the optimal film Reynolds number: only the film Reynolds number between 5 to 100 appear on the Pareto front (With the discrete method and between 5 and 75 for the NSGA II method).

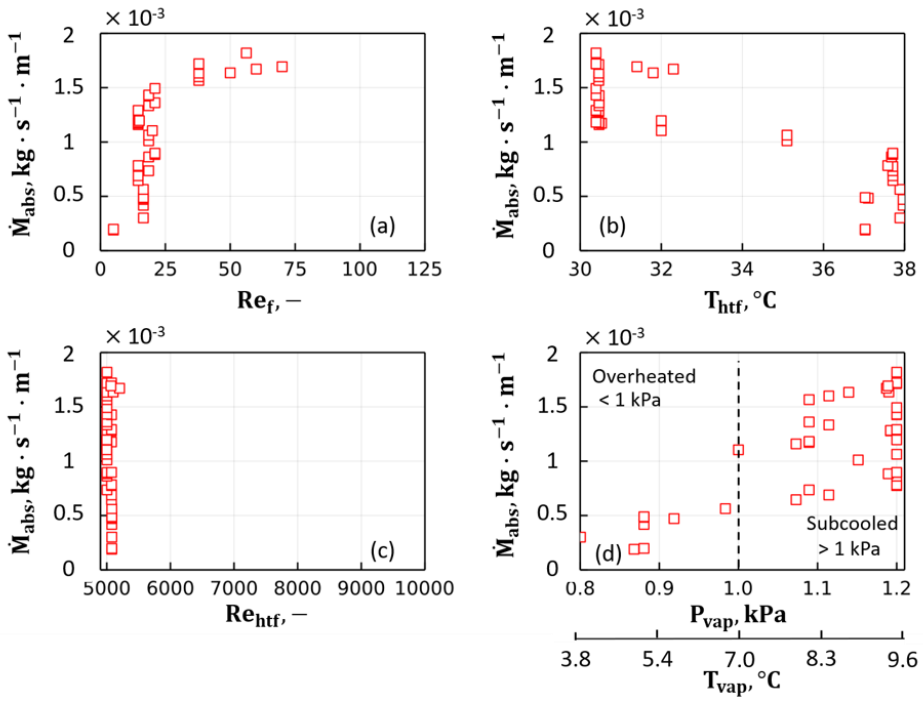

Figure 4.7: Optimal variation of $\dot{M}_{abs}$ with respect to the design variables

The analysis of the entropy generation behavior with the film Reynolds number shows that the increase of the absorbed mass flow rate is associated to an increase of the irreversibilities within the absorber. The higher absorbed mass flow rate is given by the higher entropy generation (for the solutions on the Pareto front).

The absorbed mass flow rate increases with the increase of the vapor pressure when assuming all other variables constant. As the film is assumed to enter the absorber at $C_{LiBr,in}$ = 60%, $T_{f,in}$ = 45.6°C and P = 1 kPa, decreasing the vapor pressure under 1kPa meaning superheated film at the entrance of the absorber compared to the vapor. The solution has to desorb a part of its water in order to reach the equilibrium condition: the absorbed mass flow rate $\dot{M}_{abs}$ decreases when $P_{eq,f}\left(T_{f,in}, C_{LiBr,in}\right) > P_{vap}$

compared to the case where $P_{eq,f}\left(T_{f,in}, C_{LiBr,in}\right) = P_{vap}$. On the other hand, the increase of the vapor pressure leads to the increase of the absorbed mass flow rate as the absorption phenomenon starts before the cooling effect caused by HTF is felt at the interface: the film is subcooled at the entrance of the absorber. Thus, the absorbed mass flow rate $\dot{M}_{abs}$ increases when $P_{eq,f}\left(T_{f,in}, C_{LiBr,in}\right) < P_{vap}$ compared to the case where $P_{eq,f}\left(T_{f,in}, C_{LiBr,in}\right) = P_{vap}$. However, the control of the vapor pressure is needed at the evaporator level, which means that modifying it means modifying the operation of the evaporator and consequently, impacting the entropy generation in this component.

The decrease of the inlet HTF temperature (Figure 4.7.b) leads to an increase of the absorbed mass flow rate as it increases the cooling effect of the solution, allowing to reduces the outlet temperature of the solution.

The analysis of the HTF Reynolds number shows that it is more interesting to work at the limit of the turbulent flow regime: Re_{htf} between 5000 and 5800 as shown in Figure 4.7.c. Indeed, as shown in section 4.4.2, the HTF Reynolds number above 5800 does not have a significant impact on the absorbed mass flow rate in turbulent regime the thermal resistance within the HTF is low compared to the other transfer resistances and on the other hand, the increase of this parameter induces a significant increase of the entropy generation, associated to the increase of the viscous irreversibilities.

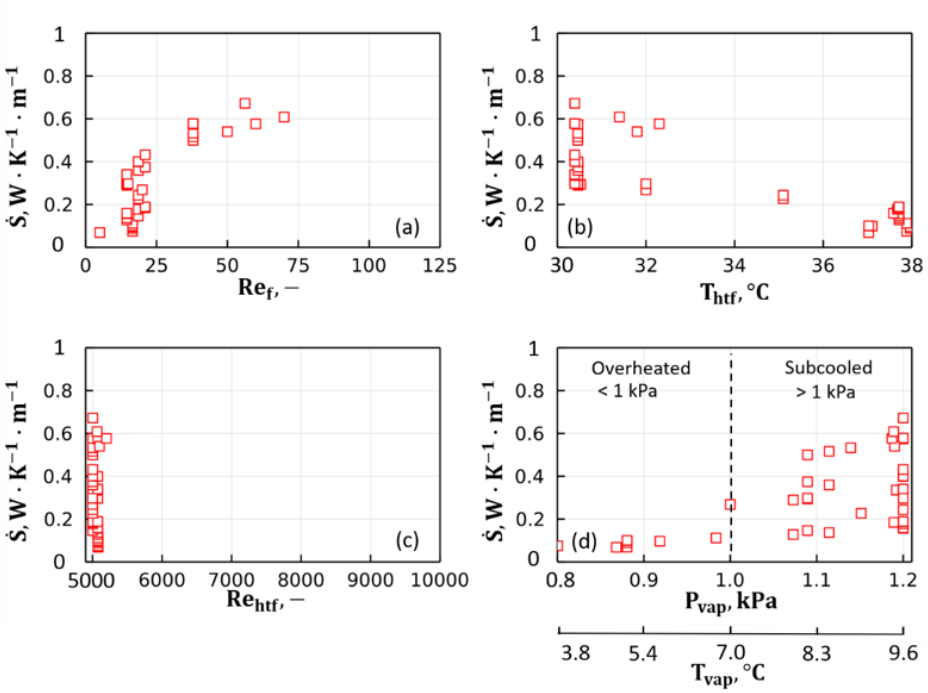

Figure 4.8: Optimal variation of $\dot{S}$ with respect to the design variables

4.4.3.2 Pareto front analysis for the recovered heat (heat transformer case)

Figures 4.9 and 4.10 illustrate the change of $\dot{Q}_w$ and $\dot{S}$ respectively, versus the design variables. As in previous section, the recovered heat increases with the film Reynolds number, HTF Reynolds number and vapor pressure while it decreases with the HTF inlet temperature.

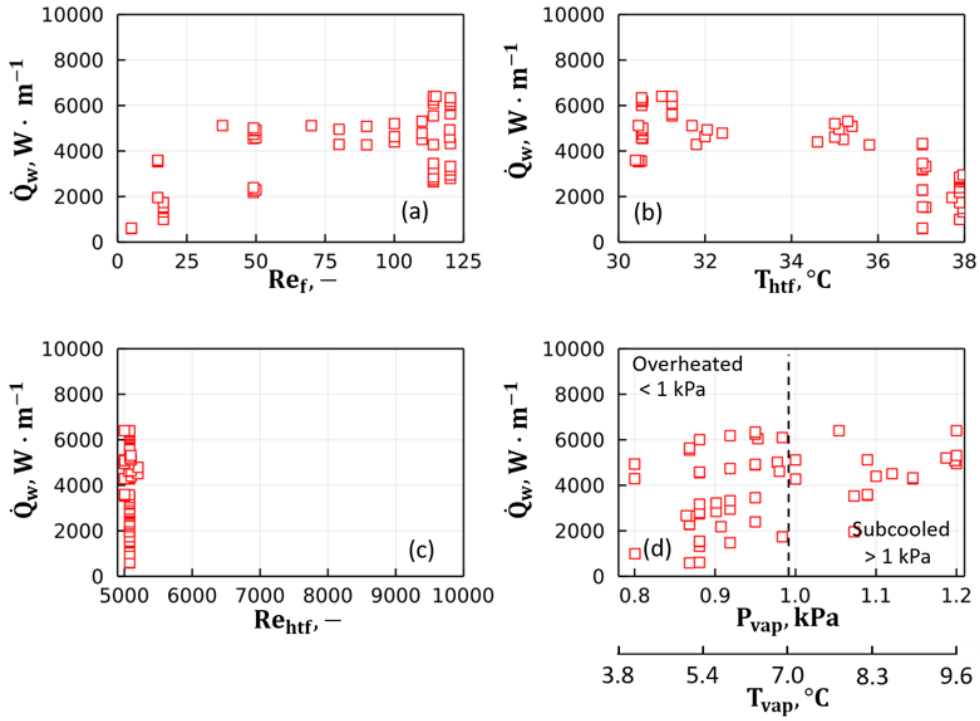

Figure 4.9: Optimal variation of $\dot{Q}_W$ with respect to influence parameters

Unlike the absorbed mass flow rate, the recovered heat does not show the existence of an optimal film Reynolds number (Figure 4.9.a). Indeed, the increase of the film Reynolds number leads to an increase of the recovered heat as it leads to an increase of the heat transfer coefficient between the HTF and the film.

The increase of the vapor pressure impacts the recovered heat (Figure 4.9.d). Indeed, as the film is assumed to enter the absorber at $C_{LiBr,in}$ = 60%, $T_{f,in}$ = 45.6°C and P = 1kPa, if the vapor pressure is lower than the equilibrium inlet film pressure, a desorption phenomenon is observed at the entrance of the absorber. The desorption is an endothermic phenomenon: a part of the energy that could be given to the HTF is used to desorb water from the solution. When the vapor pressure is equal to the equilibrium inlet film pressure (equal to 1 kPa in this study), a part of the energy released during the absorption is used to increase the film temperature while the rest is transferred to the HTF. When the vapor pressure is higher than the equilibrium inlet film pressure, the film is subcooled at the inlet, and then, a high absorption effect is observed even before the cooling effect is felt at the interface. Thus, this increases the heat recovered by the HTF. However, the same conclusion as the one given in Section 4.4.3.1 can be drawn: the vapor pressure cannot usually be used as an absorber optimization parameter as it is imposed by the evaporator.

The impact of the inlet temperature and HTF Reynolds number on the recovered heat (Figures 4.9.b and 4.9.c respectively) are the same as on the absorbed mass flow rate (Section 4.4.3.1).

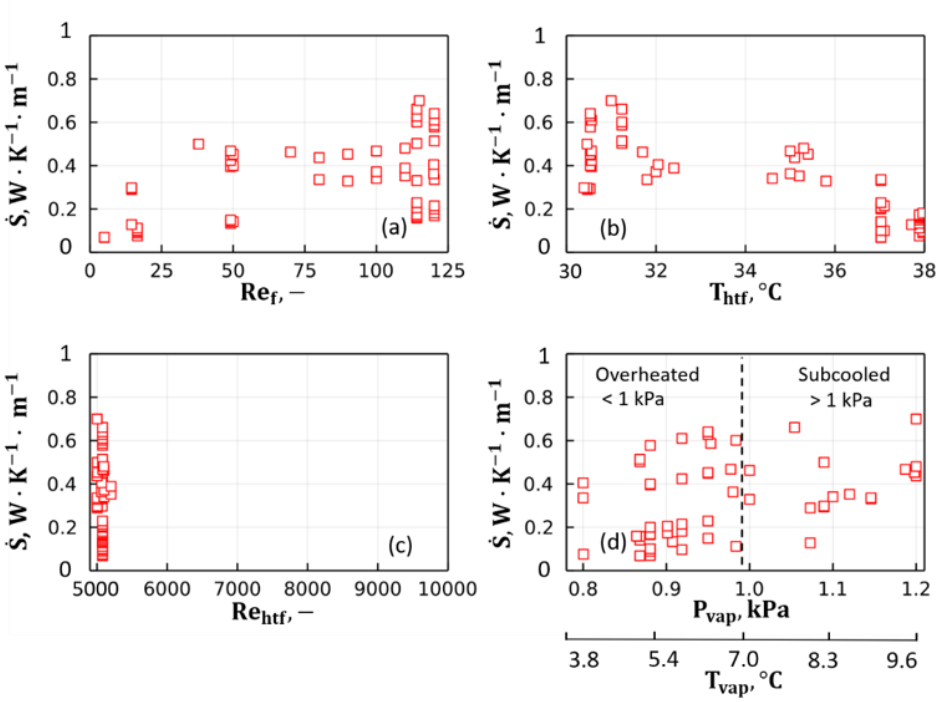

Figure 4.10: Optimal variation of Ṡ with respect to influence parameters

Conclusions

The present work allows to make a parametric analysis of the different design variables of a falling film absorber using the model developed in chapter 3 and to optimize the absorber using a multi-objective optimization (MOO). Firstly, the sources of irreversibilities are analyzed and the impact of the operating conditions, namely, the HTF and film Reynolds numbers but also the HTF inlet temperature on these irreversibilities are investigated. The increase of the HTF Reynolds number and the decrease of the HTF inlet temperature allows reducing the film Reynolds number for a set target. However, the analysis show that the film is the set of the main irreversibilities and they are mainly due to the thermal phenomenon. However, trying to reduce the film thermal irreversibilities has an impact on the other irreversibilities sources: The different types of irreversibilities are coupled and make it difficult to act on a specific source. Thus, the interest of the MOO method to improve the absorber arises. The investigation performed on the equilibrium factor shows that the abacus drawn during this project could be to obtained the ratio between the film and HTF Reynolds numbers to use in real case conditions.

In the second part of this chapter, the different design parameters, namely, the film and HTF Reynolds number, HTF inlet temperature, vapor pressure, absorber length and wall thickness were investigated using two different methods to obtain the Pareto front. It has been shown that the entropy generation can be minimized while maintaining the absorber performance. However, the Pareto front solutions show that the increase of the absorbed mass flow rate and transferred heat is associated to an increase of the entropy generation. In terms of recommendations, it is interesting to work with longer absorber and thinner wall thickness as they allow increasing the absorber performance while minimizing the entropy generation but some constraint such as the cost, size and stability of the falling film but also mechanical and strength problems must be considered during the absorber sizing. For the operating conditions (the HTF and film Reynolds numbers, HTF inlet temperature, and vapor pressure) attention

should be paid as they also depend on the operation of the other components of absorption machines. However, it is recommended to work at lower HTF inlet temperature and higher vapor pressure. Unlike to heat transformers where the maximal recovered heat is obtained at high film Reynolds number, an optimal film Reynolds number is observed for absorption chillers: the MOO is therefore very interesting in the case of chillers as it allows to identify the optimal film Reynolds number. Although the impact of the HTF Reynolds number on the absorbed mass flow rate is important in laminar regime, the HTF Reynolds number in turbulent flow regime does not have a significant impact on the absorbed mass flow rate and recovered heat; however, it significantly impacts the entropy generation due to a high increase of fluid friction. This operating variable must be maintained close to the entrance of the turbulent domain (around 5000-6000).

General conclusions

The interest in the production of low-carbon heat and cold is leading researchers to study more and more absorption machines. These thermodynamic machines are proving to be very good alternatives to traditional compression machines. However, due to their high initial investment cost and their size, research is being conducted to make them as competitive as existing vapour compression systems. Researchers agree that the absorber, which is one of the four main components of these machines, is the key to improving the overall performance of these systems. The application of the thermodynamics of irreversible processes on the absorber is recent and seems to be a good tool to understand the phenomena that occur in it as well as the sources of entropy generation - which is associated to a decrease in the coefficient of performance of the whole system.

Two numerical models have been developed. The first model aims at studying the simple case of a heat exchanger with phase change, i.e. a falling film evaporator (chapter II), while the second model is an extension of the first one and allows to study the more complex case of a heat and mass exchanger with phase change, i.e. the falling film absorber (chapter III and IV). In both cases, the models aim to understand and analyze the different sources of entropy generation. A formulation of entropy generation in the evaporator and in the absorber has been made. The difference between the two models is the existence of an additional irreversibilities due to the mass transfer phenomenon in the falling film in the absorber. Apart of the entropy generation formulation, three main originalities can be found in this thesis (according to the state of the art in Chapter I), namely:

1. The introduction of a non-null and non-infinite flow of heat transfer fluid (in laminar and turbulent regimes) in the study of the absorber behavior: this allows a modeling and simulation of the absorber in realistic study cases.

2. The analysis of the entropy generation in the component, namely the HTF, the wall and the falling film: although the falling film in an absorber seems to be the main seat of entropy generation, it is important to consider the HTF and the wall in order to evaluate their contribution in a perspective of minimizing the overall induced irreversibilities.

3. The link between the analysis of entropy generation at the local and component scales: once the sources of entropy generation are identified, localized and quantified at the local scale, their impact at the component scale has been evaluated.

Several general conclusions are presented here at both local and component scales:

Evaporator

The study of the evaporator was limited to the case of a HTF in laminar flow. Although in industry, the HTF flows generally in a turbulent regime, limiting the problem to the laminar case allows to simplify the problem while having a broad view of the phenomena during the operation of the component. The overall entropy generation increases with the increase of the temperature difference between the free surface and the film at the entrance, and with the increase of the Reynolds number of the HTF for both configurations. The analysis shows that the overall thermal entropy generation is mainly due to the irreversibilities within the HTF followed by those within the film, while the irreversibilities observed through the wall remains negligible – around 2%. The HTF irreversibilities increases with the increase of the HTF Reynolds number while it decreases with the increase of the film Reynold number for both

co and counter flow configurations. Differences between both flow configurations are mainly observed at longer evaporator length. A decrease of the overall entropy generation and of the evaporation mass flow rate is observed when increasing the film Reynolds number due the increase of the thermal resistance between the HTF and the film. To avoid the decrease of the evaporation mass flow for higher film Reynolds number, a higher HTF Reynolds number must be considered. However, other influence parameters must be studied to keep acceptable entropy generation. The impact of the thermal boundary layers on the local phenomena and consequently on the local and thus overall entropy generation has been investigated. The sources of entropy generation in falling film evaporator are the fluid friction and the temperature gradient. The local viscous entropy generation of the film and of the HTF are almost not impacted by the film inlet temperature and by the film Reynolds number. However, the HTF Reynolds number impacts the HTF local viscous entropy generation and consequently its contribution to the overall entropy generation. Furthermore, the increase of the film inlet temperature leads to an increase of the local thermal entropy generation near the free surface while it leads to a decrease of this entropy generation near the wall. The analysis confirms that the counter-current configuration has a higher performance in terms of evaporation mass flow rate compared to the co-current one due to the almost constant temperature gradient encountered in counter-current flow and that, even if the entropy generated in the counter-current flow is higher than those generated in a co-current flow. That means that higher entropy generation does not mean lower efficiency but a comprise between both must be found.

Absorber

The analysis performed in chapter III shows that the entropy generation on an absorber is only due to thermal, mass and viscous irreversibilities: the thermal and mass coupling effect is a reversible process and does not contribute to the overall entropy generation. Moreover, as for the evaporator, the development of the thermal and mass boundary layers strongly influences the local phenomena and consequently local entropy generation: for a LiBr-H_2O solution, the thermal boundary layers develop faster than the diffusive boundary layer.

In the falling film, the analysis shows that the mass irreversibilities dominates near the interface while the thermal irreversibilities dominates near the wall. However, the irreversibilities due to the mass transfer, for the LiBr-H_2O solution, is lower compared to the thermal irreversibilities produced within the film due to the low diffusion of the water absorbed into the film.

Although the component analysis shows that the main entropy generation is produced within the film for a falling film absorber, the HTF must be taken into consideration to analyze the entropy generation of falling film absorbers to obtain a more realistic evaluation of the overall irreversibilities generated during the absorption phenomenon: the contribution of irreversibilities produced within the HTF and the wall represents more than one third of total entropy generation.

All along this thesis, the analysis has been performed considering a LiBr-H_2O solution, however, the model could be extended for different working fluids because of the same physical phenomena encountered.

On the one hand, the chapter IV shows the difficulty of acting on a specific source of irreversibilities as the different types of irreversibilities are coupled and on the other hand, that in thermodynamic of finite absorber, minimizing the entropy generation while maximizing the useful effect (according to the absorber mode) can be performed. Thus, the interest of the mutli-objective optimization method to improve the absorber arises and shows that either the entropy generation can be minimized for a

desired useful effect (according to the absorber mode) or the useful effect can be maximized for a given entropy generation.

The investigation of the mutli-objective optimization method allows to obtain the optimal Preto front solutions for both absorber modes (for absorption chillers or heat transformers). However, the Pareto front solutions show that the increase of the absorbed mass flow rate and transferred heat is associated to an increase of the entropy generation and thus, other criteria such as size, cost and capacity must be considered to choose the right solution by finding a compromise between the entropy generation and the useful effect (either the absorbed mass flow rate or the transferred heat).

The analysis of the design and operating variables allows different conclusions:

- **For the design variables:** longer absorber and thinner wall thickness allow increasing the absorber energy intensity while minimizing the entropy generation but some constraint such as the cost, size and stability of the falling film but also mechanical and strength problems must be considered during the absorber sizing.

- **For the operating conditions:**

    - The HTF Reynolds number in turbulent flow regime does not have a significant impact on the absorbed mass flow rate and recovered heat; however, it significantly impacts the entropy generation due to a high increase of fluid friction. This operating variable should be maintained close to the lower bound of the turbulent domain (around 5000-6000).
    - Unlike to heat transformers where the maximal recovered heat is obtained at high film Reynolds number, an optimal film Reynolds number is observed for absorption chillers: the mutli-objective optimization is therefore very interesting in the case of chillers as it allows to identify the optimal film Reynolds number.
    - Lower HTF inlet temperature and higher vapor pressure allow obtaining higher useful effect (absorbed mass flow rate for absorption chillers or transferred heat for heat transformer). However, that also means higher irreversibilities.
    - For the operating conditions (the HTF and film Reynolds numbers, HTF inlet temperature, and vapor pressure) optimization, attention should be paid as they also depend on the operation of the other components of absorption machines.

In chapter IV, the equilibrium factor has also been introduced and can be used as an abacus to obtain the ratio between the film and HTF Reynolds numbers to use in real case conditions.

Perspectives

Although this work allowed us understanding a little more about the behavior of the evaporator and absorber components, many perspectives are open at the local scale as well as at the component and system scales:

- **Local scale**

Experimental

The local results obtained in this work should be validated by means of an experimental study. A first idea would be to use the Planar Laser Induced Fluorescence (PLIF) and Laser Induced Fluorescence (LIF) point imaging techniques developed at LEMTA (Collignon 2020) and recently at LOCIE to determine the temperature and concentration fields at the film scale. Although the mentioned methods are, for now, used to determine the temperature fields, investigations could be performed to determine the concentration filed.

Numerical

The problem of the wetting rate on plate heat exchangers at low film regimes is a recurrent problem that deserves to be treated in depth. The model developed in this project considers a total and uniform wetting. However, the reality is quite different. It would be interesting to include the wetting rate in the analysis in order to quantify the differences between total and partial wetting and their impact on local phenomena and consequently on entropy generation.

One of the limitations of the developed models is the non-adequacy of the model at film Reynolds numbers higher than 200. The effects of ripples on the film surface and potential recirculation in the film on the absorber performance cannot be evaluated with the present model. A more comprehensive model should be developed to analyze the impact of waves and recirculation on absorbed mass flow rate and transferred heat but also on entropy generation. However, the coupling of thermal, mass and turbulent hydrodynamic remains a very complex phenomenon to model.

CFD methods using graphical software such as COMSOL seem to be interesting methods for modeling the phenomena in this type of component. The HTF in turbulent regime could be better modeled and the phenomena in the falling films for Reynolds numbers higher than 200 could be better observed. Indeed, this type of software, if well used, offers several advantages in term of data visualization and computation time.

- **Component scale of the**

Although this thesis project has identified the different sources of irreversibilities, located and quantified them in the falling film evaporator as well as in the absorber, other studies remain to be done. In any component of a thermodynamic system, there are endogenous and exogenous irreversibilities but also avoidable and non-avoidable irreversibilities as mentioned in the last part of chapter I. It is therefore important to be able to distinguish the different contributions in order to be able to quantify the part of the entropy generation that can be minimized and the one where no action can be done.

A first experiment of an optimized absorber (considering the obtained pareto front solutions from chapter IV) can be set up in order to characterize the performance gain and to analyze the difference

between the values obtained in this thesis and those which will be realized in real situations by using, for example, the experimental prototype proposed by (Amin Altamirano 2021).

Another point that can be studied is the introduction of other criteria in the MOO to improve the optimization of the absorber. The criteria that can be adding are the impact of the CO_2 emission and the cost.

- **System scale**

The multi-objective optimization performed allows having the operating conditions to be used to minimize the entropy generation while preserving the performance of the absorber (the desired absorbed mass flow rate or transferred heat). However, no analysis of the impact of this optimization on the other components of the absorption machines has been done. It is therefore important to study this impact on the coefficient of performance of these machines through numerical and experimental studies. Indeed, the goal will be to maintain the absorber performance while minimizing the entropy generation using the results obtained in chapter IV in order to see if the entropy minimization has a significant impact on the operation of the whole system.

The implementation of an optimized absorber (using the variables of the Pareto front) in an absorption machine, in both operating modes – chillers or heaters, would also allow to characterize the performance gain in the whole system. This proposed study will allow evaluating how much the improvement of the absorber can improve the system performance.

Appendix

Appendix 1: Saturated Vapor Temperature

The correlation for the equilibrium (saturated) condition at the interface between the water film and the water vapor obtained by (Saul and Wagner 1987) is indicated below:

$$T_{vap,sat}(P_{sat}) = (3.37595948586144\mathrm{E}-5) \times \left(\log\left(\frac{P_{sat}}{22064000}\right)\right)^6 + (2.12003737295472\mathrm{E}-3) \times \left(\log\left(\frac{P_{sat}}{22064000}\right)\right)^5 + (5.91993855043397\mathrm{E}-2) \times \left(\log\left(\frac{P_{sat}}{22064000}\right)\right)^4 + 0.976561958843236 \times \left(\log\left(\frac{P_{sat}}{22064000}\right)\right)^3 + 10.767649771597 \times \left(\log\left(\frac{P_{sat}}{22064000}\right)\right)^2 + 88.0085016175992 \times \left(\log\left(\frac{P_{sat}}{22064000}\right)\right)^3 + 373.128542324967$$

Appendix 2: Saturated water-vapor enthalpy correlation

The saturated water-vapor enthalpy correlation obtained by (Florides et. al, 2003) is indicated below:

$$h_{vap,sat} = -0.00125397 * T_{vap,sat}^2 + 1.88060937\, T_{vap,sat} + 2500.559$$

Appendix 3: The equilibrium temperature

The equilibrium temperature given by (Islam, Wijeysundera, and Ho 2006) *is expressed by equation (A3 - 1)*

$$T_{eq}(C_{LiBr}, P) = aC_{LiBr} + b \qquad (\mathrm{A3}-1)$$

Where $a = 0.37794 \left(\frac{p}{p_0}\right)^{-0.188}$

$b = 4.8688 \times 10^{-3} \left(\frac{p}{p_0}\right)^{-0.06574}$

$p_0 = 1kPa$

The equilibrium temperature given by (McNeely 1979) *is expressed in equation (A3 - 2)*

$$T_{eq}(C_{LiBr}, P) = T_{vap}^{sat}(P) \sum_{i=0}^{3} A_i C_{LiBr}^{i} + \sum_{i=0}^{3} B_i C_{LiBr}^{i} \qquad (\mathrm{A3}-2)$$

Where

i	A_i	B_i
0	-2.00755	124.937
1	0.16976	-7.7165
2	$-3.13336\ 10^{-3}$	0.152286
3	$1.97668\ 10^{-5}$	$-7.9509\ 10^{-4}$

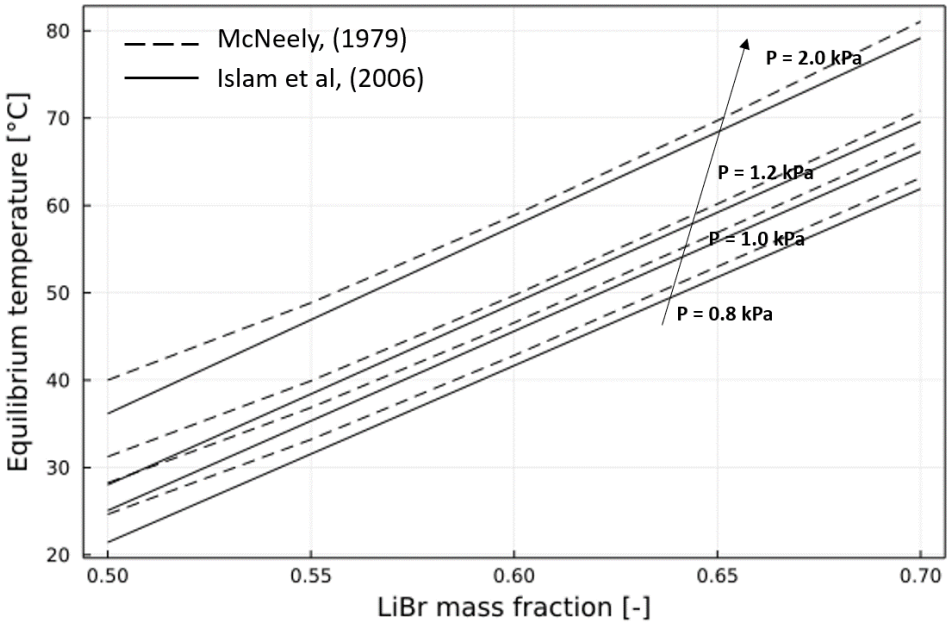

Figure A3: Equilibrium temperature for different vapor pressure and LiBr mass fraction

Appendix 4: Some mathematical tools used in continuum mechanics.

In a continuous medium, an extensive quantity A (mass, energy, entropy, etc.) contained in a volume V(t) can be written as a function of the density ρ and the intensive property a, the specific value of A referred to the unit of mass:

$$A = \iiint \rho\, a\, dV \qquad (A4-1)$$

with

a : specific property [A].kg^{-1}.

Local balance of a volume property

The variation of the quantity A contained in the volume V(t) defined by its boundary S(t) is equal to the quantity which crosses S(t) plus possibly the quantity created in the volume V(t):

$$\iiint \frac{\partial(\rho a)}{\partial t}\, dV \;=\; -\iint j_a \cdot n\, dS + \iiint \sigma_a dV \qquad (A4-2)$$

Avec ja : flux density of A passing through the surface S S ([A].m^{-2}.s^{-1}),
σa : Entropy generation of A ([A].m^{-3}.s^{-1}).

The volume V(t) being arbitrary, we obtain the expression of the local balance of the volume property (Gauss theorem Gauss):

$$\iiint \frac{\partial(\rho a)}{\partial t}\, dV \;=\; \iiint (-\nabla j_a + \sigma_a)\, dV \quad (A4-3)$$

Le volume V(t) étant arbitraire, on obtient l'expression du bilan local de la propriété volumique ($\rho\, a$) :

$$\frac{\partial(\rho a)}{\partial t} = -\nabla j_a + \sigma_a \qquad (A4-4)$$

Lagrangian derivative

On a trajectory, the variation of a quantity a can be represented by its derivative following the motion. It is obtained by temporal derivation of the function a(t,x1,x2, x3):

$$\dot{a} = \frac{da}{dt} = \frac{\partial a}{\partial t} + \sum\nolimits_i \left(\frac{\partial a}{\partial x_i}\right)\left(\frac{dx_i}{dt}\right) = \frac{\partial a}{\partial t} + \sum\nolimits_i \left(\frac{\partial a}{\partial x_i}\right) v_i \qquad (A4-5)$$

Soit

$$\dot{a} = \frac{\partial a}{\partial t} + v \cdot \nabla a \qquad (A4-6)$$

Reynolds transport theorem

The variation with time of the extensive quantity A attached to a volume V(t) is given by the Reynolds transport theorem:

$$\frac{dA}{dt} = \frac{d}{dt}\iiint \rho a\, dV \;=\; \iiint \frac{\partial(\rho a)}{\partial t}\, dV + \iint \rho a\, v \cdot n\, dS \qquad (A4-7)$$

where $\boldsymbol{v}$ is the local velocity of the boundary S(t). Using Gauss' theorem, we obtain:

$$\frac{d}{dt}\iiint \rho a\, dV \;=\; \iiint \left(\frac{\partial(\rho a)}{\partial t} + \rho a\, v\right) dV \qquad (A4-8)$$

The continuity equation allows us to simplify the integral. The conservation of mass imposes:

$$\frac{\partial \rho}{\partial t} + \nabla \cdot \rho \boldsymbol{v} = \mathbf{0} \qquad (A4-9)$$

The decomposition of the integrand appearing in (A4- 8) leads :

$$\frac{\partial \rho a}{\partial t} + \nabla \cdot (\rho a v) = \rho \frac{\partial a}{\partial t} + a \frac{\partial \rho}{\partial t} + a \nabla \cdot \rho \boldsymbol{v} + \rho \boldsymbol{v} \cdot \nabla a = \rho \left(\frac{\partial a}{\partial t} + \boldsymbol{v} \cdot \nabla a \right) + a \left(\frac{\partial \rho}{\partial t} + \nabla \cdot \rho \boldsymbol{v} \right)$$

$$\rho \frac{\partial a}{\partial t} + a \frac{\partial \rho}{\partial t} + a \nabla \cdot \rho \boldsymbol{v} + \rho \boldsymbol{v} \cdot \nabla a = \rho \left(\frac{\partial a}{\partial t} + \boldsymbol{v} \cdot \nabla a \right) + a \left(\frac{\partial \rho}{\partial t} + \nabla \cdot \rho \boldsymbol{v} \right)$$

$$= \rho \dot{a} + a \left(\frac{\partial \rho}{\partial t} + \nabla \cdot \rho \boldsymbol{v} \right)$$

Therefore, Reynold's theorem is written for any volume V(t) whose mass remains constant:

$$\frac{dA}{dt} = \frac{d}{dt} \iiint \rho a \, dV = \iiint \rho \dot{a} \, dV \qquad (A4-10)$$

Relation between Lagrangian and Eulerian derivatives of a volume quantity

By developing the Eulerian derivative of a volume quantity, we obtain, using (A4-6) and (A4-9) :

$$\frac{\partial a \rho}{\partial t} = \rho \frac{\partial a}{\partial t} + a \frac{\partial \rho}{\partial t} = \rho (\dot{a} - v \cdot \nabla a) - a \nabla \cdot \rho \boldsymbol{v} = \rho \dot{a} - \nabla \cdot (a \rho \boldsymbol{v}) \quad (A4-11)$$

Bibliography

Abu-Khader. 2012. “Plate Heat Exchangers: Recent Advances.” *Renewable and Sustainable Energy Reviews* 16 (4): 1883–91. https://doi.org/10.1016/j.rser.2012.01.009.

ADEME. 2018. “Climat, Air et Énergie.” édition 2018. Technical report, 2018.

Altamirano. 2021. “Développement d’un nouveau concept de refroidisseurs à absorption compact et à bas coût : application au cas du rafraichissement solaire pour des climats chauds.”Ph.D thesis, Université Savoie Mont-Blanc.

Altamirano, Le Pierrès, Sutz, and Domain. 2019. “H_2O-LiBr Single-Stage Solar Absorption Air Conditioner with an Innovative Bi-Adiabatic Configuration: Dynamic Model, Nominal Conditions and Typical Day Operation, “ISES Solar World Congress 2019/ IEA SHC International Conference on Solar Heating and Cooling for Buildings and Industry 2019, International Solar Energy Society, Santiago, Chili, 4-7July 2019, 1–12. https://doi.org/10.18086/swc.2019.55.01.

Altamirano, Stutz, and Le Pierrès. 2019. “Review of Small-Capacity Single-Stage Continuous Absorption Systems Operating on Binary Working Fluids for Cooling: Theoretical, Experimental and Commercial Cycles.” *International Journal of Refrigeration* 106: 350–73. https://doi.org/10.1016/j.ijrefrig.2019.06.033.

Altamirano, Stutz, and Le Pierrès. 2020. “Review of Small-Capacity Single-Stage Continuous Absorption Systems Operating on Binary Working Fluids for Cooling: Compact Exchanger Technologies.” *International Journal of Refrigeration* 114: 118–47. https://doi.org/10.1016/j.ijrefrig.2020.02.033.

Amidpour, Majid, and Mohammad Hasan Khoshgoftar Manesh. 2021. “Chapter 6 - Advanced Exergetic Evaluation of Cogeneration and Polygeneration Systems.” In *Cogeneration and Polygeneration Systems*, edited by Majid Amidpour and Mohammad Hasan Khoshgoftar Manesh, 75–93. Academic Press. https://doi.org/10.1016/B978-0-12-817249-0.00006-9.

Aminyavari, Aprile, Toppi, Garone, and Motta. 2017. “A Detailed Study on Simultaneous Heat and Mass Transfer in an In-Tube Vertical Falling Film Absorber.” *International Journal of Refrigeration* 80 (August): 37–51. https://doi.org/10.1016/j.ijrefrig.2017.04.029.

Arroiabe, Manex Martinez-Agirre, and Mounir Bou-Ali. 2022. “Numerical Analysis of Different Mass Transfer Models for Falling Film Absorbers.” *International Journal of Heat and Mass Transfer* 182 (January): 121892. https://doi.org/10.1016/j.ijheatmasstransfer.2021.121892.

ASHRAE. 2001. *ASHRAE Handbook Fundamentals : SI Edition*. SI EDITION. Amer Soc of Heating, Refrigerating & A-C Engineers.

Ayub. 2003. “Plate Heat Exchanger Literature Survey and New Heat Transfer and Pressure Drop Correlations for Refrigerant Evaporators.” *Heat Transfer Engineering* 24 (5): 3–16. https://doi.org/10.1080/01457630304056.

Babadi, and Farhanieh. 2005. “Characteristics of Heat and Mass Transfer in Vapor Absorption of Falling Film Flow on a Horizontal Tube.” *International Communications in Heat and Mass Transfer* 32 (9): 1253–65. https://doi.org/10.1016/j.icheatmasstransfer.2005.05.011.

Bartashevich. 2018. “Numerical Simulation of Non-Isothermal Absorption in a Liquid Film Moving over a Cooled Horizontal Surface under the Action of a Gas Flow.” Edited by G.V. Kuznetsov, E. Bulba, and D. Feoktistov. *MATEC Web of Conferences* 194: 01008. https://doi.org/10.1051/matecconf/201819401008.

Bejan. 1996. *Entropy Generation Minimization : The Method of Thermodynamic Optimization on Finite-Size Systems and Finite-Time Processes*. Energy and the Environment.

Ben Hafsia, Chaouachi, and Gabsi. 2015. “A Study of the Coupled Heat and Mass Transfer during Absorption Process in a Spiral Tubular Absorber.” *Applied Thermal Engineering* 76 (February): 37–46. https://doi.org/10.1016/j.applthermaleng.2014.10.079.

Bird, Stewart, and Lightfoot. 1960. *Transport Phenomena*. AIChE. Vol. 7. 2. Wiley, New york. doi.org/10.1002/aic.690070245

Bo, Ma, Lan, Chen.H, and Chen.J. 2010. “Numerical Simulation on the Falling Film Absorption Process in a Counter-Flow Absorber.” *Chemical Engineering Journal* 156 (3): 607–12. https://doi.org/10.1016/j.cej.2009.04.066.

Bo, Shoushi, Xuehu Ma, Hongxia Chen, and Zhong Lan. 2011. “Numerical Simulation on Vapor Absorption by Wavy Lithium Bromide Aqueous Solution Films.” *Heat and Mass Transfer* 47 (12): 1611–19. https://doi.org/10.1007/s00231-011-0820-x.

Bohra, Lalit Kumar, Sangsoo Lee, and Srinivas Garimella. 2019. “Visual Documentation of Transfer Processes in Horizontal-Tube Falling-Film Ammonia–Water Absorbers.” *International Journal of Refrigeration* 103 (July): 91–105. https://doi.org/10.1016/j.ijrefrig.2019.03.032.

Boudlal, and Liapidevskii. 2012. “Modulation Equations for Wave Flows of a Fluid Film along a Vertical Wall.” *Doklady Physics* 57 (1): 23–28. https://doi.org/10.1134/S102833581201003X.

Brauner. 1989. “Modelling of Wavy Flow in Turbulent Free Falling Films.” *International Journal of Multiphase Flow* 15 (4): 505–20. https://doi.org/10.1016/0301-9322(89)90050-5.

Brauner. 1991. “Non-Isothermal Vapour Absorption into Falling Film.” *International Journal of Heat and Mass Transfer* 34 (3): 767–84. https://doi.org/10.1016/0017-9310(91)90124-W.

Cellier and Ruyer-Quil. 2020. “A New Family of Reduced Models for Non-Isothermal Falling Films.” *International Journal of Heat and Mass Transfer* 154 (June): 119700. https://doi.org/10.1016/j.ijheatmasstransfer.2020.119700.

Cerezo, Best and Romero. 2011. “A Study of a Bubble Absorber Using a Plate Heat Exchanger with NH_3–H_2O, NH_3–$LiNO_3$ and NH_3–NaSCN.” *Applied Thermal Engineering* 31 (11–12): 1869–76. https://doi.org/10.1016/j.applthermaleng.2011.02.032.

Cheng, and Xingang Liang. 2012. “Computation of Effectiveness of Two-Stream Heat Exchanger Networks Based on Concepts of Entropy Generation, Entransy Dissipation and Entransy-Dissipation-Based Thermal Resistance.” *Energy Conversion and Management* 58 (June): 163–70. https://doi.org/10.1016/j.enconman.2012.01.016.

Chermiti, Hidouri, and Ben Brahim. 2011. “Entropy Generation in Gas Absorption into a Falling Liquid Film.” *Mechanics Research Communications* 38 (8): 586–93. https://doi.org/10.1016/j.mechrescom.2011.08.003.

Chermiti, Hidouri, and Ben Brahim. 2013. “Effect of a Falling Gas–Liquid Absorption Film Temperature on Entropy Generation.” *Heat and Mass Transfer* 49 (8): 1101–8. https://doi.org/10.1007/s00231-013-1154-7.

Chhay, Marx, Denys Dutykh, Marguerite Gisclon, and Christian Ruyer-Quil. 2017. “New Asymptotic Heat Transfer Model in Thin Liquid Films.” *Applied Mathematical Modelling* 48 (August): 844–59. https://doi.org/10.1016/j.apm.2017.02.022.

Collignon, Romain. 2020. “Étude des transferts de chaleur dans un film ruisselant à instabilités de surface par des méthodes de fluorescence induite par laser.” Ph.D thesis, Université de Lorraine.

Conn, Gould, and Toint.2000, Trust-Region Methods, MPS-SIAM Series on Optimization, Series Number 1.

Dardouch, Charia and Bernatchou. 2020. “Numerical Study of a Solar Absorption Refrigeration Machine.” Edited by A. Akhssas, K. Baba, L. Bahi, F. Benradi, E. Cherkaoui, M. Khamar, A. Lahmili, M. Menzhi, A. Nounah, and L. Ouadif. *E3S Web of Conferences* "Water, Waste and Environment", Sale, Morocco, 20-22 Nov 2019, 150: 01009. https://doi.org/10.1051/e3sconf/202015001009.

De Lucas, Donate, and Rodríguez. 2007. “Absorption of Water Vapor into New Working Fluids for Absorption Refrigeration Systems.” *Industrial & Engineering Chemistry Research* 46 (1): 345–50. https://doi.org/10.1021/ie061229b.

Deepak, Ashok Kumar, Mahidhar Reddy, and Subramanyam. 2017. “Thermodynamic Property Functions of NH_3-H_2O Mixture.” *Internation Journal of Mechanical Engineering and Technology (IJMET)* 8 (8): 1430–40.

Demekhin, Kalaidin, and Rastaturin. 2005. “The Effect of Wave Modes on Mass Transfer in Falling Liquid Films.” *Thermophysics and Aeromechanics* 12 (2): 10.

Deng, and Ma. 1999. “Experimental Studies on the Characteristics of an Absorber Using LiBr/H_2O Solution as Working Fluid.” *International Journal of Refrigeration* 22 (4): 293–301. https://doi.org/10.1016/S0140-7007(98)00067-X.

Ding, Xie, Ingham, Ma, and Pourkashanian. 2018. “Flow Behaviour of Drop and Jet Modes of a Laminar Falling Film on Horizontal Tubes.” *International Journal of Heat and Mass Transfer* 124 (September): 929–42. https://doi.org/10.1016/j.ijheatmasstransfer.2018.03.111.

Erregueragui, Al Mers, Boutammache, Merroun, and Bouatem. 2015. “Modélisation et optimisation de cycles frigorifiques à absorption fonctionnant avec le couple H_2O/LiBr, “ Société Française de Thermique, La Rochelle, France , 26-29 May 2015, 8.

European Comission. 2019. “European Comission.” Accessed 22nd Feb 2019. https://ec.europa.eu/clima/policies/strategies/2030_en#tab-0-0.

Fan, and Luo. 2017. “Recent Advances on Heat Exchanger-Absorber Design.” *Recent Advances in Petrochemical Science* 2 (2). https://doi.org/10.19080/RAPSCI.2017.02.555581.

Fartaj. 2004. “Comparison of Energy, Exergy, and Entropy Balance Methods for Analysing Double-Stage Absorption Heat Transformer Cycles.” *International Journal of Energy Research* 28 (14): 1219–30. https://doi.org/10.1002/er.1024.

Fernández-Seara, Uhía, and Sieres. 2007. “Analysis of an Air Cooled Ammonia–Water Vertical Tubular Absorber.” *International Journal of Thermal Sciences* 46 (1): 93–103. https://doi.org/10.1016/j.ijthermalsci.2006.03.005.

Flores. 2014. “Etude des transferts de masse et de chaleur au sein d’un absorbeur eau/bromure de lithium.” Ph.D thesis, Université de Grenoble. https://tel.archives-ouvertes.fr/tel-01062936.

Florides, Kalogirou, Tassou, and Wrobel. 2003. “Design and Construction of a LiBr–Water Absorption Machine.” *Energy Conversion and Management* 44 (15): 2483–2508. https://doi.org/10.1016/S0196-8904(03)00006-2.

Fujita, Isamu, and Eiji Hihara. 2005. “Heat and Mass Transfer Coefficients of Falling-Film Absorption Process.” *International Journal of Heat and Mass Transfer* 48 (13): 2779–86. https://doi.org/10.1016/j.ijheatmasstransfer.2004.11.028.

García-Rivera, Castro, Farnós, and Oliva. 2016. “Numerical and Experimental Investigation of a Vertical LiBr Falling Film Absorber Considering Wave Regimes and in Presence of Mist Flow.” *International Journal of Thermal Sciences* 109 (November): 342–61. https://doi.org/10.1016/j.ijthermalsci.2016.05.029.

Ghyadh, Shahad, and Hammadi. 2018. “Overview of Working Pair Used in Absorption Refrigeration Technologies.” *International Journal for Research in Applied Science and Engineering Technology* 6 (7): 662–78. https://doi.org/10.22214/ijraset.2018.7114.

Giannetti, Rocchetti, Lubis, Saito, and Yamaguchi. 2016. “Entropy Parameters for Falling Film Absorber Optimization.” *Applied Thermal Engineering* 93: 750–62. https://doi.org/10.1016/j.applthermaleng.2015.10.049.

Giannetti, Rocchetti, Saito, and Yamaguchi. 2015a. “Local Entropy Generation Analaysis of Water Vapour Absorption in a LiBr-H_2O Solution Film over a Horizontal Cooled Tube.” In , 9. https://www.researchgate.net/publication/292681680.

Giannetti, Rocchetti, Saito, and Yamaguchi. 2015b. “Irreversibility Analysis of Falling Film Absorption over a Cooled Horizontal Tube.” *International Journal of Heat and Mass Transfer* 88 (September): 755–65. https://doi.org/10.1016/j.ijheatmasstransfer.2015.05.022.

Giannetti, Rocchetti, Yamaguchi, and Saito. 2017. “Analytical Solution of Film Mass-Transfer on a Partially Wetted Absorber Tube.” *International Journal of Thermal Sciences* 118 (August): 176–86. https://doi.org/10.1016/j.ijthermalsci.2017.05.002.

Giannetti, Rocchetti, Yamaguchi, and Saito. 2018. “Heat and Mass Transfer Coefficients of Falling-Film Absorption on a Partially Wetted Horizontal Tube.” *International Journal of Thermal Sciences* 126 (April): 56–66. https://doi.org/10.1016/j.ijthermalsci.2017.12.020.

Goel, and Goswami. 2005a. “A Compact Falling Film Absorber.” *Journal of Heat Transfer* 127 (9): 957–65.

Goel, and Goswami. 2005b. “Analysis of a Counter-Current Vapor Flow Absorber.” *International Journal of Heat and Mass Transfer* 48 (7): 1283–92. https://doi.org/10.1016/j.ijheatmasstransfer.2004.10.009.

Gommed, Grossman, and Koenig. 2001. “Numerical Study of Absorption in a Laminar Falling Film of Ammonia-Water.” *ASHRAE Transactions* 107: 453–62.

Gomri. 2009. “Second Law Comparison of Single Effect and Double Effect Vapour Absorption Refrigeration Systems.” *Energy Conversion and Management* 50 (5): 1279–87. https://doi.org/10.1016/j.enconman.2009.01.019.

Gong, and Goni Boulama. 2014. “Parametric Study of an Absorption Refrigeration Machine Using Advanced Exergy Analysis.” *Energy* 76 (November): 453–67. https://doi.org/10.1016/j.energy.2014.08.038.

Gonzalez. 2005. “Simulation of Heat and Mass Transfer Phenomena in the Critical Elements of H_2O/LiBr Absorption Cooling Machines. Experimental Validation and Application to Design.” Thesis, Universitat Politècnica de Catalunya.

Goussis, and Kelly. 1991. “Surface Wave and Thermocapillary Instabilities in a Liquid Film Flow.” *Journal of Fluid Mechanics* 223: 25–45.

Govindaraju. 2005. “Analysis of Absorber Operations for the 5 KW Ammonia-Water Combined Cycle.” Ph. D thesis, University of Florida.

Grigor’eva, and Nakoryakov. 1977. “Exact Solution of Combined Heat- and Mass-Transfer Problem during Film Absorption.” *Journal of Engineering Physics* 33 (5): 1349–53. https://doi.org/10.1007/BF00860913.

Haase. 1990. *Thermodynamics of Irreversible Processes*. Dover Pubns; Reprint. Several small, light marks to edges, othe edition.

Habib, Ebady, and El-Zahar. 2019. “A Numerical Modeling of Heat and Mass Transfer for a Falling Film Absorber,” Int. J. Eng. Res. Technol, 12 (3): 287–95.

Han, Je-Chin. 2012. “Analytical Heat Transfer.” *Taylor & Francis Group*, no. ISBN 978-1-4398-6196-7: 327.

Harikrishnan, Tiwari, and Maiya. 2011. “Numerical Study of Heat and Mass Transfer Characteristics on a Falling Film Horizontal Tubular Absorber for R-134a-DMAC.” *International Journal of Thermal Sciences* 50 (2): 149–59. https://doi.org/10.1016/j.ijthermalsci.2010.10.004.

Hellman and Grossman. 1996. “Improved Property Data Correlations of Absorption Fluids for Computer Simulation of Heat Pump Cycles.” *Conference: Winter Meeting of American Society of Heating, Refrigeration and Air Conditioning Engineers, Atlanta, GA (United States), 17-21 Feb 1996; Other Information: PBD: 1996; Related Information: Is Part Of ASHRAE Transactions 1996: Technical and Symposium Papers. Volume 102, Part 1; PB: 1278 p.*

Hidouri, Chermiti, and ben brahim. 2013. “Second Law Analysis of a Gas-Liquid Absorption Film.” *Journal of Thermodynamics* 2013: 1–10. https://doi.org/10.1155/2013/909162.

Hirschfelder, Curtiss, and Bird. 1954. *The Molecular Theory of Gases and Liquids*. Cambridge University Press. Vol. 59. New York : John Wiley & Sons, Inc 531.

Hong, Yuxiang, Juan Du, and Shuangfeng Wang. 2017. “Turbulent Thermal, Fluid Flow and Thermodynamic Characteristics in a Plain Tube Fitted with Overlapped Multiple Twisted Tapes.” *International Journal of Heat and Mass Transfer* 115 (December): 551–65. https://doi.org/10.1016/j.ijheatmasstransfer.2017.08.017.

Hosseinnia, Naghashzadegan, and Kouhikamali. 2017. “Numerical Study of Falling Film Absorption Process in a Vertical Tube Absorber Including Soret and Dufour Effects.” *International Journal of Thermal Sciences* 114 (April): 123–38. https://doi.org/10.1016/j.ijthermalsci.2016.11.006.

Huaylla. 2017. “Storage of solar energy by absorption: process experimentation and modeling.” Ph.D thesis, Communauté Université Grenoble Alpes. Hal:tel-02050102.

Ibarra-Bahena, and Romero. 2014. “Performance of Different Experimental Absorber Designs in Absorption Heat Pump Cycle Technologies: A Review.” *Energies* 7 (2): 751–66. https://doi.org/10.3390/en7020751.

Incropera, Dewitt, Bergman, and Lavine. 2006. *Fundamentals of Heat and Mass Transfer*. Sixth. John Wiley & Sons.

Islam, Md. Raisul, N.E. Wijeysundera, and J.C. Ho. 2006. “Heat and Mass Transfer Effectiveness and Correlations for Counter-Flow Absorbers.” *International Journal of Heat and Mass Transfer* 49 (21–22): 4171–82. https://doi.org/10.1016/j.ijheatmasstransfer.2006.04.002.

Islam, Miyara, and Setoguchi. 2009. “Numerical Investigation of Steam Absorption in Falling Film of LiBr Aqueous Solution with Solitary Waves.” *International Journal of Refrigeration* 32 (7): 1597–1603. https://doi.org/10.1016/j.ijrefrig.2009.06.007.

Izquierdo, Lizarte, Marcos, and Gutiérrez. 2008. “Air Conditioning Using an Air-Cooled Single Effect Lithium Bromide Absorption Chiller: Results of a Trial Conducted in Madrid in August 2005.” *Applied Thermal Engineering* 28 (8–9): 1074–81. https://doi.org/10.1016/j.applthermaleng.2007.06.009.

Jeong, and Garimella. 2002. “Falling-Film and Droplet Mode Heat and Mass Transfer in a Horizontal Tube LiBr/Water Absorber.” *International Journal of Heat and Mass Transfer* 45 (7): 1445–58. https://doi.org/10.1016/S0017-9310(01)00262-9.

Jeong, and Garimella. 2004. “Optimal Design of Compact Horizontal Tube LiBr/Water Absorbers.” *HVAC and R Research*, HVAC and R Research, 11 (1): 27–44.

Julia. Accessed January 9, 2020. https://julialang.org/.

Kaita. 2001. “Thermodynamic Properties of Lithium Bromide–Water Solutions at High Temperatures.” *International Journal of Refrigeration* 24 (5): 374–90. https://doi.org/10.1016/S0140-7007(00)00039-6.

Kalliadasis, Ruyer-Quil, Scheid, and Velarde. 2012. *Falling Liquid Films*. Springler. New York.

Kang, Kunugi, and Kashiwagi. 2000. “Review of Advanced Absorption Cycles: Performance Improvement and Temperature Lift Enhancement.” *International Journal of Refrigeration* 23 (5): 388–401. https://doi.org/10.1016/S0140-7007(99)00064-X.

Karami, and Farhanieh. 2009. “A Numerical Study on the Absorption of Water Vapor into a Film of Aqueous LiBr Falling along a Vertical Plate.” *Heat and Mass Transfer* 46 (2): 197–207. https://doi.org/10.1007/s00231-009-0557-y.

Kaushik, Tyagi, and Kumar. 2017. "Finite Time Thermodynamics of Power and Refrigeration Cycles". 1st ed. Springer Cham. https://doi-org.univ-smb.idm.oclc.org/10.1007/978-3-319-62812-7.

Kawae, Shigechi, and Yamada. 1989. “Water Vapor Evaporation into Laminar Film Flow of a Lithium Bromide - Water Solution (Influence of Variable Properties and Inlet Film Thickness on Absorption Mass Transfer Rate).” *Heat Transfer Japanese Reseach* 18(3): 58–70.

Kaynakli, and Kilic. 2007. “Theoretical Study on the Effect of Operating Conditions on Performance of Absorption Refrigeration System.” *Energy Conversion and Management* 48 (2): 599–607. https://doi.org/10.1016/j.enconman.2006.06.005.

Keinath, Garimella, and Garrabrant. 2017. “Modeling of an Ammonia–Water Absorption Heat Pump Water Heater for Residential Applications.” *International Journal of Refrigeration* 83 (November): 39–50. https://doi.org/10.1016/j.ijrefrig.2017.06.007.

Kelly. 2008. “Energy Systems Improvement Based on Endogenous and Exogenous Exergy Destruction.” Ph.D. thesis, University of Berlin.

Kherris, Sahraoui, Mohammed Makhlouf, Djallel Zebbar, and Omar Sebbane. 2013. “Contribution Study of the Thermodynamics Properties of the Ammonia-Water Mixtures.” *Thermal Science* 17 (3): 891–902. https://doi.org/10.2298/TSCI110206083K.

Killion. 2003. “An Investigation of Droplets and Films Falling over Horizontal Tubes.” Ph .D. Thesis, Iowa State University. https://lib.dr.iastate.edu/rtd/19454.

Killion, and Garimella. 2001. “A Critical Review of Models of Coupled Heat and Mass Transfer in Falling Film Absorption.” *International Journal of Refrigeration* 24: 43.

Killion, and Garimella. 2002. “Liquid Films Falling Over Horizontal Tube Banks: Deviations From Idealized Flow Patterns and Implications for Heat and Mass Transfer.” *American Society of Mechanical Engineers, Heat Transfer Division, (Publication) HTD* 372 (1): 161–70.

Killion, and Garimella. 2003. “Gravity-Driven Flow of Liquid Films and Droplets in Horizontal Tube Banks.” *International Journal of Refrigeration* 26 (5): 516–26.

Killion, and Garimella. 2004a. “Simulation of Pendant Droplets and Falling Films in Horizontal Tube Absorbers.” *Journal Heat Transfer* 126 (6): 1003–13.

Killion and Garimella. 2004b. “Pendant Droplet Motion for Absorption on Horizontal Tube Banks.” *International Journal of Heat and Mass Transfer* 47 (19–20): 4403–14. https://doi.org/10.1016/j.ijheatmasstransfer.2004.04.032.

Kiyasatfar. 2018. “Convective Heat Transfer and Entropy Generation Analysis of Non-Newtonian Power-Law Fluid Flows in Parallel-Plate and Circular Microchannels under Slip Boundary Conditions.” *International Journal of Thermal Sciences*, 13.

Kyung, Herold, and Kang. 2007a. “Experimental Verification of H_2O/LiBr Absorber Bundle Performance with Smooth Horizontal Tubes.” *International Journal of Refrigeration* 30 (4): 582–90. https://doi.org/10.1016/j.ijrefrig.2006.11.005.

Kyung, Herold, and Kang. 2007b. “Model for Absorption of Water Vapor into Aqueous LiBr Flowing over a Horizontal Smooth Tube.” *International Journal of Refrigeration* 30 (4): 591–600. https://doi.org/10.1016/j.ijrefrig.2006.11.001.

Lee, Chan Ho, Yong Tae Kang, Hyun Uk Kang, and Sung Hyun Kim. 2005. “Numerical and Experimental Study for Falling Film in Ammonia Absorption Refrigeration Systems.” *Journal Of Chemical Engineering Of Japan* 38 (7): 520–27. https://doi.org/10.1252/jcej.38.520.

Li, Yin, Liang, and Zhang. 2018. “Experimental Study on Heat and Mass Transfer Performance of Falling Film Absorption over a Vertical Tube Using LiCl Solution.” *International Journal of Refrigeration* 85 (January): 109–19. https://doi.org/10.1016/j.ijrefrig.2017.09.015.

Lubis, Giannetti, Yamaguchi, Saito, and Inoue. 2017. “Experimental Performance of a Double-Lift Absorption Heat Transformer for Manufacturing-Process Steam Generation.” *Energy Conversion and Management* 148 (September): 267–78. * https://doi.org/10.1016/j.enconman.2017.05.074.

Mahamoudou, Le Pierrès and Ramousse (2022). Review of Coupled Heat and Mass Transfer Studies in Falling Film Absorbers: Modeling, Experimental and Thermodynamic Approaches. *International Journal of Refrigeration,* vol 136, p.229-244. DOI: 10.1016/j.ijrefrig.2022.01.024

Mahamoudou, Ramousse, Cellier, and Le Pierrès. 2022. “Thermodynamic Analysis in Laminar Falling Film Evaporator.” *Applied Thermal Engineering*, June, 118814. https://doi.org/10.1016/j.applthermaleng.2022.118814.

Mascarenhas and Mudawar. 2013. “Investigation of Eddy Diffusivity and Heat Transfer Coefficient for Free-Falling Turbulent Liquid Films Subjected to Sensible Heating.” *International Journal of Heat and Mass Transfer* 64 (September): 647–60. https://doi.org/10.1016/j.ijheatmasstransfer.2013.04.061.

McClintock. 1951. “The Design of Heat Exchangers for Minimum Irreversibility.” *ASME Paper 51-A-108*, 1951.

McNeely. 1979. “Thermophysical Properties of Aqueous Solutions of Lithium Bromide.” *ASHRAE Transactions* 85 (1): 413–34.

Medrano, Marc, and al. 2002. “Absorption of Water Vapour in the Falling Film of Water–Lithium Bromide inside a Vertical Tube at Air-Cooling Thermal Conditions.” *International Journal of Thermal Sciences* 41 (9): 891–98. https://doi.org/10.1016/S1290-0729(02)01383-2.

Mehrez. 2019. “Caractérisation et Modélisation d’un Système de Climatisation Par Absorption.” Ph.D thesis, Université Grenoble Alpes.

Meyer. 2014. “Analytical Solution for Combined Heat and Mass Transfer in Laminar Falling Film Absorption with Uniform Film Velocity – Isothermal and Adiabatic Wall.” *International Journal of Refrigeration* 48 (December): 74–86. https://doi.org/10.1016/j.ijrefrig.2014.08.005.

Meyer, and Ziegler. 2014. “Analytical Solution for Combined Heat and Mass Transfer in Laminar Falling Film Absorption Using First Type Boundary Conditions at the Interface.” *International Journal of Heat and Mass Transfer* 73 (June): 141–51. https://doi.org/10.1016/j.ijheatmasstransfer.2014.01.074.

Michel, Le Pierrès, and Stutz. 2017. “Performances of Grooved Plates Falling Film Absorber.” *Energy* 138 (November): 103–17. https://doi.org/10.1016/j.energy.2017.07.026.

Miller. 1998. “The Experimental Analysis of Aqueous Lithium Bromide Vertical Film Absorption.” *Office of Scientific and Technical Information Technical Reports*, 304.

Miller, and Keyhani. 2001a. “The Correlation of Simultaneous Heat and Mass Transfer Experimental Data for Aqueous Lithium Bromide Vertical Falling Film Absorption.” *J. Sol. Energy Eng.* 123 (2): 30–42.

Miller, and Keyhani. 2001b. “The Effect of Roll Waves on the Hydrodynamics of Falling Films Observed in Vertical Column Absorbers.” *ASME Heat Pump Technical Session*, 2001.

Ministre de la transition écologique. 2021. “Chiffres Clés de l’énergie.” SDES.

Mittermaier, and Ziegler. 2014. “A Numerical Model for Combined Heat and Mass Transfer in a Laminar Liquid Falling Film with Simplified Hydrodynamics.” *International Journal of Heat and Mass Transfer* 70 (March): 990–1002. https://doi.org/10.1016/j.ijheatmasstransfer.2013.11.075.

Morosuk and Tsatsaronis. 2006a. “Splitting the Exergy Destruction into Endogenous and Exogenous Parts Application to Refrigeration Machines.” In *Proceedings of the 19th International Conference on Efficiency, Cost, Optimization, Simulation and Environmental Impact of Energy Systems*, 1:165–72. National Technical University of Athens, Greece.

Morosuk and Tsatsaronis 2006b. “The ‘Cycle Method’ Used in the Exergy Analysis of Refrigeration Machines: From Education to Research.” In , 1:157–63. National Technical University of Athens, Greece.

Morosuk and Tsatsaronis. 2008. “A New Approach to the Exergy Analysis of Absorption Refrigeration Machines.” *Energy* 33 (6): 890–907. https://doi.org/10.1016/j.energy.2007.09.012.

Morosuk and Tsatsaronis. 2009. “Advanced Exergetic Evaluation of Refrigeration Machines Using Different Working Fluids.” *Energy* 34 (12): 2248–58. https://doi.org/10.1016/j.energy.2009.01.006.

Mortazavi, and Moghaddam. 2016. “Laplace Transform Solution of Conjugate Heat and Mass Transfer in Falling Film Absorption Process.” *International Journal of Refrigeration* 66 (June): 93–104. https://doi.org/10.1016/j.ijrefrig.2016.02.013.

Myat, Thu, Kim, Chakraborty, Chun, and Ng. 2011. “A Second Law Analysis and Entropy Generation Minimization of an Absorption Chiller.” *Applied Thermal Engineering* 31 (14–15): 2405–13. https://doi.org/10.1016/j.applthermaleng.2011.04.004.

Nakoryakov, Bufetov, Grigor’eva, and Dekhtyar’. 2003. “Heat and Mass Transfer During Vapor Absorption by a Stagnant Solution Layer.” *Journal of Applied Mechanics and Technical Physics* 44: 236–42.

Nakoryakov, and Grigor’eva. 1977. “Combined Heat and Mass Transfer during Absorption in Drops and Films.” *Journal of Engineering Physics* 32: 243–47.

Nakoryakov, and Grigor’eva. 1997. “Analysis of Exact Solutions to Heat and Mass Transfer Problems for Absorption with Films or Streams.” *Theor.Found.Chem.Eng.* 31: 119–26.

Nakoryakov, and Grigor’eva. 2010. “Nonisothermal Absorption in Thermotransformers.” *Journal of Engineering Thermophysics* 19 (4): 196–271. https://doi.org/10.1134/S1810232810040028.

Nakoryakov, Grigoryeva, and Bartashevich. 2011. “Heat and Mass Transfer in the Entrance Region of the Falling Film: Absorption, Desorption, Condensation and Evaporation.” *International Journal of Heat and Mass Transfer* 54 (21–22): 4485–90. https://doi.org/10.1016/j.ijheatmasstransfer.2011.06.032.

Nakoryakov, Ostapenko and Bartashevich. 2012. “Heat and Mass Transfer in the Liquid Film on a Vertical Wall in Roll-Wave Regime.” *International Journal of Heat and Mass Transfer* 55 (23–24): 6514–18. https://doi.org/10.1016/j.ijheatmasstransfer.2012.06.054.

Nakoryakov, Vladimir and Bartashevich. 2017. “Analytical and Numerical Solution of Conjugate Heat and Mass Transfer in Falling Film Absorption Process.” Edited by N. Bardis, J. Quartieri, C. Guarnaccia, and N. Doukas. *ITM Web of Conferences* 9: 01011. https://doi.org/10.1051/itmconf/20170901011.

Narváez-Romo, Beethoven, Chhay, Zavaleta-Aguilar and Simões-Moreira. 2017. “A Critical Review of Heat and Mass Transfer Correlations for LiBr-H_2O and NH_3 -H_2O Absorption Refrigeration Machines Using Falling Liquid Film Technology.” *Applied Thermal Engineering* 123 (August): 1079–95. https://doi.org/10.1016/j.applthermaleng.2017.05.092.

Neveu, Pierre. 2002. “Apports de la thermodynamique pour la conception et l’intégration des procédés.” Université de Perpignan. tel-00995431.

Nguyen, Nghia-Hieu, Hiep-Chi Le, and Quoc-An Hoang. 2018. “Heat and Mass Transfer of NH_3-H_2O Falling-Film Absorption on Horizontal Round Tube Banks.” *Mathematics and Computer Science* 3 (4): 93. https://doi.org/10.11648/j.mcs.20180304.13.

Nikbakhti, Wang, Hussein, and Iranmanesh. 2020. “Absorption Cooling Systems – Review of Various Techniques for Energy Performance Enhancement.” *Alexandria Engineering Journal* 59 (2): 707–38. https://doi.org/10.1016/j.aej.2020.01.036.

Onsager. 1931a. “Reciprocal Relations in Irreversible Processes. I.” *Physical Review* 37 (4): 405–26. https://doi.org/10.1103/PhysRev.37.405.

Onsager. 1931b. “Reciprocal Relations in Irreversible Processes. II.” *Physical Review* 38 (12): 2265–79. https://doi.org/10.1103/PhysRev.38.2265.

Papaefthimiou, Karampinos, and Rogdakis. 2006. “A Detailed Analysis of Water-Vapour Absorption in LiBr–H_2O Solution on a Cooled Horizontal Tube.” *Applied Thermal Engineering* 26 (17–18): 2095–2102. https://doi.org/10.1016/j.applthermaleng.2006.04.010.

Papaefthimiou, Koronaki, Karampinos, and Rogdakis. 2012. “A Novel Approach for Modelling LiBr–H_2O Falling Film Absorption on Cooled Horizontal Bundle of Tubes.” *International Journal of Refrigeration* 35 (4): 1115–22. https://doi.org/10.1016/j.ijrefrig.2012.01.015.

Perier-Muzet and Stutz. 2021. “Numerical Study of the Effectiveness of a Vertical Falling Plate Film Absorber for an Absorption Chiller.” *International Journal of Refrigeration* 127 (July): 221–29. https://doi.org/10.1016/j.ijrefrig.2021.02.013.

Pierson, and Whitaker. 1977. “Some Theoretical and Experimental Observations of the Wave Structure of Falling Liquid Films.” *Industrial & Engineering Chemistry Fundamentals* 16 (4): 401–8. https://doi.org/10.1021/i160064a002.

Pussoli. 2012. “Optimization of Peripheral Finned-Tube Evaporators Using Entropy Generation Minimization.” *International Journal of Heat and Mass Transfer* 55: 7838–46.

Qiu, Qinggang. 2018. “3D Numerical Study of the Liquid Film Distribution on the Surface of a Horizontal-Tube Falling-Film Evaporator.” *International Journal of Heat and Mass Transfer*, 10.

Raisul Islam, Wijeysundera, and Ho. 2004. “Simplified Models for Coupled Heat and Mass Transfer in Falling-Film Absorbers.” *International Journal of Heat and Mass Transfer* 47 (2): 395–406. https://doi.org/10.1016/j.ijheatmasstransfer.2003.07.001.

Rogdakis and Papaefthimiou. 2002. “A Simplified Thermodynamic Analysis of a LiBr-H_2O Vertical Tube Absorber.” In , 455–62. https://doi.org/10.1115/IMECE2002-39118.

Rogdakis, Papaefthimiou, and Karampinos. 2003. “A Realistic Approach to Model LiBr–H_2O Smooth Falling Film Absorption on a Vertical Tube.” *Applied Thermal Engineering* 23 (17): 2269–83. https://doi.org/10.1016/S1359-4311(03)00188-1.

Rosa, Pontes, Costa, Penteado, Esche, and Repke. 2020. “An Equation-Oriented Novel Approach for Modeling the Falling Film Absorber Using Rigorous Thermodynamic and Transport Description.” *Chemical Engineering Research and Design* 159 (July): 179–94. https://doi.org/10.1016/j.cherd.2020.04.006.

Rotem, and Neilson. 1969. “Exact Solution for Diffusion to Flow down an Incline.” *The Canadian Journal of Chemical Engineering* 47 (4): 341–46. https://doi.org/10.1002/cjce.5450470407

Sabir, Suen, and Vinnicombe. 1996. “Investigation of Effects of Wave Motion on the Performance of a Falling Film Absorber.” *International Journal of Heat and Mass Transfer* 39 (12): 2463–72. https://doi.org/10.1016/0017-9310(95)00336-3.

Salvagnini and Taqueda. 2004. “A Falling-Film Evaporator with Film Promoters.” *Ind. Eng. Chem. Res*, no. 43: 6832–35.

Saul, and Wagner. 1987. “International Equations for the Saturation Properties of Ordinary Water Substance.” *Journal of Physical and Chemical Reference Data* 16 (4): 893–901.

Sciacovelli, Verda, and Sciubba. 2015. “Entropy Generation Analysis as a Design Tool—A Review.” *Renewable and Sustainable Energy Reviews* 43 (March): 1167–81. https://doi.org/10.1016/j.rser.2014.11.104.

Seol and Lee. 2005. “Experimental Study of Film Flow and Heat/Mass Transfer in LiBr–H_2O Solution Flowing over a Cooled Horizontal Tube.” *International Communications in Heat and Mass Transfer* 32 (3–4): 445–53. https://doi.org/10.1016/j.icheatmasstransfer.2004.07.007.

Shukri, Abdullah Sahal. 2016. “Pressure Loss of Turbulent Power Law Fluid Flow Between Two Parallel Rough Plates.” University of California Riverside.

Soto Francés, and Pinazo Ojer. 2003. “Validation of a Model for the Absorption Process of H_2O(Vap) by a LiBr(Aq) in a Horizontal Tube Bundle, Using a Multi-Factorial Analysis.” *International Journal of Heat and Mass Transfer* 46 (17): 3299–3312. https://doi.org/10.1016/S0017-9310(03)00121-2.

Srikhirin, Aphornratana, and Chungpaibulpatana. 2001. “A Review of Absorption Refrigeration Technologies.” *Renewable and Sustainable Energy Reviews* 5 (4): 343–72. https://doi.org/10.1016/S1364-0321(01)00003-X.

Subramaniam, Vishwanath, Sriram Chandrasekaran, and Srinivas Garimella. 2021. “A 2-D Numerical Analysis of Heat and Mass Transfer in Lithium Bromide-Water Falling Films and Droplets.” *International Journal of Heat and Mass Transfer* 177 (October): 121518. https://doi.org/10.1016/j.ijheatmasstransfer.2021.121518.

Subramaniam, Vishwanath, and Srinivas Garimella. 2009. “From Measurements of Hydrodynamics to Computation of Species Transport in Falling Films.” *International Journal of Refrigeration* 32 (4): 20.

Subramaniam, Vishwanath, and Srinivas Garimella. 2014. “Numerical Study of Heat and Mass Transfer in Lithium Bromide-Water Falling Films and Droplets.” *International Journal of Refrigeration* 40 (April): 211–26. https://doi.org/10.1016/j.ijrefrig.2013.07.025.

Sun, Fu, and Zhang. 2012. “A Review of Working Fluids of Absorption Cycles.” *Renewable and Sustainable Energy Reviews* 16 (4): 1899–1906. https://doi.org/10.1016/j.rser.2012.01.011.

Tahir, Mabrouk, and Koc. 2019. “Review on CFD Analysis of Horizontal Falling Film Evaporators in Multi Effect Desalination Plants.” *Desalination and Water Treatment* 166: 296–320. https://doi.org/10.5004/dwt.2019.24487.

Takamatsu, Hiroshi, Hikaru Yamashiro, Nobuo Takata, and Hiroshi Honda. 2003. “Vapor Absorption by LiBr Aqueous Solution in Vertical Smooth Tubes.” *International Journal of Refrigeration* 26 (6): 659–66. https://doi.org/10.1016/S0140-7007(03)00038-0.

Thu, Kim, Myat, Chun, and Ng. 2013. “Entropy Generation Analysis of an Adsorption Cooling Cycle.” *International Journal of Heat and Mass Transfer* 60 (May): 143–55. https://doi.org/10.1016/j.ijheatmasstransfer.2012.12.055.

Triche. 2018. “Étude numérique et expérimentale des transferts couplés de masse et de chaleur dans l’absorbeur d’une machine à absorption ammoniac-eau.” Ph. D Thesis, Communauté Université Grenoble Alpes. HAL. https://tel.archives-ouvertes.fr/tel-01696252.

https://doi.org/10.1016/j.ijheatmasstransfer.2017.04.008.

Tsatsaronis, George, and Moung-Ho Park. 2002. “On Avoidable and Unavoidable Exergy Destructions and Investment Costs in Thermal Systems.” *Energy Conversion and Management*, 12.

Wakim. 2018. “Etude des machines à absorption pour la valorisation de la chaleur fatale basse température.” Ph.D thesis, Université de recherche Paris Sciences et Lettres. HAL Id : tel-01778402.

Wang, Amos and Kalyanmoy, eds. 2011. *Multi-Objective Evolutionary Optimisation for Product Design and Manufacturing*. London: Springer London. https://doi.org/10.1007/978-0-85729-652-8.

Wang, Li, Xu, Yao, Liu, Su and Wang. 2020. “Review on Liquid Film Flow and Heat Transfer Characteristics Outside Horizontal Tube Falling Film Evaporator: Cfd Numerical Simulation.” *International Journal of Heat and Mass Transfer* 163 (December): 120440. https://doi.org/10.1016/j.ijheatmasstransfer.2020.120440.

Wonchala, Hazledine and Boulama. 2014. “Solution Procedure and Performance Evaluation for a Water–LiBr Absorption Refrigeration Machine.” *Energy* 65 (February): 272–84. https://doi.org/10.1016/j.energy.2013.11.087.

Wu. 2016. “Simultaneous Heat and Mass Transfer in Laminar Falling Film on the Outside of a Circular Tube.” *International Journal of Heat and Mass Transfer* 93 (February): 1089–99. https://doi.org/10.1016/j.ijheatmasstransfer.2015.11.031.

Yoon, Phan, Moon, and Bansal. 2005. “Numerical Study on Heat and Mass Transfer Characteristic of Plate Absorber.” *Applied Thermal Engineering* 25 (14–15): 2219–35. https://doi.org/10.1016/j.applthermaleng.2005.01.004.

Yoon, Phan, Moon, Lee, and Jeong. 2008. “Heat and Mass Transfer Characteristics of a Horizontal Tube Falling Film Absorber with Small Diameter Tubes.” *Heat and Mass Transfer* 44 (4): 437–44. https://doi.org/10.1007/s00231-007-0261-8.

Yuan, and Herold. 2005. “Thermodynamic Properties of Aqueous Lithium Bromide Using a Multiproperty Free Energy Correlation.” *HVAC&R Research* 11 (3): 377–93. https://doi.org/10.1080/10789669.2005.10391144.

Yusoff, Yusliza, Mohd Salihin Ngadiman, and Azlan Mohd Zain. 2011. “Overview of NSGA-II for Optimizing Machining Process Parameters.” *Procedia Engineering* 15: 3978–83. https://doi.org/10.1016/j.proeng.2011.08.745.

Zarea, Farshad, Mehryan, Saffarian, and Beherghani. 2014. “Optimal Design of Plate-Fin Heat Exchangers by a Bees Algorithm.” *Applied Thermal Engineering* 69 (1–2): 267–77. https://doi.org/10.1016/j.applthermaleng.2013.11.042.

Zhan, Yin, You, Zheng, Li, and Zhang. 2019. “Numerical and Experimental Investigation on the Heat and Mass Transfer of Falling Film and Droplet Regimes in Horizontal Tubes LiBr-H_2O Absorber.” *Applied Thermal Engineering* 146 (January): 752–67. https://doi.org/10.1016/j.applthermaleng.2018.10.046.

Zhang and Gao. 2016. “Analytical Solution of Velocity for Ammonia-Water Horizontal Falling-Film Flow.” *Applied Thermal Engineering* 101 (May): 131–38. https://doi.org/10.1016/j.applthermaleng.2016.03.003.

Zio and Bazzo. 2011. “Level Diagrams Analysis of Pareto Front for Multiobjective System Redundancy Allocation.” *Reliability Engineering & System Safety* 96 (5): 569–80. https://doi.org/10.1016/j.ress.2010.12.016.